Fundamental principles behind plasmon-induced processes in polarizable systems

by

Gowri Udayangani Kuda Singappulige

B.Sc., University of Colombo, 2015

AN ABSTRACT OF A DISSERTATION

submitted in partial fulfillment of the requirements for the degree

DOCTOR OF PHILOSOPHY

Department of Chemistry
College of Arts and Sciences

KANSAS STATE UNIVERSITY
Manhattan, Kansas

2021

Abstract

Plasmonic materials enhance light-induced processes because they can accumulate a plethora of energy in a wide range of the electromagnetic spectrum. Understanding the natural laws that govern the plasmon-induced processes such as plasmon decay and photocatalysis remains a challenge due to the ultrafast dynamics of plasmons. Real-time propagation techniques with a quantum mechanical description of electrons in molecules and materials has become a valuable tool to mimic such processes and investigate the dynamical pathways. In this thesis, we explore the plasmon decay mechanisms and the effect of light-related parameters on photocatalytic dissociation of molecules using time-dependent density functional theory.

We identified a decay of the plasmon-like excited state in the tetrahedral Ag_8 cluster within tens of femtoseconds after the resonant external electric field is turned off. The time-dependent off-diagonal density matrix elements, P_{OV} (t), demonstrated that while the single-particle transitions that are responsible for the excited state of interest decline, new transitions start to grow in the absence of the electric field. It was remarkable that these newly emerging transitions oscillate with twice the incident frequency, as evident from the energy domain off-diagonal elements, P_{OV} (ω), Our work on larger tetrahedra, octahedra, and nanorods discovered nonlinear optical enhancement in silver nanoparticles regardless of their size and shape, which arises as a result of plasmon decay. Up to four-photon absorptions were detected in some cases. Additionally, well-separated excited states with a strong oscillator strength appear to decay faster, while a dense manifold of excited states leads to coupling between the closely lying neighboring states.

We also examined the effect of nuclear vibrations on the decay of the plasmon-like peak in naphthalene. We found that certain normal modes induce a decay of the dipole response

within a few hundreds of femtoseconds. Interestingly, the time-dependent difference density indicates for the first time that a dark electronic state, which lies close in energy to the resonant state, results in this decay.

Finally, we present a study on the effect of various electric field parameters including the field strength, polarization direction, and the nature of the excited state on the photodissociation of an oxygen molecule that is bound to a plasmonic silver nanocluster. We observed a strong dependence of the field strength on the photodissociation of oxygen. In addition, the light that was polarized along the direction of charge transfer tended to increase the O-O bond breaking.

Fundamental principles behind plasmon-induced processes in polarizable systems

by

Gowri Udayangani Kuda Singappulige

B.Sc., University of Colombo, 2015

A DISSERTATION

submitted in partial fulfillment of the requirements for the degree

DOCTOR OF PHILOSOPHY

Department of Chemistry
College of Arts and Sciences

KANSAS STATE UNIVERSITY
Manhattan, Kansas

2021

Approved by:

Major Professor
Christine M. Aikens

Copyright

Abstract

Plasmonic materials enhance light-induced processes because they can accumulate a plethora of energy in a wide range of the electromagnetic spectrum. Understanding the natural laws that govern the plasmon-induced processes such as plasmon decay and photocatalysis remains a challenge due to the ultrafast dynamics of plasmons. Real-time propagation techniques with a quantum mechanical description of electrons in molecules and materials has become a valuable tool to mimic such processes and investigate the dynamical pathways. In this thesis, we explore the plasmon decay mechanisms and the effect of light-related parameters on photocatalytic dissociation of molecules using time-dependent density functional theory.

We identified a decay of the plasmon-like excited state in the tetrahedral Ag_8 cluster within tens of femtoseconds after the resonant external electric field is turned off. The time-dependent off-diagonal density matrix elements, P_{OV} (t), demonstrated that while the single-particle transitions that are responsible for the excited state of interest decline, new transitions start to grow in the absence of the electric field. It was remarkable that these newly emerging transitions oscillate with twice the incident frequency, as evident from the energy domain off-diagonal elements, P_{OV} (ω). Our work on larger tetrahedra, octahedra, and nanorods discovered nonlinear optical enhancement in silver nanoparticles regardless of their size and shape, which arises as a result of plasmon decay. Up to four-photon absorptions were detected in some cases. Additionally, well-separated excited states with a strong oscillator strength appear to decay faster, while a dense manifold of excited states leads to coupling between the closely lying neighboring states.

We also examined the effect of nuclear vibrations on the decay of the plasmon-like peak in naphthalene. We found that certain normal modes induce a decay of the dipole response

within a few hundreds of femtoseconds. Interestingly, the time-dependent difference density indicates for the first time that a dark electronic state, which lies close in energy to the resonant state, results in this decay.

Finally, we present a study on the effect of various electric field parameters including the field strength, polarization direction, and the nature of the excited state on the photodissociation of an oxygen molecule that is bound to a plasmonic silver nanocluster. We observed a strong dependence of the field strength on the photodissociation of oxygen. In addition, the light that was polarized along the direction of charge transfer tended to increase the O-O bond breaking.

Table of Contents

List of Figures

List of Tables

Acknowledgements

I would like to express my sincere gratitude for my PhD advisor Prof. Christine Aikens for her incredible support and guidance throughout my graduate studies. Thank you, Christine, for inspiring me to take on challenges and shaping me to a better version of myself.

My graduate research would not have been successful without the wonderful collaborators Prof. Xiaosong Li, Dr. David Lingerfelt, Andrew Wildman, Prof. Christopher Ackerson and his team, Prof. Bossmann, Kayla Eschliman, and Anjana Delpe-Acharige.

I am grateful to senior members of the Aikens group, Dr. Ravithree Senanayake, Dr. Dimuthu Weerawardene, and Dr. Fahri Alkan for sharing their knowledge with me. Thank you to my fellow group members Pratima Pandeya, Olivia Hull, Zhen Liu, Shana Hevenridge and Yuchen Wang for their moral support and peer motivation. I would also like to extend my appreciation to Dr. Bin Liu and his group members for constructive discussions.

I would like to acknowledge the current members of my PhD committee, Prof. Paul Smith, Prof. Christer Aakeröy, Prof. Uwe Thumm, and Dr. Hitesh Bindra, for their time and constructive feedback. I would also like to thank the previous members of my committee, Dr. Viktor Chikan and Dr. Santosh Aryal for their guidance and support in the past years.

Last, but not least, thank you to my family for your outpouring love, laughter and support. You are the reason that I go one step further every day.

Dedication

To my father, in loving memory.

Chapter 1 - Introduction

1.1 Plasmon Resonance, its Applications, and Challenges

The surface plasmon resonance, arising from the strong interaction between light and certain metallic systems, results in attractive tunable properties including absorption, scattering, and local-field enhancement.[1-4] The collective oscillation of surface electrons from one side of a nanoparticle to the other side is responsible for these strong absorption properties.[3-4] Nanoparticles synthesized with noble metals like gold and silver are well known for absorbing light in the UV/Vis or near-IR regions.[1-2, 5] Polycyclic aromatic hydrocarbons are also gaining attention as terahertz and infrared plasmonic materials.[6-8] Therefore, these materials are of great interest to enhance the efficiency of artificial photosynthesis, photocatalysis, bioimaging, photosensitizers, etc. A comprehensive understanding of what governs these extraordinary optical properties and their dynamics is essential for these materials to be effectively used in large-scale applications. The fundamental principles behind static optical properties have been well-described from a theoretical perspective.[9-14] However, little is known from theory about the ultrafast excited-state dynamics and photo-induced reaction pathways in plasmonic systems. This thesis provides theoretical insights into the light-induced processes in polarizable systems at the femtosecond and picosecond time scales. We look at the mechanisms of excited-state decay as well as the light-related factors affecting small molecule activation in plasmon-enhanced photocatalysis.

1.1.1 Origin of the Plasmon Resonance

The mystery of ancient colored glasses including the Lycurgus cup, which shows different colors when illuminated from inside and outside, was unraveled in the early 20th century by the pioneering work of Gustav Mie[9] describing the strong absorption and scattering of nanospheres, whose diameter is smaller than the half of the incident wavelength ($d \ll \lambda/_2$).[4, 9] It is well known

today that the plasmonicity of these nanoparticles arises due to the collective oscillation of electrons that is triggered by the incident light.[1, 3, 5, 11-12, 15-16] In the presence of an external electromagnetic field, electrons are pushed towards one side of the particle, resulting in a dipole due to the positive and negative opposite ends (Figure 1.1a).[17] The subsequent high kinetic energy of electrons causes the electrons to oscillate back and forth. The principal frequency of oscillation is found to be characteristic of the materials under illumination, which is identified in the absorption spectrum. Metal nanoparticles including Ag, Au, Cu, and Al exhibit a strong peak in the extinction spectrum, which accounts for both absorption and scattering cross sections, across the UV/Vis or near IR region. The specific wavelengths of this strong absorption are determined by the size, shape, atomic composition, and the surrounding environment of the nanoparticle.[1-3, 12, 14] Figure 1.1b illustrates the structural dependency of the plasmon resonance wavelength on the geometry and material.[18]

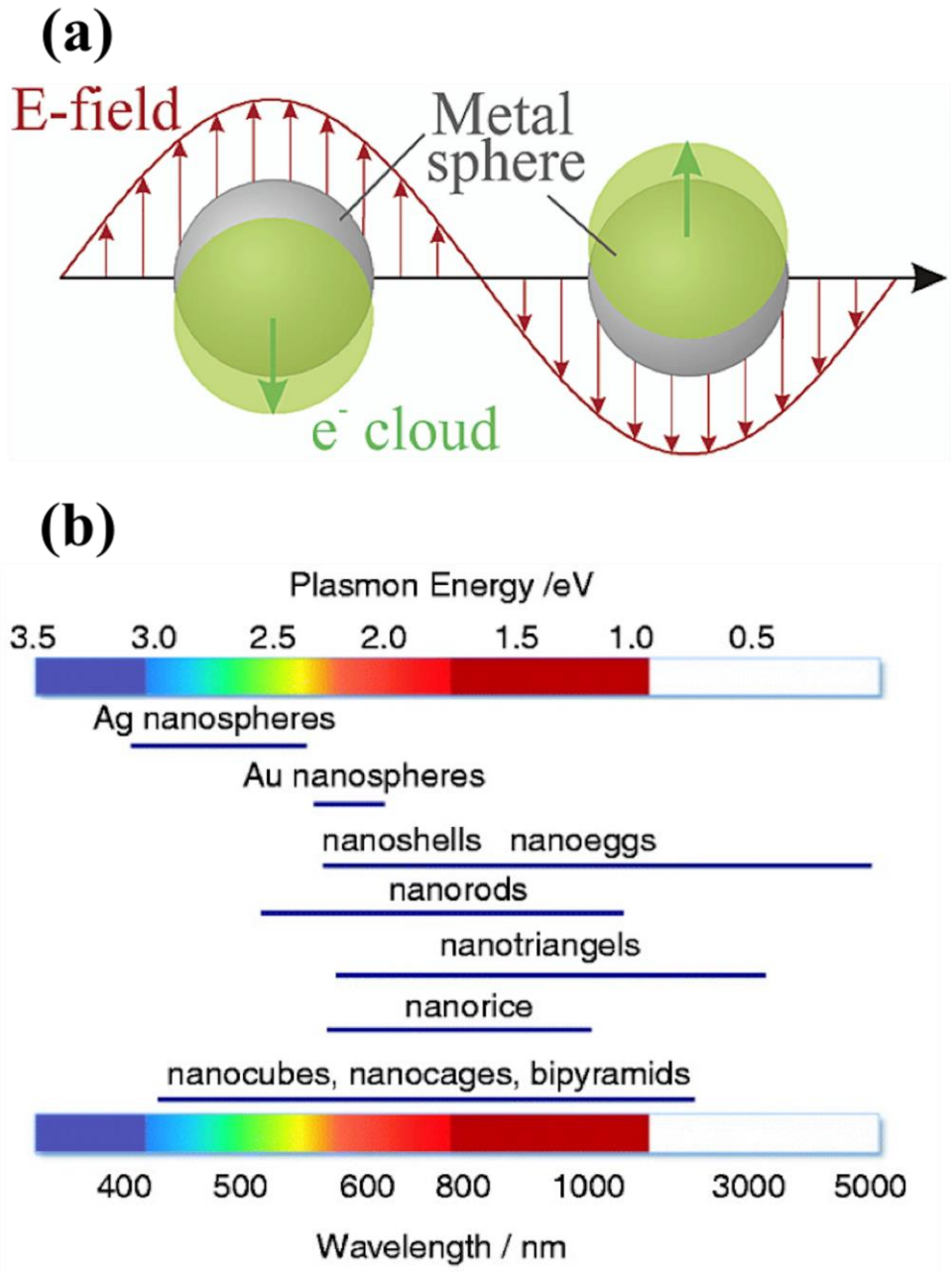

Figure 1.1. (a) Classical picture of plasmonic oscillation in a subwavelength nanoparticle. Reprinted from Ref.[17] with permission. Copyright 2003 American Chemical Society. (b) Shape- and composition-dependence of the spectral properties of nanoparticles. Reproduced from Ref.[18].

Plasmonicity is well described using classical electromagnetic theory, which considers the interaction of light with a dielectric medium.[1, 4, 9] However, particles are described as spheres or nanorods that are larger than a few nanometers. An atomic description of the material is not

included in such classical methods. As a result, the concept of plasmonicity in molecular systems, like atomic nanowires or clusters with a few atoms, has been a topic of debate.[19-22] Some argue that the idea of collective oscillation of electrons in a plasmonic nanoparticle may not be directly transferable to smaller systems.[20, 22] Nevertheless, a quantum mechanical description of these small molecular systems can distinguish between the plasmons and single-electron excitations.[11-12, 23-25] Collective contributions from multiple single-particle transitions, superatomic nature of the excitations, and strong oscillator strengths are the key factors to identify the plasmon-like states in small molecular systems, including Ag/Au nanoclusters and polycyclic aromatic hydrocarbons.[11-12, 23-24] In addition, explicit time-propagation studies confirm the plasmonic nature of small clusters using the oscillating charge density.[25-28] Overall, electronic structure and excited-state properties reveal the origin of plasmonic properties in systems of interest.

1.1.2 Light-Induced Processes Enhanced by Plasmonic Materials

The ability of plasmonic nanostructures to concentrate a large amount of visible light helps improve photovoltaic cells, photocatalysis, bioimaging and sensing techniques.[29-33] This section reviews recent work related to plasmon-enhanced processes.

Plasmonic materials maximize the efficiency of solar cells during various steps in the solar energy conversion process. Conventional photovoltaic semiconductors, like TiO_2 and ZnO, possess a narrow band gap that limits the solar energy absorption to less than 5% of the visible spectrum.[32, 34] The localized surface plasmon resonances in Ag/Au/Cu/Al nanoparticles are ideal to extract most of the solar energy above and below the semiconductor's band gap.[5, 34-39] Ongoing experimental studies focus on synthesizing nanoparticle-semiconductor hybrids that can achieve high current density.[40-43] Embedding plasmonic silver and gold metals on TiO_2 particles, coating SiO_2 on metal crystals, and preparing particles with Au core and SiO_2 outer shells have been

reported.[42] In a recent study, Singh *et al.*[43] reported more than three times higher photocurrent density generation from Ag-TiO_2 thin films than from traditional TiO_2 photoanodes. However, the overall efficiency is reportedly low for these hybrids and continuous research is underway, especially in the electron transfer stage after absorbing solar energy.[15-16, 32, 43-45] Plasmon-induced hot carrier generation plays an important role at this stage.[44-49] A recent study by Song *et al.*[45] reports about 50% hot electron transfer from 1.7 nm size silver nanoparticles to nanoporous anatase TiO_2 films.

Studies on metal/semiconductor composites for photoelectrochemical reactions, including water splitting and carbon dioxide reduction, with a goal of transforming solar energy into chemical energy by producing H_2 and useful fuels are also on the rise.[50-58] The effect of morphology and intrinsic properties in metal clusters and metal/semiconductor hybrids (with Au, Ag and Pt metals) on photoelectrochemical transformation have been widely studied.[50, 59] Numerous theoretical works have been dedicated to understanding the formation and dynamics of hot carriers on plasmonic materials that are valuable in these solar energy conversion processes.[26, 47, 49, 60-61] For example, electronic structure calculations suggest that while Ag with a low-lying d-band compared to Au may be beneficial for generating hot carriers in a wider energy window, Ag may not be optimal for extracting hot carriers due to the fast decay of these hot carriers.[47, 60]

Photoactivation of small molecules for industrial and renewable energy purposes is another active area of plasmon research. Bond breaking of very stable molecules like H_2, O_2, N_2, CO_2, and NH_3 require high temperature and pressure, due to the high activation barrier associated with bond dissociation.[62-65] Catalysis using metals excited at the plasmon resonance has shown not only an enhancement of dissociation ability, but also selective product formation.[62, 66-67] Room temperature H_2 dissociation on plasmonic gold,[67] CO_2 conversion on Al@Cu_2O antenna-reactor

heterostructures,[54] and NH_3 dissociation on aluminum based complexes[68] are a few examples of plasmon-driven small molecule activation. Photo-dissociation of oxygen on silver surfaces has been demonstrated experimentally towards selective production of epoxide.[31, 62, 66, 69-70] Kazuma *et al*. also recently showed the photodissociation of S-S bond in dimethyl disulfide (CH_3SSCH_3) on Cu and Ag surfaces.[71] Recent theoretical studies also provide evidence that plasmonic nanomaterials can easily break strong bonds in small molecules in the presence of light.[63, 72-76] Overall, Ag, Au, Cu, and Al metals appear to enhance chemical transformation under the illumination of visible light.[31, 52, 62, 77-81]

Silver-containing plasmonic nanomaterials have become promising materials for solar cell design,[82] water splitting reactions,[45] small molecule activation[62, 70] and drug detection.[83] However, the ultrafast plasmon loss in silver is the main issue regarding its efficiency. Section 1.3 discusses the concept of plasmon dynamics and our current knowledge of possible plasmon decay pathways.

1.2 Molecular Plasmons in Acenes

Graphene-based materials display plasmonic features in the infrared and terahertz regions.[84-86] Studies demonstrate tunable spectral properties[84-85, 87] and propagating plasmons[88] in graphitic compounds, which support light manipulating methods like nanoimaging and optical devices. Dating back only to a few decades, graphene plasmonics is a relatively new area of research compared to the plasmonic properties in noble metal nanoparticles.[89] Therefore, insights into its physical phenomena are still under investigation. One interesting property of graphene is its long-lasting plasmon lifetime compared to the noble metals, which is attributed to polariton formation.[6-8, 90-91] Polaritons refer to the phenomenon that the light is trapped/localized into a part of the molecule due to nuclear rearrangement. Therefore, incorporating nuclear motion is vital to understand the dynamical nature of the plasmons in graphene. Most theoretical work has been

focused on studying the building blocks of graphene such as acenes and polycyclic aromatic hydrocarbons (PAH).[6-7, 12, 28] In addition, optical response of graphene nanostructures has been studied using both classical and quantum electromagnetic theories.[92-95]

The origin of spectroscopic properties in acenes has been extensively studied both experimentally[96-98] and theoretically.[99-104] The optical features of acenes consist of a weak α peak, a strong β peak and several p-band peaks. Naphthalene is shown as an example in Figure 1.2. The α and β peaks are polarized along the long axis of acenes (Figure 1.2b). The strong β peak arises due to the constructive contribution of multiple single-particle transitions, whereas the weak α peak originates from the destructive contribution from the same transitions. In addition to the α and β peak, the p-band peaks arise from single-particle transitions that are polarized along the plane of the molecule (Figure 1.2b). Due to the collective nature of the excitations, the β peak is considered to be plasmon-like.[104]

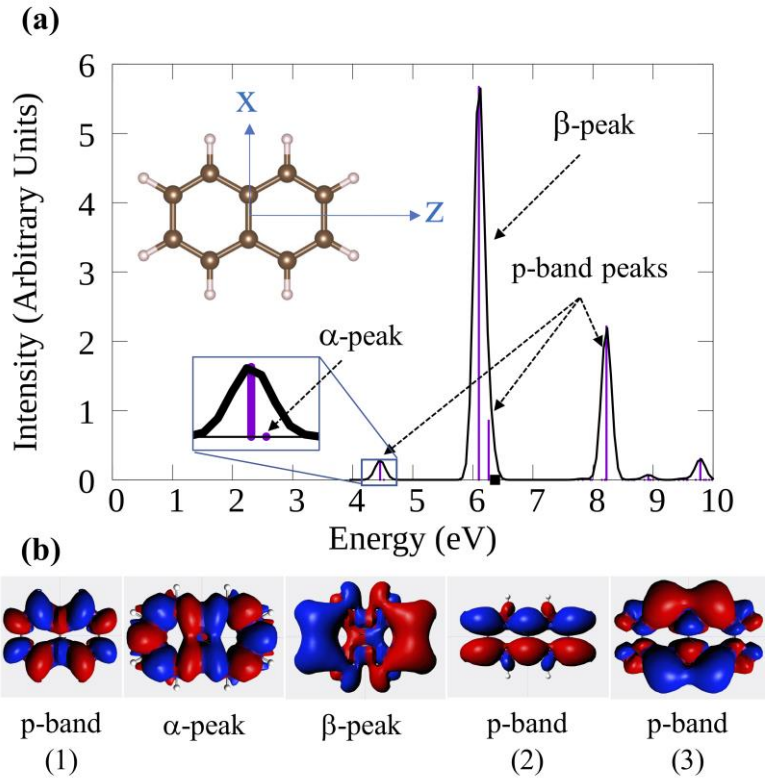

Figure 1.2. Spectral features of naphthalene. (a) Electronic absorption spectrum computed using LR-TDDFT. Reprinted with permission from Ref.[28]. Copyright 2020 American Chemical Society. (b) Transition fit densities of excited states demonstrating the polarization direction (cartesian axes shown in (a)).

Even though the origin of static electronic structure properties in acenes have been well-established, knowledge of the dynamics of plasmon-like states in acenes or polycyclic aromatic hydrocarbons is limited. Plasmon dynamics in acenes focusing on the effect of nuclear motion on the plasmon-like β peak is discussed in Chapter 5.

1.3 Plasmon Dynamics

1.3.1 Plasmon Decay

Although plasmonic materials have the potential to boost the efficiencies of applications discussed in section 1.1.2, rapid plasmon decay remains a challenge.[7, 105-106] After absorbing light by metallic nanomaterials, several processes including electron dephasing, scattering, and

vibrational relaxation can occur (Figure 1.3).[105] In addition, some materials exhibit radiative decay via photoluminescence.[2, 7] Electron dephasing and scattering are typically faster (femtoseconds) than electron-phonon scattering and vibrational resonance (picoseconds). Beyond this time scale, the energy may also dissipate into the surrounding environment as heat.[105]

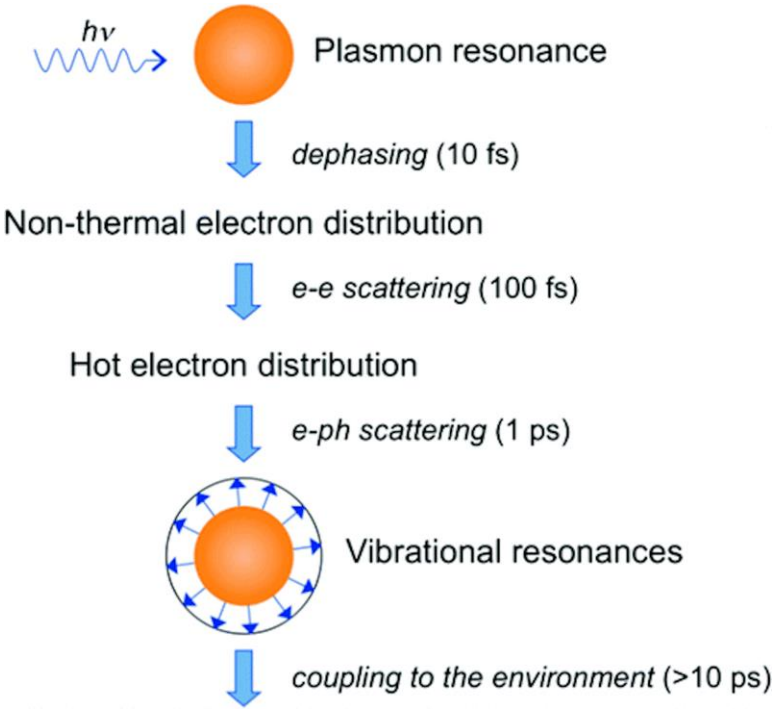

Figure 1.3. General scheme of events that occur after illuminating metal nanoparticles and their approximate timelines. Reprinted with permission from Ref. [105]. Copyright 2011 American Chemical Society.

Noble metal nanoparticles undergo rapid dephasing due to the electron-electron scattering which occurs on the femtosecond time scale.[3, 106-108] Experimental[44, 46, 48] and theoretical[47-49] work predicts that hot-carrier generation in metallic systems is another plasmon decay pathway. Hot-carrier generation, however, has its own advantages in photovoltaic and photocatalytic applications and is thought to enhance the solar energy conversion processes. Nevertheless, the lifetime and the specific decay mechanism are unknown and are thought to be different from one material to another. Identifying the mechanism in a given material is vital to improve its applicability in light-

induced processes. Therefore, we carry out first-principles electron dynamics research to unravel the fundamentals of plasmon decay in silver nanoclusters.

1.3.2 The Fate of Plasmon Resonances in Nanoclusters: A Theoretical Perspective

Due to the lack of fundamental knowledge of the plasmon decay mechanism and electron transfer process during the energy and chemical conversions, most theoretical studies have been dedicated to exploring subsequent processes that occur after light absorption.[26, 47, 49, 61] For example, using Fermi's golden rule to calculate plasmon decay into hot carriers, Forno and coworkers showed that small metal spheres (Na, K, Al, Cu, Ag, and Au) that are less than 16 nm induce more hot carriers compared to larger 40 nm clusters.[49] Sundraraman *et al*. demonstrated the sensitivity of electronic structure, especially the d-band in Au, Ag and Au, on the formation of hot carriers.[47] Recent real-time electron dynamics work by Rossi and others demonstrated the variation in hot electron and hole distribution on various facets of icosahedral silver nanoclusters.[61] Overall, the effect of size, shape, dielectric environment, and surface structure on hot carrier generation in nanoclusters ranging from few tens to hundreds of atoms have been explored using theory.[26, 44, 46-49, 60-61, 67]

Introducing vibrational degrees of freedom in first principles time propagation calculations on silver nanoclusters is a challenge due to computational complexity. A handful of research has been done using the Ehrenfest molecular dynamics method. Donati and coworkers demonstrated drastic decay of the plasmon-like longitudinal state of a model silver nanowire resulting from the out-of-chain vibrational motion.[109] Dynamics of plasmon-induced small molecule activation on silver atomic chains has also been recently studied.[75, 110] These recent works bring attention towards the underexplored Ehrenfest approach as a promising tool for studying electron-nuclear dynamics.

1.4 Linear and Nonlinear Optical Properties

The response of matter due to its interaction with radiation can be measured by the amount of absorbance. Experimentally, one would measure the transmittance from a sample subjected to light i.e., the ratio of the transmitted intensity and the incident intensity, and convert the response into absorption, by taking the negative log of transmittance, to identify the optical response of the material.[111] Optical spectroscopy refers to the interaction of matter with the visible range of the electromagnetic radiation and results in electronic excitations of the materials under illumination. In the conventional weak perturbation limit, the response is linearly proportional to the external electric field and the higher order dependencies can be neglected.[112] In fact, the strong plasmonic nature in small nanomaterials (less than 20 nm) originates from linear absorption in the visible region.[113] The theoretical computations of the linear optical response are discussed in section 2.3.

However, at the strong perturbation limit, the induced dipole moment starts to depend on higher-order terms of the external electric field resulting in nonlinear optical phenomena such as two-photon absorption.[112, 114] The theoretical details of nonlinear absorption will be discussed in the section 2.6. Experimental studies[115-116] report strong second-order nonlinear optical response in silver and gold nanoparticles. Second- and third-order polarizability calculations[117-118] also provide more evidence for nonlinear optical response in silver nanoclusters. In recent real-time dynamics work, Yan *et al*.[119] report an enhancement of the nonlinear response of a silver atomic chain upon adsorbing polar molecules such as water. We demonstrate for the first time the emergence of nonlinear optical response as a result of plasmon decay in silver nanoclusters, which will be discussed in Chapters 3 and 4 in this thesis.

1.5 Objectives

This thesis focuses on mechanistic studies of light-induced processes such as plasmon decay and photodissociation in electronically polarizable systems. There is a timely need to understand the ultrafast decay mechanisms of plasmonic states in order to effectively use plasmonicity in large-scale applications. While it is experimentally challenging to detect electron dynamics at femtosecond time scales, theoretical time propagation methods are able to capture ultrafast dynamics. The work presented in this thesis investigates the decay of plasmon-like states in silver nanoparticles and acenes using real-time propagation techniques such as real-time time-dependent density functional theory (RT-TDDFT) and Ehrenfest dynamics. The goal of the projects discussed in Chapters 3 and 4 is to identify the fate of the plasmon-like states in silver nanoclusters at a very fast time scale. The dynamics is constrained in the electronic degrees of freedom for the silver clusters. Chapter 5 moves to incorporating the nuclear degrees of freedom and studies the effect of the nuclear vibrational motion on the plasmonic state of naphthalene.

Once a thorough understanding of the excited state dynamics of silver nanoparticles is achieved, we study the effect of various parameters of the incident light on the photoexcitation of molecular oxygen on a silver cluster in Chapter 6. Silver has been found to be significantly better performing towards oxygen activation.[62, 69, 120] We will examine the excited states of the $O_2@Ag_8$ complex and the dissociation trends with applied electric field strength, polarization direction and excitation energy.

Chapter 2 - Theoretical Methods

2.1 Fundamentals of Electronic Structure Theory

2.1.1 Time-Independent Schrödinger Equation

The primary goal in quantum mechanics is to solve the time-independent Schrödinger equation (TISE) (2.1.1)[121], where $\hat{\mathcal{H}}$ (Hamiltonian) is the total energy operator and Φ is the total wavefunction, which formulates the state of electrons in a fixed nuclear potential. The Hamiltonian of a system with M nuclei and N electrons can be constructed as in (2.1.2)[121], which accounts for the kinetic energy of the electrons and nuclei, electron-nuclear potential energy, electron-electron repulsion, and the nuclear-nuclear repulsion energies. Note that we use atomic units throughout this chapter.

$$\hat{\mathcal{H}}|\Phi\rangle = E|\Phi\rangle \tag{2.1.1}$$

$$\begin{aligned}\hat{\mathcal{H}} &= -\sum_{i=1}^{N}\frac{1}{2}\nabla_i^2 - \sum_{A=1}^{M}\frac{1}{2M_A}\nabla_A^2 - \sum_{i=1}^{N}\sum_{A=1}^{M}\frac{Z_A}{r_{iA}} + \sum_{i=1}^{N}\sum_{j>i}^{N}\frac{1}{r_{ij}} + \sum_{A=1}^{M}\sum_{B>A}^{M}\frac{Z_A Z_B}{R_{AB}} \\ &= \hat{T}_e + \hat{T}_n + \hat{V}_{e-n} + \hat{V}_{e-e} + \hat{V}_{n-n}\end{aligned} \tag{2.1.2}$$

Under the Bohn-Oppenheimer approximation,[122-123] which originates from the idea that the ultrasmall electrons move very fast relative to the large, slow-moving nuclei, the kinetic energy of the nuclei ($\hat{T}_n$) is neglected and the nuclear-nuclear potential ($\hat{V}_{n-n}$) is held as a constant. Under this approximation, the wavefunction can be rewritten in the form of an electronic wavefunction that is parametrically dependent upon the nuclear coordinates. The problem is therefore narrowed down to solving the electronic structure problem with electronic Hamiltonian, $\hat{\mathcal{H}}_{el} = \hat{T}_e + \hat{V}_{e-n} + \hat{V}_{e-e}$, and electronic wavefunction Ψ_{el}.[121-124]

The electronic wavefunction of a single electron can be expressed as a product of a spatial and a spin function, altogether called a spin orbital, $\chi(x) = \psi(r)\alpha(\omega)$ or $\chi(x) = \psi(r)\beta(\omega)$. The spatial function of an electron is described using a basis set (section 2.1.2), typically a set of Slater- or Gaussian-type functions, while the spin of an electron can have either up or down spin, commonly denoted as alpha $\alpha(\omega)$ and beta $\beta(\omega)$ respectively. In this context, a molecular orbital (MO) is defined as the wavefunction of a single electron. While seemingly simple, the TISE can only be solved exactly for one-electron systems such as the hydrogen atom and H_2^+. Hence, quantum chemistry methods have been developed over the years to better represent the electronic system more efficiently.

The Hartree-Fock (HF) method provides a fundamental framework to obtain an approximate solution to the TISE; it is the simplest ab-initio method.[125] In a nutshell, the electronic wavefunction is approximated as a Slater determinant (2.1.3) of single particle wavefunctions and the energy is determined self consistently.[121, 124] In this thesis, we use Kohn-Sham density functional theory whose formalism is similar to Hartree-Fock.

$$\Psi_{el}(x_1, x_2, \cdots, x_N) = \frac{1}{\sqrt{N!}} \begin{vmatrix} \chi_i(x_1) & \chi_j(x_1) & \dots & \chi_k(x_1) \\ \chi_i(x_2) & \chi_j(x_2) & \dots & \chi_k(x_2) \\ \vdots & \vdots & \dots & \vdots \\ \chi_i(x_N) & \chi_j(x_N) & \dots & \chi_k(x_N) \end{vmatrix} \qquad (2.1.3)$$

2.1.2 Basis Sets

Defining a set of spatial functions to accurately describe electrons in atoms and molecules is a key aspect of improving a quantum chemical computation. Two most common types of basis sets are Slater-type and Gaussian-type basis functions; the forms of a 1s-like orbital defined in the two types are given in (2.1.4), where ζ and α are known as Slater and Gaussian orbital exponents, respectively.[121, 126]

$$\psi_{1s}^{STO} = \left(\frac{\zeta^3}{\pi}\right)^{1/2} e^{-\zeta r} \text{ and } \psi_{1s}^{GTO} = \left(\frac{\alpha^3}{\pi}\right)^{3/4} e^{-\alpha r^2} \quad (2.1.4)$$

Gaussians are computationally more feasible to handle than Slater orbitals. However, the accuracy in Gaussian-type functions degrades at the nucleus. As a solution, a Slater-type orbital was constructed using a linear combination of a few Gaussian functions (known as primitives) and denoted as STO-NG, where N is the number of primitives.[126] A minimal basis can be defined using one such function per one atomic orbital (1s, 2s, $2p_x$, $2p_y$, $2p_z$, etc.).[121, 126] Incorporating more than one function per orbital, often designated as double-ζ (DZ) for two functions or triple-ζ (TZ) for three functions, was introduced to improve the accuracy.[126] Sometimes it is cost efficient to treat the core orbitals with a minimal basis, while representing the valence orbitals with two or three functions; this is known as a split-valence basis set. For instance, 6-31G is a well-known Gaussian-type function with one contracted Gaussian function of 6 primitives assigned for inner shell orbitals and two contracted Gaussians for the valence shell, one with 3 primitives and a single diffuse primitive (with a smaller α). The distortion of the orbitals when forming bonds between atoms is often accounted using additional polarization functions (e.g. DZP and 6-31G(d,p).[126] We used the 6-31G(d,p) (also noted as 6-31G** in the literature) basis set for the work on naphthalene presented in this dissertation. The notation (d,p) indicates the addition of d-type orbitals to atoms other than H and p-type orbitals to H to account for the polarization.

2.1.3 Relativistic Effects

The relativistic effects arise from the high kinetic and potential energy of electrons in atoms with large nuclei and is often not taken into account in standard ab-initio methods.[127-128] When computing properties of molecular systems with heavy atoms including Ag and Au, inclusion of relativistic effects has been shown to be critical.[127-128] Relativistic effects can be directly added to the Hamiltonian as an additional term in (2.1.2), or indirectly with effective core potentials

(ECP).[128-129] In the ECP method, the potential energy coming from the core electrons is computed without the explicit treatment of the electrons and therefore improves the efficiency for large atoms.[129-130] Another advantage of ECPs is that the relativistic effects can also be added to the core potential, often called relativistic effective core potential, which improves the accuracy for heavy-atom systems with a comparatively low cost compared to an all-electron relativistic method.[129-130] For our calculations on silver clusters, we used the LANL2DZ[127, 131-132] basis set. This particular basis set replaces the core electrons of heavy atoms (up to [Kr] in silver, for example) with a relativistic effective core potential and treats the valence electrons with double-ζ basis functions.[127, 131]

2.2 Density Functional Theory

In the HF method, the many-body electronic wavefunction with N electrons depends on $3N$ spatial and N spin coordinates. In 1964, Hohenberg and Kohn[133] introduced density functional theory (DFT) for an inhomogeneous electron gas, where the electronic structure is described in terms of the electron density. The electronic density depends only on 3 spatial coordinates, which lowers the computational scaling of typical density functional theory calculations to N^3 compared to N^4 in Hartree-Fock. In this section, basic concepts and the formalisms of DFT will be discussed in detail.

2.2.1 Hohenberg-Kohn Existence Theorem

The Hohenberg-Kohn existence theorem[133] proves that for a non-degenerate ground state, there exists a unique electron probability density, $\rho_0(r)$, that determines any molecular electronic property such as the energy. The term 'density functional' originates from the fact that such properties can be written as a functional, which is a function of a density function that depends on the spatial coordinates. The existence theorem states that there is a unique one-to-one mapping

between the ground-state density, ρ_0, and the external potential, $v_{ext}(r)$. The external potential in a molecular system is the nuclear potential acting on the electrons and hence is external to the system of electrons. The value of $v_{ext}(r)$ is different for each position of nuclear coordinates. Also, as the external potential has a one-to-one correspondence with the density, it shares a unique one-to-one correspondence with the Hamiltonian, therefore allowing us to find the ground-state energy of the system, E_0, given by (**2.2.1**). The parameter $\bar{T}[\rho_0]$ is the electronic kinetic energy and $\bar{V}_{ee}[\rho_0]$ is the electron-electron repulsion energy. The overbars denote the average.[133-137]

$$E_0 = E_v[\rho_0] = \int \rho_0(r) v_{ext}(r) dr + \bar{T}[\rho_0] + \bar{V}_{ee}[\rho_0]$$
$$= \int \rho_0(r) v_{ext}(r) dr + F[\rho_0] \qquad (2.2.1)$$

The term $F[\rho]$ is known as the Hohenberg-Kohn functional from which the total energy (here denoted as E_0 for ground state) of a system is defined.[138] However, the form of functionals $\bar{T}[\rho_0]$ and $\bar{V}_{ee}[\rho_0]$ are unknown. Therefore, the ground-state energy E_0 cannot be calculated from ρ_0. However, the Hohenberg-Kohn variational theorem along with the Kohn-Sham formalism outlines a practical protocol to overcome this issue.

2.2.2 Hohenberg-Kohn Variational Theorem

The Hohenberg-Kohn variational theorem narrows down the problem further by proving that the electronic density that minimizes the total energy is the ground state density of the system. Hence, for any trial density ρ_{tr}, the inequality $E_0 \leq E[\rho_{tr}]$ holds, where the exact energy can be obtained if and only if the correct density ρ_0 is used with the correct functional form of $E_v[\rho_0]$. However, the forms of the density functionals, $\bar{T}[\rho_0]$ and $\bar{V}_{ee}[\rho_0]$, remain unsolved for many-electron problem.[133]

2.2.3 Kohn-Sham Formalism

The Hohenberg-Kohn theorems show how to compute ground-state electronic properties from the ground-state density ρ_0 using (**2.2.1**), but they do not provide a practical method to find neither ρ_0 nor E_0 (from ρ_0). Kohn and Sham[136] tackled this problem by mapping a system of interacting electrons to a fictitious noninteracting system of electrons. The Kohn-Sham equations (2.2.2) have the form of a single-particle Schrödinger equation, where $\hat{h}_j^{KS}$ is the one-electron Kohn-Sham Hamiltonian and the $\psi_j^{KS}(r_j)$ are referred to as Kohn-Sham spatial orbitals. The potential energy functions $v_s(r_i)$ act on the ground-state electron density ρ_s which is composed of N noninteracting (fictitious) single-particle electrons that equals to the electron density of the interacting system of interest ρ_0.

$$\hat{h}_j^{KS}\psi_j^{KS}(r_j) = \left[-\frac{1}{2}\nabla_j^2 + v_s(r_j)\right]\psi_j^{KS}(r_j) = \varepsilon_j^{KS}\psi_j^{KS}(r_j) \qquad (2.2.2)$$

Because the ground-state electron density of the fictitious noninteracting system (ρ_s) and the system of interest ($\rho = \rho_0$) is the same, the density of the N-particle system, whose wavefunction is a Slater determinant of the spin-orbitals $\chi_j^{KS}(r_j) = \psi_j^{KS}(r_j)\alpha_j$ or $\psi_j^{KS}(r_j)\beta_j$, is given by (2.2.3).

$$\rho = \rho_s = \sum_{i=1}^{n} \left|\psi_j^{KS}(r_j)\right|^2 \qquad (2.2.3)$$

The Hohenberg-Kohn functional $F[\rho]$ of the interacting system (2.2.4) can be expressed as the sum of the noninteracting kinetic energy $T_s[\rho]$ (2.2.5), the classical electrostatic energy of the charge distribution $U[\rho]$ (2.2.6), and the so-called exchange-correlation (XC) energy $E_{XC}[\rho]$. The $E_{XC}[\rho]$ ideally contains the correction to the kinetic energy $\bar{T}[\rho] - T_s[\rho]$ and the exchange and correlation contributions of electrons, which are not included in the classical Coulomb repulsion energy $U[\rho]$.

$$F[\rho] = T_s[\rho] + U[\rho] + E_{XC}[\rho] \tag{2.2.4}$$

$$T_s[\rho] = -\frac{1}{2}\sum_{j=1}^{n}\int d^3r\psi_j^*(r_j)\,\nabla^2\psi_j(r_j) \tag{2.2.5}$$

$$U[\rho] = -\frac{1}{2}\int d^3r d^3r' \frac{\rho(r)\rho(r')}{|r-r'|} \tag{2.2.6}$$

All the terms in the Hohenberg-Kohn functional $F[\rho]$ have a known form except for $E_{XC}[\rho]$. Therefore, the form of the $E_{XC}[\rho]$ should be approximated. If the correct $E_{XC}[\rho]$ is known, the density functional theory is an exact method in solving the TISE. Kohn-Sham density functional theory has become very successful in predicting many physical properties with a considerable accuracy.[139]

Note that the Kohn-Sham equations (2.2.2) as well as the ground-state electron density (2.2.3) depend on the Kohn-Sham spatial orbitals $\psi_j^{KS}(r_j)$. Therefore, the Kohn-Sham equations need to be solved self-consistently, starting with an approximation to the wavefunctions (consequently the density).

2.2.4 Exchange-Correlation Functionals

As described in the section 2.2.3, the exchange-correlation (XC) functional needs to be approximated due to the fact that the explicit form of the exchange-correlation functional $E_{XC}[\rho]$ is not known. Different approximations have been introduced in the literature and are examined in this section.

As discussed in the initial work by Hohenberg, Kohn and Sham,[133, 136] the simplest form of $E_{XC}[\rho]$ can be expressed as in (2.2.7) assuming a slowly varying local density with distance. The exchange and correlation energy per electron, ϵ_{XC}, is computed using homogeneous electron gas theories.[140] This is called the local density approximation (LDA), and there are several LDA-

type XC functionals published with various parametrizations of different properties. Molecular properties like bond lengths and vibrational energies are found to be predicted surprisingly well with LDA functionals, even though the binding energies usually overestimated.[139, 141]

$$E_{XC}^{LDA}[\rho] = \int dr \epsilon_{XC}(\rho)\rho \tag{2.2.7}$$

However, the electron density of molecular systems can vary in space considerably from a uniform electron gas and can benefit from improvements to the LDA formalism.[135, 139] An example of an improvement is by adding the density gradient dependence into the ϵ_{XC} (2.2.8). This method is known as the generalized gradient approximation (GGA). The electron dynamics work on silver nanoclusters discussed in this thesis use the BP86[142-143] GGA functional. The meta-GGA functionals are the next level of improvement to the exchange-correlation functional, by considering the second-derivative dependence of the density and/or the kinetic energy density, but are not used in this thesis.

$$E_{XC}^{GGA}[\rho] = \int dr \epsilon_{XC}(\rho, \nabla\rho)\rho \tag{2.2.8}$$

Hybrid functionals mix the LDA, GGA, and/or meta-GGA exchange and/or correlation functionals with some amount of the exact Hartree-Fock exchange using empirical mixing parameters. The study of naphthalene (Chapter 5) in this thesis was conducted using the B3LYP[144-145] hybrid functional (2.2.9) with the optimized parameters $a_0 = 0.20$, $a_X = 0.72$, and $a_C = 0.81$. B3LYP is known to perform better for organic molecules while remaining computationally affordable.[146]

$$E_{XC}^{B3LYP} = E_{XC}^{LDA} + a_0(E_X^{exact} - E_X^{LDA}) + a_X \Delta E_X^{B88} + a_C \Delta E_C^{PW91} \tag{2.2.9}$$

Another class of density functionals is the range-separated, or long-range corrected (LC), functionals. In brief, long-range corrected functionals decompose the exchange portion of the functional into short- and long-range terms.[147-151] These functionals perform well for a broad range

of molecular properties including long-range charge transfer and bond dissociation. We use the LC-ωPBE[152] functional for the oxygen dissociation project discussed in this thesis.

The widely used XC functionals under the above classifications are listed in Table 2.1, where it is important to note that when the functional gets more accurate, it becomes more computationally expensive.

Table 2.1 Popular exchange-correlation functionals and their classifications.[141, 153-155] (Jacob's ladder)

Classification	Functional Name
LDA	SVWN, Xα,
GGA	BP86, PBE, BLYP
Hybrid	B3LYP, PBE0, BHHLYP, LC-ωPBE
meta-GGA	TPSS, M06, M06-L, M06-2X

2.3 Time-Dependent Electronic Structure Theory

2.3.1 Electronic Excited States

Section 2.1.2 explained how density functional theory can be used to calculate ground electronic states. This section focuses on the origin and the computational methods needed to compute excited electronic states. When visible light shines on a material, that light is absorbed by the system and excites the electrons into higher electronic states. At this point, the electronic subsystem is no longer in its ground state. The optical spectrum, which compares the incident and emitted light, shows the absorption energies that are characteristic to the excited electronic states of a given molecular system. In other words, from a typical optical spectroscopic measurement, we obtain the information of the electronic excited states compared to the ground state. Additionally, there are certain excitations that are allowed within the dipolar approximation, which are the ones that stand out with a non-zero oscillator strength in the spectrum, also known as bright states. Symmetry-adapted selection rules explain why some states are bright and others are dark,

and will be discussed further in section 2.7. Computing the excited states and the corresponding oscillator strengths for a molecular system requires solving the time-dependent Schrödinger equation, in order to determine the response of the material to an external perturbation. The time-dependent response is converted to the energy/frequency by Fourier transformation to obtain the theoretical absorption spectrum.[156-161] The basic theorems related to response property calculation and the linear-response approach will be discussed in the sections 2.3.2 and 2.3.3 respectively.

2.3.2 Time-Dependent Density Functional Theory

Similar to the Hohenberg-Kohn-Sham formalism in the ground-state DFT, the existence of a unique one-to-one mapping between the time-dependent density $\rho(t)$ and the time-dependent external potential $v_{ext}(t)$ was proven by Runge and Gross.[156] In other words, $v_s[\rho](t) = \rho[v_s](t)$. This theorem led to a time-dependent Kohn-Sham equation, which is given in (2.3.1).[156, 161] The external potential operator $v_s[\rho](r,t)$ and the Kohn-Sham wavefunctions $\psi_j^{KS}(r,t)$ are now time-dependent.

$$i\frac{\partial \psi_j^{KS}(r,t)}{\partial t} = \left[-\frac{1}{2}\nabla^2 + v_s[\rho](r,t)\right]\psi_j^{KS}(r,t) \tag{2.3.1}$$

where,

$$v_s(r,t) = v_{ext}(r,t) + \int d^3r' \frac{\rho(r',t)}{|r-r'|} + v_{XC}(r,t) \tag{2.3.2}$$

The time-dependent external potential, $v_{ext}(r,t)$, includes the form of the external perturbation resembling an electromagnetic light source such as a laser pulse, in addition to the nuclear-electronic potential. The second term is the usual Hartree potential accounting for the Coulomb interaction, and $v_{XC}(r,t)$ is the exchange-correlation functional, which is approximated as described in section 2.2.4. Similar to the time-independent Kohn-Sham orbital representation, the time-dependent electronic density is related to the molecular orbitals via (2.3.3).

$$\rho(r,t) = \sum_{i=1}^{N} \left|\psi_j^{KS}(r,t)\right|^2 \tag{2.3.3}$$

Practical methods of computing the excitation energies and oscillator strengths from the time-dependent electronic structure theory have been explored for several decades. In the weak perturbation regime, the linear-response theory offers an affordable and accurate (excited-states well below the first ionization potential) formalism.[162] This method is known as linear-response time-dependent density functional theory (LR-TDDFT) and is discussed in section 2.3.3. The second method is to explicitly solve the time-dependent Kohn-Sham equations using numerical propagation techniques, which is called as real-time time-dependent density functional theory (RT-TDDFT). The real-time method is extensively used in the work of this thesis and its formalism will be discussed in section 2.4.

2.3.3 Linear-Response Density Functional Theory

When the external perturbation $v_{ext}(r,t)$ is weak enough, the density response, or the density change $\delta\rho(r,t)$, linearly depends on the external field strength via (2.3.4). The density-density response function $\chi(r,r',t-t')$ for a system characterized by the time-dependent Hamiltonian is defined as (2.3.5), where $\theta(t-t')$ is the step function, Φ_0 is the total ground-state wavefunction, and $\hat{\rho}(r,t)$ is the time-dependent density operator.[158-159, 161, 163]

$$\delta\rho(r,t) = \int_{-\infty}^{t} dt' \int dr'\, \chi(r,r',t-t') v_{ext}(r',t') \tag{2.3.4}$$

$$\chi(r,r',t-t') = \frac{1}{i}\theta(t-t')\langle\Phi_0|[\hat{\rho}(r,t),\hat{\rho}(r',t')]|\Phi_0\rangle \tag{2.3.5}$$

The density-density response function converted into the frequency domain using Fourier transformation is given in (2.3.6), where $\Omega_I = E_I - E_0$ are the excitation energies. The summation is over I excited states of the system. The value of η is a small positive number related to the

artificial lifetime of the response, $e^{-\eta t}$.[163] The frequency domain expression of the density-density response gives poles at excitation energies of the system Ω_I and the transition densities as residues.[157-159, 161, 163-164]

$$\chi(r,r',\omega) = \int_{-\infty}^{\infty} dt\, e^{i\omega t}\chi(r,r',t) = \sum_I \frac{\langle\Phi_0|\hat{\rho}(r)|\Phi_I\rangle\langle\Phi_I|\hat{\rho}(r')|\Phi_0\rangle}{\omega-\Omega_I+i\eta} - \frac{\langle\Phi_0|\hat{\rho}(r')|\Phi_I\rangle\langle\Phi_I|\hat{\rho}(r)|\Phi_0\rangle}{\omega+\Omega_I+i\eta} \quad (2.3.6)$$

By expanding the equation in the Kohn-Sham electron-hole transition basis and assuming that the field is turned off at the time of measurement, Casida introduced an eigenvalue problem to solve for the excitation energies.[157, 165] The eigenvalue equation (2.3.7)[159, 164-165] is a matrix diagonalization problem which gives the states with excitation energies Ω_I. The terms $K^H_{ia,jb}$ and $K^{XC}_{ia,jb}$ are the Hartree and exchange-correlation coupling matrices respectively and the P_{ia} elements are the MO-based density matrix elements. This is the standard procedure to compute the absorption spectrum of a system using TDDFT, and the results are reasonably accurate for the low-lying excitations.[157-158, 160-161, 164-165]

$$\begin{bmatrix} A & B \\ B^* & A^* \end{bmatrix}\begin{bmatrix} X \\ Y \end{bmatrix} = \Omega_I \begin{bmatrix} 1 & 0 \\ 0 & -1 \end{bmatrix}\begin{bmatrix} X \\ Y \end{bmatrix} \quad (2.3.7)$$

Where $A_{ia,jb} = (\varepsilon_a - \varepsilon_i)\delta_{ab}\delta_{ij} + K^H_{ia,jb} + K^{XC}_{ia,jb}$,

$$B_{ia,jb} = K^H_{ia,bj} + K^{XC}_{ia,bj},$$

$X_{ia} = P_{ai}$, $Y_{ia} = P_{ia}$, i,j: occupied levels and a,b: virtual levels

The oscillator strength of the I^{th} excited state is computed using (2.3.8).[164-165] The sum over transition dipole moments of the single particle transitions, $\langle\psi_i|\vec{r}|\psi_a\rangle$, gives rise to the total transition dipole moment of the excitation I, $\langle\Phi_0|\vec{r}|\Phi_I\rangle$ and $F_{ia\uparrow,I}$ and $F_{ia\downarrow,I}$ account for the transition of alpha- and beta-spin electrons.

$$f_I = \frac{2}{3}\Omega_I |\langle \Phi_0 | \vec{r} | \Phi_I \rangle|^2 = \frac{2}{3}\omega_I \left| \sum_{ia} \sqrt{\frac{2\omega_{ia}}{\omega_I}} F_{ia} \langle \psi_i | \vec{r} | \psi_a \rangle \right|^2 \quad (2.3.8)$$

where $\vec{r} = \vec{x}, \vec{y}, \vec{z}$, and $F_{ia} = \frac{P_{ia}+P_{ai}}{\sqrt{\omega_{ia}}}$

Overall, LR-TDDFT computes the excitation energies and their oscillator strengths. In addition, the information about single-particle transitions that are responsible for each excitation is also obtained from Kohn-Sham LR-TDDFT.

2.4 Real-Time Time-Dependent Method

2.4.1 Real-Time Time-Dependent Density Functional Theory

In real-time density functional theory (RT-TDDFT), the idea is to propagate the density in real time according to the time-dependent Kohn-Sham equation given in (2.3.1). For a time-varying Hamiltonian, an analytical solution to the TDSE does not exist. However, assuming the Hamiltonian is time-independent during an infinitesimal time step Δt, the Kohn-Sham orbitals, ψ_j^{KS}, can be propagated numerically using a time evolution operator (2.4.1), where $h_j^{KS}(t)$ is the Kohn-Sham Hamiltonian at time t.[159-160, 166-168]

$$\psi_j^{KS}(t + \Delta t) = e^{-ih_j^{KS}(t)\Delta t/\hbar} \psi_j^{KS}(t) \quad (2.4.1)$$

This thesis focuses on the time-dependent optical response, i.e., the electronic response to an external perturbation. The time-dependent Kohn-Sham matrix $K(t)$ in the orthonormal basis is introduced as $K(t) = K_0(t) - \mu \cdot E(t)$, where $K_0(t)$ is the perturbation-free Kohn-Sham matrix, $E(t)$ is the time-dependent perturbation, and μ is the dipole moment. The form of the external potentials $E(t)$ will be discussed later. Usually, $E(t)$ is treated as a classical electronic potential consisting of a vector potential and a scalar potential. In the Liouville formalism, the time-dependent Kohn-Sham equation can be written as (2.4.2), where $P(t)$ is the time-dependent density matrix,.[168]

$$i\frac{dP(t)}{dt} = [K(t), P(t)] \tag{2.4.2}$$

Among the various numerical propagation algorithms, the projects discussed in this thesis use the efficient modified midpoint unitary transformation (MMUT)[169-170] algorithm to propagate the electron density in real-time. The unitary transformation matrix $U(t)$ is defined as (2.4.3), where C and ε are the eigenvectors and eigenvalues of the Kohn-Sham matrix respectively.

$$U(t) = exp\big(i\Delta t K(t)\big) = C(t) \cdot exp\big(i\Delta t \varepsilon(t)\big) \cdot C^{\dagger}(t) \tag{2.4.3}$$

2.4.1.1 Absorption Properties from Real-Time TDDFT

To compute the absorption properties from a real-time simulation, we apply a step-function external field,[159, 171-172] given in (2.4.4), to perturb the electron density along each cartesian direction. This approach mimics the simultaneous excitation of all electronic states and allows us to capture the response of the electronic system. The time-dependent dipole moment in the absence of the external field is then Fourier transformed into the energy domain, $\widetilde{D}(\omega)$, to compute the absorption cross section $\sigma(\omega)$ using (2.4.5), where $\tilde{E}(\omega)$ is the energy domain external perturbation.[160] The response in any direction would be identical for an isotropic molecular system. In the case of an asymmetric system, three separate simulations, where the applied electric field is polarized along the x, y, and z directions, are carried out and the response is summed to generate the total absorption spectrum.

$$E(t) = \begin{cases} E_0; t < 0 \\ 0; t > 0 \end{cases} \tag{2.4.4}$$

$$\sigma(\omega) = \frac{4\pi\omega}{c}\frac{Im\big[\tilde{E}(\omega) \cdot \widetilde{D}(\omega)\big]}{\big|\tilde{E}(\omega)\big|^2} \tag{2.4.5}$$

where $\widetilde{D}(\omega) = \frac{1}{2\pi}\int_{-\infty}^{\infty}\big(\mu(t) - \mu(0)\big)e^{i\omega t}dt$

2.4.1.2 Resonant Excitations and Time-Dependent Variables

To understand the excited-state dynamics, we use a trapezoidal-shaped perturbation oscillating with the resonant energy of excitation. The perturbation is applied for a certain period of time (typically 0-20 fs) to mimic the effect from a continuous-wave laser with resonant frequency (Figure 2.1).

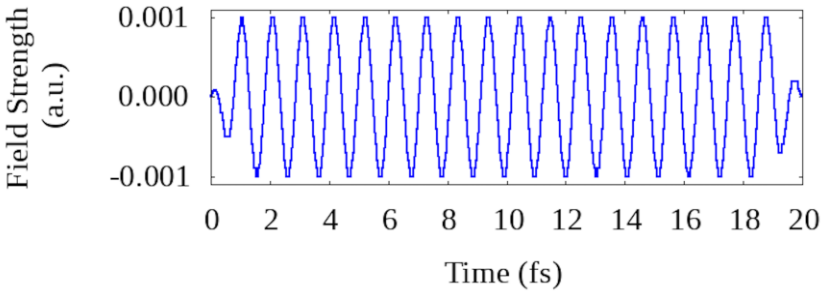

Figure 2.1. Trapezoidal-shaped electric field oscillating with 4 eV of energy.

In this thesis, we study several time-dependent variables to explain the electron dynamics: dipole moment components, quadrupole moments, density matrix elements, and orbital populations. The instantaneous dipole moment is computed using (2.4.6), where Z_A is the nuclear charge of atom A, R_A is the nuclear position of atom A, and D' and $P'(t)$ are the dipole matrix and the density matrix respectively.[167, 169] The prime sign indicates the atomic-orbital (AO) basis whereas variables without primes indicate the orthonormal molecular-orbital (MO) basis.

$$\mu(t) = \sum_A Z_A R_A - D' \cdot P'(t) \tag{2.4.6}$$

The Kohn-Sham orbital population of orbital j, $n_j(t)$, is computed by projecting the density matrix into the field-free orbital basis with (2.4.7).[169]

$$n_j(t) = C_j^\dagger(0) \cdot P(t) \cdot C_j(0) \tag{2.4.7}$$

The density matrix elements projected on the field-free molecular orbital basis, $P_{MO}(t)$, are computed at each electronic step using (2.4.8).[173]

$$P_{MO}(t) = C_0^{\dagger} \cdot P(t) \cdot C_0 \tag{2.4.8}$$

In order to visualize the electron density change compared to the ground state, we computed and analyzed the time-dependent difference densities $\rho^{diff}(t)$ using (2.4.9), where $\rho'(t)$ and $\rho^0(t)$ are the electron densities at time t in two trajectories with and without the external electric field, respectively.[28] We use this formalism in both electron and electron-nuclear dynamics simulations discussed in Chapters 4 and 5.

$$\rho^{diff}(t) = \rho'(t) - \rho^0(t) \tag{2.4.9}$$

2.5 Ab-Initio Molecular Dynamics

In sections 2.1 through 2.4 we discussed the ground and excited electronic structure assuming that the electrons move in a field of fixed nuclei. Here, we turn our attention to the molecular motion in addition to the electron dynamics. In this thesis, chapter 5 addresses the effect of vibrational motion on the plasmon dynamics and chapter 5 studies the photodissociation of molecular oxygen using nonadiabatic molecular dynamics.

2.5.1 Born-Oppenheimer Molecular Dynamics (BOMD)

The simplest formalism for ab-initio molecular dynamics uses the Born-Oppenheimer approximation described in section 2.1.[122] In Born-Oppenheimer molecular dynamics (BOMD), the forces acting on nuclei (F_a) are calculated using (2.5.1) where $E_0(R)$, the ground-state electronic energy, is computed from ab-initio electronic structure methods discussed in section 2.1.2.[174-177] The term $V_{n-n}(R)$ is the nuclear repulsion energy. Electronic potential energy surfaces (PES) are a landscape of the energy in the electronic subsystem from a given set of nuclear coordinates. In BOMD, the nuclear movement is computed using the classical Newtonian motion on these electronic potential energy surfaces (2.5.1), hence classifying BOMD as a mixed quantum

classical molecular dynamics scheme. It is worth emphasizing that the ground electronic state contributes to the potential energy surface in BOMD and no excited electronic states are considered.

$$F_A = M_A \ddot{R}_A = -\nabla_A [E_0(R) + V_{n-n}(R)] \tag{2.5.1}$$

Having calculated the forces that drive the atoms, one can proceed to move the nuclei using a numerical integrator such as leapfrog[178-179] or velocity Verlet.[180-182] The widely used velocity Verlet algorithm was used in the work of this thesis and will be briefly discussed in this section. The momentum of atom A at time $t_{k+1/2}$ is calculated using the current momentum $p_A(t_k)$, the energy gradient with respect to the coordinates of atom A, $g_A(t_k)$, and the time step Δt_N according to (2.5.2). Using the midpoint momentum and the current position of the nucleus, the new position and momentum of atom A are calculated using (2.5.3) and (2.5.4). The TDSE is solved to get the new gradient and thereby the new momentum. The loop keeps going until the desired total time limit is reached.

$$p_A\left(t_{k+1/2}\right) = p_A(t_k) - \frac{1}{2} g_A(t_k) \cdot \Delta t_N \tag{2.5.2}$$

$$x_A(t_{k+1}) = x_A(t_k) + \frac{p_A\left(t_{k+1/2}\right)}{M_A} \cdot \Delta t_N \tag{2.5.3}$$

$$p_A(t_{k+1}) = p_A\left(t_{k+1/2}\right) + \frac{1}{2} g_A(t_{k+1}) \cdot \Delta t_N \tag{2.5.4}$$

2.5.2 Mean-field Ehrenfest Molecular Dynamics

Although many chemical problems benefit from the Born-Oppenheimer approximation, this approximation breaks down in most photochemical and photophysical processes.[183-184] In these cases, excited electronic states are sufficiently populated and nonadiabatic transitions between electronic states can occur. Nonadiabaticity refers to the involvement of excited electronic

states and transitions between two or more electronically adiabatic potential energy surfaces.[185] Accurate modeling of such nonadiabatic processes like laser-induced chemistry, dynamics at metal or semiconductor surfaces, and electron transfer in molecular, biomolecular or electrochemical systems require proper integration of electronic response to fast moving nuclei.

Over the last few decades, several nonadiabatic molecular dynamics (NA-MD) schemes have been proposed and widely used. Among them, Ehrenfest dynamics, Tully's trajectory surface hopping (TSH) and the multiple spawning method are some of the most extensively used techniques.[186] A schematic illustration[186] of these methods is shown in Figure 2.2. In Ehrenfest and surface hopping techniques, the nuclei are treated classically and electrons are treated quantum mechanically. The most expensive and the most accurate method, multiple spawning, includes the quantum effects of nuclei (through a wave function representation of nuclei) that follow classical trajectories.[176, 186] In the surface hopping dynamics, the electronic transitions can occur between two potential energy surfaces near conical intersections based on the hopping probability, which depends on the energy difference between the two states, the non-adiabatic coupling matrix elements, and nuclear momenta. This technique involves a collection of such trajectories; each propagates on a pure adiabatic state at any given time. This gives a stochastic representation of which states are populated. The TSH method becomes computationally demanding when incorporating systems with many atoms because of the necessity of computing adiabatic excited wavefunctions at each timestep in all trajectories. In contrast, Ehrenfest dynamics, which is also called the mean-field method, propagates the atoms in an effective potential averaged over the adiabatic states based on their populations.

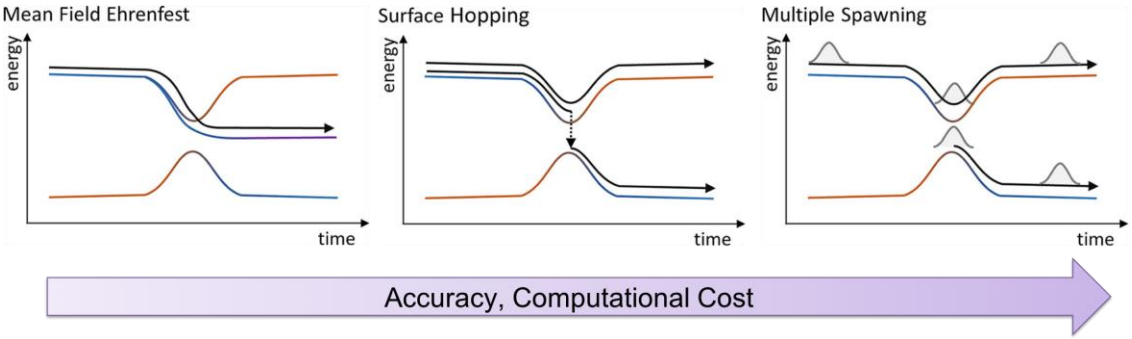

Figure 2.2. Common NA-MD schemes. Reprinted with permission from Ref.[186]. Copyright 2018 American Chemical Society.

The main approximation in the mean-field method is that the energy of the system at a particular time for a given atomic configuration can be considered as the expectation value over all the possible adiabatic states. The force on the atoms can be calculated from the negative gradient of the effective energy of the system as shown in (2.5.5).[174, 182, 187]

$$M_A \ddot{R}_A = -\nabla_A E_{eff} = -\nabla_A \langle \Phi | H_{el} | \Phi \rangle = -g_A \qquad (2.5.5)$$

2.5.2.1 Numerical Integration Methods for Solving TDSE

Integration of the Ehrenfest dynamics using a single time step would require very small time-step (fractions of attoseconds) to account for the fast motion of electrons. On the other hand, to observe the nuclear motion, one needs to run the simulation at least for a few picoseconds or longer. To address this issue efficiently, different approaches that improve the computational efficiency of Ehrenfest dynamics have been implemented. One such propagator, the relax and drive procedure proposed by Micha and co-workers,[188-189] incorporates two different time scales to propagate electron and nuclear motions. During the *relax* step, the electronic TDSE is solved assuming fixed nuclear positions while the drive step includes the motion of atoms.

In this thesis, we use the three-time-step integrator,[182] which includes velocity Verlet (section 2.5.1), a nuclear-position-coupled midpoint Fock integrator, and time-dependent Hartree-Fock with a modified midpoint and unitary transformation (section 2.4.1). The concept was first

applied at the Hartree-Fock level of theory[182] and it has been further integrated into Kohn-Sham density functional theory.[190] A schematic representation of this three-time-step integrator is shown in Figure 2.3. The three time-steps Δt_N, Δt_{Ne}, and Δt_e correspond to the nuclear velocity Verlet, nuclear-position-coupled midpoint Fock integrator, and modified mid-point and unitary transformation (MMUT)[169-170] steps, respectively. The Fock matrix F' (AO-based) is calculated as the sum of one and two electron integrals, $h'(x)$ and $G'(x, P')$ respectively as shown in (2.5.6).[182] Note that the Fock matrix is a function of nuclear coordinates (x) and the electronic density (P'). Due to the slower motion of nuclei compared to that of electrons, it is reasonable to fix the nuclei for several electronic steps (MMUT steps, Δt_e) before recalculating the integrals. Under this assumption, each nuclear Verlet step is divided into n smaller Δt_{Ne} steps; at each step, the Fock matrix is calculated using the integrals calculated at the midpoint of Δt_{Ne} (at $t' + \Delta t_{Ne}/2$) and the density at this time step, $P'(t)$.

$$F' = h'(x) + G'(x, P')$$

where

$$h'_{\mu,\upsilon}(x) = \left\langle \chi_\mu \middle| -\frac{1}{2}\nabla^2 - \sum_A \frac{Z_A}{|r - r_A|} \middle| \chi_\upsilon \right\rangle \text{ and} \tag{2.5.6}$$

$$G'(x, P') = \sum_{\lambda,\sigma} P'_{\lambda\sigma} \left\{ \left[\chi_\mu(1)\chi_\nu(1) \left| \frac{1}{r_{12}} \right| \chi_\lambda(2)\chi_\sigma(2) \right] - \left[\chi_\mu(1)\chi_\sigma(1) \left| \frac{1}{r_{12}} \right| \chi_\lambda(2)\chi_\upsilon(2) \right] \right\}$$

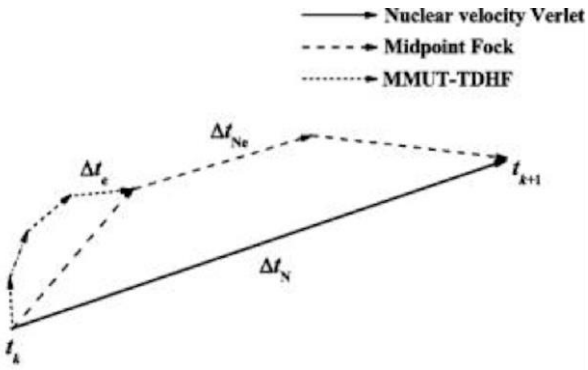

Figure 2.3. Three-time-scale integration scheme for Ehrenfest Dynamics. Reprinted from Ref.[182], with the permission of AIP Publishing.

2.5.2.2 Excitation of Electronic States and Vibrational Modes

In the electron-nuclear dynamics projects, the electronic excitations were activated using either a step-field perturbation or a continuous-wave perturbation as discussed in sections 2.4.1.1 and 2.4.1.2 respectively. In addition to excitation of the electronic states, we selectively activate a vibrational mode to identify the effect of vibrational motion on electronic excitation dynamics and vice versa. To specifically activate each vibrational mode, we compute the atomic velocities assuming a Boltzmann-sampled vibrational energy of the normal mode with five quanta at room temperature.[28, 109] The choice of number of quanta is discussed in Chapter 4.

2.6 Non-Linear Optical Properties

In the previous sections, we discussed the linear response of a system to light under the assumption that the polarizability is linearly proportional to the strength of the electric field, E. The total response function, however, can be expanded to include higher-order terms given in (2.6.1),[191] where α, β, and γ are the first, second and third order hyperpolarizability tensors, respectively. Nonlinear optical effects become significant at intense electric fields and in certain materials.[112, 191-192] While the LR-TDDFT formalism is based on the first-order response, the RT-TDDFT method is able to capture higher-order nonlinear response.

$$\mu_{ind} = \alpha E + \frac{\beta}{2!}E^2 + \frac{\gamma}{3!}E^3 + \cdots \quad (2.6.1)$$

2.7 Symmetry-Adapted Selection Rules

As discussed in section 2.3.1, only the bright dipolar states will be prominent in a typical optical spectrum. The concept of bright and dark dipolar states originates from the symmetry-adapted selection rules. For a closed-shell molecule with all electrons paired, the ground electronic state is always totally symmetric; i.e., the ground state of a water molecule, which belongs to the C_{2v} point group, would belong to the A_1 irreducible representation (C_{2v} character table is provided in Appendix A). In essence, the dipolar selection rules for the allowed excited states indicate that any excitation that belongs to an irreducible representation to which one of the linear functions (x, y, z) belongs is a dipolar-allowed (aka one-photon allowed) transition.[193] In the water example, excitations to A_1, B_1, and B_2 excited states are bright whereas A_2 states would be dark. In addition, the excited states with A_1 irreducible representation will be excited with z-polarized light only because the z linear function belongs to the A_1 irreducible representation whereas x and y belong to the B_1 and B_2 representations.

The selection rules for nonlinear optical properties can be explained in the same way. A two-photon absorption, which is a second-order response property, will be allowed if the state belongs to an irreducible representation to which any quadratic function belongs.[194-195] In the C_{2v} example, any state will be allowed via two-photon absorption because all four irreducible representations contain at least one quadratic function.

Chapter 3 - Ultrafast Nonlinear Plasmon Decay Processes in Silver Nanoclusters

Gowri U. Kuda-Singappulige, David B. Lingerfelt, Xiaosong Li, and Christine M. Aikens, J. Phys. Chem. C **2020**, 124, 37, 20477–20487

3.1 Abstract

Tunable plasmonic properties of metallic nanostructures play a significant role in enhancing various photo-optical phenomena including solar energy conversion, nonlinear optics, photoluminescence and photocatalysis. Understanding the fast plasmon decay mechanisms is essential for developing practical applications utilizing these light-matter interaction processes, but has been a challenge both experimentally and computationally. Among theoretical simulation methods, real-time density functional theory (RT-TDDFT) is a valuable tool to monitor the electron dynamics of molecules subjected to an electric field. Herein, we use the RT-TDDFT method to identify the possible plasmon decay mechanisms of the bare tetrahedral Ag_8 nanocluster. We excite the strong linear plasmonic states and examine dipole response and the electron dynamics in the system. Variation of density matrix elements related to occupied and virtual orbital pairs reveals that the one-photon allowed transitions, which have been excited due to the incident electric field, experience ultrafast decay into high energy transitions, specifically to two-photon allowed transitions. The tetrahedral symmetry representations of these transitions confirm that some of these high energy transitions are only allowed via two-photon absorption whereas others can be activated via both one- and two- photon

absorption. Moreover, this work suggests that the collective excitations present in the system play an important role in accumulating an enormous amount of energy to enhance nonlinear processes. Overall, this work provides insights into a possible plasmon decay mechanism of nanoclusters which is activation of nonlinear processes such as two-photon absorption.

3.2 Introduction

In the presence of electromagnetic radiation, the conduction electrons of noble metal nanoparticles oscillate with a resonant frequency with respect to the nanoparticle core; this phenomenon is known as a localized surface plasmon resonance and results in a strong peak in the optical absorption/extinction spectrum. The frequency and the strength of the oscillation depends on the size, shape and the composition of the nanoparticles.[196-198] Plasmonic features of noble metal nanoparticles including strong absorption of UV/visible and near-infrared (near-IR) portions of the electromagnetic spectrum lead to their use in solar cells,[16, 199-200] bio-medical applications,[201-204] nonlinear optical convertors,[35, 116, 205-209] etc. However, the plasmon resonance decays quickly over time when the irradiation is turned off. Since applications typically benefit from slower damping, there is growing research interest in understanding the possible plasmon decay mechanisms. Excited electrons can slowly decay radiatively into photons[210] and this process is well-understood because they have nanosecond decay times and can be studied experimentally using time-resolved measurements.[198, 211] Faster electron scattering and non-radiative decay pathways, however, have been a subject of debate in recent literature. The electronic dephasing of metal nanoparticles occurs at a fast rate, which is typically within a few tens to hundreds of femtoseconds.[106, 212-213] Therefore, it is experimentally challenging to capture the mechanisms involved in the ultrafast plasmon resonance dynamics. Theoretical computations help understand these fast-electronic processes and ultimately provide a pathway to manipulate the plasmonic

properties of nanoparticles. Classical electrodynamic methods such as Mie theory[214] and discrete dipole approximation (DDA)[215] can be successfully applied to simulate the optical response of large nanoparticles (diameter > 10 nm).[216] However, they do not explicitly treat electrons and are unable to examine processes such as electron-electron scattering and other quantum effects.[14, 217]

Time-dependent density functional theory (TDDFT), especially real-time time-dependent density functional theory (RT-TDDFT),[159, 166] is a powerful tool to monitor fast electron dynamics. This method is currently available in a variety of codes[159, 218-221] and provides optical absorption spectra that are consistent with the results from conventional linear-response time-dependent density functional theory (LR-TDDFT) for diverse systems in a weak field.[27, 222] A recent review on RT-TDDFT has been provided by Goings et al.[160] Due to its computational efficiency for large systems as well as its applicability in the nonlinear regime, RT-TDDFT is beneficial for exploring plasmonic properties and electron dynamics of metal nanoparticles.[26, 171-172, 223-224] Nevertheless, the RT method often lacks information about the origin of the excitations that is naturally generated by the LR method. Several studies, however, show that this information can be resolved. Ding et al.[171] analyzed the time evolution of molecular orbital occupation numbers and demonstrated that collective and in-phase oscillations of single-particle transitions are associated with the transverse plasmon excitations of silver nanowires. Moreover, the variation of the off-diagonal elements of the density matrix corresponding to a pair of occupied and unoccupied orbitals provides a straightforward picture of the time variation of electronic transitions.[225-228] Repisky and co-workers first proposed the dipole-weighted matrix analysis to interpret the molecular orbital transitions corresponding to the spectral energies.[225-226] Bruner et al. introduced a Padé approximation to accelerate the transform of the individual contributions into the frequency domain and demonstrated its efficiency on gas phase water and a nickel porphyrin system.[227] Rossi

et al. recently used this concept to present a benchmark study on small benzene derivatives followed by application to icosahedral silver nanoparticles consisting of 55 to 561 atoms.[228] Sinha-Roy et al. showed the ability to accurately extract transition densities of the excited states from a single δ-kick RT-TDDFT calculation.[229]

The above-mentioned studies were generally limited to static spectral properties rather than the time evolution of plasmons. One exception is a recent theoretical study in which Ma and coworkers[26] suggested that the plasmon resonance of the Ag_{55} cluster decays into single particle excitations that can be identified as hot carriers. In addition, real-time electron dynamics simulations done by Rossi et al.[230] have also identified the plasmon dephasing into hot carriers in large silver nanoparticles. In a recent theoretical study, Yan et al.[119] showed that the hot carriers generated by plasmon decay in silver atomic chains lead to nonlinear effects. It is clear that plasmon induced nonlinear processes including second harmonic generation have become a hot topic in the photonics field.[231-237] However, a clear understanding of plasmon decay mechanisms has not yet been achieved; to fully understand plasmon decay mechanisms, the fast electron dynamics of nanoparticles upon irradiation with light must be further studied within a quantum mechanical framework. In this work, we investigate the electron dynamics of a tetrahedral Ag_8 cluster with RT-TDDFT simulations to explore its fast plasmon decay mechanisms.

3.3 Computational Details

The electron dynamics of the Ag_8 (T_d) cluster was studied using RT-TDDFT in a development version of the Gaussian software.[236] The BP86[140-141] exchange-correlation functional with the LanL2DZ[129, 237-238] effective core potential basis set were used for all calculations. Geometry optimization calculations were carried out followed by TDDFT calculations on the optimized structures (coordinates provided in the SI). The highly symmetric T_d isomer of the Ag_8 cluster has been previously observed to be the global minimum structure (Figure 3.1, inset).[239] We first compared the optical absorption properties of Ag_8 obtained from both LR-TDDFT and RT-TDDFT. In the LR calculations, 800 electronic excitations were calculated to obtain the optical absorption energies up to around 9 eV. A Gaussian broadening with a full width at half maximum (FWHM) of 0.2 eV was used when plotting absorption spectra with LR-TDDFT to account for the experimental vibrational broadening at room temperature. To determine the spectral properties from RT-TDDFT, the electron density is converged to self-consistency in the presence of a step function external field applied along the z axis with an amplitude of 0.001 a.u. (~3.57×10^{13} W/cm^2). In this manner, all electronic states are excited simultaneously. Then, the density is propagated for 120 fs with a time step of 0.0012 fs. The time-dependent dipole moment is related to the absorption cross section by Fourier transformation into the frequency domain.[158, 164] An exponential damping corresponding to a Lorentzian spectral line shape (1/ Γ = 855 a.u. of time) was added to the time-dependent dipole moment $D'(t) = D(t)exp^{-\pi\Gamma t}$, where $D(t)$ is the observed dipole moment and $D'(t)$ is the damped dipole moment) before Fourier transformation, which gives a broadening similar to our LR-TDDFT calculations.

To explore the plasmon decay mechanisms, we study the electron dynamics of the Ag_8 cluster subjected to a trapezoidal-shaped electric field along the z axis using RT-TDDFT. The field is gradually increased to its highest amplitude of 0.001 a.u. (~3.57×10^{13} W/cm^2) over the time period from 0 to 1 fs. The field is then applied continuously at a constant amplitude and a constant frequency until 19 fs when the amplitude function starts to decrease, and is completely turned off at 20 fs (Figure B-1a). The gradual increase and decrease avoid artifacts that can arise from a sudden application of a continuous wave field. In this way, one can study the electron dynamics of a system excited by a quasi-monochromatic laser, which we will refer to as a continuous wave throughout the text, applied for a certain period of time. The variation of the dipole moment of Ag_8 resulting from the applied field is shown in Figure B-1b. The Fourier transform of a field applied with a frequency corresponding to 3.96 eV confirms that the excitation is indeed centered around 3.96 eV (Figure B-1c). In this work, the frequencies that are resonant with the lowest two excitation energies of the Ag_8 cluster, as determined by LR-TDDFT, are used as the frequencies of the applied electric fields. The electron density is allowed to propagate for a total time of 240 fs with a 0.002 fs step size and the dipole response was inspected.

Numerical propagation of the time-dependent Kohn-Sham equation is used to determine the electron dynamics via the time-dependent density matrix in the molecular orbital basis.[169, 242] The time-dependent Kohn-Sham equation in an orthonormal basis is given in (3.3.1), where $P(t)$ is the time-dependent density matrix in the orthonormal basis, $K(t)$(3.3.2) is the time-dependent Kohn-Sham matrix under the influence of an external electric field $E(t)$, and $K_0(t)$ is the unperturbed Kohn-Sham matrix.

$$i\frac{dP(t)}{dt} = [K(t), P(t)] \tag{3.3.1}$$

$$K(t) = K_0(t) - \mu \cdot E(t) \tag{3.3.2}$$

The Kohn-Sham matrix in its eigenspace is written as:

$$C^{\dagger}(t_n) \cdot K(t_n) \cdot C(t_n) = \varepsilon(t_n) \tag{3.3.3}$$

where $C(t_n)$ and $\varepsilon(t_n)$ are the eigenvectors and eigenvalues of the perturbed Kohn-Sham matrix respectively. The electron density is propagated using the modified mid-point unitary transformation algorithm (MMUT).[169-170] In this formalism the unitary transformation matrix *U* at time t_n is calculated as follows where Δt is the time step:

$$U(t_n) = exp\big(i\Delta t K(t_n)\big) = C(t_n) \cdot exp\big(i\Delta t \varepsilon(t_n)\big) \cdot C^{\dagger}(t_n) \tag{3.3.4}$$

The density matrix at time t_{n-1} is then propagated to time t_{n+1} using $U(t_n)$ (3.3.5).

$$P(t_{n+1}) = U(t_n) \cdot P(t_{n-1}) \cdot U^{\dagger}(t_n) \tag{3.3.5}$$

At each time step, the time-varying density matrix is also transformed into the eigenbasis of the initial perturbation-free Kohn-Sham matrix (i.e., the canonical molecular orbital basis) according to (3.3.6), with $C_0^{\dagger} \cdot K_0(t_0) \cdot C_0 = \varepsilon_0(t_0)$. P_{MO} refers to the density matrix in the molecular orbital basis. We examine the variation of off-diagonal elements of the density matrix $P_{OV,}$ corresponding to pairs of occupied (O) and virtual (V) molecular orbitals, to track the contributions from each occupied-to-virtual molecular orbital pairs to the total electron dynamics. The Fourier analysis of P_{OV} identifies the frequency of its oscillation. Exploring these time-varying off-diagonal elements of the MO-based density matrix after exciting a single electronic state is our unique approach to discover the possible electronic transitions that emerge as a result of the plasmon decay.

$$P_{MO}(t) = C_0^{\dagger} \cdot P(t) \cdot C_0 \tag{3.3.6}$$

3.4 Results and Discussion

3.4.1 Electronic structure and absorption properties of Ag_8

An orbital energy level diagram of the tetrahedral Ag_8 cluster illustrating the primary orbitals that are involved in the electronic transitions is shown in Figure 3.1. In addition to the standard orbital designations under tetrahedral symmetry, the orbitals are also labeled with their closest spherical superatomic[243] molecular orbital notation. In superatomic nomenclature,[243] capital letters such as S and P are used to represent molecular orbitals that are delocalized throughout the entire nanocluster; the letters S and P indicate that these molecular orbitals have the same nodal symmetry as the spherical harmonics representing *s* and *p* atomic orbitals. Then, the electronic configuration arising from eight 5*s* valence electrons of silver atoms can be designated as $1S^2 1P^6$. As shown in Figure 3.1, the 1S orbital (45) with a_1 symmetry lies very low in energy compared to the frontier orbitals. The HOMO level is triply degenerate corresponding to a 1P-like set of orbitals (74-76) with t_2 symmetry. An additional set of molecular orbitals that are mostly localized on the silver atoms and arise from linear combinations of atomic 4d orbitals lies between the 1S and 1P levels; this set of orbitals is denoted as the d-band. The specific T_d point group symmetry representations of these d-band orbitals are shown in Figure 3.1. The 1D-type virtual orbitals (77-79, 81-82) are split into two sets with t_2 and e symmetry due to the tetrahedral geometry of the cluster. The superatomic 2S orbital (80) with a_1 symmetry lies between the two sets of 1D orbitals. Above these orbitals, the degenerate 2P orbitals (83-85) lie higher in energy followed by 1F-type orbitals (87-92); the triply degenerate 2P orbitals have t_2 symmetry and the 1F orbitals split into three sets with a_1, t_1 and t_2 representations in the tetrahedral environment. The HOMO-LUMO gap of the tetrahedral Ag_8 cluster is found to be 2.31 eV at the BP86/LanL2DZ level of theory.

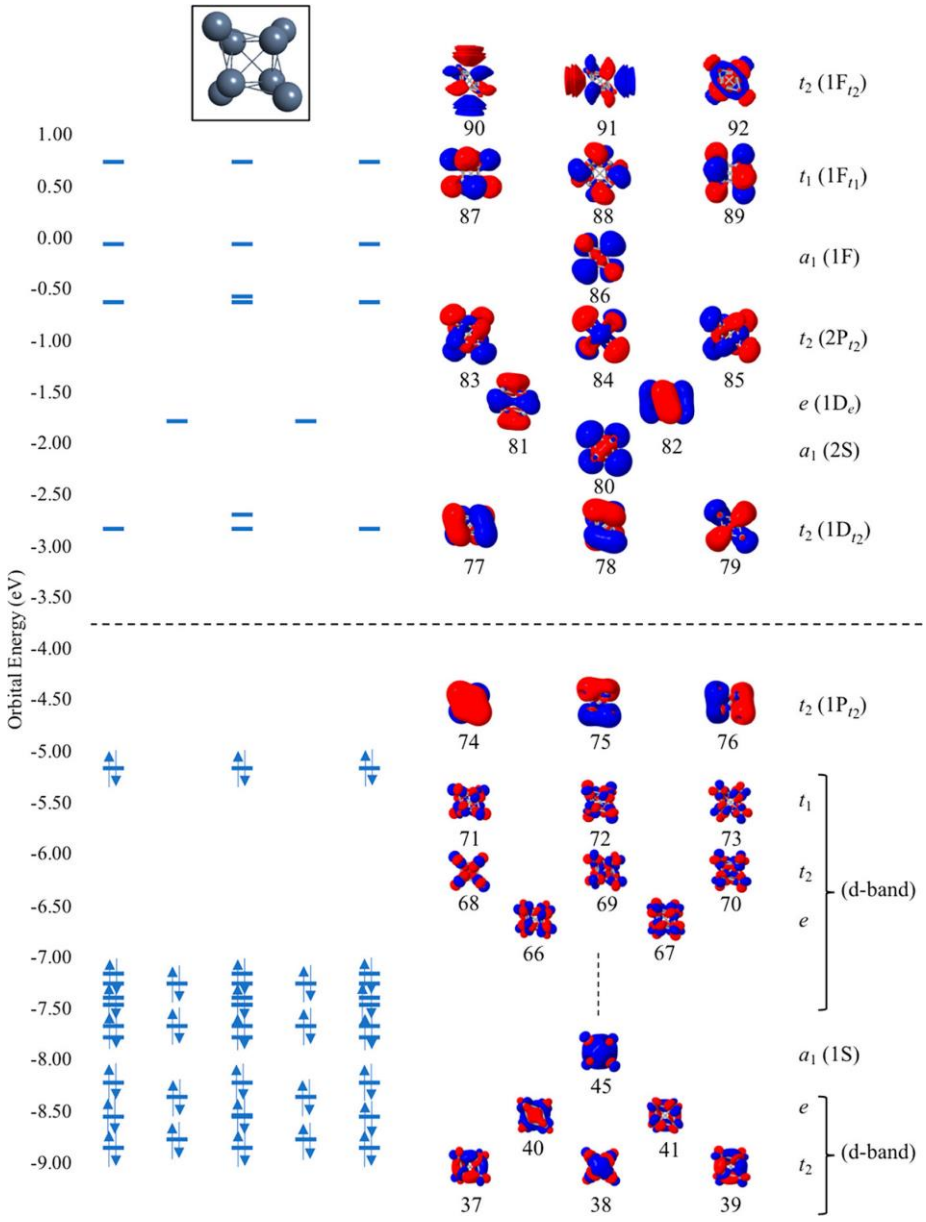

Figure 3.1. Molecular structure and the orbital energy level diagram of the tetrahedral Ag_8 cluster. Shapes and the tetrahedral point group symmetry representations of the orbitals are displayed with the relevant spherical assignment for the superatomic orbitals in parentheses. A horizontal dashed line separates the occupied and virtual orbitals.

The absorption spectrum of the Ag_8 tetrahedron contains two sharp peaks at 3.05 eV and 3.96 eV as calculated from linear-response TDDFT (Figure 3.2). The peak at 3.05 eV arises due to electronic transitions from the occupied 1P orbitals into the unoccupied 1D and 2S orbitals (Table B-1). For the excitation at 3.96 eV, the largest contribution comes from 1P → 1D

transitions, although some 1P → 2S and d-band → 1D transitions also contribute slightly (Table B-2). The electronic transitions between superatomic orbitals of Ag_8 follow the spherical selection rule, $\Delta L = \pm 1$, for these lowest two excitations. Moreover, these transitions follow the specific selection rules for dipole-allowed electronic transitions in a molecule with T_d point group symmetry. The absorption spectrum calculated from the RT-TDDFT calculation, i.e. the Fourier-transformed dipole moment, reproduces the spectrum calculated from LR-TDDFT (Figure B-2). Molecular orbital occupation number variation and their Fourier transforms (Figure B-3) as well as the Fourier analysis of the off-diagonal density matrix elements (Figure B-4) support the spectral transition information revealed by LR-TDDFT. Most importantly, since these excitations arise due to the constructive contribution of multiple electronic transitions, we can identify that they correspond to a molecular analog of a plasmon resonance in this nanocluster; thus, the electronic dynamics in this nanocluster provide important information about possible plasmon decay mechanisms.

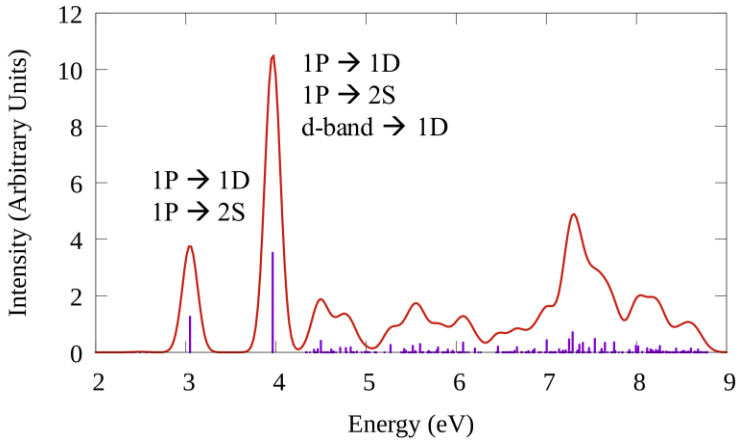

Figure 3.2. LR-TDDFT excitation spectrum of the tetrahedral Ag_8 cluster and the transitions responsible for the peaks at 3.05 eV and 3.96 eV. (Purple: LR stick spectrum; red: convoluted spectrum using gaussian curves with Gaussian FWHM = 0.2 eV).

3.4.2 Real-time TDDFT of Ag_8 with a continuous wave field

To study the plasmon dynamics of this system, continuous wave external electric fields with resonant frequencies of 3.05 eV and 3.96 eV are applied and the dipole moment variations over time are examined. We first focus on the most intense peak, which appears at 3.96 eV. The time variation of the applied field oscillating with a frequency corresponding to 3.96 eV is shown in Figure 3.3a. (An expanded view from 0 fs to 20 fs is shown in Figure B-1a; its corresponding Fourier transform in Figure B-1c confirms that the pulse will excite electronic states centered around 3.96 eV.) The dipole moment of the silver cluster subjected to this continuous wave field is shown in Figure 3.3b. Due to the continuous energy supplied during the first 20 fs, the dipole moment resonating with the applied field frequency continues to increase until the field is turned off at 20 fs (Figure 3.3b and B-1b). After the external field is turned off, the dipole moment starts to decrease but continues to oscillate at the resonant frequency. The magnitude of the dipole moment continues to drop until about 175 fs when it again starts to rise. This behavior of the dipole moment implies that the collective (dipolar plasmon-like) behavior in the Ag_8 cluster is decaying between 20 and 175 fs. However, it should be noted that in our simulation the total energy is conserved and the nuclei are fixed; thus, energy cannot flow into vibrational modes. In the absence of any energy dissipation processes, the energy arising from the interaction of the nanoparticle with the electric field will stay in electronic states for the entire length of the simulation, although it may flow between different electronic states that have different dipole moments. In a "real" system, this energy will decay to nuclear degrees of freedom (typically on the time scale of 100s of fs) and then to the bath (1000s of fs). Thus, although we would expect beating if we were to run the simulation in this paper for many hundreds or thousands of fs, this would not truly simulate what may occur experimentally. We are most interested in the short-time decay dynamics of the

electronic states. Therefore, the question arises of where the energy flows when the dipolar oscillation decreases during the initial dipolar decay.

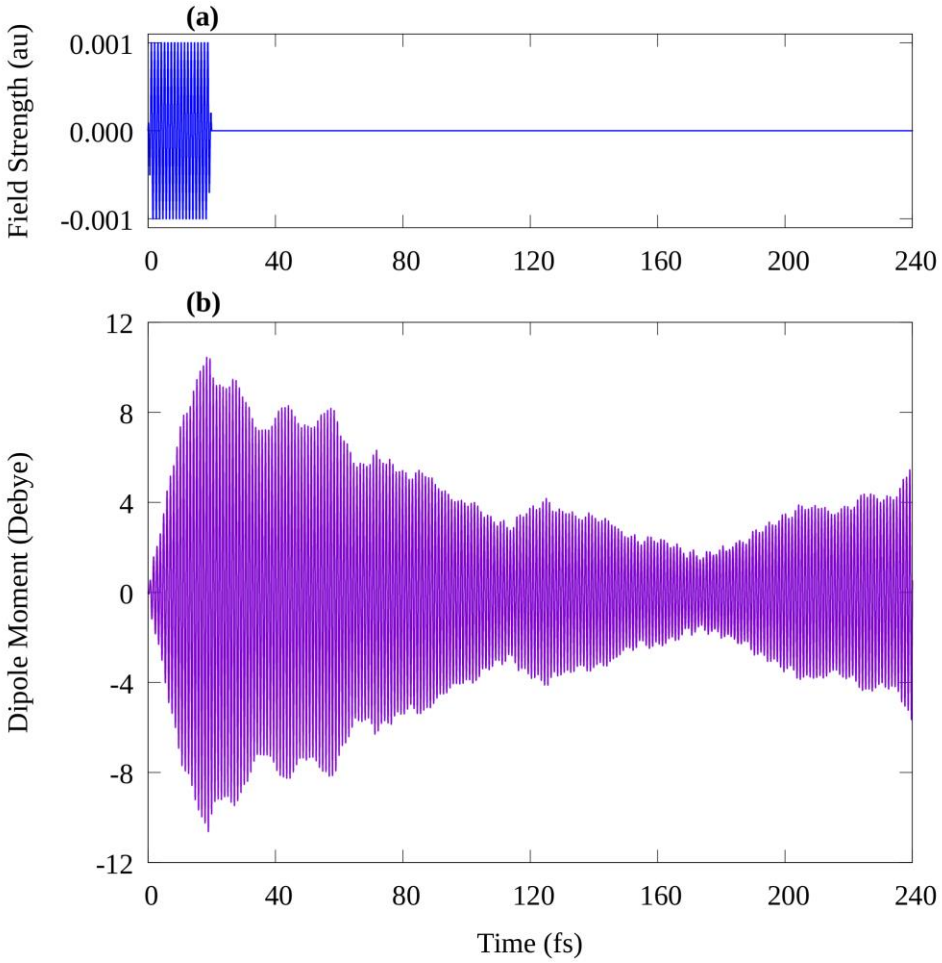

Figure 3.3. Variation of (a) applied electric field and (b) dipole moment along z axis. The continuous wave electric field is applied with a frequency of 3.96 eV.

To identify the energy transfer over the course of the electron dynamics simulation, we analyze the variation of the off-diagonal density matrix elements, P_{OV}, corresponding to occupied-virtual molecular orbital pairs. The value of P_{OV} at a certain time indicates the amount of single particle electronic transition occurring between the occupied and the virtual orbital at that time. Variation of the P_{OV} element corresponding to a transition between an occupied 1P-type molecular orbital (75) and a virtual 1D-type orbital (81) (Figure 3.4a) follows the same temporal pattern as the dipole moment variation, where the transition is the strongest around 20 fs and decays to a

minimum near 175 fs. Similar variations albeit with smaller magnitudes are observed for the 1P → 2S (Figure 3.4b) and d-band → 1D transitions (Figure B-d). The corresponding Fourier transforms in Figure 3.4c indicate that these transitions are related to the activation of the plasmonic excitation at 3.96 eV. Further analysis of the orbital occupation variation in individual orbitals shows that the electron population of occupied orbital 75 decays until 20 fs and starts to grow after 20 fs, whereas the population of virtual orbital 81 shows an anticorrelation with that of occupied orbital 75 (Figure B-6, middle), demonstrating that the dynamics of this electron transition as measured by orbital occupation numbers are similar to the dynamics manifested by $P_{75\text{-}81}$. The continuous drop of $P_{75\text{-}81}$ even after 60 fs through about 175 fs is clearly shown in the variation of corresponding orbital occupations. Here we note that when we excite the system with a continuous wave electric field corresponding to a resonant energy of the molecule, the frequency domain dipole response as well as the molecular orbital responses slightly shift towards higher energy. For instance, when an energy of 3.96 eV is applied to the system as a continuous wave electric field, the frequency domain responses for both the dipole moment and the off-diagonal density matrix elements peak at 4.03 eV. The shift in the time-dependent response in RT-TDDFT where the system is perturbed significantly away from the ground state has been previously reported by several researchers.[167, 244-246] In this work, the amount of this observed peak shifting was less than 0.1 eV and can be considered to be very small.

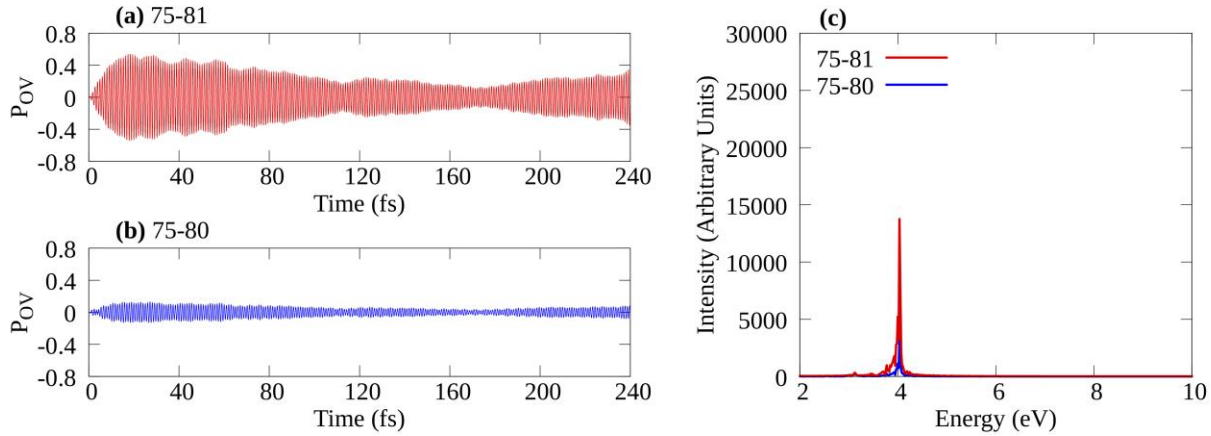

Figure 3.4. Variation of density matrix elements corresponding to the occupied and virtual pairs (a) 1P – 1D and (b) 1P – 2S; (c) corresponding Fourier transforms. The continuous wave electric field is applied with a frequency of 3.96 eV.

Overall, variation of 1P → 1D, 1P → 2S and d-band → 1D transitions follow the same pattern as the dipole moment variation oscillating with the resonant frequency; these transitions were also identified from the linear-response calculations described above as the transitions responsible for the collective plasmon-like peak at 3.96 eV. Point group symmetries indicate that these 1P → 1D, 1P → 2S and d-band → 1D transitions are electric dipole-allowed, owing to the fact that the irreducible representations of the corresponding direct products contain the T_2 representation (Table 3.1). Density matrix element variations corresponding to the dipole-allowed transitions separated into their point group representations are presented in Figure B-5.

Table 3.1. Tetrahedral point group representations of the orbitals involved in the transitions which give rise to the peaks at 4.03 eV and 8.07 eV and the decomposition of their direct products. Note: The continuous wave electric field is applied with a frequency of 3.96 eV.

Excitation energy (eV)	Transitions	Spherical assignments	Symmetry	Direct product decomposition into irreducible representation
4.03	75 → 81 74 → 81	1P → 1D	$t_2 \rightarrow e$	$T_1 + T_2$

	76 → 77	1P → 1D	$t_2 \rightarrow t_2$	$A_1 + E + T_1 + T_2$
	75 → 80	1P → 2S	$t_2 \rightarrow a_1$	T_2
	66 → 78 66 → 79	d-band → 1D	$e \rightarrow t_2$	$T_1 + T_2$
8.07	45 → 86	1S → 1F	$a_1 \rightarrow a_1$	A_1
	72 → 92 71 → 90 73 → 90	d-band → 1F	$t_1 \rightarrow t_2$	$A_2 + E + T_1 + T_2$
	68 → 90 69 → 91 69 → 92 70 → 91 70 → 92	d-band → 1F	$t_2 \rightarrow t_2$	$A_1 + E + T_1 + T_2$

Because the time-dependent behavior of the dipole-allowed transitions resembles the variation of the dipole moment, these transitions do not reveal any new information regarding the energy transfer processes that are active during the 20-175 fs time period. However, several other transitions were found to behave in a different manner. Interestingly, the P_{OV} matrix element corresponding to the 45 (1S) → 86 (1F) transition grows significantly even after the field is switched off at 20 fs (Figure 3.5a). The oscillation of this transition corresponds to an energy of 8.07 eV (Figure 3.5b), which is twice the resonant frequency. In addition to this transition between two superatomic orbitals, some d-band transitions also gain energy and oscillate with a frequency corresponding to 8.07 eV (Figure 3.5b, c). A summary of transitions oscillating with 8.07 eV frequency is illustrated in Figure B-7. As compared in Figure 3.6, the decay of $P_{75\text{-}81}$ (1P → 1D transition) and growth of $P_{45\text{-}86}$ (1S → 1F transition) are related. The density matrix element $P_{75\text{-}81}$ starts to increase right away as the field is applied and keeps increasing until the field is turned off

at 20 fs. In contrast, $P_{45\text{-}86}$ starts to increase at around 5 fs and continues to grow even after 20 fs (Figure 3.6). Anticorrelated dynamics of occupation numbers for orbitals 45 (occupied) and 86 (virtual) underscore the electron transition dynamics occurring between these two orbitals (Figure B-6, bottom). The inverse correlation between the two types of transitions (1P → 1D with 1ω, where ω is 3.96 eV, and 1S → 1F with 2ω), especially after the field is turned off, suggests that the energy flows from the dipole-allowed transitions into different transitions with twice the plasmon energy. Similarly, around 175 fs the electron occupation in orbital 75 (1P) reaches a maximum at essentially 2 electrons, while the occupation of 81 (1D) drops back to 0 electrons (Figure B-6, middle). This corresponds to the time at which the dipole moment of the system reaches a minimum. At the same time, the electron occupation of orbital 45 (1S) reaches a minimum (~1.75 electrons) while the occupation of orbital 86 (1F) reaches a maximum (~0.25 electrons) (Figure B-6, bottom). The magnitude of the dipole moment as well as the P_{OV} elements corresponding to dipole-allowed transitions start to increase after about 175 fs (Figure 3.3b and Figure 3.6). This might suggest that the dipole-allowed transition could undergo a revival at some time. Comparatively, P_{OV} elements related to the two-photon allowed transitions drop after 175 fs (Figure B-7). This illustrates why a permanent decay of the dipole moment may not be possible under the adiabatic conditions used in these simulations. In reality, however, a revival back to the initial states may not actually occur. At longer time scales, energy transfer to vibrational energy may play a role in addition to energy transfer to the bath.

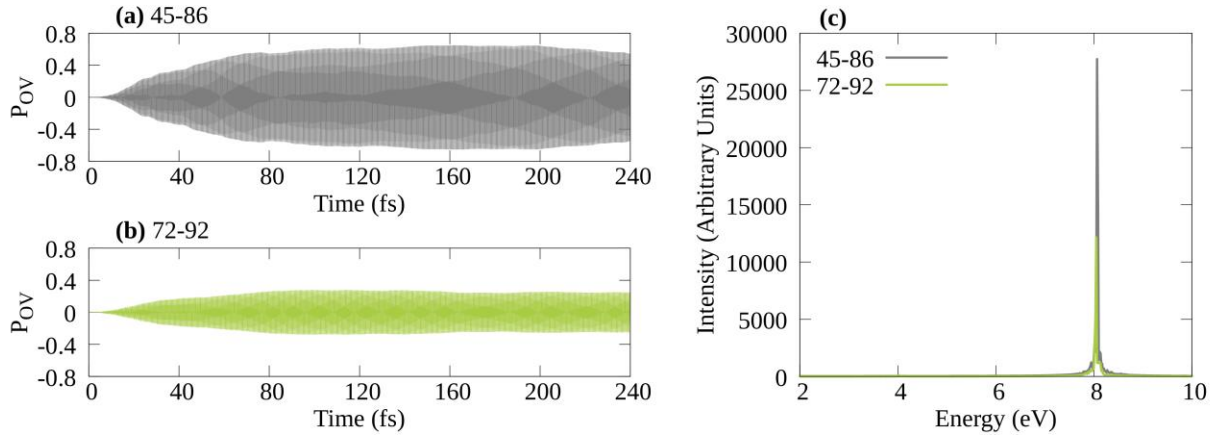

Figure 3.5. Variation of density matrix elements corresponding to the occupied and virtual pairs (a) 1S – 1F (45-86) and (c) d-band – 1F (72-92); (b) corresponding Fourier transforms. The continuous wave electric field is applied with a frequency of 3.96 eV.

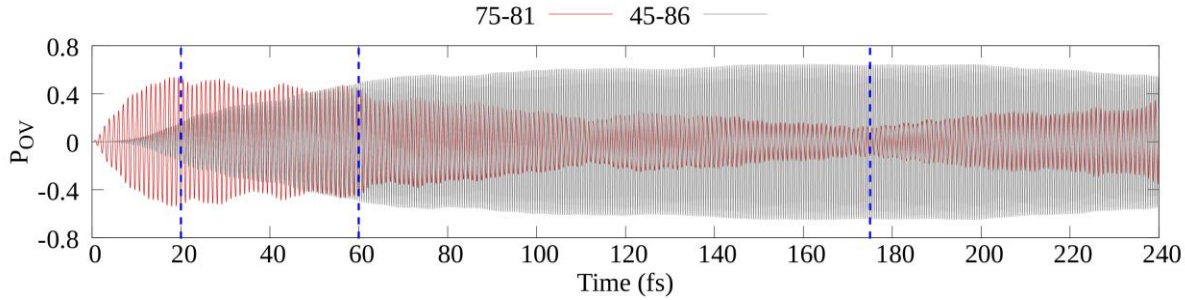

Figure 3.6. Decay of $P_{75\text{-}81}$ and growth of $P_{45\text{-}86}$ when the continuous wave electric field is applied with a frequency of 3.96 eV.

The energy of the continuous wave field is clearly centered around the energy corresponding to the applied frequency without significant excitation at higher energies (Figure B-1b), even though the continuous wave field is only applied for 20 fs. Therefore, the non-linear effects arise as a result of the electron dynamics in the nanocluster, not because of direct excitation arising from the short-time application of the continuous wave field.

When a system is excited with a resonant electric field, excitation of the dipole-allowed transitions is expected. However, here we not only observe these one-photon excitations but also numerous two-photon absorptions due to the presence of a strong electric field. The selection rules for allowed two-photon absorption are analogous to the selection rules for Raman scattering.[194-

[195, 247-248] Therefore, for a two-photon absorption to be allowed, the direct product of the representations of the initial and final molecular orbitals corresponding to an electronic state should contain a quadratic representation such as xy, yz, x^2, y^2, etc. Referring to the character table of the T_d point group, if the direct product of symmetries of the two orbitals involved in a transition includes A_1, E or T_2, then that transition can be allowed for two-photon absorption. As shown in Table 3.1, 1S → 1F and d-band → 1F transitions, which give rise to the excitation at 8.07 eV, are in fact two-photon allowed. Importantly, we observe that the transition between superatomic 1S and 1F orbitals, which is of A_1 symmetry, is forbidden for one-photon absorption but allowed with two-photon excitation. Therefore, the applied field is strong enough to create nonlinear effects resulting in this excitation with A_1 symmetry. Additionally, in a tetrahedral molecule, which does not have a center of inversion, there can be transitions that are both one- and two-photon allowed. The transitions between d-band (t_1/t_2) and 1F (t_2) orbitals can be both one- and two-photon allowed because the direct products $t_1 \otimes t_2$ and $t_2 \otimes t_2$ yield T_2 symmetry.

We also reduced the strength of the electric field by a factor of 10 and identified the same behavior albeit with decreased magnitudes for the dipole moment and density matrix elements. The comparison of the dipole moment variation and the corresponding Fourier transforms for the applied field strengths 0.001 a.u. and 0.0001 a.u. are presented in Figure B-8. Figure B-9 and Figure B-10 illustrate the variation of density matrix elements and their Fourier transforms corresponding to one- and two-photon allowed transitions respectively. The dipole moment as well as the P_{OV} values of one-photon allowed transitions decrease by a factor of 3-7 while the P_{OV} values of two-photon allowed transitions decreases by a factor of 17-19 when the electric field is weaker by a factor of 10. Although this decrease is not at the maximum factor of 100 that could be expected for a second-order nonlinear process, it is larger than the factor of 10 that would be

expected for a purely linear process, thereby implicating nonlinear processes. Dipole decay occurs more rapidly for the stronger applied field, which correlates with the observation that the two-photon allowed transitions are activated more during the simulation with the stronger field. It is possible in larger plasmonic nanoparticles that the very strong near-fields created by the collective oscillation of the conduction electrons upon resonant excitation even with a low-intensity laser are sufficient to induce plasmon decay via two-photon processes; this should be the topic of a future study.

We likewise examined the electron dynamics of Ag_8 excited at the resonant energy of 3.05 eV. Similar to the previous results, the dipole moment along the z axis (Figure 3.7b) is dominated by the 1P → 1D and 1P → 2S transitions (Figure 3.8,b) that make up the excitation at 3.05 eV, consistent with LR-TDDFT findings. The magnitudes of the corresponding P_{OV} elements and the dipole moment increase until the field is turned off and start to decay after that. These transitions again start to grow at about 80 fs. Over the 240-fs simulation, we observe these transitions and dipole moments fall and rise several times indicating energy transfer to and from other transitions. The corresponding Fourier transforms show a peak at around 3.07 eV (Figure 3.8c), confirming their contribution to the resonant peak (note that the system was excited with a continuous wave electric field oscillating with a frequency of 3.05 eV and we observe a peak shifting of 0.02 eV here). There are three types of transitions, $t_2 \rightarrow e$, $t_2 \rightarrow t_2$ and $t_2 \rightarrow a_1$, that follow the dipole moment signature and all of them yield the T_2 representation (Table 3.2 and Figure B-11). Therefore, they are dipole-allowed according to the T_d point group symmetry rules. Here also we perceive the activation of two-photon excitations. Figure 3.8d,e illustrates the variation of P_{OV} for the transitions from low-lying d orbitals to 2S and 1D orbitals oscillating with twice the resonant frequency, i.e. 6.19 eV (Figure 3.8f, Table 3.2, Figure B-12). As shown in Table 3.2, the

symmetries of these transitions follow the selection rules for two-photon absorption because their direct products include the A_1, E or T_2 representations. The inter-band transition of d electrons to the 2S level is the major two-photon transition when the system is initially excited at 3.05 eV. Because this transition has E symmetry, it requires a strong field to be activated via multiple photons. Similar to the previous discussion, these d-band transitions do not occur as soon as the field is applied but start to increase their strength at around 5 fs. This clearly implies the ultrafast decay of one-photon excitations into two-photon excitations.

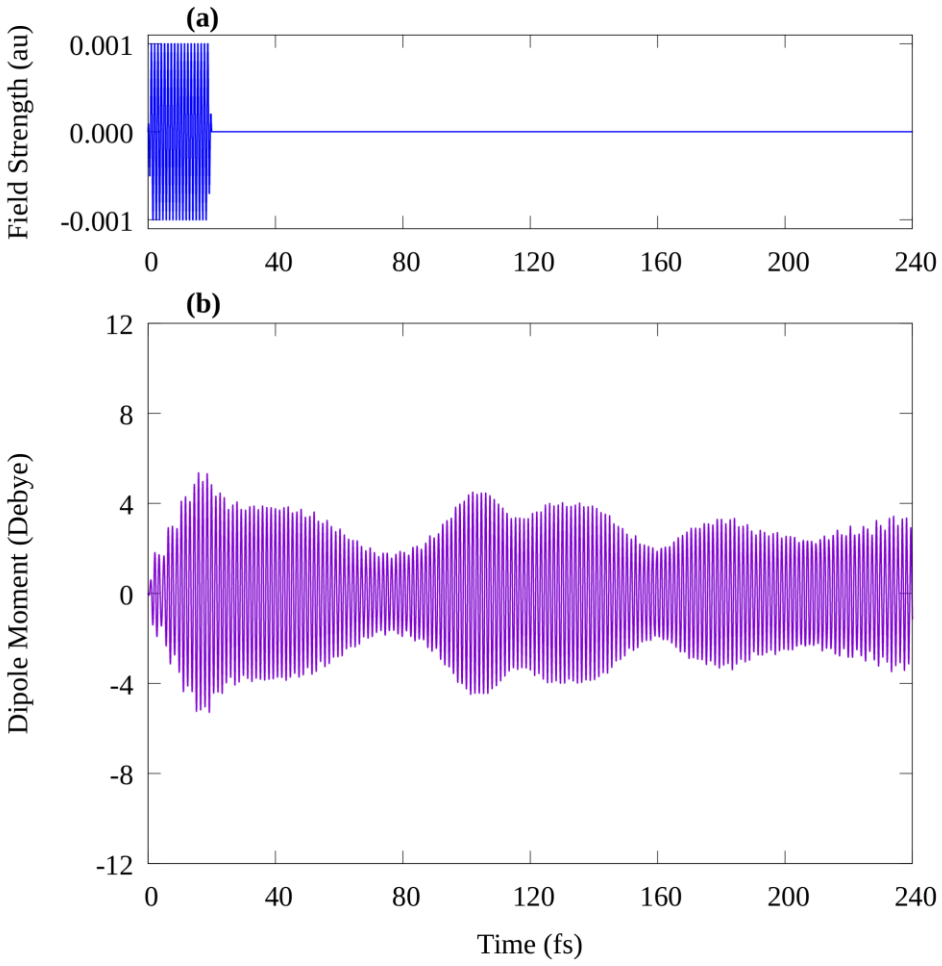

Figure 3.7. Variation of (a) applied electric field and (b) dipole moment along z axis. The continuous wave electric field is applied with a frequency of 3.05 eV.

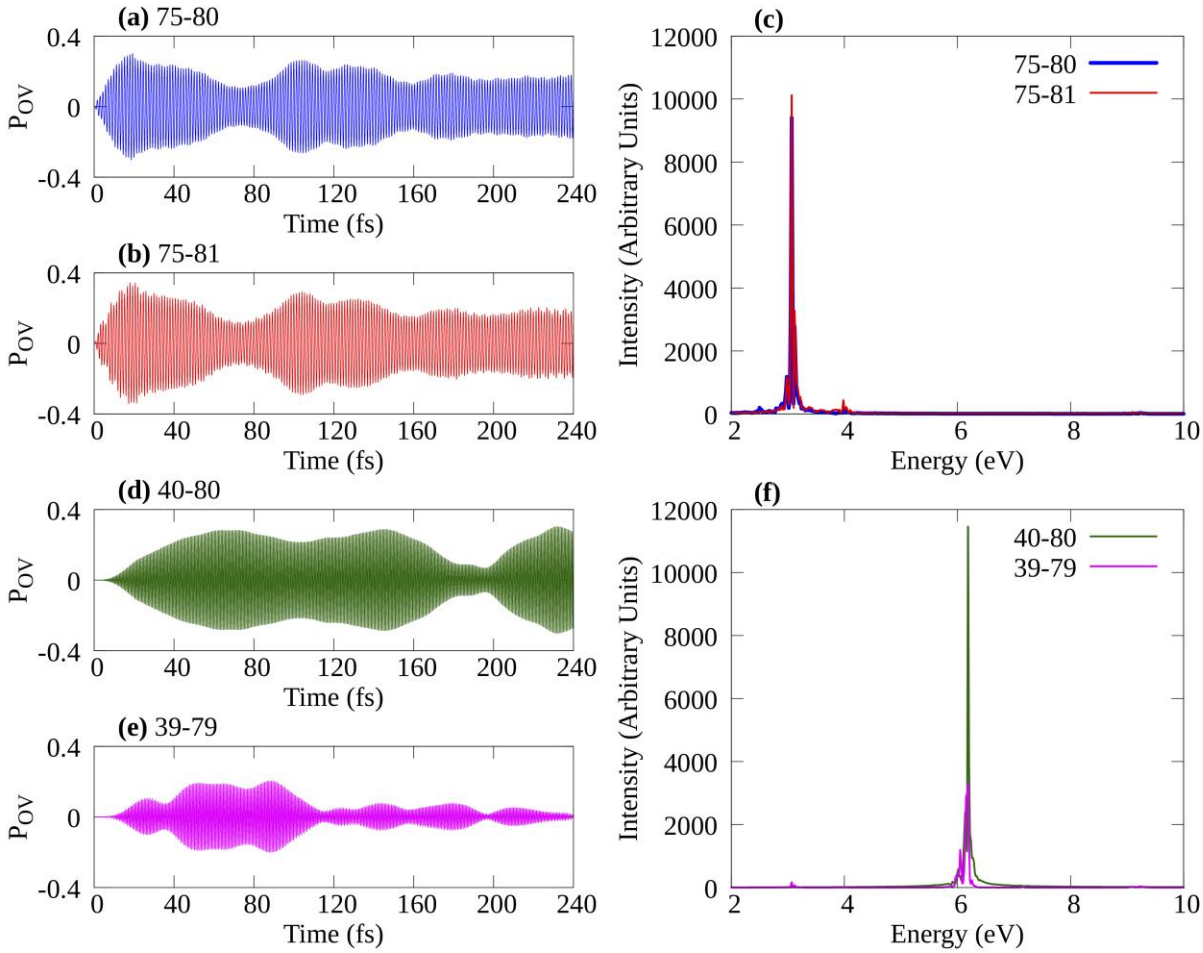

Figure 3.8. Variation of P_{OV} corresponding to (a) 1P → 2S, (b) 1P → 1D transitions and (c) corresponding Fourier transforms; variation of (d) d-band → 2S, (e) d-band → 1D transitions and (f) corresponding Fourier transforms. The continuous wave electric field is applied with a frequency of 3.05 eV.

Table 3.2. Tetrahedral point group representations of the orbitals involving in the transitions that give rise to the peaks at to 3.07 eV and 6.19 eV and the decomposition of their direct products. Note: The continuous wave electric field is applied with a frequency of 3.05 eV.

Excitation energy (eV)	Transitions	Spherical assignments	Symmetry	Direct product decomposition into irreducible representation
3.07	74 → 81 75 → 81 76 → 81	1P → 1D	$t_2 \rightarrow e$	$T_1 + T_2$
	74 → 79 76 → 77 74 → 78 75 → 77 75 → 79 76 → 78	1P → 1D	$t_2 \rightarrow t_2$	$A_1 + E + T_1 + T_2$
	74 → 80 75 → 80 76 → 80	1P → 2S	$t_2 \rightarrow a_1$	T_2
6.19	40 → 80	d-band → 2S	$e \rightarrow a_1$	E
	38 → 78 37 → 77 39 → 79	d-band → 1D	$t_2 \rightarrow t_2$	$A_1 + E + T_1 + T_2$
	45 → 80	1S → 2S	$a_1 \rightarrow a_1$	A_1

In both cases where the system is excited by a continuous wave electric field (with energies of 3.05 eV and 3.96 eV), the collective plasmon resonance of this tetrahedral Ag_8 cluster decays into high-energy excited states with twice the resonant energy, resembling the two-photon absorption phenomenon. The electric field intensity of 0.001 a.u. (~3.57×10^{13} W/cm^2) is strong

enough to induce nonlinear effects of this tetrahedral cluster, and weaker nonlinear processes are also observed for the applied electric field with an intensity of 0.0001 a.u. Tetrahedral symmetry may play an important role in allowing these two-photon absorption processes because there are states that could be accessible via both one- and two-photon absorption. Nonetheless, the strongest contributions to the high-energy two-photon absorptions around 6.19 eV and 8.07 eV arise from transitions with E and A_1 symmetry, respectively, which are prohibited in the linear regime. Overall, the role of shape and symmetry in enabling nonlinear absorption processes in nanoclusters will be a valuable area for further study.

In the tetrahedral Ag_8 cluster, the two lowest excited states at 3.05 eV and 3.96 eV have T_2 symmetry leading to the possibility that each of these plasmon-like states can also be activated via two photon-absorption if they are excited with a frequency corresponding to half of the resonant excited state energy. To test this possibility, we applied continuous wave electric fields with energies of 1.525 eV and 1.98 eV (corresponding to half of the energy of the strong, collective states at 3.05 eV and 3.96 eV) using electric field intensities of 0.001 a.u. However, we observed neither a continuous increment of the dipole moment while the field is applied, nor two-photon absorption for these frequencies. Variation of the applied field, dipole moment and the Fourier transformed dipole moment compared with the LR peak positions for these two frequencies are shown in Figures B-13 and B-14. In both cases, the time variation of the dipole moment resembles that of the applied field rather than an increasing dipole moment while the field is applied. The magnitude of the dipole moment in both cases is around 1 Debye, which is weaker compared to the corresponding dipole moment when excited at a plasmonic frequency (i.e. 10 Debye and 5 Debye when excited with resonant frequencies of 3.96 eV and 3.05 eV, respectively). After 20 fs, the dipole moment oscillates with either of the two lowest plasmonic frequencies. Surprisingly,

when excited with a continuous electric field oscillating with an energy of 1.525 eV, after 20 fs the dipole response oscillates with a frequency corresponding to 3.96 eV excitation rather than with 3.05 eV, which would have been twice the applied frequency. Furthermore, the 1.98 eV excitation leads to an oscillation of the dipole moment with a frequency corresponding to a peak at 3.05 eV instead of one at 3.96 eV which would be expected if nonlinear processes were occurring in this situation. This remarkable observation suggests that even in the presence of a strong field, two-photon absorption may not occur for all incident wavelengths of light, regardless of whether the corresponding two-photon excitations are allowed. However, wavelengths corresponding to resonant excitations such as plasmon resonances can significantly enhance the possibility of two-photon absorption. Plasmonic systems can absorb a massive amount of energy when excited at plasmon resonance frequency and can use that energy to initiate multi-photon processes. Therefore, plasmonicity appears to be a driving force for the activation of nonlinear absorption properties.

3.5 Summary

Herein we demonstrate a possible plasmon-enhancement of nonlinear susceptibility in the tetrahedral Ag_8 cluster. Electron dynamics in this silver cluster subjected to a continuous wave electric field oscillating at two plasmonic resonance frequencies were examined using RT-TDDFT. We observe an ultrafast decay of the dipolar response after the external field is turned off, especially when the strongly dipole-allowed plasmon-like state is excited. The unique approach used in this work, the analysis of the time-dependent off-diagonal density matrix elements in the MO basis, reveals that the dominant transitions that govern the resonant plasmonic state decay in the absence of the electric field, whereas the density matrix elements related to several other MO transitions continue to rise. Surprisingly, these growing matrix elements oscillate at twice the incident frequency demonstrating a strong second-order nonlinear response. This work shows that the dipole-allowed one-photon excitations can be transformed into two-photon allowed states in this tetrahedral cluster which can be considered a plasmon-mediated nonlinear response. The distinct point group symmetry selection rules for one- and two-photon absorption confirm the linear and nonlinear transitions respectively. This work also reveals the fact that the incident electric field must be in resonance with strong collective excited states such as plasmon resonances to substantially boost the nonlinear properties. This work establishes an interesting area of research, i.e. ultrafast plasmon decay via nonlinear processes, for future understanding of energy enhancement and transfer processes in plasmonic materials.

3.6 Supporting Information Available

Coordinates of Ag_8 cluster. Applied continuous wave field and the dipole moment of the Ag_8 cluster in both time and energy domains. Transitions responsible for the lowest energy peaks of the Ag_8 cluster at 3.05 eV and 3.96 eV. Absorption spectra comparison for LR and RT-TDDFT methods. Analysis of spectral properties from the molecular orbital occupation number variation and off-diagonal elements of the density matrix during time propagation. Decay and growth of off-diagonal density matrix elements when external continuous wave electric fields oscillating with frequencies of 3.96 eV and 3.05 eV are applied. Variation of the occupation numbers for selected molecular orbitals (3.96 eV excitation). Comparison of the dipole response and the P_{OV} values when the applied field strengths are 0.001 a.u. and 0.0001 a.u. Variation of applied field, dipole moment along z axis and Fourier transformed dipole moment when continuous wave electric fields oscillating with frequencies of 1.525 eV and 1.98 eV are applied.

3.7 Acknowledgments

This material is based on work supported by the Department of Energy under grant DE-SC0012273. The computing for this project was performed on the Beocat Research Cluster at Kansas State University, which is funded in part by NSF grants CHE-1726332, CNS-1006860, EPS-1006860, and EPS-0919443. The development of the first-principles electronic dynamics is supported by the U.S. Department of Energy (DE-SC0006863 to X.L.). The development of the linear-response TDDFT method for computational spectroscopy was supported by the National Science Foundation (CHE-1856210 to X.L.).

Chapter 4 - Non-Linear Optical Properties in Silver Nanoclusters

Gowri U. Kuda-Singappulige and Christine M. Aikens

4.1 Abstract

Inspired by the recent work on nonlinear optical activation in silver nanoparticles, we investigate the plasmon decay pathways in atomistic silver clusters of various sizes and shapes using real-time time-dependent density functional theory (RT-TDDFT). Variation of the dipole moment demonstrates that the plasmon-like states in silver nanoclusters, which build up rapidly in the presence of light, are highly sensitive to the external electric perturbation and rapidly fall after the electric field is turned off. However, higher-order nonlinear optical properties continue to develop in the absence of the electric field. Regardless of shape and size, nonlinear optical response occurs in all silver clusters investigated in this work, including Ag_{10}^{+2} (T_d), Ag_{13}^{+5} (I_h), Ag_{13}^{-1} (O_h), Ag_{19}^{+1} (D_{5h}), Ag_{20} (T_d), and Ag_{55}^{-3} (I_h). The multiphoton absorption phenomenon which emerges as a result of rapid plasmon decay in silver materials sheds light on nonlinear optical enhancement.

4.2 Introduction

Plasmonic nanostructures are well-known as promising boosters for light-induced processes including solar energy conversion,[249-254] photo-induced catalysis,[78, 254-255] and colorimetric sensing.[33, 256-257] The strongly absorbed light rapidly decays via several pathways[105, 258-261] limiting the efficiency of plasmonic materials. It is well-known that the plasmonic properties, such as the characteristic resonant energy and the absorption cross section, are determined by the molecular configuration at the atomic level.[14, 24, 262-264] Plasmon decay time and mechanism are no exceptions; different materials show different rates of plasmon decay.[7, 106-108] Experimental findings suggest that electron dephasing and scattering in metal nanoparticles typically occur on the femtosecond timescale while electron-photon coupling and thermal dissipation take a few hundreds of picoseconds.[3, 48, 105, 107-108]

The specific decay pathways can vary from one material to another. We are interested in a fundamental understanding of plasmon decay pathways in noble metal nanoparticles. Specifically, silver nanoclusters show impressive enhancement of the photoactivation in many applications.[78, 249-250, 252, 254] However, the short excited-state lifetime of silver, on the femtosecond timescale,[254] affects the productivity of these applications. Due to the ultrafast nature of the silver plasmons, detecting its decay mechanisms remains challenging using experimental techniques.

Theoretical real-time electron dynamics methods are ideal to study such fast processes. Ma and coworkers[26] studied plasmon dynamics of the Ag_{55} (I_h) cluster using real-time time-dependent density functional theory (RT-TDDFT) and suggested that the plasmonic energy is transferred into single-particle excitations, otherwise known as hot carriers. A study by Rossi *et al.*[61] regarding the spatial distribution of hot carriers in icosahedral nanoparticles found that the hot electrons distribute over the low-coordinated sites whereas the hot holes tend to spread out homogeneously

over the nanoparticles, showing the importance of the atomic structure in hot carrier generation. Yan et al.[119] found double excitations in Ag_4 and Ag_6 atomic chains and additional higher-order response with increased chain size. Gieseking[117] used semi-empirical methods to examine possible third-order nonlinear optical activation in silver nanorods. Our recent theoretical work[173] on the Ag_8 (T_d) cluster proposed an interesting decay channel, nonlinear optical enhancement, as demonstrated by the density matrix elements in the time and energy domains and the dipole/quadrupole selection rules.

In this study, we investigate the size and shape dependence of the nonlinear optical transformation. In addition to the density matrix elements, we include the analysis of the time-propagating difference density to identify the change in electron density distribution over time compared to the ground electronic density. We show that higher-order nonlinear effects can be activated in silver nanoclusters.

4.3 Methods

All of the calculations including geometry optimization, static optical response, and real-time electron dynamics were performed at the BP86[142-143]/LANL2DZ[240] level of theory with a development version of the Gaussian[238] package. After geometry optimization, we compute the optical absorption spectrum using linear-response time-dependent density functional theory (LR-TDDFT)[157, 165] and identify several low-energy excitations to study their dynamics. Then, we excite selected states separately, using a continuous-wave[173] electric field polarized along certain cartesian axes, and propagate electron density using real-time time-dependent density functional theory (RT-TDDFT).[159-160, 168, 172, 228] The nanoclusters Ag_{10}^{+2} (T_d), Ag_{13}^{+5} (I_h), Ag_{13}^{-1} (O_h), Ag_{20} (T_d), and Ag_{55}^{-3} (I_h) are isotropic, so only a z-polarized electric field was investigated because an identical response is expected in any direction. For the cylindrical-shaped Ag_{19}^{+1} (D_{5h}) nanorod,

both longitudinal and transverse peaks were studied by applying z-and x-polarized electric fields separately. The time-dependent density matrix elements, P_{OV} (t), in the molecular orbital (MO) basis were studied in all cases. Ref. [173] contains a detailed description of computing the time-dependent MO-based density matrix elements, P_{OV} (t). We choose only a subset of the density matrix elements arising from molecular orbitals near the fermi level to be saved during the time propagation to reduce memory demand.

The time-dependent difference density $\rho^{diff}(t)$ is calculated according to (4.3.1),[28] where $\rho'(t)$ and $\rho^0(t)$ are the time-dependent electron density with and without the external electric field, respectively. We use the time-dependent difference density and the transition fit density (from LR-TDDFT) for some cases to identify various electronic states emerging over time. The difference densities provide pictorial information of the electron density that helps elucidate the fate of the dipolar excitation.

$$\rho^{diff}(t) = \rho'(t) - \rho^0(t) \tag{4.3.1}$$

4.4 Results and Discussion

The silver nanoparticles considered in this work, Ag_{10}^{+2} (T_d), Ag_{13}^{+5} (I_h), Ag_{13}^{-1} (O_h), Ag_{19}^{+1} (D_{5h}), Ag_{20} (T_d), and Ag_{55}^{-3} (I_h), and their absorption spectra calculated from LR-TDDFT are illustrated in Figure 4.1. We discuss the real-time dynamics of low-lying excitations of each cluster in detail in the following sections.

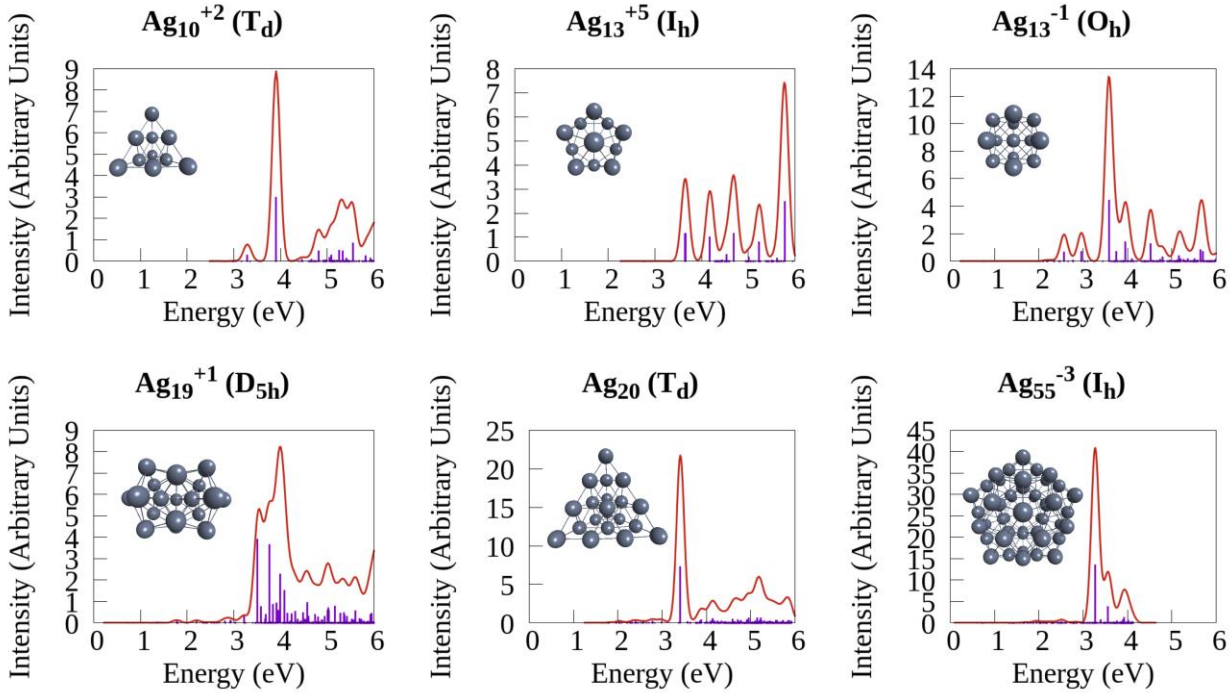

Figure 4.1. LR-TDDFT spectra of silver nanoparticles. Purple: LR-TDDFT stick spectra; Red: convoluted spectra with a Gaussian FWHM = 0.2 eV.

4.4.1 Ag_{10}^{+2} (T_d)

The linear optical spectrum of the Ag_{10}^{+2} (T_d) cluster possesses a weak absorption peak at 3.29 eV and a strong peak at 3.91 eV (Figure 4.1). The strong peak at 3.91 eV is consistent with our previous work.[10] The corresponding single-particle transitions involved in this excited state, as computed from LR-TDDFT, are provided in Table C-1. We calculate the time variation and the Fourier transform of the dipole moment when Ag_{10}^{+2} (T_d) is excited with external fields with frequencies resonant to the two states at 3.29 eV and 3.91 eV (Figure 4.2). The weak state at 3.29

eV does not experience a gradual increment of the dipolar response while the field is on (Figure 4.2a, 0-20 fs), but instead appears to couple with the stronger state at 3.91 eV, as indicated by the beating pattern of the dipole moment (Figure 4.2a) and the appearance of a peak at 3.91 eV in the Fourier transform (Figure 4.2b). In contrast, the strong electronic state at 3.91 eV manifests a continuous increment of the dipolar response during the perturbation (0-20 fs in Figure 4.2c). After the field is turned off at 20 fs, the magnitude of the dipole moment starts to decrease until around 45 fs, when it starts to revive again (Figure 4.2c). This revival was previously reported[173] in the dynamics of the Ag_8 (T_d) cluster due to the saturation of the orbital population which is consistent for Ag_{10}^{+2} (T_d) in this study. In addition, the Fourier analysis of the dipole moment (Figure 4.2d) confirms that this state does not couple with any nearby states.

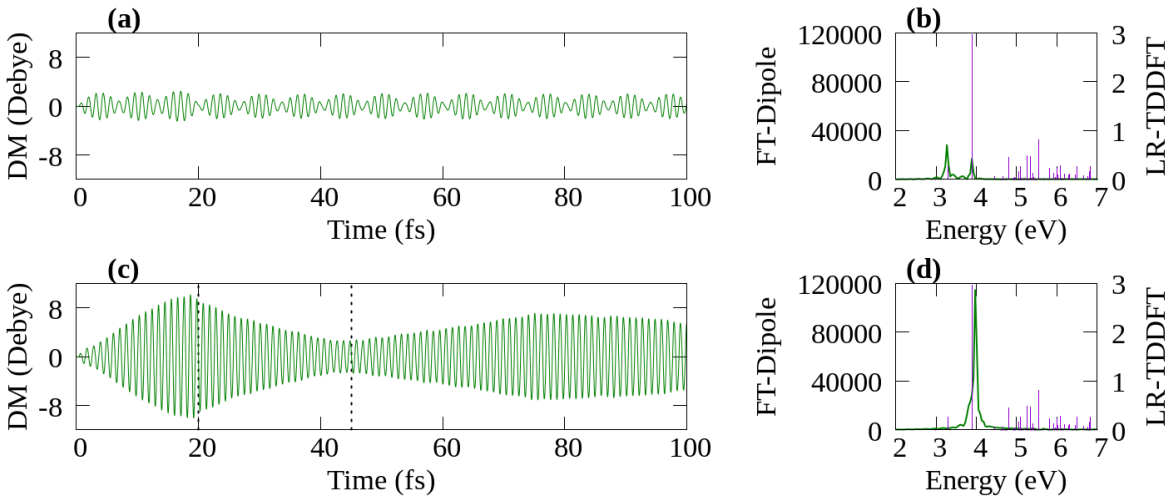

Figure 4.2. (a) Dipole moment and (b) the corresponding Fourier transform when Ag_{10}^{+2} (T_d) is excited with a frequency resonant with the 3.29 eV excited state. (c) The dipole moment and (d) the corresponding Fourier transform when Ag_{10}^{+2} (T_d) is excited with a frequency resonant with the 3.91 eV excited state. The vertical dotted lines indicate the time at 20 fs and 45 fs.

We now turn to the variation of the off-diagonal elements, P_{OV} (t), to identify which single-particle transitions become excited while the dipole response of 3.91 eV excitation decays. As predicted by LR-TDDFT (Table C-1), the transitions that are responsible for this excited state have

the same time-varying behavior as the dipole moment variation in Figure 4.2c and oscillate with the resonant frequency, 3.91 eV (Figure C-1). Moreover, these single-particle transitions adhere to the dipole-allowed symmetry rules (Table C-2). On the contrary, there are additional transitions whose dynamics are significantly different from the dipole variation (Figure 4.3). These excitations continue to increase after 20 fs until ~45 fs, which is in contrast to the dipolar behavior. More importantly, these transitions oscillate with twice the resonant frequency (Figure 4.3), indicating that these transitions arise from two-photon absorption. We confirmed that these transitions follow two-photon absorption selection rules (Table C-2). All two-photon transitions do not behave in the same way. For instance, $P_{78\text{-}104}$ continues to increase even after 45 fs whereas $P_{84\text{-}108}$ shows a gradual decay, and the decrease of $P_{84\text{-}108}$ after ~45 fs is faster compared to the decrement in $P_{86\text{-}109}$. However, they all oscillate with the common 2ω energy, 7.82 eV. These results confirm the possibility of two-photon absorption for various nanoparticle sizes.

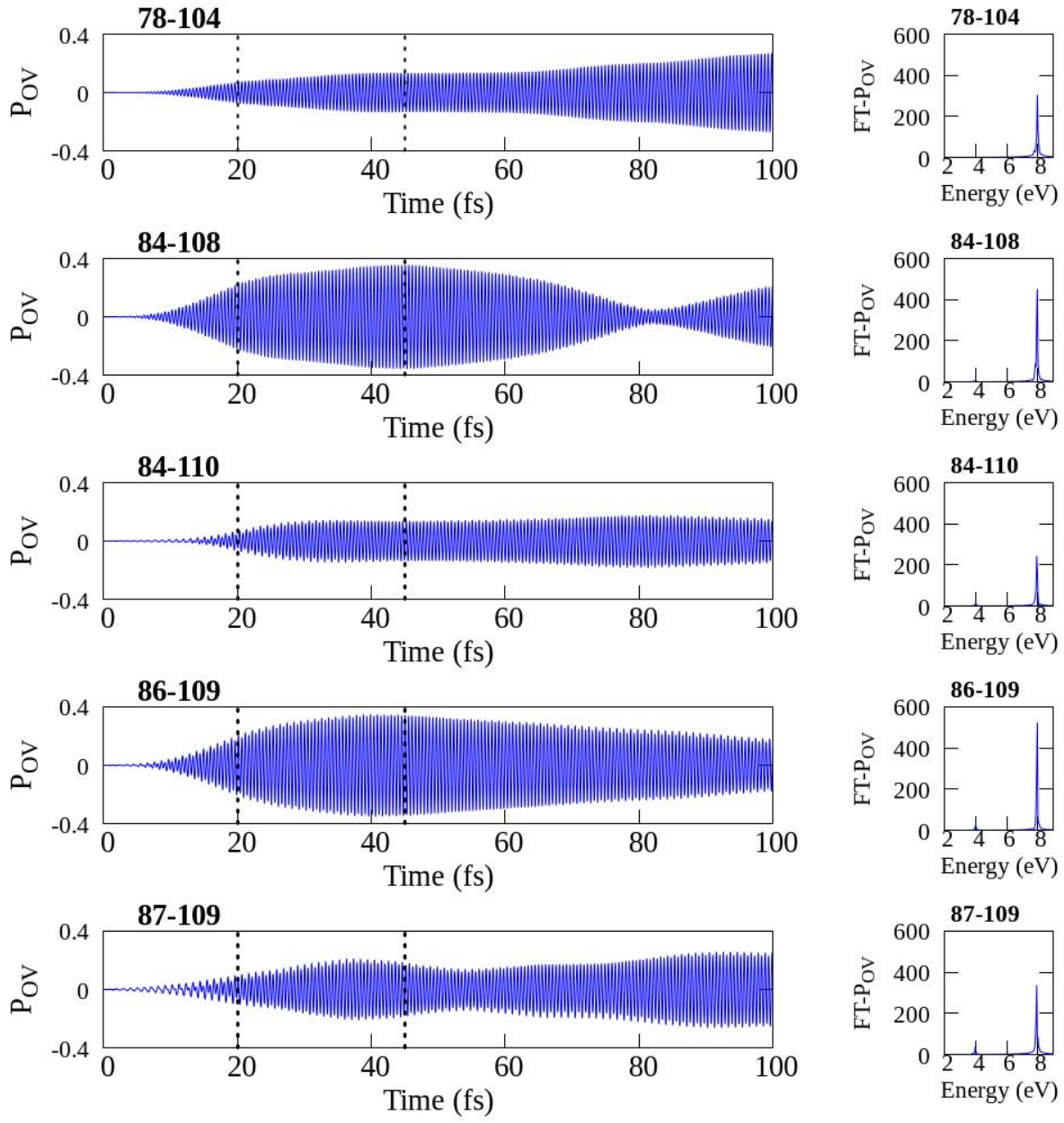

Figure 4.3. Left: Variation of P_{OV} elements oscillating with 2ω frequency (7.82 eV) after the 3.91 eV state of Ag_{10}^{+2} (T_d) is activated. Right: The corresponding Fourier transforms. The vertical dotted lines indicate the time at 20 fs and 45 fs.

It is clear from the above analysis that the density matrix elements in the energy-domain, P_{OV} (ω), provide critical information about the dominant oscillating frequency or frequencies of each single-particle transition and can be used to identify multiphoton absorptions. We analyze the maximum intensity of each P_{OV} (ω) and the corresponding energy to compact the energy-domain

data into the molecular-orbital space representing the single-particle transitions near the fermi level (Figure 4.4). The plot of maximum intensities (Figure 4.4a) illustrates the most significant single-particle transitions involved during the real-time dynamics, and the energy plot (Figure 4.4b) reveals their primary energy of oscillation. These correlated heatmaps of P_{OV} (ω) provide a comprehensive overview of the strong single-particle transitions and their principal oscillating frequency. We will utilize these heatmaps to identify multiphoton absorption in various silver nanoparticles considered in this work. As illustrated in Figure 4.4, we identify three areas with strong P_{OV} (ω) (red/orange/yellow) in the MO subspace during the dynamics resulting from excitation of the 3.91 eV state in Ag_{10}^{+2} (T_d). Figure 4.4b confirms that the strong transitions between the occupied (orbital numbers 92-94) and virtual orbitals (numbers 95-99) are the traditional one-photon allowed transitions, which oscillate with 1ω of energy (purple, 3.91 eV). The bright areas corresponding to the transitions from occupied 75-79 to virtual 104 and from occupied 81-88 to virtual 108-110 (Figure 4.4a) are found to be two-photon transitions (light blue, 7.82 eV). Higher-order nonlinear absorptions were not observed upon excitation of the Ag_{10}^{+2} (T_d) 3.91 eV state within the selected MO subspace. However, by examining the entire range of molecular orbitals in Ag_{10}^{+2} (T_d), we observed weak three-photon absorption that occurs farther away from the frontier level (Figure C-2). Overall, we detected two-photon absorption in Ag_{10}^{+2} (T_d) as a result of excited-state decay, similar to the Ag_8 (T_d) cluster results described in Ref. [173]. Higher-order nonlinear response was found to be negligible.

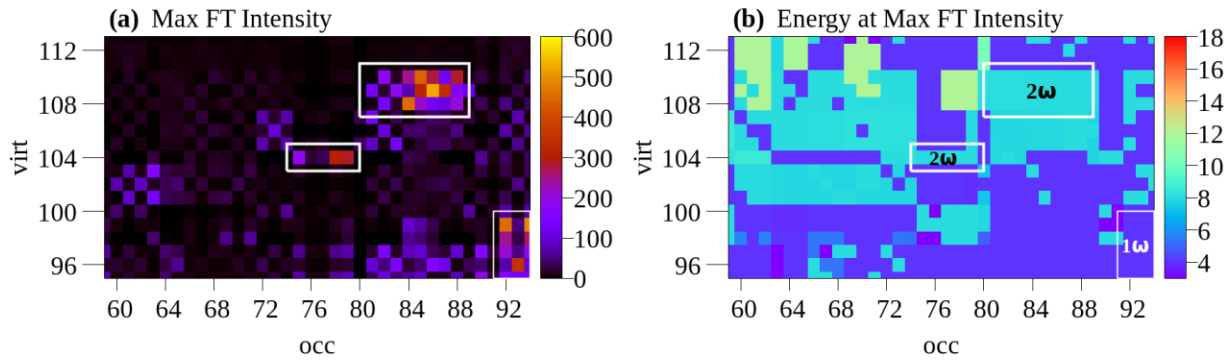

Figure 4.4. (a) Maximum intensity of P_{OV} (ω) and (b) corresponding energy at maximum intensity when the 3.91 eV state of Ag_{10}^{+2} (T_d) is activated. Areas with strong intensities are highlighted in white boxes.

4.4.2 Ag_{13}^{+5} (I_h)

At the BP86/LANL2DZ level of theory, we observe five peaks below 6 eV in the Ag_{13}^{+5} (I_h) LR-TDDFT spectrum (Figure 4.1). The splitting of the spectrum of Ag_{13}^{+5} (I_h) is subject to change with different exchange-correlation (XC) functionals (Figure C-3), as highlighted in the literature.[24] In this work we consider the spectrum with the BP86 XC functional for consistency. We examined the dynamics of the first five peaks of Ag_{13}^{+5} (I_h). When an electric field is applied that is resonant with the 3.65 eV excitation, the dipole moment continues to grow until the field is on, but the dipole decreases in the absence of the external electric field (Figure 4.5). The beating pattern of the time-dependent dipole moment and its Fourier transform (Figure 4.5) confirms that this excitation slightly couples with the neighboring state at 4.18 eV. For all five excitations, the dipole moment oscillates mainly with the resonant frequency (Figure 4.5); the lowest four excitations (3.65, 4.18, 4.69, and 5.24 eV) slightly couple with neighboring states, whereas the strong peak at 5.78 eV shows negligible coupling to the other four states. This may be due to the fact that the 5.78 eV state is nearly double the strength of the first four states, which themselves

are relatively similar in oscillator strength. Because the first state (3.65 eV) shows a fast decay of the dipolar response without the external field, we will look closer into its dynamics.

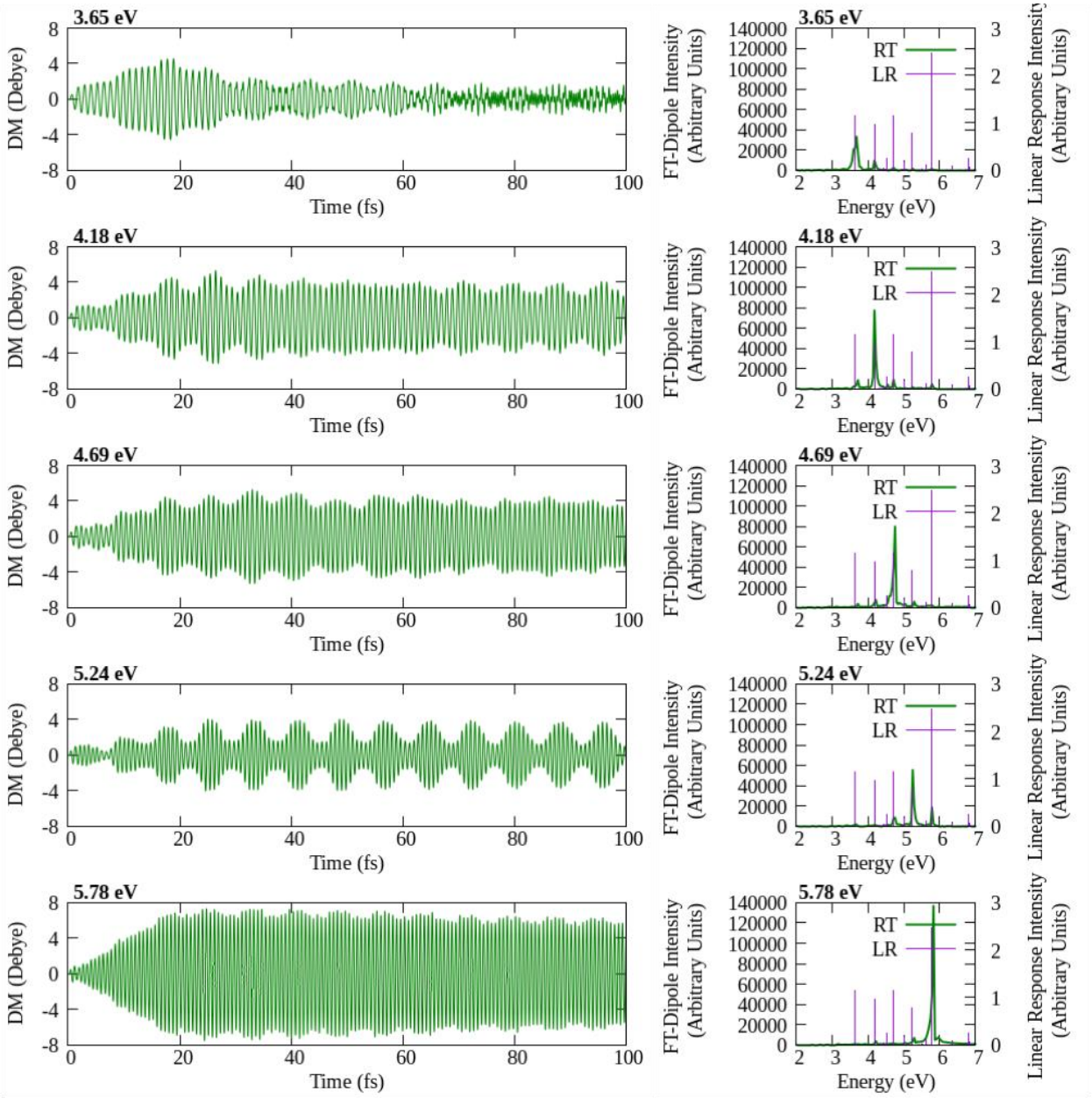

Figure 4.5. Left: Variation of the dipole moment of Ag_{13}^{+5} (I_h) when excited with electric fields resonant with the lowest five excitations. Right: The corresponding Fourier transforms.

In addition to the fast decay of the dipolar response in the 3.65 eV case, we notice a high-energy oscillation in the dipole moment from 70 to 120 fs (blue area in Figure 4.6a). Short-time Fourier transforms (STFT) in the 20-70 fs and 70-120 fs windows (Figure 4.6b) indicate a high-energy peak at about 11 eV, which corresponds to three-photon absorption, in addition to the coupling with the neighboring states such as the one at 4.18 eV. The intensity of the STFT of the dipole moment in the 20-70 fs region oscillating at the resonant energy of 3.65 eV (Figure 4.6b, red) decreases significantly during the 70-120 fs time frame (Figure 4.6b, blue). However, the peak at ~11 eV slightly increases in the 70-120 fs range. These results indicate the decay of the resonant state into 3ω excitations. We also examined the heat maps of the P_{OV} (ω) elements (Figure C-4), which confirms several strong transitions oscillating with an energy corresponding to 3ω from occupied orbital ranges 93-96 and 99-107 into virtual orbitals 143-147. Two- and four-photon absorption do not appear in the dipolar response due to symmetry restrictions. However, the heat maps of P_{OV} (ω) (Figure C-4) confirm multi-photon absorptions occur including 2ω and 4ω excitations. Furthermore, Figure C-5 illustrates the time variation of selected P_{OV} elements corresponding to multi-photon absorptions, which supports their involvement in the fast decay of the 3.65 eV state for the Ag_{13}^{+5} (I_h) cluster.

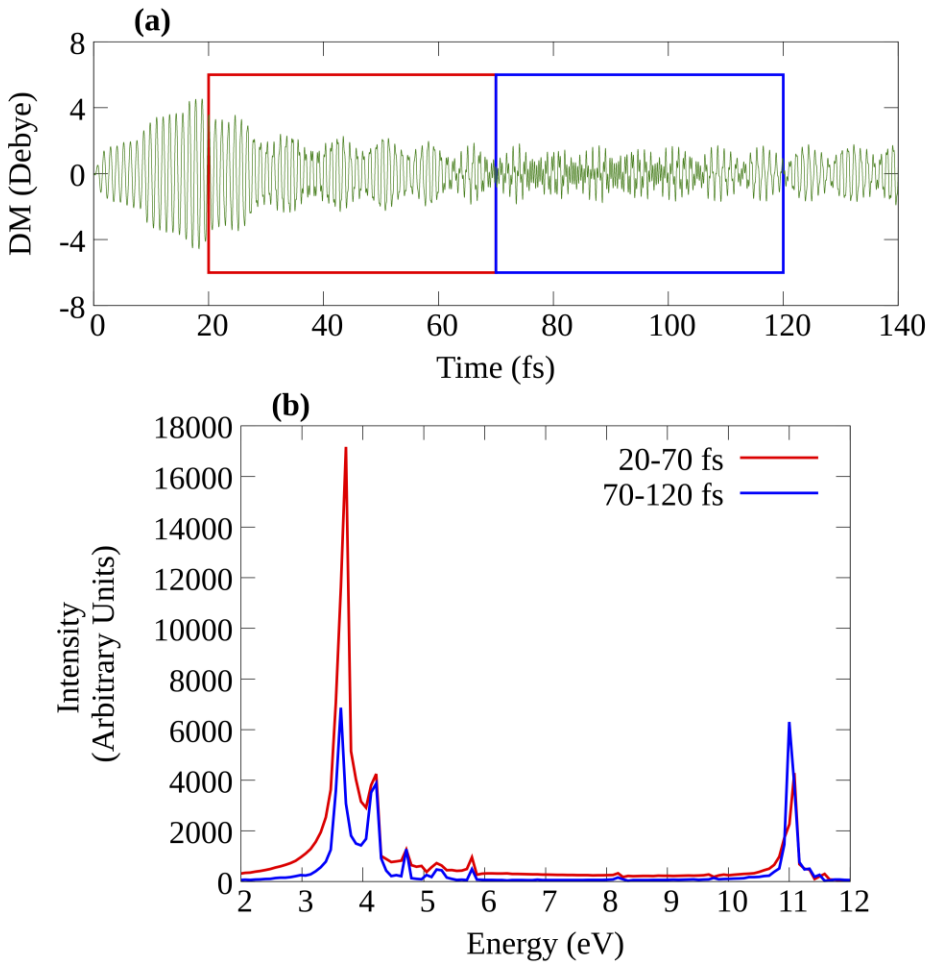

Figure 4.6. (a) Time variation and (b) short-time Fourier transforms of dipole moment in Ag_{13}^{+5} (I_h) upon excitation with 3.65 eV.

The dipolar decay is not significant when Ag_{13}^{+5} (I_h) is excited with the higher-energy excitations, 4.18, 4.69, 5.24, and 5.78 eV. Nevertheless, the analysis of P_{OV} (ω) elements (Figures C-6-9) indicates weak two-photon absorption activation in these excitations. These findings of negligible dipolar decay and weak multiphoton absorption suggest that the nonlinear optical activation is governed by excited state decay; faster dipolar decay results in a strong nonlinear activation and vice versa. Overall, the icosahedral Ag_{13}^{+5} cluster show strong nonlinear activation

as a result of the decay of the lowest state, 3.65 eV. The other states below 6 eV do not show a drastic decay.

4.4.3 Ag_{13}^{-1} (O_h)

Figure 4.7 shows the dipole moment in the time and energy domains when the first three electronic states at 2.57, 2.96, and 3.58 eV in Ag_{13}^{-1} (O_h) are excited. Among these three lowest-energy states, the low-intense, low-energy states at 2.57 eV and 2.96 eV tend to couple with the neighboring states and do not show a significant dipolar response to the perturbation even during the first 20 fs. However, the state at 3.58 eV with a strong oscillator strength shows a strong dipolar activation which suggests its plasmonic feature. The dipolar response decays moderately after the field is switched off. The analysis of the P_{OV} (ω) elements (Figure C-10) shows a considerable activation of multiphoton (2ω and 3ω) absorption when the nanocluster is excited with an electric field resonant with the 3.58 eV state. These results suggests that the strong excited states are more sensitive to the external electric field than the weak states are. Upon turning the field off, the stronger states quickly start to decay as a result of multiphoton transitions, which are less affected by the absence of the external perturbation. This might be a reason why plasmons decay very quickly compared to non-plasmonic states.

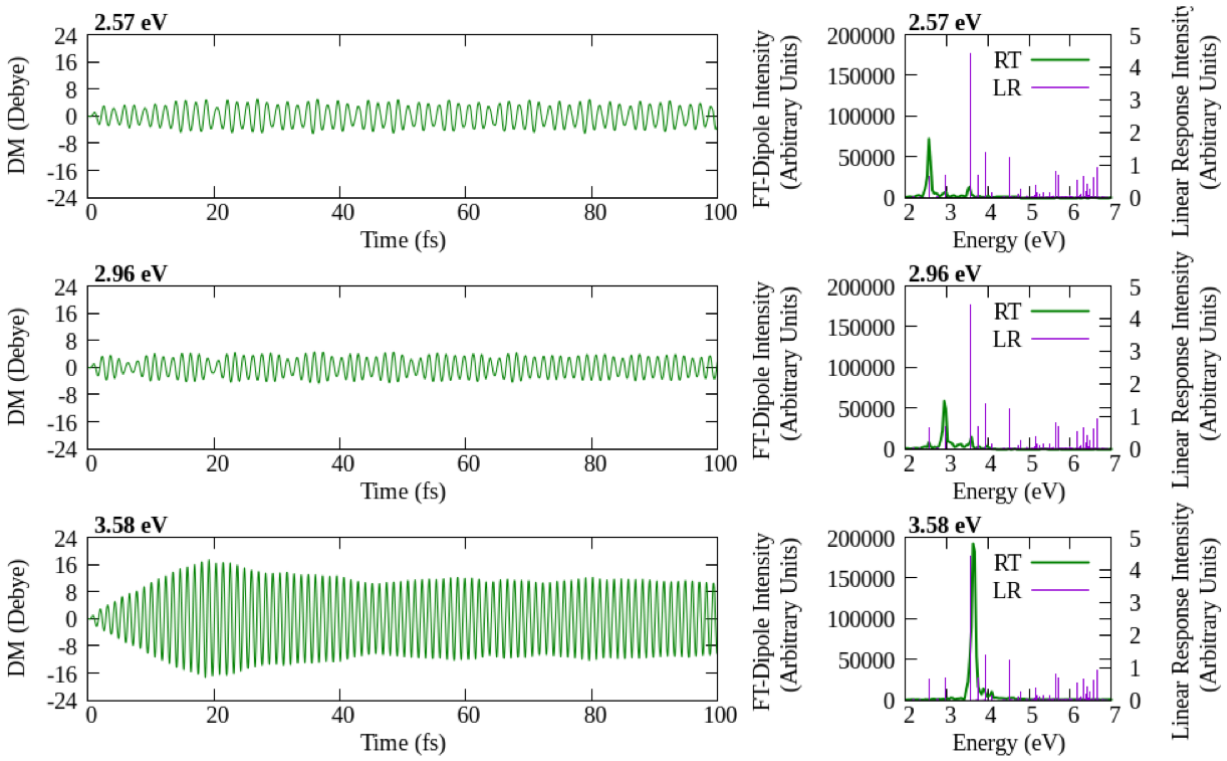

Figure 4.7. Left: Variation of the dipole moment of Ag_{13}^{-1} (O_h) when excited with electric fields resonant with the 2.57, 2.96, and 3.58 eV states. Right: The corresponding Fourier transforms.

4.4.4 Ag_{19}^{+1} (D_{5h})

In the 3.5-4.0 eV energy range of the optical spectrum of Ag_{19}^{+1} (D_{5h}), two strong longitudinal peaks at 3.51 and 3.76 eV and a strong doubly degenerate transverse peak at 3.99 eV are observed at the BP86/LANL2DZ level of theory. The longitudinal peaks are inherently polarized along the long axis of the nanorod, which is the z axis in this work. The transverse peak is inherently polarized along the short axes. Due to the symmetry, the transverse peak is doubly degenerate, with one state polarized along x and one along y axis. Here, we study the dynamics upon application of external electric fields that are resonant with each of these states; the applied electric field is z-polarized for the longitudinal excitations and x-polarized for the transverse excitation. The real-time dynamics show that all three states attain a strong dipolar optical activity under the perturbation (Figure 4.8). Although a continuous decrement was observed in the

previously described Ag_{10}^{+2} (T_d), Ag_{13}^{+5} (I_h), and Ag_{13}^{-1} (O_h) clusters, the beating nature of the dipole moment and the Fourier transforms in Ag_{19}^{+1} (D_{5h}) (Figure 4.8) suggest couplings between close lying states for all three peaks considered. We propose that this is due to the dense manifold of excited states in the 3-4 eV range in the Ag_{19}^{+1} (D_{5h}) optical spectrum, which allows the states to effortlessly couple with each other. From the P_{OV} (ω) analysis (Figures C-11-13), strong two-photon absorptions and weak three-photon absorption are evident for the transitions within the subset of frontier orbitals considered in this work. Therefore, it can be concluded that rod-like nanoclusters show multiphoton absorptions similar to more isotropic systems. In addition, it is evident that the coupling between states is likely to occur in nanoclusters with a dense manifold of excited states.

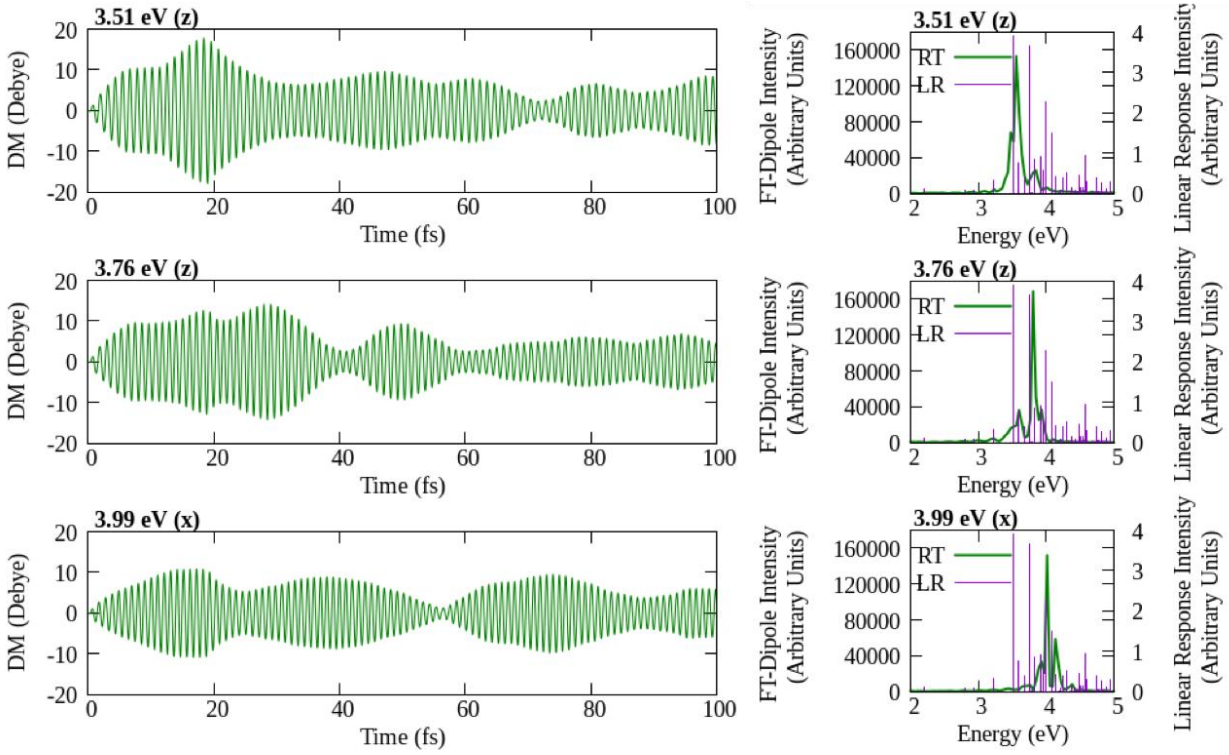

Figure 4.8. Left: Variation of the dipole moment of Ag_{19}^{+1} (D_{5h}) when excited with electric fields resonant with the longitudinal excited states at 3.51 and 3.76 eV (z-polarized) and the transverse excited state at 3.99 eV (x-polarized). Right: The corresponding Fourier transforms.

4.4.5 Ag_{20} (T_d)

The Ag_{20} (T_d) cluster is the largest tetrahedral cluster investigated in this study. A strong plasmon-like peak at 3.41 eV appears in the Ag_{20} (T_d) absorption spectrum (Figure 4.1), which is consistent with previous work.[10, 13] This state can be considered to plasmonic[13] and its dynamics are of great interest. During the real-time propagation of the 3.41 eV state, we see a dramatic decay of the dipole response in Ag_{20} (T_d) after 20 fs (Figure 4.9). The heatmaps (Figure C-14) show significant amounts of strong two-photon absorption and weak three-photon absorption. To identify which excitations might be activated during the dipolar decay, we visualized the time-dependent difference density when the 3.41 eV state of Ag_{20} (T_d) is activated.

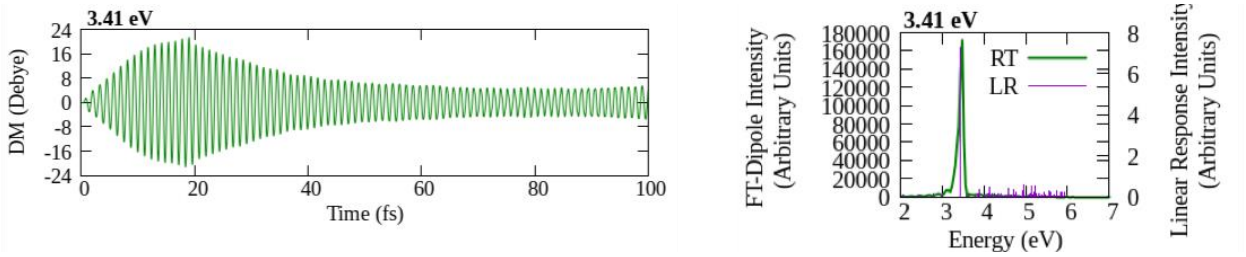

Figure 4.9. Left: Variation of the dipole moment of Ag_{20} (T_d) when excited with an electric field resonant with the strong excited state at 3.41 eV. Right: The corresponding Fourier transform.

While the field is on, the difference density, $\rho^{diff}(t)$, has a clear dipolar nature, indicated by the negative and positive densities on either side of the cluster compared to the localized ground electronic density, which gradually increase over time (Movie C-1). Figure 4.10a and b show snapshots of $\rho^{diff}(t)$ around 20 fs and 80 fs. We compare and contrast the time-dependent difference density with the transition densities of the excited states obtained from LR-TDDFT. From the identical shapes of the difference density at 20 fs (Figure 4.10a) and the transition density

of the strong state at 3.41 eV (Figure 4.10c), it is clear that the electron density resonates with the 3.41 eV state at the beginning of the real-time propagation.

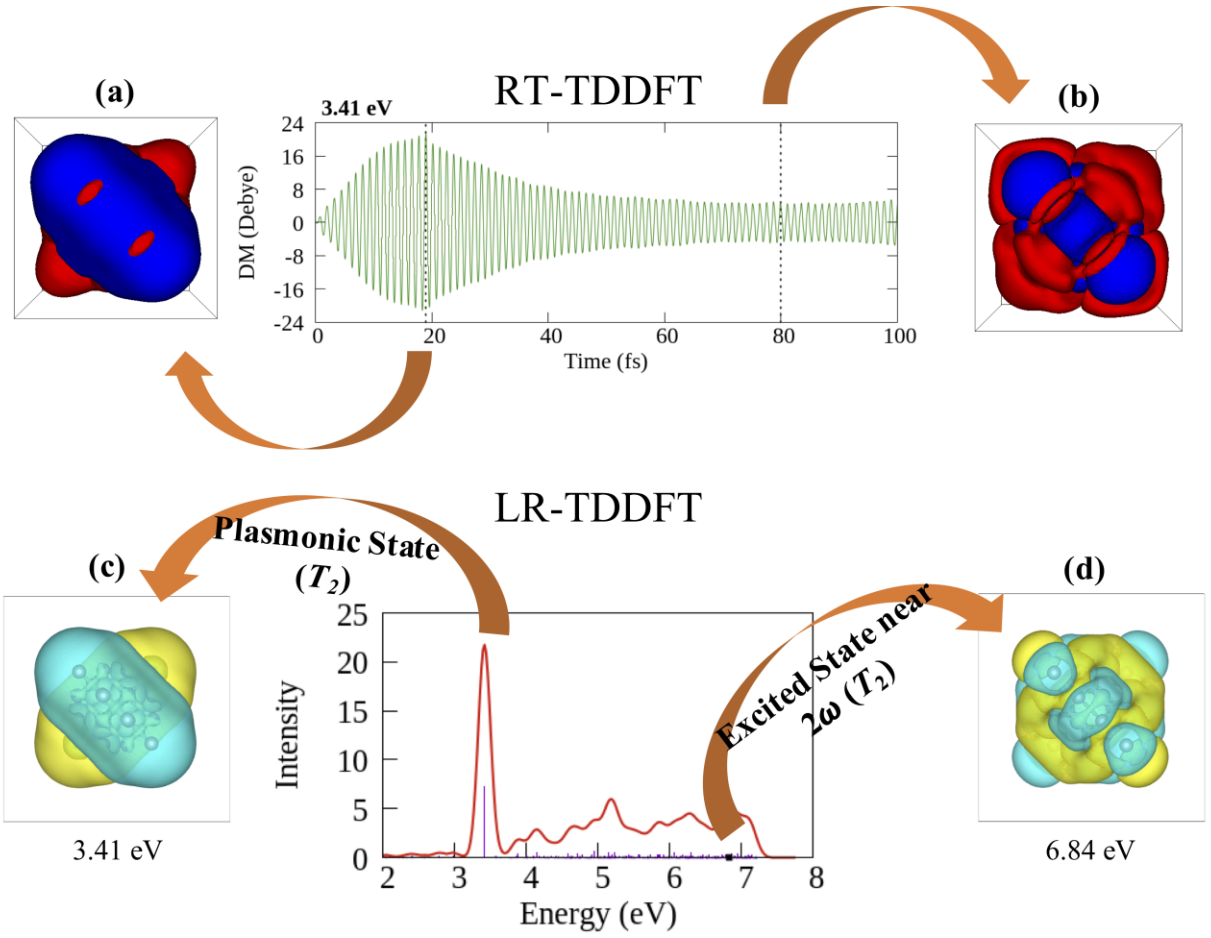

Figure 4.10. Snapshots of RT-TDDFT difference densities at (a) 20 fs and (b) 80 fs. LR-TDDFT transition densities of excited states at (c) 3.41 and (d) 6.84 eV.

The maximum dipole moment of ~20 Debye at around 20 fs gradually decreases in the absence of the electric field. The dipole magnitude reduces to ~5 Debye at 80 fs (Figure 4.10), signifying a gradual plasmon decay. The difference density at 80 fs (Figure 4.10b) also shows that the dipole moment has dampened significantly. Both the dipole moment and the difference density indicate a clear plasmon decay in tetrahedral Ag_{20} cluster within tens of femtoseconds. Interestingly, we observe a distinct quadrupolar character in the difference density at 80 fs, when

the dipole moment has reduced substantially (Figure 4.10b). Of particular interest, the difference density at 80 fs (Figure 4.10b) resembles the transition density of the excited state at 6.84 eV (Figure 4.10d), which lies close to twice the resonant energy, 3.41 eV. Other states near 6.84 eV do not display a transition density with this type of quadrupolar character. Therefore, it is clear that the plasmon-like dipolar state in this tetrahedral Ag_{20} cluster decays into a high-energy quadrupolar state near 2ω energy. This confirms that second harmonic generation is responsible for the drastic decay of the plasmon. Moreover, the symmetry of the 6.84 eV state is T_2, which is both one- and two-photon allowed according to the T_d point group symmetry rules. The presence of a T_2 state near twice the resonant energy might be the reason that this tetrahedron show plasmon decay into a second-order nonlinear state. Therefore, we propose that the tetrahedral systems can easily access the states near 2ω due to symmetry, which may lead to faster plasmon decay compared to nanoparticles with other shapes.

4.4.6 Ag_{55}^{-3} (I_h)

The largest system we examined is the Ag_{55}^{-3} (I_h) cluster. The molecular orbital diagram of Ag_{55}^{-3} (I_h) is illustrated in Figure 4.11. The occupied 5s silver atomic orbitals in Ag_{55}^{-3} (I_h) fill the spherical superatomic-type[243] molecular orbitals, which are delocalized over the entire cluster, with the $1S^2 1P^6 1D^{10} 2S^2 1F^{14} 1P^6 1G^{18}$ electronic configuration. Due to the icosahedral symmetry, splitting of some degenerate orbitals (1F and 1G, for instance) is observed. In addition, a densely populated d-band, which represents the molecular orbitals made up of linear combinations of 4d silver atomic orbitals, lies between 1P and 1D levels. In the absorption spectrum of Ag_{55}^{-3} (I_h) cluster, a strong plasmon-like peak appears at 3.27 eV at the BP86/LANL2DZ level of theory, which is comparable with the peak at 3.6 eV in neutral Ag_{55} (I_h) at the LDA/Plane-wave basis level reported by Ma and coworkers.[26] The single-particle transitions that are responsible for this strong

peak at 3.27 eV are intra-band transitions within the superatomic orbitals, and transitions from the d-band (below 500) were not encountered (Table C-3).

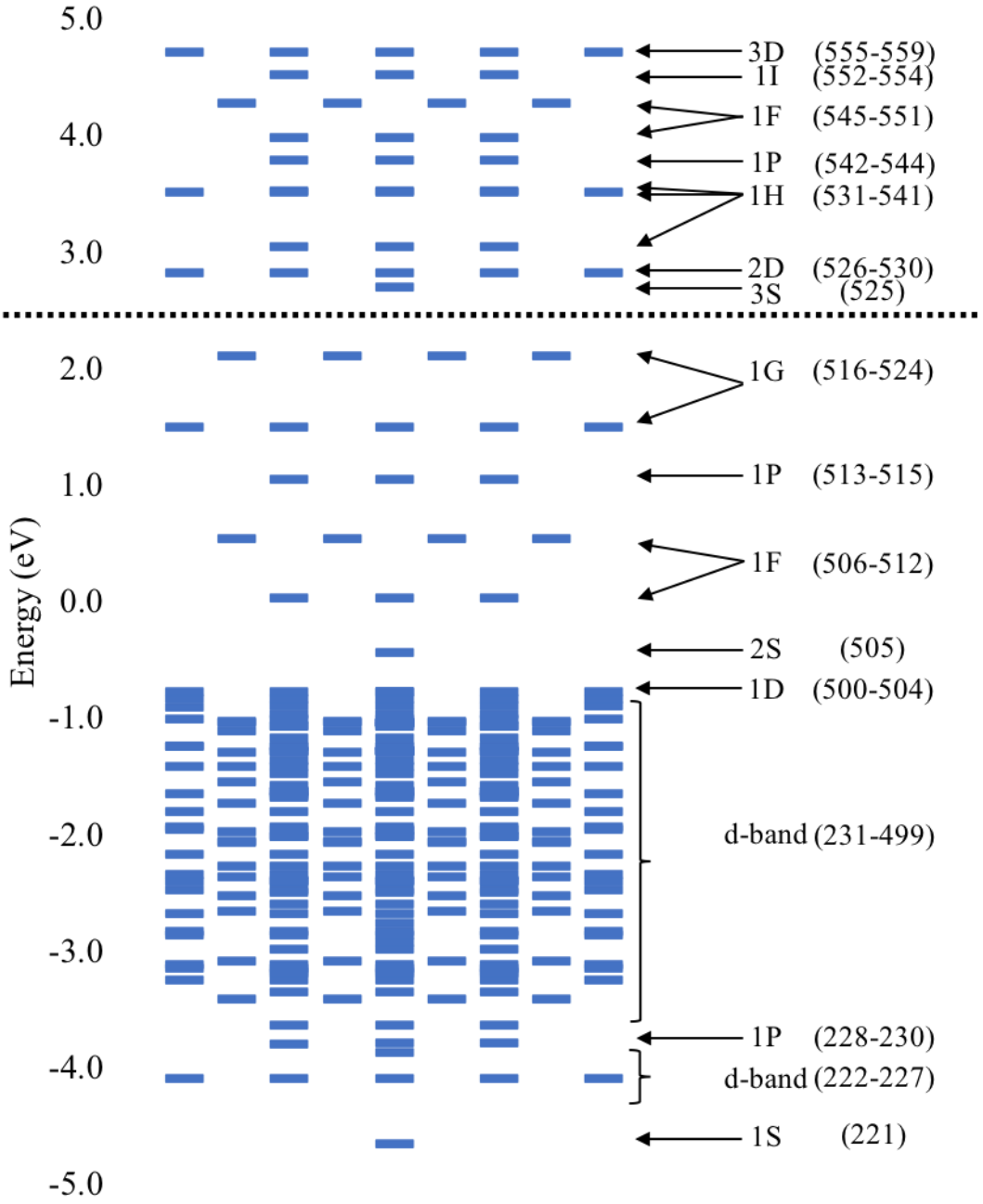

Figure 4.11. Molecular orbital diagram of Ag_{55}^{-3} (I_h). The dotted horizontal line separates the occupied and unoccupied orbitals. Characterization of superatomic and d-band orbitals with their numbers are listed.

When Ag_{55}^{-3} (I_h) is excited with this strong 3.27 eV state, the magnitude of the dipole moment increases up to a maximum of ~35 Debye at around 20 fs (Figure 4.12 Left) while resonating with the incident frequency (Figure 4.12 Right). In the absence of the external perturbation, we observe a sudden decrement of the dipole moment within a few femtoseconds (20-25 fs) followed by a second rise at about 25 fs (Figure 4.12 Left). However, the dipole moment only rises to about 30 Debye, which is smaller than it was near 20 fs. The dipole moment continues to show a beating pattern throughout the simulation. A similar beating pattern within a few femtoseconds was also observed in previous real-time work, reporting that the single-particle transitions whose energy difference is closer to the resonant energy, also known as hot carriers, result in this ultrafast decay within tens of femtoseconds.[26] In contrast, we notice that the off-diagonal elements corresponding to the transitions that are oscillating with the resonant frequency couple with the neighboring weak states at 3.39 and 3.56 eV (Figure C-15). Interestingly, these transitions that contribute to the 3.27 eV state (521-524 → 579-581, 513-115 → 552-554 and 505 → 531-533) are mutually responsible for the 3.39 and 3.56 eV states as well (Table C-3). Furthermore, they are transitions between superatomic-type orbitals and no d-band transitions involved. Therefore, we argue that interference between the close-lying states with mutual single-particle transitions is responsible for the beating of the dipolar response, versus the hot carrier generation reported in previous work.[26]

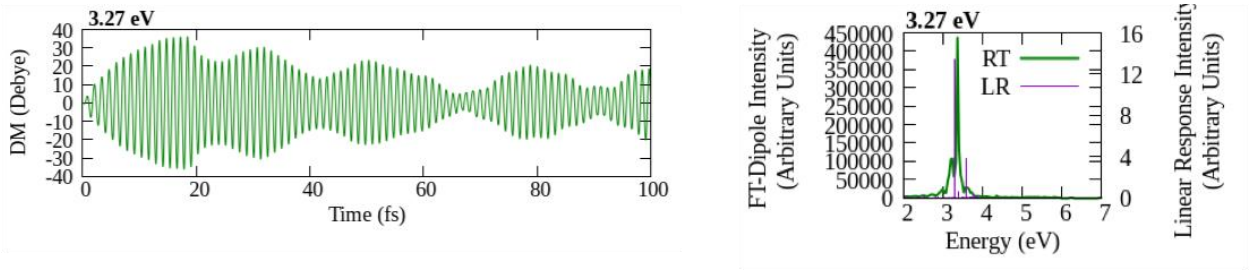

Figure 4.12. Left: Variation of the dipole moment of Ag_{55}^{-3} (I_h) when excited with an electric field resonant with the 3.27 eV state. Right: The corresponding Fourier transform.

More importantly, we found an overall dipolar decay over the 20-65 fs time frame (Figure 4.12 Left). Interestingly, the P_{OV} (t) elements corresponding to transitions between the low-lying d-band (231-499) and superatomic orbitals show an increment after 20 fs (Figure 4.13 Left). These single-particle transitions oscillate with twice the resonant energy, confirming the emergence of two-photon absorption (Figure 4.13 Right). The two-photon transitions start to grow at about 10 fs or later and continue to develop even after 20 fs after the electric field is turned off. Figure C-16 provides a summary of density matrix elements in the time and energy domains for the most significant transitions. By inspecting the heatmaps of P_{OV} elements (Figure C-17), we observe transitions that oscillate with 1ω or 2ω of energy, unlike the slowly varying single-particle transitions from d-band to LUMO level reported in previous work.[26] Moreover, the strong dipole allowed single-particle transitions belong to the T_{1u} irreducible representation in the I_h point group symmetry, whereas transitions oscillating with 2ω belong to either the A_g or H_g representations, which are in accordance with the one- and two-photon selection rules, respectively.

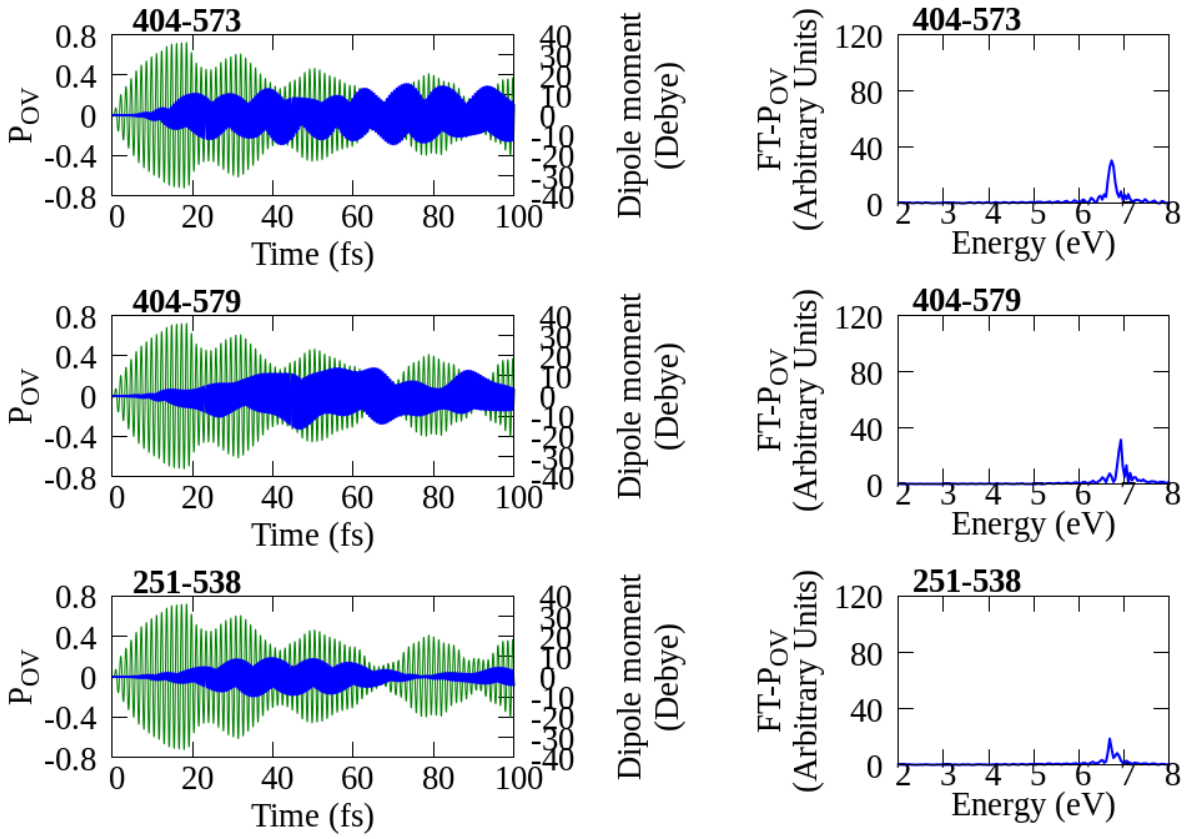

Figure 4.13. Left: Variation of P_{OV} elements oscillating with 2ω frequency when the 3.27 eV state of Ag_{55}^{-3} (I_h) is activated. Right: The corresponding Fourier transforms. Blue: P_{OV}, Green: Dipole moment.

4.4.7 Discussion

As a general trend, tetrahedral systems, Ag_8,[173] Ag_{10}^{+2}, and Ag_{20} exhibit strong plasmon-like optical properties. This work demonstrates ultrafast decay of such states due to strong two-photon absorption. One rationale for this strong second-order optical activity in tetrahedral systems might be its symmetry, which allows dipole-allowed T_2 transitions to be easily accessible via two-photon excitation. However, another aspect in these nanoclusters is that the plasmon-like states decay fast, are well separated from nearby states, and multi-state interference is avoided. In contrast, the closely lying excited states in Ag_{13}^{+5} (I_h), Ag_{13}^{-1} (O_h), and Ag_{19}^{+1} (D_{5h}) tend to couple

with each other. Nevertheless, higher-order nonlinear properties are still significant in these clusters. The Ag_{55}^{-3} (I_h) cluster also shows at least second harmonic generation from the single-particle transitions that are far from the fermi level, especially from d-band to superatom-type orbitals. One could explore the entire density matrix for completeness, but the magnitudes of the transitions far from the HOMO-LUMO level appear to be relatively weak.

4.5 Conclusions

Our RT-TDDFT studies on various silver clusters show that when strong excitations (which exhibit large oscillator strengths in LR-TDDFT spectra) are excited, the dipolar response continuously grows as long as the electric field is applied. However, the magnitude of the dipole moment starts to decay after the external perturbation is turned off. In contrast, relatively weak excitations tend to couple with neighboring stronger states throughout the simulation and do not show any decay behavior after turning the electric field off. We suggest that the plasmonic nature of the excited states and the decay process are related.

The optical spectra of tetrahedral clusters, Ag_{10}^{+2} (T_d) and Ag_{20} (T_d), are each dominated by a strong peak (at 3.91 eV and 3.41 eV, respectively), which can be treated as a plasmon-like state. Strong two-photon absorptions are evident from the variation of P_{OV} elements in these tetrahedral clusters. In addition, the time-dependent difference density of Ag_{20} (T_d) manifests how the dipole moment magnitude grows while the external field is applied and later decays into a quadrupolar state, tens of femtoseconds after the perturbation is turned off. The transition density from LR-TDDFT confirms that this newly emerging state lies close to the 2ω energy range. Overall, we predict that the plasmon resonances in large-scale tetrahedral nanoparticles are prone to fast decay, but are great sources of second-harmonic generation due to their tetrahedral symmetry.

In addition to two-photon absorption, strong higher-order absorptions up to 4ω were observed during the dynamics of the 3.65 eV state of Ag_{13}^{+5} (I_h) and the 3.58 eV state of Ag_{13}^{-1} (O_h), causing them to decay rapidly. Excitations of the longitudinal and transverse peaks of the Ag_{19}^{-1} (D_{5h}) nanorod also indicate an overall decay of the dipolar response due to the strong two-photon absorption and weak three-photon absorption. In addition, the densely packed excited states

of this nanorod lead to coupling between the states, resulting in beating patterns in the dipolar response. The 3.27 eV state of the Ag_{55}^{-3} (I_h) cluster also confirms that the interference of the mutual single-particle transitions that are responsible for the neighboring excited state introduces a temporal fall and rise in the dipole response within a few femtoseconds. Moreover, a slower decay within tens of femtoseconds was observed in Ag_{55}^{-3} (I_h) as a consequence of the two-photon absorption from the inter-band transitions.

Overall, this study provides evidence from real-time electron dynamics that nonlinear optical responses occur in silver clusters, regardless of shape and size, as their strong excited states fade away. Even though the rapid plasmon decay in silver materials is not desired for certain applications, the resulting multiphoton absorption phenomenon can be effectively used in nonlinear optical processes.

4.6 Supporting Information Available

The molecular orbital transitions responsible for the excited state at 3.91 eV in the Ag_{10}^{+2} (T_d) cluster calculated from LR-TDDFT. Variation of P_{OV} elements oscillating with the resonant frequency (3.91 eV) of Ag_{10}^{+2} (T_d) and the corresponding Fourier transforms. Symmetry-adapted selection rules for one- and two-photon allowed transitions of Ag_{10}^{+2} (T_d) excited at 3.91 eV. Heat maps of maximum intensity of P_{OV} (ω) and corresponding energy at maximum intensity for all states studied. Absorption spectra for Ag_{13}^{+5} (I_h) calculated with various exchange-correlation functionals. Variation of P_{OV} (t) elements and corresponding Fourier transforms oscillating with 1ω, 2ω, 3ω, and 4ω energy when the 3.65 eV state of Ag_{13}^{+5} (I_h) is activated. The molecular orbital transitions responsible for the excited states at 3.27, 3.39, and 3.56 eV in Ag_{55}^{-3} (I_h). Variation of selected P_{OV} (t) elements in Ag_{55}^{-3} (I_h) corresponding to the single-particle transitions that are mutually contributing to the 3.27, 3.39, and 3.56 eV states. Variation of selected P_{OV} (t) elements

and their Fourier transforms, $P_{OV}(\omega)$, when the 3.27 eV state of Ag_{55}^{-3} (I_h) is excited by a resonant electric field.

Movie C-1: Time variation of the difference density when the 3.41 eV state of Ag_{20} (T_d) is activated.

4.7 Acknowledgments

This material is based on work supported by the Department of Energy under grant DE-SC0012273. The computing for this project was performed on the Beocat Research Cluster at Kansas State University, which is funded in part by NSF grants CHE-1726332, CNS-1006860, EPS-1006860, and EPS-0919443. The authors thank Prof. Xiaosong Li for the RT-TDDFT/Ehrenfest code.

Chapter 5 - Ultrafast Nonradiative Decay of a Dipolar Plasmon-like State in Naphthalene

Gowri U. Kuda-Singappulige, Andrew Wildman, David B. Lingerfelt, Xiaosong Li, and Christine M. Aikens, J. Phys. Chem. A **2020**, 124, 47, 9729–9737

5.1 Abstract

Motivated by the uncertainty in our understanding of ultrafast plasmon decay mechanisms, we examine the effect of nuclear vibrations on the dynamical behavior of the strong plasmon-like dipole response of naphthalene, known as the β peak. The real-time time-dependent density functional (RT-TDDFT) method coupled with Ehrenfest molecular dynamics is used to describe the interconnected nuclear and electronic motion. Several vibrational modes promote drastic plasmon decay in naphthalene. The most astonishing finding of this study is that activation of one particular vibrational mode (corresponding to the B_{1u} representation in D_{2h} point group symmetry) leads to a continuous drop of the dipole response corresponding to the β peak into a totally symmetric, dark, quadrupolar electronic state. A second B_{1u} mode provokes the sharp plasmon-like peak to split due to the breaking of structural symmetry. Nonadiabatic coupling between a B_{2g} vibrational mode and the β peak (a B_{1u} electronic state) gives rise to a B_{3u} vibronic state, which can be identified as one of the p-band peaks that resides close in energy to the β peak energy. Overall, strong nonadiabatic coupling initiates plasmon decay into nearby electronic states in acenes, most importantly into dark states. These findings expand our knowledge about possible

plasmon decay processes and pave the way for achieving high optical performance in acene-based materials such as graphene.

5.2 Introduction

Interaction of light with subwavelength materials gives rise to a remarkable phenomenon called a plasmon resonance. Upon interacting with incident light at a plasmon resonance frequency, the electrons of plasmonic materials undergo collective oscillations. Because of the potential applications of plasmonic systems in photocatalysis,[35, 265] non-linear optics,[35, 205, 208] and biomedical applications,[29] etc., plasmonics has become a hot topic in the photonics community. Noble metal nanoparticles comprised of gold and silver can be regarded as the first plasmonic materials ever used, dating back to ancient Rome, although this plasmonicity was not recognized then. To date, many different noble metal nanoparticles of different sizes, shapes and surface environments have been synthesized, each having unique optical properties.[266-269] However, due to the low abundance and high cost of noble metals, alternative materials are of interest, including heavily-doped semiconductor materials as well as 2D materials.[270-272] In particular, due to the strong light confinement effects and tunability of graphene in the terahertz and infrared regions, graphene-based 2D structures have emerged as possible platforms for plasmon-driven devices.[84-86, 88, 273-274] In addition, recent studies have proposed large enhancements of non-linear properties in graphene.[275-279] However, plasmon loss in graphene severely hampers the performance of optical devices and thus the structural modulation of graphene-based 2D materials to minimize the energy loss is an active research area.[88, 280-281]

The performance of plasmonic devices can be hampered by energy dissipation in plasmonic materials.[258, 260] Researchers have proposed that the plasmon can decay via fast formation of hot carriers, electron dephasing, and comparatively slow vibrational dissipation.[7, 105-

[106, 212-213] Different pathways may facilitate plasmon decay in different substances. Nevertheless, identifying the most probable non-radiative decay mechanisms in a given type of materials is vital to identify the normal modes that bring about fast plasmon decay, so that they might be hindered in intelligent device designs.

The purpose of this work is to understand possible mechanisms of fast plasmon dynamics in acenes, the building blocks of graphene, from a theoretical perspective. The low-energy absorption spectra of acenes including naphthalene have been previously reported experimentally[96, 98] as well as with different theoretical methods.[99-104] The p-band peaks, the α peak, and the β peak are the main spectral features of acenes. The lowest energy p-band peak and the α peak of naphthalene, also known as ^1L_a and ^1L_b respectively, are observed in the visible region with weak intensities. While the p-band excitations arise due to electron transitions along the short axis of the molecule, the α and β peaks arise from transitions along the long axis. The strong β peak, which is in the UV region, has a plasmon-like character manifested by the constructive nature of the responsible single-particle transitions.[104] Therefore, it is valuable to explore the fast decay processes of this plasmon-like β peak in naphthalene by means of first-principles theories, which can ultimately provide insights into how energy may flow in larger graphene-based plasmonic materials. For example, recent studies demonstrate that electron-phonon coupling plays a key role in intramolecular singlet fission process in low-energy excitations in acenes.[282-286] In this work, we focus on the influence of nuclear motion on the electron dynamics of the strong collective excitation in naphthalene.

In order to describe the ultrafast plasmonic processes accurately, incorporation of a quantum mechanical treatment of electrons is crucial. The well-known linear-response theory[157, 165] can describe static response properties such as electronic absorption spectra of molecules that

result from a weak external field. This method is computationally feasible for calculating low-energy excited states of small metal nanoparticles.[157, 241, 264, 287-291] However, the frequency domain description of electronic excitations provided by this technique limits its usefulness for our purpose of disentangling the influence of vibrations on the electronic evolution of a system in a superposition of ground and excited states. Real-time electron dynamics methods,[159-160, 166] on the other hand, allow us to access the fluctuation of excited state population in both linear and non-linear regimes and have been developed based on different quantum mechanical approaches such as time-dependent configuration interaction (TD-CI)[292-295] and time-dependent Hartree-Fock/density functional theories (TDHF/TDDFT).[159, 166, 169-170, 218-219, 242, 296] Smith et al.[101] studied the electron dynamics of acenes with a pulsed field at a frequency of 1.55 eV using real-time TDHF method and observed that the lowest energy excited state polarized parallel to the applied field, α peak in naphthalene, strongly couples to the field.

Many real-time electron dynamics methods examine only electron movement assuming that the nuclei are stationary. To identify the effect of nuclear motion on the plasmon decay, an ab-initio molecular dynamics (AIMD) method that is capable of accessing excited electronic states should be employed. Most standard AIMD schemes are based on an adiabatic Born-Oppenheimer approximation where the nuclear motion is governed by the ground state electronic potential.[297-300] For our goal of this study however, electronic excited states such as the plasmon-like excitation should be considered, as well as the transitions between excited states, which requires going beyond the adiabatic approximation. Among the current nonadiabatic techniques, the Ehrenfest molecular dynamics scheme serves as the most feasible way to incorporate real-time propagation of excited electrons in an AIMD framework due to its computational tractability relative to other nonadiabatic schemes.[186, 301] In this method, the nuclei are treated classically while the electrons

are treated quantum mechanically, and the atoms move in a trajectory whose forces are derived from a mean-field potential of the electronic states.[182, 187, 302] The mean-field nature of the Ehrenfest dynamics is ideal for simulating a dense manifold of excited states such as those involved in plasmon-like excitations. This work adopts the Ehrenfest molecular dynamics approach coupled with real-time time-dependent density functional theory (RT-TDDFT)[109, 303] to investigate the dynamics of the strong β peak of naphthalene upon activation of several vibrational modes to capture possible plasmon decay pathways.

5.3 Methodology

We study the effect of vibrational motion on the plasmon dynamics of naphthalene using Ehrenfest molecular dynamics implemented in a development version of the Gaussian software package.[238] Geometry optimizations, frequency calculations, Born-Oppenheimer molecular dynamics (BOMD) and Ehrenfest electron-nuclear dynamics were carried out with the B3LYP[144-145, 304] exchange-correlation functional and 6-31G(d,p)[305-309] basis set. The atomic coordinates of the optimized naphthalene are given in Table D-1. The transition densities corresponding to excited sates and time-dependent difference densities are visualized using Vesta[310] software. The transition densities provide a qualitative picture of the electron density difference in an excited state compared to the density of the ground state.

We follow a similar procedure as in the work of Donati et al.[109] to identify the effect of vibrational motion on the variation of the strong plasmon-like β peak. The electron density is converged in the presence of an electric field perturbation of 0.001 au (~3.57×10^{13} W/cm^2) applied along the longitudinal axis of naphthalene to mimic the activation of the strong β peak excitation. The field is removed after convergence, and the system starts to propagate using Ehrenfest dynamics where a single normal mode on the ground electronic state is selectively activated at the

beginning of propagation. The initial nuclear velocities were generated randomly, corresponding to an amount of energy equivalent to 5 quanta of the chosen vibrational energy at the equilibrium geometry. The previous work by Donati et al.[109] shows that the plasmon decay in silver nanowires is accelerated with the number of vibrational quanta and we choose 5 quanta to show the effect more clearly. However, our work shows that for naphthalene 5 quanta of energy is a special case which is discussed later in the text. The current implementation of the Ehrenfest dynamics[182, 187] utilizes a triple-step integrator to account for different time scales for the nuclear velocity-Verlet algorithm (Δt_N),[180] nuclear-position coupled midpoint Kohn-Sham integrator (Δt_{Ne}) and RT-TDDFT using modified midpoint and unitary transformation (Δt_e). In this work we use time steps Δt_N = 0.1 fs, Δt_{Ne} = 0.01 fs and Δt_e= 0.001 fs.

5.4 Results and Discussion

5.4.1 Optical Absorption Properties from LR-TDDFT

Figure 5.1 illustrates the absorption spectrum of naphthalene calculated using LR-TDDFT with the B3LYP/6-31G(d,p) level of theory, highlighting the different types of excitations. The α and β peaks arise at 4.52 eV and 6.10 eV respectively. The three p-band peaks occur at 4.46 eV, 6.26 eV and 8.22 eV. As naphthalene belongs to the D_{2h} point group, the α and β peaks can be assigned to the B_{1u} representation while the p-band peaks can be assigned to the B_{3u} representation according to the cartesian axes of naphthalene shown in Figure 5.1. Furthermore, it has been previously identified that while the weak α peak arises due to the destructive combination of the two molecular orbital (MO) transitions, HOMO → LUMO + 1 and HOMO – 1 → LUMO, the stronger β peak is a result of constructive addition of the same MO transitions.[103-104] Due to the constructive interference and resulting strong absorption of the β peak, a molecular analog of plasmonic nature can be identified in naphthalene. The calculated excited state energies and the

contributing MO transitions of naphthalene at the equilibrium geometry are tabulated in Table D-2.

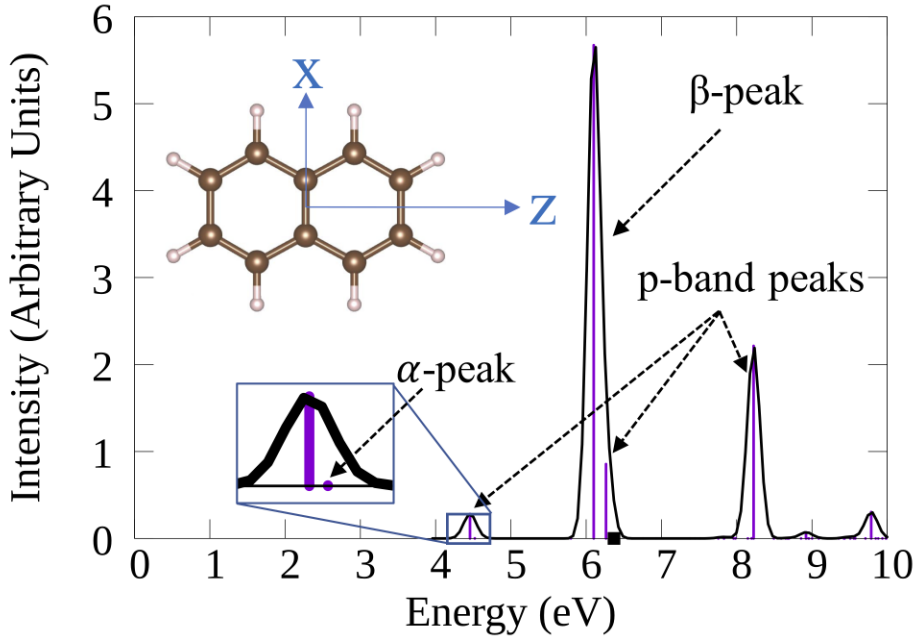

Figure 5.1. Absorption spectrum of naphthalene calculated from LR-TDDFT (Purple: LR stick spectrum; black: convoluted spectrum using Gaussian curves with Gaussian FWHM = 0.2 eV). Insets show the axes assignments used in the text and a zoomed-in version of part of the spectrum showing the low-intensity α peak. The black square at 6.37 eV indicates a dark electronic state with A_g symmetry.

5.4.2 Effect of Vibrational Modes on Plasmon Dynamics

In order to understand the effect of vibrational motion of the molecule on the change of the β band, we activate one vibrational mode with simultaneous excitation of the electronic states polarized along the z axis; the change of the β peak is monitored over time. Vibrational mode energies on the ground electronic state and their D_{2h} point group representations are given in Table D-3.

5.4.2.1 Mode 32 (B_{1u})

The most intriguing vibrational mode which gives rise to a drastic change in the dipole moment over time is normal mode 32 (1407.82 cm^{-1}), which belongs to the B_{1u} representation. First, we compare the dipole response from a BOMD simulation in ground electronic state with that from an Ehrenfest simulation where the electrons are excited along the long axis of naphthalene (Figure 5.2a). As shown in Figure 5.2b, this vibrational mode (and any other mode with B_{1u} representation) is antisymmetric with respect to the reflection through the *xy* plane. Therefore, both electronic and nuclear excitations with B_{1u} symmetry lead the *z*-component of the dipole moment to deviate from 0. Electronic excitation creates a high frequency oscillation centered around the lower frequency oscillation contributed by the nuclear vibration. We examined all of the B_{1u} vibrational modes and observed that the Ehrenfest and BOMD simulations exhibit the same low-frequency nuclear vibrational pattern in all cases (Figure D-1). This suggests that electronic perturbation does not noticeably affect the nuclear motion in these simulations.

In the Ehrenfest excited state dynamics with mode 32 activated, we observe a continuous decrement of the dipole strength over the first 600 fs (Figure 5.2a) and as a consequence, a clean decay of the plasmon-like β peak (Figure 5.2c). This behavior of the dipole moment demonstrates almost an extinction of the plasmon-like excited state. This leads to the question of where the energy goes over this time scale and whether the system is accessing any "dark" plasmon states. Unlike B_{2g} or B_{3g} normal modes, a B_{1u} mode cannot lead to vibronic coupling to another excitation polarized along either *x* or *y* directions. (A discussion of the symmetry considerations for vibronic coupling is provided in the SI). As expected, the variations in the *x*- and *y*-components of the dipole moment do not show a significant increment while the *z*-component of the dipole moment decreases. Our hypothesis is that this B_{1u} normal mode coupling with the B_{1u} electronic excitation

leads to energy transfer into a dark electronic state with A_g symmetry that is allowed by vibronic coupling.

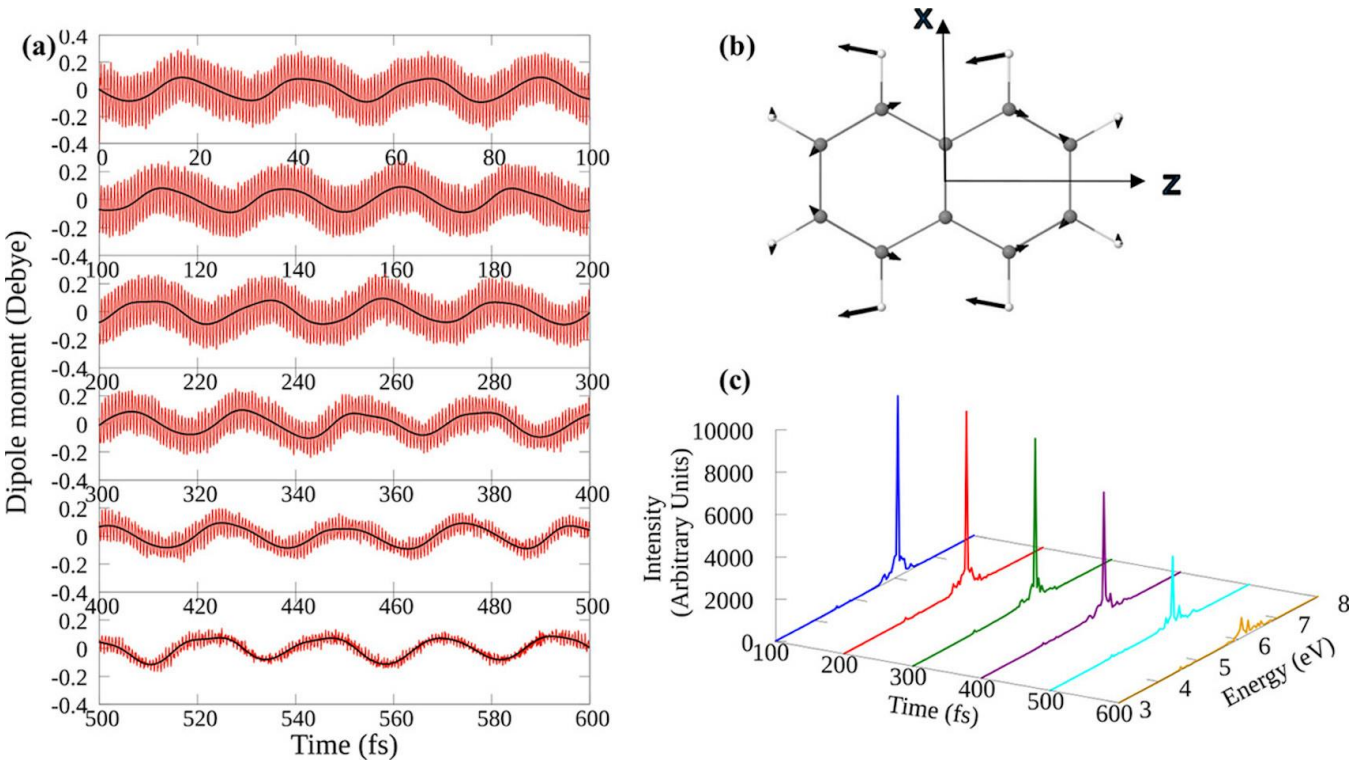

Figure 5.2. (a) *z*-component of the dipole moment when mode 32 (B_{1u}) is activated with 5 quanta. Red: Ehrenfest excited state dynamics; Black: ground state BOMD. (b) Vector representation of normal mode 32. (c) Short-time Fourier transforms of 100-fs windows of the *z*-component of the dipole moment during Ehrenfest dynamics.

However, activation of this totally symmetric dark mode cannot be captured from the dipole response. Instead, the variation of the excited state density compared to the ground state density can be used to answer the question of which states the initial plasmon energy dissipates into. We calculate the difference density $\rho_{m32}^{diff}(t)$ using (5.4.1) where $\rho'_{m32}(t)$ represents the time-dependent electron density during the Ehrenfest dynamics where normal mode 32 is activated and the electric step field is applied, and $\rho^0_{m32}(t)$ is the electron density from a similar calculation without an applied electric field. In other words, the difference density reveals how the electron density in the excited state deviates from the ground state in a time-varying situation.

$$\rho_{m32}^{diff}(t) = \rho'_{m32}(t) - \rho_{m32}^{0}(t) \tag{5.4.1}$$

The dipole moment variation along the *z* axis over 600 fs is illustrated in Figure 5.3a and expanded views from 0 to 1 fs and from 580 to 581 fs are shown in Figure 5.3b and 3c, respectively. The density difference maps calculated using (5.4.1) at the beginning of the simulation are shown in Figure 5.3d. The initial difference density at 0 fs can be compared with the transition density corresponding to the β peak excitation shown in Figure 5.3e, which clearly exhibits the activation of the β peak at the beginning of the Ehrenfest simulation. The positive and negative lobes at the two ends of naphthalene indicate that the electrons have moved from one end to the other compared to the delocalized ground state electron density. The dipole moment variation between positive and negative values clearly displays the electron density sloshing back and forth from one end to the other end of the molecule, in keeping with the traditional picture of a "plasmon-like" excitation. The positive and negative lobes completely change signs from 0 fs to 0.37 fs (Figure 5.3d). The dipole moment at 0.37 fs is now positive compared to its negative initial value (Figure 5.3b). Both the dipole moment and the density difference plot return to initial positions near 0.7 fs. Throughout the beginning of the simulation, the time variation of the electron density clearly manifests the character of the plasmon-like electronic excited state (β peak) of the molecule (Figure 5.2c).

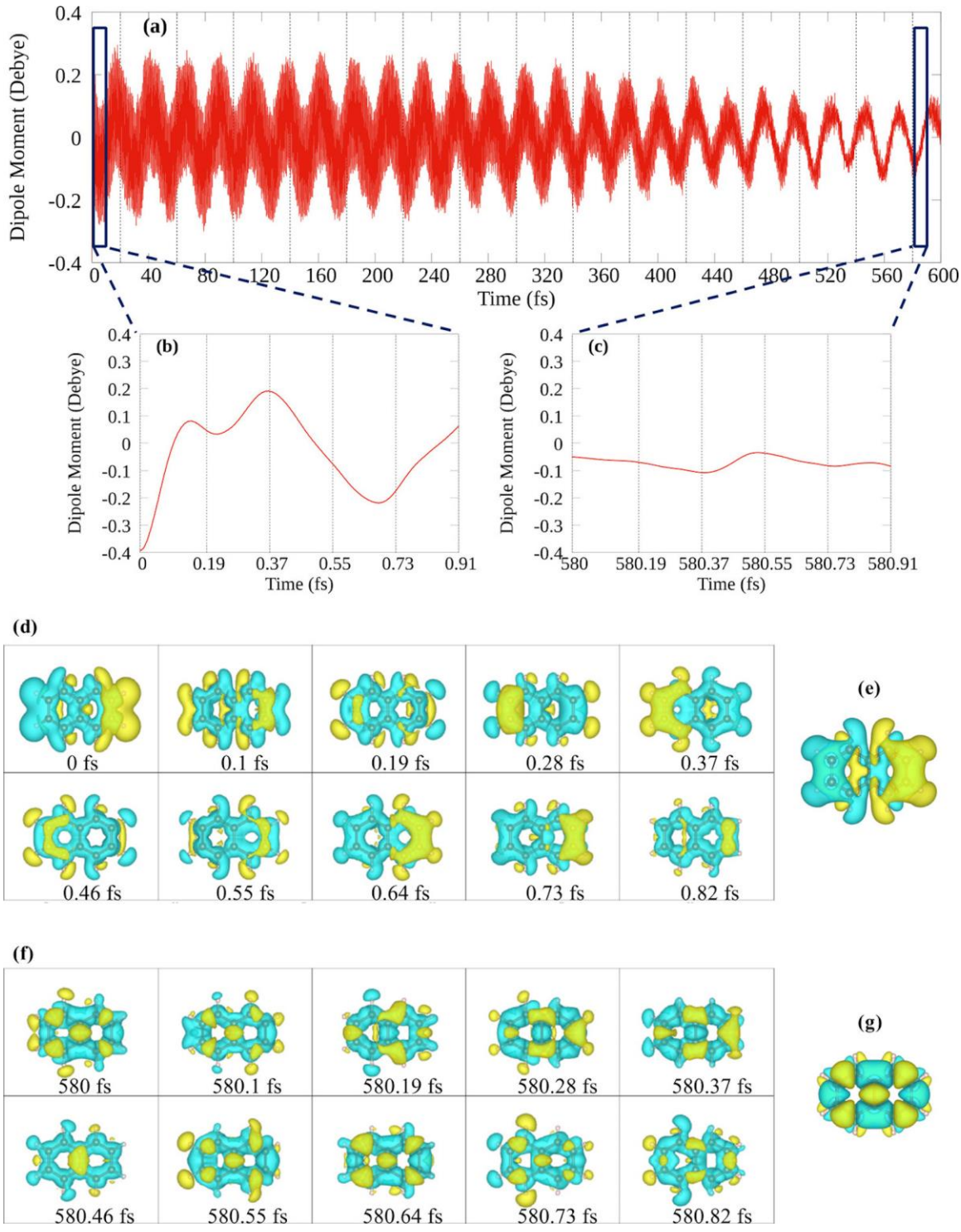

Figure 5.3. (a) Variation of the *z*-component of the dipole moment for normal mode 32. Detailed dipole moment variation (b) from 0 to 1 fs, (c) from 580 to 581 fs. (d) Variation of the density difference from 0 fs to 1 fs, (e) transition density of the beta peak (6.10 eV), (f) variation of the density difference from 580 fs to 581 fs and (g) transition density of the 6th excited state (6.37 eV, dark mode). Color code for figures d-g ; yellow: positive; cyan:

negative. Isovalues 1×10^{-5} and 5×10^{-4} were used for difference densities (d and f) and transition densities (e and g) respectively.

The strength of the dipole moment decreases gradually from about 300 fs to 600 fs (Figure 5.3a). To analyze the origin of this behavior, we closely examine the variation of the difference density during 580 fs to 581 fs (Figure 5.3f), where the dipole moment has lost its strength to a great extent. The density difference no longer has a dipolar character as it did at the initial stages. Instead, the difference density plots throughout this time interval have a quadrupole character. Most importantly, the shape of these difference densities resembles the shape of the transition density corresponding to the 6th excited state (Figure 5.3g), which is a totally symmetric electronic state (A_g) and hence dipole-forbidden for the D_{2h}-symmetric naphthalene molecule (Electronic transitions from A_g ground state into B_{1u}, B_{2u}, or B_{3u} excited states are allowed). This dark A_g state has been experimentally identified by Bergman and Jortner[311] using two-photon absorption spectroscopy. Our innovative application of difference densities demonstrates that strong nonadiabatic coupling along this B_{1u} vibrational coordinate can facilitate internal conversion to the dark A_g state. Vibronic selection rules confirm that the direct product of the irreducible representations for the vibrational state (B_{1u}) and the electronic state (B_{1u}) gives rise to a vibronically allowed A_g state (See SI). Above all, the appearance of this dark state correlated with the near-vanishing of the plasmon-like peak clearly illustrates the hitherto-hypothesized mechanism that plasmon decay may occur into nearby dark states.

We extended the simulation with mode 32 until 1200 fs and observed a revival of the β peak after 600 fs. Because the total energy is conserved in the system (i.e. no loss mechanisms are present in a simulation with a single molecule and no bath), we can expect such a revival over time due to the couplings between the excited states; the system will not be completely trapped in a particular state.

We also examined the dipole response when mode 32 is activated with various number of quanta (0-10) during Ehrenfest dynamics. We observe that only 5 quanta and 10 quanta lead to a decay within 600 fs, but not the ones above or below 5 and 10 quanta of energy (Figure D-2). This raises the fact that the 5 and 10 quanta are special cases. One thought was that the energy difference between the β peak (6.10 eV) and the dark state (6.37 eV), 0.27 eV, might match with the vibrational energy of 5 quanta (and 10 quanta) in mode 32 (= 0.960 eV). However, we do not see this energy matching suggesting further investigations on the energetics in the future.

The energy conservation during an Ehrenfest molecular dynamics simulation when different quanta of mode 32 are activated is shown in Figure D-3. We observe that the quality of energy conservation diminishes over time with increasing number of quanta. However, the total energy in the 5 quanta case varies only within 5×10^{-5} au (0.00136 eV) during 0-600 fs and can be considered as negligible.

5.4.2.2 Mode 10 (B_{1u})

Another B_{1u} normal mode that leads to changes in the dipole response over time is mode 10 (634.99 cm^{-1}). Like any other B_{1u} mode, the *z*-component of the dipole moment exhibits a clear vibrational signature in both BOMD and Ehrenfest dynamics (Figure 5.4a). The vector representation of this B_{1u} normal mode (Figure 5.4b) displays its antisymmetric nature with respect to the reflection through the xy plane. Note that significant changes in the carbon rings occur in mode 10 (Figure 5.4b) compared to mode 32 (Figure 5.2b).

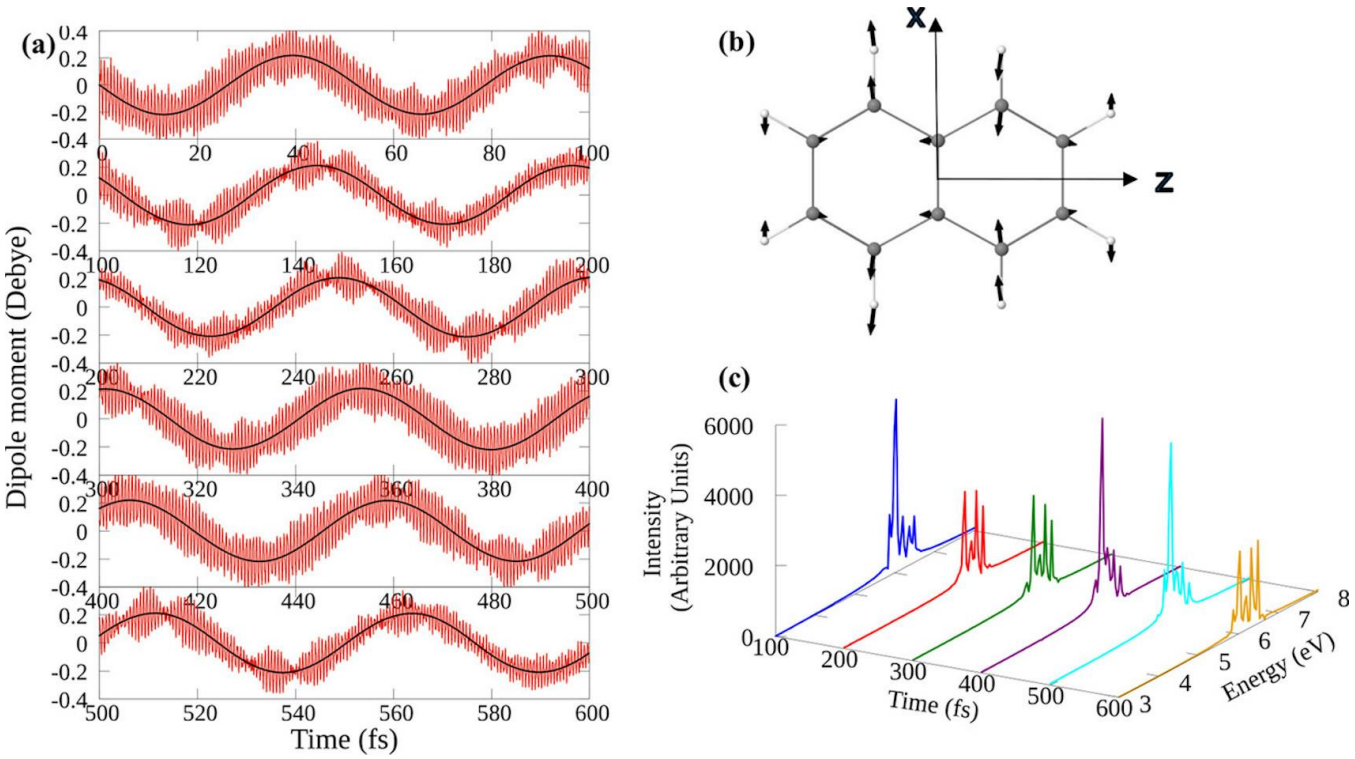

Figure 5.4. (a) *z*-component of the dipole moment when mode 10 (B_{1u}) is activated with 5 quanta. Red: Ehrenfest excited state dynamics; Black: ground state BOMD. (b) Vector representation of normal mode 10. (c) Short-time Fourier transforms of 100-fs windows of the *z*-component of the dipole moment during Ehrenfest dynamics.

The strength of the dipole moment in this case decreases until about 300 fs and then starts to rise again. This is also illustrated by the short-time Fourier transforms arising from 100 fs windows of the dipole moment given in Figure 5.4c. In addition, a splitting of the plasmonic β peak throughout the simulation is observed. To distinguish the spectral changes due to the structural distortions, we analyze the static LR-TDDFT absorption spectrum of the most distorted geometry of naphthalene when mode 10 is activated, i.e. the geometric structure at 40.0 fs. The distortion of the carbon rings due to the motion of normal mode 10 leads to a splitting of the β peak (Figure 5.5). The original β peak at the equilibrium geometry (6.10 eV) has shifted to lower energy at 5.96 eV and a new peak appears at 6.46 eV. In addition to the HOMO – 1 → LUMO and HOMO → LUMO + 1 transitions,

which are the transitions responsible for the β peak, the two transitions HOMO – 2 → LUMO + 1 and HOMO – 1 → LUMO + 2 contribute slightly to the peak at 5.96 eV (Table D-4). Interestingly, these new transitions appear to be the highest contributors to the peak at 6.46 eV with a slight contribution from HOMO – 1 → LUMO and HOMO → LUMO + 1 transitions. This indicates that lowering of the D_{2h} point group symmetry corresponding to the equilibrium geometry of naphthalene into C_{2v} symmetry at distorted geometries allows new electronic states to emerge. The multiple peaks appearing in the Fourier transforms in Figure 5.4c are due to the coupling between excited states mediated by the structural distortions. We observe a splitting of the β peak with 0 quanta of energy of mode 10 but a reduction of the dipole strength was not observed (Figure D-4). In conclusion, the B_{1u} normal mode 10 reduces the symmetry of naphthalene which subsequently leads to a splitting of the β peak. In contrast, because mode 32 does not lead to considerable changes in the carbon atom positions, the most distorted structure of mode 32 shows negligible changes in the plasmonic peak. We thus conclude that only the vibrational modes that significantly distort the molecular symmetry tend to split the plasmon-like peak. Nonetheless, normal modes similar to 32 can access electronic states that are optically dark (from the ground state) via ultrafast nonradiative decay from a higher-lying state, as described above.

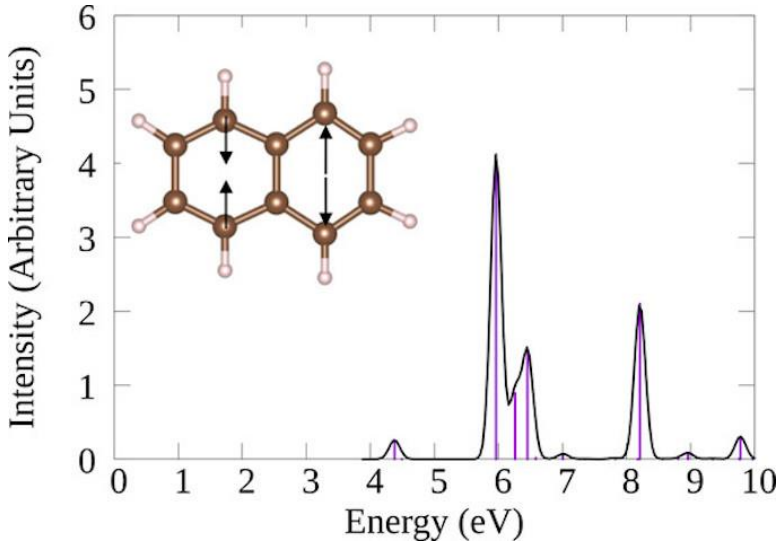

Figure 5.5. LR-TDDFT absorption spectrum of the geometry of naphthalene at 40.0 fs during the Ehrenfest simulation where the normal mode 10 is activated. The inset shows the geometry of naphthalene at 40.0 fs and the arrows indicate the movement of the carbon atoms compared to the equilibrium geometry.

5.4.2.3 Modes with B_{2g} symmetry

According to the vibronic coupling selection rules in a D_{2h} molecule, excited B_{2g} vibrational states could couple with excited B_{1u} electronic states (polarized along the *z* axis) to give rise to B_{3u} vibronic states, which are polarized along the *x* direction. The variation of the *z*- and *x*-components of the dipole moment when mode 35 (1501.48 cm^{-1}, B_{2g}) is activated with 5 quanta along with the excitation of the β peak are shown in Figure 5.6a (green). The *z*-component of the dipole moment decreases in magnitude from 0 fs until about 40 fs when it starts to increase again. We observe this decay and growth throughout the 600 fs simulation. Interestingly, at times when the magnitude of the *z*-component of the dipole moment decreases, the *x*-component of the dipole moment increases and vice versa, thereby showing the coupling between the dipole moments along the two orthogonal directions. The Fourier transform of the oscillations of the *z*-component of the dipole moment yields a peak at 6.05 eV (green curve in Figure 5.6b) which is very close to the β

peak energy (pink stick at 6.10 eV in Figure 5.6b). In comparison, the Fourier transformed *x*-component of the dipole moment gives rise to two peaks at 6.23 eV and 6.28 eV (blue curve in Figure 5.6b) which lie near the second p-band excitation energy at 6.26 eV. The slight shifting and the splitting of both green and blue curves are probably due to the interactions between the two electronic states. This phenomenon is even more noticeable when the B_{2g} normal modes in the 1100-1700 cm^{-1} energy range are excited with zero quanta; they exhibit similar coupling of the *z*- and *x*-components of the dipole moment after electronic excitation in the *z*-direction (Figures D-5 and D-6).

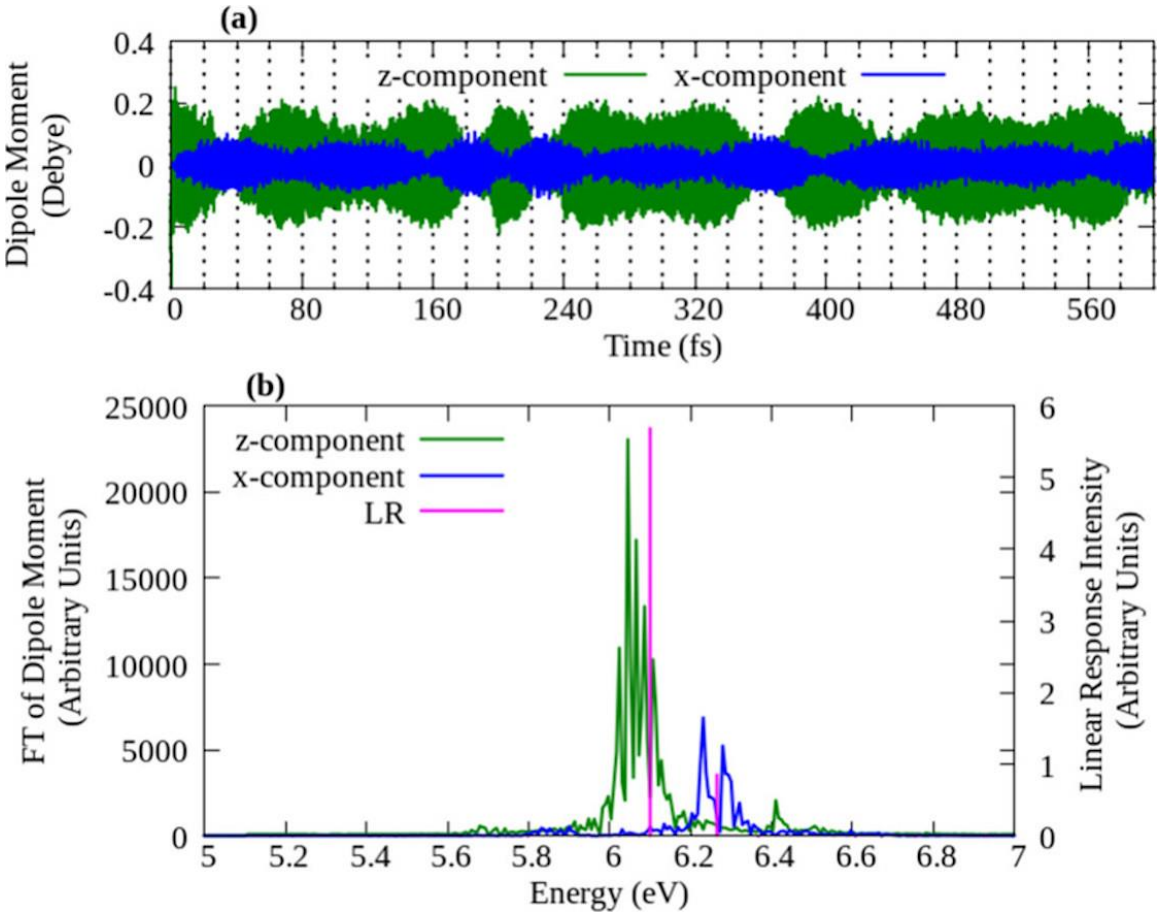

Figure 5.6. (a) Variation of the dipole moment when mode 35 (B_{2g}) is activated with 5 quanta. (b) Fourier transforms of dipole moment components compared with the LR-TDDFT excitation energy positions. green: *z*-component; blue: *x*-component of the dipole moment; pink: LR-TDDFT stick spectrum.

5.5 Summary

The heart of this work is the elucidation of an important plasmon decay pathway, which is activation of dark electronic states mediated by strong nonadiabatic coupling related to certain normal modes. We examined the changes of the strong dipole response of naphthalene when different vibrational modes are activated. The most interesting one, mode 32 (B_{1u}), shows a continuous decrease in the dipole response over 600 fs. Upon activation of this normal mode, a comparison of the excited electron density to the density of the ground state shows that the initial dipolar nature of the electronic oscillation ultimately decays into a quadrupolar form resembling the transition density of the dark electronic excited state that resides close in energy to the bright state.

Another interesting nuclear motion that affects the plasmonic peak is normal mode 10 (B_{1u}). This mode largely breaks the symmetry of the molecule compared to the equilibrium geometry, leading to a splitting of the β peak.

The nonadiabatic coupling of B_{2g} normal modes with the B_{1u} plasmon-like β peak, which is polarized along the long axis of naphthalene, initiates energy transfer to the nearest p-band with B_{3u} symmetry, which is polarized along the short axis. Thus, initial excitation polarized in one direction can lead to a dipole response in a different direction.

Although 5 quanta of vibrational energy would be somewhat higher than one would expect at normal experimental conditions, this work highlights a new understanding of plasmon decay. Nonadiabatic coupling may be one of the dominant pathways of plasmon loss in acenes and potentially in graphene because multiple vibrational modes can couple the plasmon-like state to other excited states as shown in this work. In addition, fast plasmon decay via nonadiabatic coupling may occur not only in graphene-based plasmonic materials but also in noble metal

nanoparticles as governed by the corresponding symmetry rules. This work offers a new route to manipulate the optical properties of plasmonic materials via designing materials with longer (or shorter) plasmon decay lifetimes by adjusting how the vibrational modes couple to the bright and dark electronic excitations.

5.6 Supporting Information Available

Optimized coordinates of naphthalene. MO transitions responsible for selected excitations in naphthalene. Energies and symmetry representations of normal modes of naphthalene. Variation of the *z*-component of the dipole moment for B_{1u} normal modes of naphthalene during Ehrenfest dynamics and BOMD in the ground electronic state. Symmetry-adapted selection rules for pure electronic transitions and vibronic transitions. MO transitions responsible for excitations in the most distorted geometry of naphthalene during activation of normal mode 10. Time and frequency domain *z*- and *x*-components of the dipole moment during an Ehrenfest dynamics with electrons excited along the *z* direction and B_{2g} normal modes of naphthalene activated with zero quanta.

5.7 Acknowledgments

This material is based on work supported by the Department of Energy under grant DE-SC0012273. The computing for this project was performed on the Beocat Research Cluster at Kansas State University, which is funded in part by NSF grants CHE-1726332, CNS-1006860, EPS-1006860, and EPS-0919443. The development of the first-principles electronic dynamics is supported by the U.S. Department of Energy (DE-SC0006863 to X.L.). The development of the linear-response TDDFT method for computational spectroscopy was supported by the National Science Foundation (CHE-1856210 to X.L.).

Chapter 6 - Theoretical Insights into Plasmon-Driven Oxygen Activation on a Tetrahedral Ag_8 Cluster

Gowri U. Kuda-Singappulige and Christine M. Aikens

6.1 Abstract

Research on small molecule dissociation on plasmonic silver nanoparticles is on the rise. Herein we investigate the effect of various parameters of light, i.e., field strength, polarization direction and energy of oscillation, on the dynamics of oxygen upon photoexcitation of the $O_2@Ag_8$ composite using real-time time-dependent density functional theory calculations with Ehrenfest dynamics. From our excited-state dynamics calculations, we found that increasing the strength of the external electric field brings a significant contribution to the O-O dissociation. In addition, the polarization direction of the incident light becomes important, especially at weaker field strengths. The light that is polarized along the direction of charge transfer from the metal to adsorbate was found to enhance the bond breaking of O_2 more than the light polarized along other directions. We also found that at the weakest electric field strength, oxygen molecule stays adsorbed to the silver cluster when the incident light resonates with low-energy excited states and desorbs away from the metal cluster with high-energy excitations.

6.2 Introduction

Silver is known as a selective catalyst for epoxidation reactions over other transition metals.[120, 312-325] However, the large rate limiting step associated with the molecular oxygen dissociation on metal catalysts requires the reactions to be operated at high temperature.[120, 315, 319, 324] Such extreme conditions result in low energy efficiency, deformation of the catalyst and less selectivity for desired products.[62, 326-327] Fortunately, photoactivation of oxygen on plasmonic silver nanostructures eliminates the requirements of intense operating conditions.[31, 62, 69] Due to the complexity and ultrafast nature of plasmon-mediated processes, unraveling the basic principles behind light-induced molecular dissociation is challenging. Hence, the nature of the energy transfer between the plasmonic silver nanoparticle to the adsorbate is still unclear. Several experimental and theoretical works suggest that the direct charge transfer from photo-excited silver nanoparticles to molecular oxygen may dominate over the indirect hot-carrier transformation.[31, 62, 66, 69-70]

Resolving photo-driven processes at the molecular scale is key to designing and enhancing the performance of novel photocatalysts. Several theoretical investigations on plasmon-induced small molecule activation pathways have been performed using both jellium model and ab-initio methods.[62, 66, 69-70, 72] However, these studies are based on static electronic structure properties and the linear perturbative regime. Time-dependent simulations equipped with a complete quantum mechanical treatment of the electrons provide a comprehensive description of the photo-induced dissociation pathway. Recent real-time electron dynamics work by Kumar and coworkers demonstrate the ultrafast hot electron transfer from silver to carbon monoxide molecules in a Ag_{147}–CO system.[74] A handful of dynamical studies used both electron and nuclear degrees of freedom to mimic the dissociation mechanism. Several groups report H_2 and H_2O splitting

triggered by the plasmon excitation of gold surfaces.[76, 328-330] Yan et al. showed that the splitting of a H_2 molecule adsorbed at the end of silver nanowires of various sizes occurs only at the resonant frequency of the nanowire and is enhanced with strong electric field.[110] Our recent work demonstrates the effects of field strength and the applied field direction on N_2 dissociation on silver nanowires.[75] However, the photo-dissociation of molecular O_2 on silver nanoparticles has not yet been studied using quantum dynamics. Ultrasmall silver clusters as small as Ag_7 have been synthesized under certain experimental conditions.[331-332] Nevertheless, dynamical studies on oxygen activation on such experimentally observed ultrasmall silver clusters have not yet been performed, although these studies can elucidate which factors lead to more efficient photo-dissociation.

In this work, we study the dissociation of oxygen on a tetrahedral Ag_8 cluster in real time. We conduct ab-initio molecular dynamics simulations upon electronic excitation of the $O_2@Ag_8$ composite system with a strong electric field. This approach provides the flexibility to investigate the effect of the strength, oscillating frequency, and the polarization direction of the applied field on the oxygen dissociation ability.

6.3 Methods

First, we determined the most stable binding site of molecular oxygen on a tetrahedral Ag_8 cluster ($O_2@Ag_8$). Due to the presence of oxygen, which has a triplet ground state for the isolated molecule, the triplet multiplicity was employed in this work. We confirmed that the triplet ground state of the lowest energy $O_2@Ag_8$ isomer is about 2 eV more stable than the singlet excited state of the same geometry. Next, the dissociation dynamics of oxygen starting from the most stable configuration of $O_2@Ag_8$ upon electronic excitation was investigated using the Ehrenfest molecular dynamics method coupled with real-time time-dependent density functional theory (RT-

TDDFT). A trapezoidal-shaped electric field with field strengths of 0.01 au (3.57×10^{14} W/cm^2), 0.03 au (1.07×10^{15} W/cm^2), and 0.05 au (1.78×10^{15} W/cm^2) were used. The variation of the applied electric field oscillating with 4.25 eV is shown in Figure E-1. We considered x, y, and z polarization directions of the applied field with several resonance energies. We aligned the O_2@Ag_8 system in a way such that the intermolecular axis between Ag_8 to O_2 occurs along the z-axis. Due to the binding fashion of O_2 to Ag_8 in this lowest energy structure, the long axis of molecular oxygen is parallel to the y-axis. During the Ehrenfest dynamics, we kept the nuclear motion of the Ag_8 cluster frozen. The three-time-step integration scheme for Ehrenfest dynamics used in this study is discussed elsewhere[182, 187] and we used a nuclear time step (Δt_N) of 0.1 fs, a nuclear-position coupled midpoint Kohn-Sham integrator (Δt_{Ne}) of 0.01 fs, and a modified midpoint and unitary transformation (MMUT) step Δt_e of 0.001 fs. We checked the energy convergence with smaller timesteps and observed no dynamical changes and no significant improvement of the energy convergence. We also noticed that the energy convergence is poor at large electric field strengths. All the trajectories were initiated with a total nuclear kinetic energy of 0.0014250 au (3.7415 kJ/mol) which corresponds to the translational energy at 300 K. We use the unrestricted LC-ωPBE[333]/LANL2DZ[131, 239-240] level of theory for all calculations in a development version of the Gaussian program.[238] The visualization tools MacMolPlt[334] and Jmol were used for visualizing molecules and molecular orbitals respectively, and VESTA[310] was employed for visualizing transition densities.

6.4 Results and Discussion

In this work, we study the photodissociation dynamics of oxygen in the O_2@Ag_8 composite to identify the effect of electric-field-related parameters on the bond breaking. First, we examine

the ground state geometrical, electronic, and optical properties of $O_2@Ag_8$, then examine the dynamics of this system after photoexcitation with various applied electric fields.

6.4.1 Geometrical and electronic properties of $O_2@Ag_8$

At the LC-ωPBE/LANL2DZ level of theory, we found that the tetrahedral geometry of bare Ag_8 cluster is energetically preferred; previous literature[335-338] has debated whether this cluster exhibits T_d or D_{2d} symmetry. Various binding sites of molecular oxygen to the tetrahedral Ag_8 cluster were optimized and the total energies of different configurations are shown in Figure E-2. In the most stable configuration of $O_2@Ag_8$ (Figure 6.1center), the oxygen molecule binds to the two silver atoms with Ag–O bond lengths 2.25 Å and 2.29 Å. The O–O bond length, 1.36 Å, lies between the bond lengths of the O_2 double bond (1.24 Å, LC-ωPBE/LANL2DZ) and the single bond in H_2O_2 (1.47 Å, LC-ωPBE/LANL2DZ). This bond expansion of the oxygen molecule adsorbed on the silver cluster compared to the isolated oxygen molecule is in agreement with previous theoretical work done on both silver clusters[66] and slab models.[69, 314, 322] Interaction with the silver cluster results in a splitting of the π/π^* orbitals of the oxygen molecule and orbital mixing with the silver orbitals. One of the two empty π^* beta-spin orbitals (81β) lowers its energy when attached to Ag_8 and becomes occupied (Figure 6.2 Left). The bond elongation of oxygen when bound to a silver cluster is facilitated by this electronic structure modification.

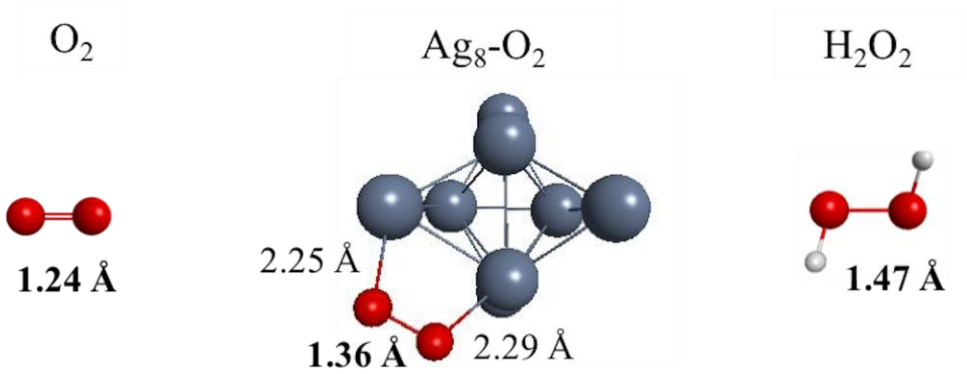

Figure 6.1. Comparison of O–O bond lengths in O_2 (left), $O_2@Ag_8$ (center) and H_2O_2 (right)

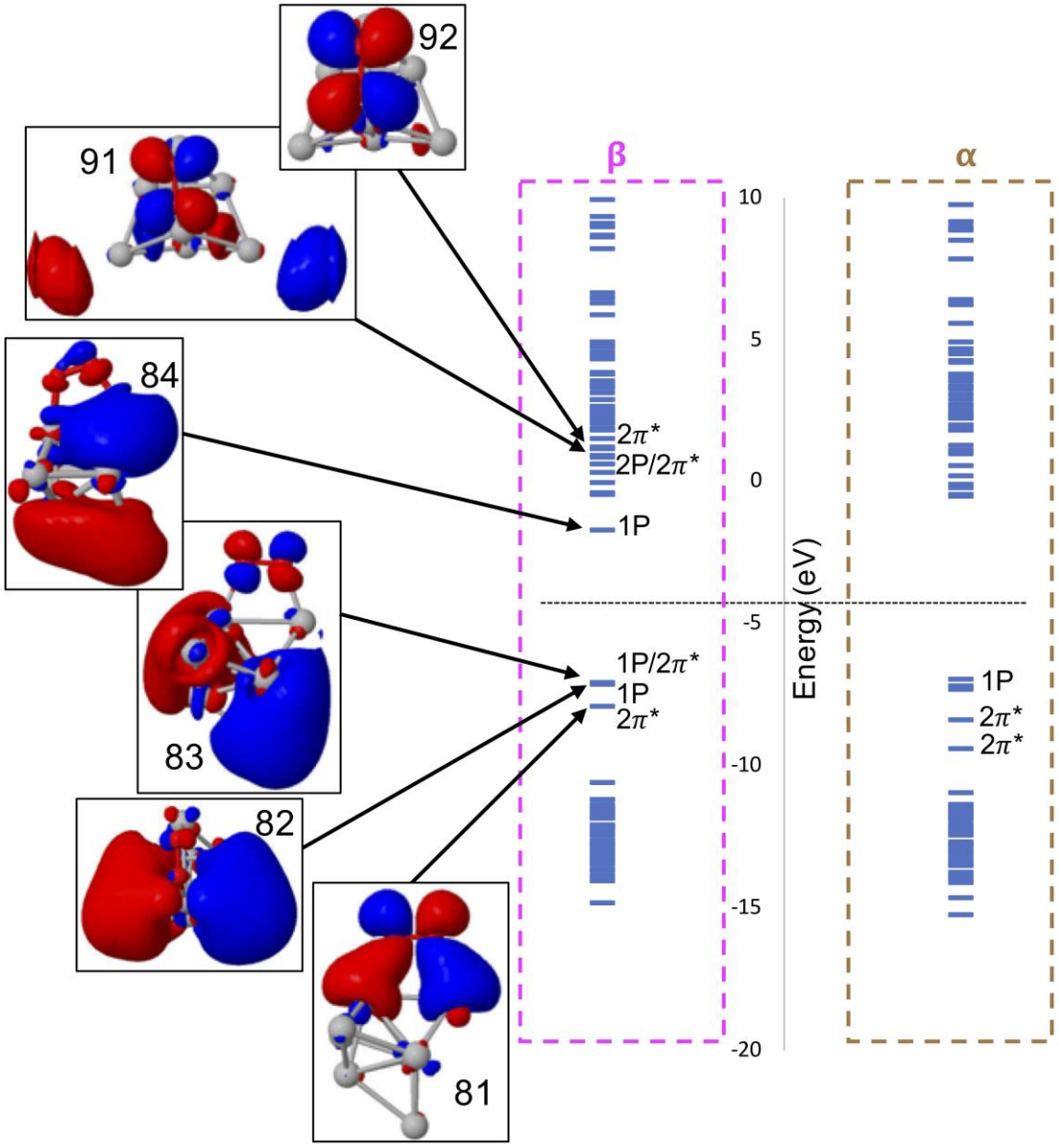

Figure 6.2. Energy level diagram of O_2@Ag_8 composite. Beta- and alpha-spin orbitals are shown on the left and right respectively. Molecular orbitals with beta-spin 1P superatom-type[243] orbitals in Ag_8 cluster (82β, 83β, and 84β) and orbitals with π* character on oxygen (81β, 83β, 91β and 92β) are also shown. Orbitals 83β and 91β are examples of mixed Ag_8 superatomic and O_2 π* orbitals. The horizontal dotted line separates the occupied and virtual orbitals.

The electronic structure of the bare Ag_8 tetrahedron[173] consists of a triply-degenerate HOMO level with 1P superatom-type[243] orbitals. In the O_2@Ag_8 composite, the isotropic

symmetry is broken, causing the splitting of the 1P-like orbitals. One of the three 1P-like orbitals, 84β, becomes higher in energy and is unoccupied (Figure 6.2 Left) while the occupied 82β and 83β orbitals remain nearly degenerate. In contrast, the three 1P-like alpha-spin orbitals are occupied and nearly triply degenerate (Figure 6.2 Right).

6.4.2 Absorption properties of $O_2@Ag_8$

The calculated linear-response absorption spectrum and the transition density maps corresponding to selected excitations are shown in Figure 6.3. The molecular orbital transitions responsible for these peaks and their transition electric dipole moment contributions obtained from LR-TDDFT are given in Table E-1. The excitations at 3.31, 3.73, 3.81, and 4.25 eV have equal contributions from both alpha and beta spin orbital transitions, whereas the 4.58 eV excitation has more contributions from beta-spin transitions. We will discuss the dynamics of these states later in the text. The transition density maps of the selected excitations pictorially show the inherent polarization of each excited state (Figure 6.3d), which were determined by the most probable polarization directions based on the transition electric dipole moments (Table E-1). For instance, the inherent x polarization of the 3.81 eV excitation is clearly visible in both alpha- and beta-spin transition density maps in Figure 6.3d. The 3.73 eV peak, however, shows combined x and y polarizations. The alpha-spin transition density of the 4.25 eV peak clearly shows a z polarization, but also shows a slight y polarization in the beta-spin transition density on the O_2 molecule. Overall, the excitation at 3.31 eV is mostly polarized along the x direction, 3.73 eV is polarized along both x and y directions, 3.81 eV along x, 4.25 eV along z, and 4.58 along y. The excited states that have contributions from electronic transitions into empty orbitals with π* character (91β and 92β) are of great interest because they are expected to facilitate O_2 dissociation by further

lengthening the O-O distance. Among the selected states, the excited states at 4.25 eV and 4.58 eV contain transitions into orbitals 91β and/or 92β.

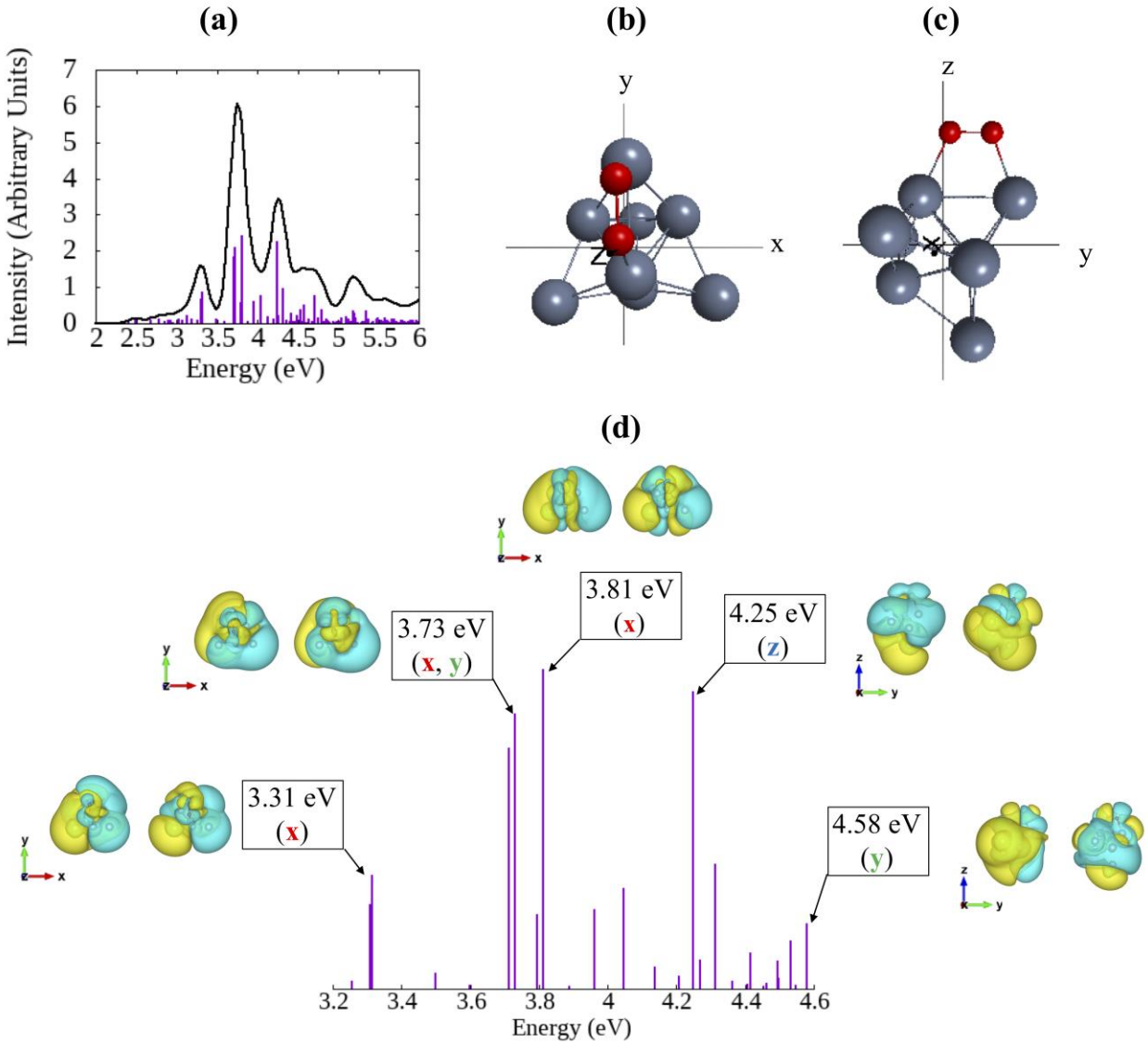

Figure 6.3. (a) Linear-response absorption spectrum; (b) and (c) two views of the O_2@Ag_8 composite system. (d) Transition densities of selected excitations (isovalue=1×10^{-5}). The alpha- and beta-spin transition density maps for each excitation are given on the left and right, respectively. The molecular orientation in the transition densities for 3.31, 3.37, and 3.81 eV excitations is (b) and the orientation for the 4.25 and 4.58 eV excitations is (c).

6.4.3 Photo-excited molecular dynamics with Ehrenfest/RT-TDDFT coupled approach

We now study the dynamics of the O_2 molecule upon state-specific excitation of the five states discussed above. We compare and contrast the variation of the O-O distance after applying various electric fields for 20 fs with different energies (3.31, 3.73, 3.81, 4.25 and 4.58 eV), polarization directions (x, y and z), and field strengths (0.01, 0.03 and 0.05 au) (Figure 6.4). The oxygen molecule is considered to be dissociated if the O-O bond distance surpasses 2 Å by the end of the 100-fs trajectory.

6.4.3.1 Effect of the applied field strength on the dissociation of O_2

Figure 6.4a-c indicates that none of the selected excitations polarized along any direction leads to dissociation of O_2 with the 0.01 au field strength. With the 0.03 au field strength, the three highest-energy excitations (3.81, 4.25 and 4.58 eV) applied along the z direction (Figure 6.4d) and the two highest excitations (4.25 and 4.58 eV) applied along the y direction (Figure 6.4e) lead to dissociation. Notice that in Figure 6.4d, the excitation at 3.73 eV (green) lengthens the O-O bond as high as 2.014 Å, but the bond eventually contracts back to the molecular limit. Therefore, we classify the excitation of the 3.73 eV state with a 0.03 au z-polarized field as not dissociated. The x-polarized electric field with a 0.03 au field strength does not promote O_2 dissociation (Figure 6.4f) for any excitation energy.

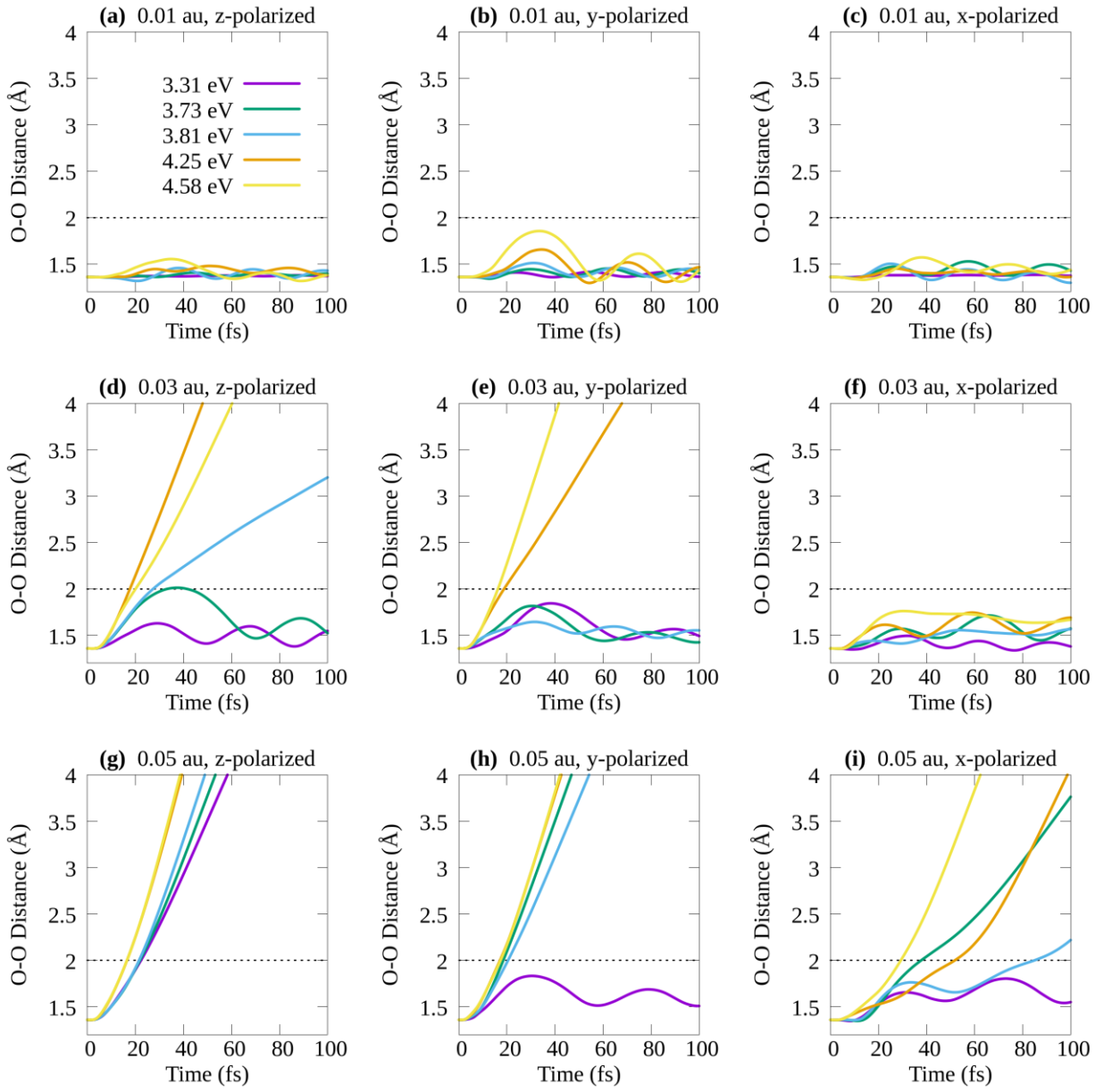

Figure 6.4. Variation of O-O distance during Ehrenfest dynamics. The three rows represent the maximum field strengths of the applied field (0.01 au, 0.03 au and 0.05 au) and the three columns separate the polarization directions of the applied field (x, y and z). Resonant excitation energies are shown with different colors. The horizontal dotted line marks the dissociative limit of O-O distance = 2 Å considered in this work.

With the 0.05 au field strength, all 5 excitations lead to dissociation when the field is polarized along the z direction (Figure 6.4g). When the light is y- or x-polarized (Figure 6.4h and

i), the highest 4 excitations (3.73, 3.81, 4.25 and 4.58 eV) facilitate the dissociation. The oxygen molecule remains undissociated with the 3.31 eV excitation polarized along the y and x directions. Based on the increasing number of dissociative trajectories at increasing field strengths, 0.01, 0.03, and 0.05 au, it is clear that O_2 dissociation on Ag_8 cluster is accelerated by strong electric fields.

Figure 6.5 compares the dependence of the dissociation on the field strength, focusing on 0.03 au (solid lines) and 0.05 au (dashed lines) field strengths. Dissociation is not observed with the 0.01 au field strength. The z-polarized excitation corresponding to 4.58 eV (black lines in Figure 6.5a) shows a strong field dependency on the O_2 dissociation; dissociation occurs faster with 0.05 au (black dashed) and slower with 0.03 au (black solid). On the other hand, the y-polarized 4.58 eV excitation appears to have similar dynamics for these two field strengths, although the 0.05 au field results in a slightly faster dissociation than the 0.03 au field. The x-polarized 4.58 eV excitation only promotes dissociation with the 0.05 au field. Under 4.25 eV excitation (Figure 6.5b), applied fields with both y and z polarization directions have faster O_2 dissociation with the 0.05 au field than with the 0.03 au field. The x-polarized 4.25 eV excitation with the 0.03 au field does not dissociate O_2, similar to the 4.58 eV case. Dynamics simulations with the 3.81, 3.73, and 3.31 eV excitations (Figure 6.5c-e) also confirm that a stronger applied field is more likely to promote dissociation than a weaker field.

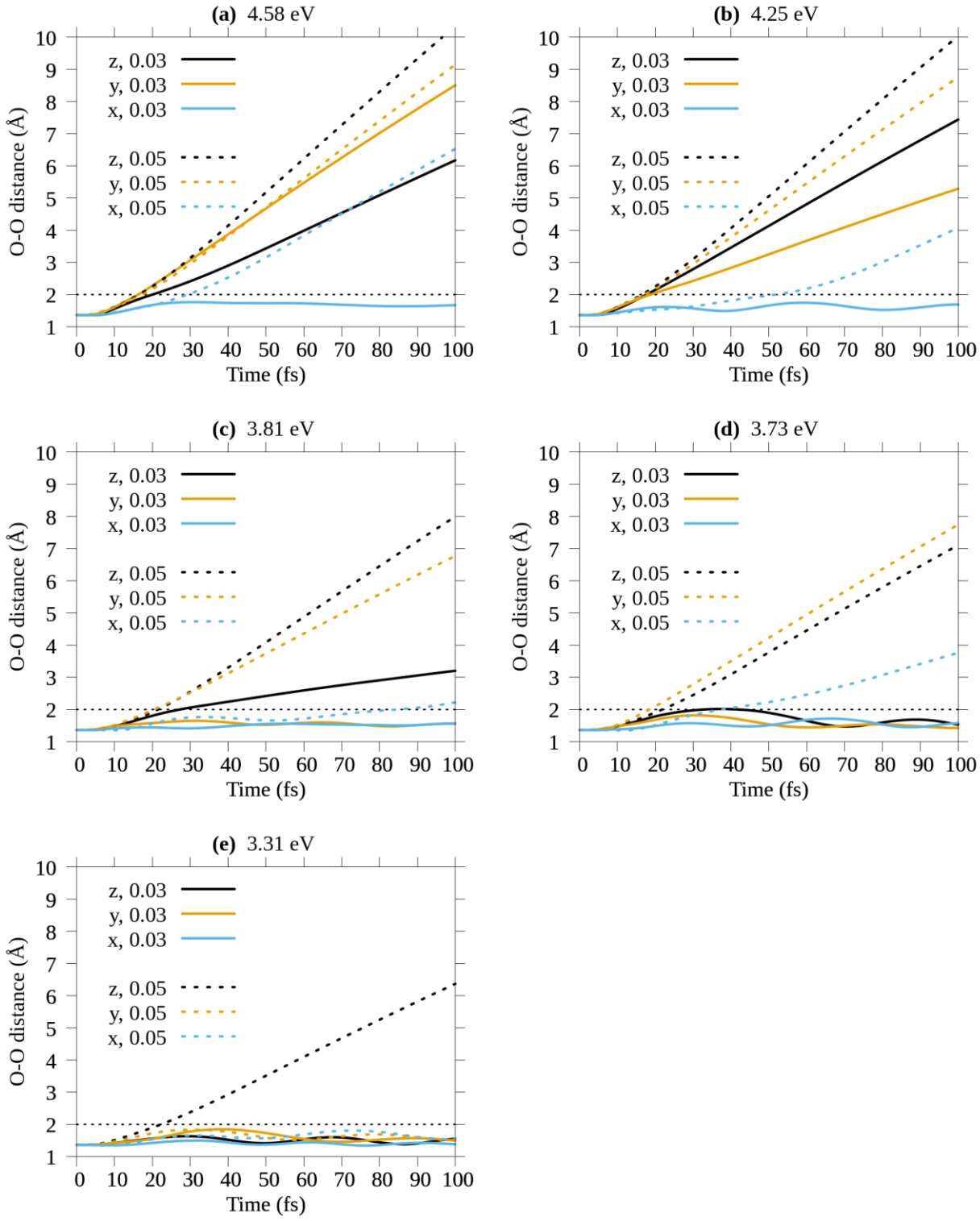

Figure 6.5. Variation of O-O distance during Ehrenfest dynamics with 0.03 au (solid lines) and 0.05 au (dashed lines) maximum field strengths oscillating with selected resonant frequencies, a) 4.58 eV, b) 4.25 eV, c) 3.81 eV, d) 3.73, and e) 3.31 eV. Black: z-polarized

field; Gold: y-polarized light; Blue: x-polarized light. The horizontal dotted line marks the dissociative limit of 2 Å considered in this work.

6.4.3.2 Effect of the polarization direction of the applied field on the dissociation of O_2

Dissociation trends appear to depend on the polarization direction of the applied field in addition to the magnitude of the electric field. Among the three excitations that lead to dissociation with the 0.03 au field (solid lines in Figure 6.5), y-polarized light appears to dissociate oxygen faster with 4.58 eV excitation (Figure 6.5a) than z-polarized light does. However, with 4.25 and 3.81 eV states (Figure 6.5b and c), the z-polarized field leads to faster dissociation. It is important to note that the 4.58 eV excitation has an inherent y-polarization, while the 4.25 and 3.81 eV excitations are inherently polarized along z and x respectively (Figure 6.3d and Table E-1). One might suggest that the inherent polarization direction of the excitations also plays a role in faster dissociation. However, as pointed out before, the x-polarized field with the 0.03 au field strength (solid blue lines in Figure 6.5) does not stimulate dissociation, including the 3.81 or 3.31 eV states which inherit x-polarization. Instead, the z-polarized field induces dissociation even for states that are inherently x-polarized. Therefore, we suggest that the inherent polarization direction may have some effect on the dissociation, but this is not the dominant factor. We observe that the z- and y-polarized light appear to dissociate oxygen more easily than x-polarized light does. This suggests that the molecular geometry (in this case, with the z axis representing the intermolecular axis and O_2 aligned along the y axis) may play a more dominant role than the inherent polarization of an excited state. Interestingly, the charge transfer from the nanoparticle to the molecular oxygen occurs along the z direction in the considered orientation of $O_2@Ag_8$. The fast dissociation with the z-polarized field suggests that charge transfer from a plasmonic nanoparticle to the adsorbate is likely to be the driving force for oxygen dissociation on silver.

When the system is excited with the strong 0.05 au field (dashed lines in Figure 6.5), both z- (black) and y-polarized (gold) fields show almost similar O_2 dissociation. The z-polarization causes a slightly larger O-O bond length at any given time except for the 3.73 eV excitation, which resonates with a state that possesses both y and x polarization. The slightly larger bond distance with y-polarized light oscillating at 3.73 eV with a field strength of 0.05 au (dashed lines in Figure 6.5d) and at 2.58 eV with a strength of 0.03 au (solid lines in Figure 6.5a) may be due to the inherent y polarization of these excitations, which triggers electron excitation along the long axis of O_2, thus facilitating the dissociation.

6.4.3.3 Dissociation, Desorption and Adsorption

At the end of each trajectory, molecular oxygen may be dissociated (with a broken O-O bond), desorbed (with an intact O-O bond but broken Ag-O bonds) or adsorbed (if O_2 is still bound to Ag_8); the state of O_2 at 100 fs is classified in Table 6.1 as dissociated (Dis), desorbed (Des) or adsorbed (Ads) for each applied electric field. A dissociation is considered to have the O-O bond distance > 2 Å and the Ag-O distance > 2.6 Å by the end of the 100 fs trajectory. The Ag-O distances for each simulation are presented in Figures E-3 and E-4. The O_2 desorbed state is defined as O-O distance < 2 Å and Ag-O distance > 2.6 Å. Molecular adsorption of O_2 is classified as O-O distance < 2 Å and Ag-O bond distance < 2.6 Å. In all dissociative cases, we observed that the oxygen atoms are moving away from the Ag_8 cluster. In other words, no atomic adsorptions were encountered.

Table 6.1. Classification of the dynamics trajectories as dissociation (O-O > 2 Å and Ag-O > 2.6 Å, green), desorption (O-O < 2 Å and Ag-O > 2.6 Å, orange), and adsorption (O-O < 2 Å and Ag-O < 2.6 Å, blue) for O_2 on Ag_8 with various resonant energies, polarization directions and field strengths.

	Applied Polarization	Field Strength (au)		
		0.01	0.03	0.05
3.31 eV	z	Ads	Des	Dis
(x)	y	Ads	Des	Des
	x	Ads	Des	Des
3.73 eV	z	Ads	Des	Dis
(x,y)	y	Ads	Des	Dis
	x	Ads	Des	Dis
3.81 eV	z	Ads	Dis	Dis
(x)	y	Ads	Des	Dis
	x	Des	Des	Dis
4.25 eV	z	Des*	Dis	Dis
(z)	y	Des*	Dis	Dis
	x	Des	Des	Dis
4.58 eV	z	Des	Dis	Dis
(y)	y	Des	Dis	Dis
	x	Des	Des	Dis

*Ag-O distance goes beyond the desorption limit, 2.6 Å, but starts to decrease at about 80 fs (Figure E-3a,b and E-4a,b).

The analysis of O-O distances revealed that the 0.01 au field strength is not strong enough to dissociate O_2. Interestingly, the Ag-O bond distances demonstrate that O_2 can either stay adsorbed on Ag_8 cluster with low energy excitations or desorb away from the Ag_8 cluster, as molecular oxygen, with high energy excitations with the 0.01 au electric field. With 0.03 and 0.05 au field strengths, O_2 is no longer adsorbed, and instead either desorbs or dissociates. As discussed in the earlier section, the dissociation for stronger fields is governed by the polarization direction

of the applied field in the order of z>y>x. By examining these bond distances, we see that when O_2 is not dissociated, it moves away from the silver nanoparticle with the 0.03 and 0.05 au fields.

6.5 Conclusions

In this work we found that multiple factors affect the plasmon-enhanced dissociation of O_2 on a tetrahedral Ag_8 cluster. The dissociation is primarily influenced by the strength of the field. While the 0.01 au field does not lead to dissociation, 0.03 au and 0.05 au fields lead to dissociation in certain cases suggesting that the stronger applied fields facilitate photo-dissociation. In addition, an effect of polarization direction of the field was observed. We found that z-polarized light leads to faster dissociation with the weaker 0.03 au field, while both y- and z- polarized light perform competitively with the stronger 0.05 au field. Interestingly, the z direction in this $O_2@Ag_8$ composite system is the direction of electronic movement in a charge transfer excitation. The substantial contribution from z-polarized light towards faster dissociation implies that the charge transfer from the photo-induced Ag_8 cluster to the O_2 molecule may be a prominent mechanism of O_2 dissociation. In both 0.03 and 0.05 au cases, we observe that both z- and y-polarized fields have more tendency to break molecular oxygen than x-polarized states do. The x-polarized field always shows either slow or no dissociation. The significant contribution from y-polarized light suggests that excitation of electrons along the molecular axis of O_2 can also increase the dissociation, especially when the resonant excitation is inherently polarized along the O-O bond.

In addition, we observe that O_2 prefers to stay adsorbed at weak field strength, 0.01 au, when the incident light is resonant with low-energy excited states. However, upon high-energy excitation, O_2 prefers to desorb from the silver cluster. At stronger field strengths, 0.03 and 0.05 au, high-energy excitations trigger dissociation whereas low-energy excitations cause the desorption of molecular oxygen.

6.6 Supporting Information Available

Time variation of the applied electric field during the Ehrenfest dynamics. Total energies of optimized configurations of O_2 on Ag_8 cluster. The coordinates of the minimum-energy $O_2@Ag_8$ structure. Excited-state energy, transition electric dipole moment, oscillator strengths, MO transitions and their weights in the $O_2@Ag_8$ composite. Variation of Ag-O distances during Ehrenfest dynamics.

6.7 Acknowledgments

This material is based on work supported by the Department of Energy under grant DE-SC0012273. The computing for this project was performed on the Beocat Research Cluster at Kansas State University, which is funded in part by NSF grants CHE-1726332, CNS-1006860, EPS-1006860, and EPS-0919443. The authors thank Prof. Xiaosong Li for the RT-TDDFT/Ehrenfest code.

Chapter 7 - Outlook

The knowledge we achieve from this work has opened up several areas of research. Firstly, nonlinear optical activation in silver clusters was not previously found as a decay pathway. Other plasmonic materials may also show nonlinear optical activation as a result of plasmon decay and future investigations should be carried out to search for such compounds. Certain materials may not show nonlinear properties, and searching for such materials may help improve novel photovoltaic and photocatalysis technologies. Investigating the effect of nuclear motion on the plasmonic dissipation is another research direction. The complexity of excited-state potential energy surfaces in noble metal nanomaterials requires implementing new and affordable computational tools to accurately describe the dynamics. Recent improvement of the fewest switches surface hopping (FSSH)[339] technique with many-body treatment of excited states[340] is a potential nonadiabatic method that is worth exploring for noble metal nanoparticles. Secondly, the pioneering work in this thesis on dark spectral properties opens up a whole new area of research where the plasmon loss can be avoided. Attention must be paid to create materials that suppress the specific vibrational modes that lead to symmetry breaking and hence going into dark states. Finally, our work on effect of applied field strength properties demonstrates that the strong fields are more likely to break bonds and opens up the question of what may be the weakest field strength required for molecular dissociation. Future studies that closely investigate the dissociation/no-dissociation field limit are underway.

References

1. Jiang, N.; Zhuo, X.; Wang, J. Active Plasmonics: Principles, Structures, and Applications. *Chem. Rev.* **2018**, *118*, 3054-3099.

2. Eustis, S.; El-Sayed, M. A. Why Gold Nanoparticles are More Precious than Pretty Gold: Noble Metal Surface Plasmon Resonance and its Enhancement of the Radiative and Nonradiative Properties of Nanocrystals of Different Shapes. *Chem. Soc. Rev.* **2006**, *35*, 209-217.

3. Amendola, V.; Pilot, R.; Frasconi, M.; Maragò, O. M.; Iatì, M. A. Surface Plasmon Resonance in Gold Nanoparticles: A Review. *J. Phys. Condens. Matter* **2017**, *29*, 203002.

4. Garcia, M. A. Surface Plasmons in Metallic Nanoparticles: Fundamentals and Applications. *J. Phys. D* **2011**, *44*, 283001.

5. Wang, L.; Hasanzadeh Kafshgari, M.; Meunier, M. Optical Properties and Applications of Plasmonic-Metal Nanoparticles. *Adv. Funct. Mater.* **2020**, *30*, 2005400.

6. Chapkin, K. D.; Bursi, L.; Clark, B. D.; Wu, G.; Lauchner, A.; Tsai, A.-L.; Nordlander, P.; Halas, N. J. Effects of Electronic Structure on Molecular Plasmon Dynamics. *J. Phys. Chem. C* **2020**, *124*, 20450-20457.

7. Chapkin, K. D.; Bursi, L.; Stec, G. J.; Lauchner, A.; Hogan, N. J.; Cui, Y.; Nordlander, P.; Halas, N. J. Lifetime Dynamics of Plasmons in the Few-Atom Limit. *Proc. Natl. Acad. Sci. U.S.A.* **2018**, *115*, 9134.

8. Lauchner, A.; Schlather, A. E.; Manjavacas, A.; Cui, Y.; McClain, M. J.; Stec, G. J.; García de Abajo, F. J.; Nordlander, P.; Halas, N. J. Molecular Plasmonics. *Nano Lett.* **2015**, *15*, 6208-6214.

9. Mie, G. A Contribution to the Optics of Turbid Media, Especially Colloidal Metallic Suspensions. *Ann. Phys* **1908**, *25*, 377-445.

10. Aikens, C. M.; Li, S.; Schatz, G. C. From Discrete Electronic States to Plasmons: TDDFT Optical Absorption Properties of Ag n (n = 10, 20, 35, 56, 84, 120) Tetrahedral Clusters. *J. Phys. Chem. C* **2008**, *112*, 11272-11279.

11. Zhang, R.; Bursi, L.; Cox, J. D.; Cui, Y.; Krauter, C. M.; Alabastri, A.; Manjavacas, A.; Calzolari, A.; Corni, S.; Molinari, E., et al. How To Identify Plasmons from the Optical Response of Nanostructures. *ACS Nano* **2017**, *11*, 7321-7335.

12. Guidez, E. B.; Aikens, C. M. Quantum Mechanical Origin of the Plasmon: from Molecular Systems to Nanoparticles. *Nanoscale* **2014**, *6*, 11512-11527.

13. Gieseking, R. L.; Ratner, M. A.; Schatz, G. C. Semiempirical Modeling of Ag Nanoclusters: New Parameters for Optical Property Studies Enable Determination of Double Excitation Contributions to Plasmonic Excitation. *J. Phys. Chem. A* **2016**, *120*, 4542-4549.

14. Morton, S. M.; Silverstein, D. W.; Jensen, L. Theoretical Studies of Plasmonics using Electronic Structure Methods. *Chem. Rev.* **2011**, *111*, 3962-3994.

15. Hsu, L.-Y.; Ding, W.; Schatz, G. C. Plasmon-Coupled Resonance Energy Transfer. *J. Phys. Chem. Lett.* **2017**, *8*, 2357-2367.

16. Zhang, Y.; He, S.; Guo, W.; Hu, Y.; Huang, J.; Mulcahy, J. R.; Wei, W. D. Surface-Plasmon-Driven Hot Electron Photochemistry. *Chem. Rev.* **2018**, *118*, 2927-2954.

17. Kelly, K. L.; Coronado, E.; Zhao, L. L.; Schatz, G. C. The Optical Properties of Metal Nanoparticles: The Influence of Size, Shape, and Dielectric Environment. *J. Phys. Chem. B* **2003**, *107*, 668-677.

18. Höppener, C.; Novotny, L. Exploiting the Light–Metal Interaction for Biomolecular Sensing and Imaging. *Q. Rev. Biophys.* **2012**, *45*, 209-255.

19. Kümmel, S.; Andrae, K.; Reinhard, P. G. Collectivity in the Optical Response. of Small Metal Clusters. *Appl. Phys. B* **2001**, *73*, 293-297.

20. Garcia de Abajo, F. J.; Sapienza, R.; Noginov, M.; Benz, F.; Baumberg, J.; Maier, S.; Graham, D.; Aizpurua, J.; Ebbesen, T.; Pinchuk, A., et al. Plasmonic and New Plasmonic Materials: General Discussion. *Faraday Discuss.* **2015**, *178*, 123-49.

21. Krauter, C. M.; Schirmer, J.; Jacob, C. R.; Pernpointner, M.; Dreuw, A. Plasmons in Molecules: Microscopic Characterization Based on Orbital Transitions and Momentum Conservation. *J. Chem. Phys.* **2014**, *141*, 104101.

22. Bonacic-Koutecky, V.; Fantucci, P.; Koutecky, J. Quantum Chemistry of Small Clusters of Elements of Groups Ia, Ib, and IIa: Fundamental Concepts, Predictions, and Interpretation of Experiments. *Chem. Rev.* **1991**, *91*, 1035-1108.

23. Bernadotte, S.; Evers, F.; Jacob, C. R. Plasmons in Molecules. *J. Phys. Chem. C* **2013**, *117*, 1863-1878.

24. Gieseking, R. L. M.; Ashwell, A. P.; Ratner, M. A.; Schatz, G. C. Analytical Approaches To Identify Plasmon-like Excited States in Bare and Ligand-Protected Metal Nanoclusters. *J. Phys. Chem. C* **2020**, *124*, 3260-3269.

25. Weissker, H.-C.; López-Lozano, X. Surface Plasmons in Quantum-Sized Noble-Metal Clusters: TDDFT Quantum Calculations and the Classical Picture of Charge Oscillations. *Phys. Chem. Chem. Phys.* **2015**, *17*, 28379-28386.

26. Ma, J.; Wang, Z.; Wang, L.-W. Interplay Between Plasmon and Single-Particle Excitations in a Metal Nanocluster. *Nat. Commun.* **2015**, *6*, 10107/1-12.

27. Weerawardene, K. L. D. M.; Aikens, C. M. Comparison and Convergence of Optical Absorption Spectra of Noble Metal Nanoparticles Computed Using Linear-Response and Real-Time Time-Dependent Density Functional Theories. *Comput. Theor. Chem.* **2018**, *1146*, 27-36.

28. Kuda-Singappulige, G. U.; Wildman, A.; Lingerfelt, D. B.; Li, X.; Aikens, C. M. Ultrafast Nonradiative Decay of a Dipolar Plasmon-like State in Naphthalene. *J. Phys. Chem. A* **2020**, *124*, 9729-9737.

29. Khlebtsov, N. G.; Dykman, L. A. Optical Properties and Biomedical Applications of Plasmonic Nanoparticles. *J. Quant. Spectrosc. Radiat. Transf.* **2010**, *111*, 1-35.

30. Langer, J.; Novikov, S. M.; Liz-Marzán, L. M. Sensing Using Plasmonic Nanostructures and Nanoparticles. *Nanotechnology* **2015**, *26*, 322001.

31. Linic, S.; Aslam, U.; Boerigter, C.; Morabito, M. Photochemical Transformations on Plasmonic Metal Nanoparticles. *Nat. Mater.* **2015**, *14*, 567-576.

32. Wu, N. Plasmonic Metal-Semiconductor Photocatalysts and Photoelectrochemical Cells: A Review. *Nanoscale* **2018**, *10*, 2679-2696.

33. Zeng, J.; Zhang, Y.; Zeng, T.; Aleisa, R.; Qiu, Z.; Chen, Y.; Huang, J.; Wang, D.; Yan, Z.; Yin, Y. Anisotropic Plasmonic Nanostructures for Colorimetric Sensing. *Nano Today* **2020**, *32*, 100855.

34. Cushing, S. K.; Wu, N. Plasmon-Enhanced Solar Energy Harvesting. *Electrochem Soc. Interface* **2013**, *22*, 63-67.

35. Yu, H.; Peng, Y.; Yang, Y.; Li, Z.-Y. Plasmon-Enhanced Light–Matter Interactions and Applications. *Npj Comput. Mater.* **2019**, *5*, 45.

36. Cushing, S. K.; Wu, N. Progress and Perspectives of Plasmon-Enhanced Solar Energy Conversion. *J. Phys. Chem. Lett.* **2016**, *7*, 666-675.

37. Enrichi, F.; Quandt, A.; Righini, G. C. Plasmonic Enhanced Solar Cells: Summary of Possible Strategies and Recent Results. *Renew. Sustain. Energy Rev.* **2018**, *82*, 2433-2439.

38. Li, J.; Cushing, S. K.; Meng, F.; Senty, T. R.; Bristow, A. D.; Wu, N. Plasmon-Induced Resonance Energy Transfer for Solar Energy Conversion. *Nat. Photonics* **2015**, *9*, 601-607.

39. Kluczyk, K.; David, C.; Jacak, J.; Jacak, W. On Modeling of Plasmon-Induced Enhancement of the Efficiency of Solar Cells Modified by Metallic Nano-Particles. *Nanomaterials* **2019**, *9*.

40. Singh, G.; Verma, S. S. Plasmon Enhanced Light Trapping in Thin Film GaAs Solar Cells by Al Nanoparticle Array. *Phys. Lett. A* **2019**, *383*, 1526-1530.

41. Tran, V. T.; Nguyen, H.-Q.; Kim, Y.-M.; Ok, G.; Lee, J. Photonic–Plasmonic Nanostructures for Solar Energy Utilization and Emerging Biosensors. *Nanomaterials* **2020**, *10*.

42. Jiang, R.; Li, B.; Fang, C.; Wang, J. Metal/Semiconductor Hybrid Nanostructures for Plasmon-Enhanced Applications. *Adv. Mater.* **2014**, *26*, 5274-5309.

43. Singh, S. V.; Kumar, M. P.; Anantharaj, S.; Mukherjee, B.; Kundu, S.; Pal, B. N. Direct Evidence of an Efficient Plasmon-Induced Hot-Electron Transfer at an in Situ Grown Ag/TiO_2 Interface for Highly Enhanced Solar H_2 Generation. *ACS Appl. Energy Mater.* **2020**, *3*, 1821-1830.

44. Clavero, C. Plasmon-Induced Hot-Electron Generation at Nanoparticle/Metal-Oxide Interfaces for Photovoltaic and Photocatalytic Devices. *Nat. Photonics* **2014**, *8*, 95-103.

45. Song, J.; Long, J.; Liu, Y.; Xu, Z.; Ge, A.; Piercy, B. D.; Cullen, D. A.; Ivanov, I. N.; McBride, J. R.; Losego, M. D., et al. Highly Efficient Plasmon Induced Hot-Electron Transfer at Ag/TiO_2 Interface. *ACS Photonics* **2021**.

46. Wu, K.; Rodriguez-Cordoba, W. E.; Yang, Y.; Lian, T. Plasmon-Induced Hot Electron Transfer From the Au Tip to CdS Rod in CdS-Au Nanoheterostructures. *Nano Lett.* **2013**, *13*, 5255-63.

47. Sundararaman, R.; Narang, P.; Jermyn, A. S.; Goddard, W. A., 3rd; Atwater, H. A. Theoretical Predictions for Hot-Carrier Generation from Surface Plasmon Decay. *Nat. Commun.* **2014**, *5*, 5788.

48. Brongersma, M. L.; Halas, N. J.; Nordlander, P. Plasmon-Induced Hot Carrier Science and Technology. *Nat. Nanotechnol.* **2015**, *10*, 25-34.

49. Dal Forno, S.; Ranno, L.; Lischner, J. Material, Size, and Environment Dependence of Plasmon-Induced Hot Carriers in Metallic Nanoparticles. *J. Phys. Chem. C* **2018**, *122*, 8517-8527.

50. Zhang, Q.; Thrithamarassery Gangadharan, D.; Liu, Y.; Xu, Z.; Chaker, M.; Ma, D. Recent Advancements in Plasmon-Enhanced Visible Light-Driven Water Splitting. *J. Materiomics* **2017**, *3*, 33-50.

51. Wu, N. Plasmonic Metal–Semiconductor Photocatalysts and Photoelectrochemical Cells: A Review. *Nanoscale* **2018**, *10*, 2679-2696.

52. Atabaev, T. S. Plasmon-Enhanced Solar Water Splitting with Metal Oxide Nanostructures: A Brief Overview of Recent Trends. *Front. Mater. Sci.* **2018**, *12*, 207-213.

53. Mascaretti, L.; Dutta, A.; Kment, Š.; Shalaev, V. M.; Boltasseva, A.; Zbořil, R.; Naldoni, A. Plasmon-Enhanced Photoelectrochemical Water Splitting for Efficient Renewable Energy Storage. *Adv. Mater.* **2019**, *31*, 1805513.

54. Robatjazi, H.; Zhao, H.; Swearer, D. F.; Hogan, N. J.; Zhou, L.; Alabastri, A.; McClain, M. J.; Nordlander, P.; Halas, N. J. Plasmon-Induced Selective Carbon Dioxide Conversion on Earth-Abundant Aluminum-Cuprous Oxide Antenna-Reactor Nanoparticles. *Nat. Commun.* **2017**, *8*, 27.

55. DuChene, J. S.; Tagliabue, G.; Welch, A. J.; Cheng, W.-H.; Atwater, H. A. Hot Hole Collection and Photoelectrochemical CO_2 Reduction with Plasmonic Au/p-GaN Photocathodes. *Nano Lett.* **2018**, *18*, 2545-2550.

56. Centi, G.; Perathoner, S. Opportunities and Prospects in the Chemical Recycling of Carbon Dioxide to Fuels. *Catal. Today* **2009**, *148*, 191-205.

57. Goeppert, A.; Czaun, M.; Jones, J.-P.; Surya Prakash, G. K.; Olah, G. A. Recycling of Carbon Dioxide to Methanol and Derived Products – Closing the Loop. *Chem. Soc. Rev.* **2014**, *43*, 7995-8048.

58. Wei, R.-B.; Kuang, P.-Y.; Cheng, H.; Chen, Y.-B.; Long, J.-Y.; Zhang, M.-Y.; Liu, Z.-Q. Plasmon-Enhanced Photoelectrochemical Water Splitting on Gold Nanoparticle Decorated ZnO/CdS Nanotube Arrays. *ACS Sustain. Chem. Eng.* **2017**, *5*, 4249-4257.

59. Zhang, P.; Wang, T.; Gong, J. Mechanistic Understanding of the Plasmonic Enhancement for Solar Water Splitting. *Adv. Mater.* **2015**, *27*, 5328-5342.

60. Bernardi, M.; Mustafa, J.; Neaton, J. B.; Louie, S. G. Theory and Computation of Hot Carriers Generated by Surface Plasmon Polaritons in Noble Metals. *Nat. Commun.* **2015**, *6*, 7044.

61. Rossi, T. P.; Erhart, P.; Kuisma, M. Hot-Carrier Generation in Plasmonic Nanoparticles: The Importance of Atomic Structure. *ACS Nano* **2020**, *14*, 9963-9971.

62. Christopher, P.; Xin, H.; Linic, S. Visible-Light-Enhanced Catalytic Oxidation Reactions on Plasmonic Silver Nanostructures. *Nat. Chem.* **2011**, *3*, 467-472.

63. Martirez, J. M. P.; Carter, E. A. Prediction of a Low-Temperature N_2 Dissociation Catalyst exploiting Near-IR–to–Visible Light Nanoplasmonics. *Sci. Adv.* **2017**, *3*, eaao4710.

64. Hagman, B.; Posada-Borbón, A.; Schaefer, A.; Shipilin, M.; Zhang, C.; Merte, L. R.; Hellman, A.; Lundgren, E.; Grönbeck, H.; Gustafson, J. Steps Control the Dissociation of CO_2 on Cu(100). *J. Am. Chem. Soc.* **2018**, *140*, 12974-12979.

65. Ojwang, J. G. O.; Stewart McWilliams, R.; Ke, X.; Goncharov, A. F. Melting and Dissociation of Ammonia at High Pressure and High Temperature. *J. Chem. Phys.* **2012**, *137*, 064507.

66. Huang, Y.-F.; Zhang, M.; Zhao, L.-B.; Feng, J.-M.; Wu, D.-Y.; Ren, B.; Tian, Z.-Q. Activation of Oxygen on Gold and Silver Nanoparticles Assisted by Surface Plasmon Resonances. *Angew. Chem., Int. Ed.* **2014**, *53*, 2353-2357.

67. Mukherjee, S.; Libisch, F.; Large, N.; Neumann, O.; Brown, L. V.; Cheng, J.; Lassiter, J. B.; Carter, E. A.; Nordlander, P.; Halas, N. J. Hot Electrons Do the Impossible: Plasmon-Induced Dissociation of H_2 on Au. *Nano Lett.* **2013**, *13*, 240-247.

68. Swearer, D. F.; Zhao, H.; Zhou, L.; Zhang, C.; Robatjazi, H.; Martirez, J. M. P.; Krauter, C. M.; Yazdi, S.; McClain, M. J.; Ringe, E., et al. Heterometallic Antenna−Reactor Complexes for Photocatalysis. *Proc. Natl. Acad. Sci. U.S.A.* **2016**, *113*, 8916.

69. Lin, C.; Ikeda, K.; Shiota, Y.; Yoshizawa, K.; Kumagai, T. Real-Space Observation of Far- and Near-Field-Induced Photolysis of Molecular Oxygen on an Ag(110) surface by Visible Light. *J. Chem. Phys.* **2019**, *151*, 144705.

70. Seemala, B.; Therrien, A. J.; Lou, M.; Li, K.; Finzel, J. P.; Qi, J.; Nordlander, P.; Christopher, P. Plasmon-Mediated Catalytic O_2 Dissociation on Ag Nanostructures: Hot Electrons or Near Fields? *ACS Energy Lett.* **2019**, *4*, 1803-1809.

71. Kazuma, E.; Jung, J.; Ueba, H.; Trenary, M.; Kim, Y. Real-Space and Real-Time Observation of a Plasmon-Induced Chemical Reaction of a Single Molecule. *Science* **2018**, *360*, 521.

72. Torbatian, Z.; Hashemifar, S. J.; Akbarzadeh, H. First-Principles Insights into Interaction of CO, NO, and HCN with Ag_8. *J. Chem. Phys.* **2014**, *140*, 084314.

73. Bao, J. L.; Carter, E. A. Surface-Plasmon-Induced Ammonia Decomposition on Copper: Excited-State Reaction Pathways Revealed by Embedded Correlated Wavefunction Theory. *ACS Nano* **2019**, *13*, 9944-9957.

74. Kumar, P. V.; Rossi, T. P.; Kuisma, M.; Erhart, P.; Norris, D. J. Direct Hot-Carrier Transfer in Plasmonic Catalysis. *Faraday Discuss.* **2019**, *214*, 189-197.

75. Hull, O. A.; Lingerfelt, D. B.; Li, X.; Aikens, C. M. Electronic Structure and Nonadiabatic Dynamics of Atomic Silver Nanowire–N_2 Systems. *J. Phys. Chem. C* **2020**, *124*, 20834-20845.

76. Wu, Q.; Zhou, L.; Schatz, G. C.; Zhang, Y.; Guo, H. Mechanistic Insights into Photocatalyzed H_2 Dissociation on Au Clusters. *J. Am. Chem. Soc.* **2020**, *142*, 13090-13101.

77. Tian, Y.; Tatsuma, T. Mechanisms and Applications of Plasmon-Induced Charge Separation at TiO_2 Films Loaded with Gold Nanoparticles. *J. Am. Chem. Soc.* **2005**, *127*, 7632-7637.

78. Kale, M. J.; Avanesian, T.; Christopher, P. Direct Photocatalysis by Plasmonic Nanostructures. *ACS Catal.* **2014**, *4*, 116-128.

79. Long, J.; Chang, H.; Gu, Q.; Xu, J.; Fan, L.; Wang, S.; Zhou, Y.; Wei, W.; Huang, L.; Wang, X., et al. Gold-Plasmon Enhanced Solar-to-Hydrogen Conversion on the {001} Facets of Anatase TiO_2 Nanosheets. *Energy Environ. Sci.* **2014**, *7*.

80. Kazuma, E.; Kim, Y. Mechanistic Studies of Plasmon Chemistry on Metal Catalysts. *Angew. Chem., Int. Ed. Engl.* **2019**, *58*, 4800-4808.

81. Martirez, J. M. P.; Bao, J. L.; Carter, E. A. First-Principles Insights into Plasmon-Induced Catalysis. *Annu. Rev. Phys. Chem.* **2021**, *72*, 99-119.

82. Santbergen, R.; Temple, T. L.; Liang, R.; Smets, A. H. M.; Swaaij, R. A. C. M. M. v.; Zeman, M. Application of Plasmonic Silver Island Films in Thin-Film Silicon Solar Cells. *J. Opt.* **2012**, *14*.

83. Huang, L.; Wan, J.; Wei, X.; Liu, Y.; Huang, J.; Sun, X.; Zhang, R.; Gurav, D. D.; Vedarethinam, V.; Li, Y., et al. Plasmonic Silver Nanoshells for Drug and Metabolite Detection. *Nat. Commun.* **2017**, *8*, 220.

84. Ju, L.; Geng, B.; Horng, J.; Girit, C.; Martin, M.; Hao, Z.; Bechtel, H. A.; Liang, X.; Zettl, A.; Shen, Y. R., et al. Graphene Plasmonics for Tunable Terahertz Metamaterials. *Nat. Nanotechnol.* **2011**, *6*, 630-634.

85. Chen, P.-Y.; Argyropoulos, C.; Farhat, M.; Gomez-Diaz, J. S. Flatland Plasmonics and Nanophotonics Based on Graphene and Beyond. *Nanophotonics* **2017**, *6*, 137.

86. Grigorenko, A. N.; Polini, M.; Novoselov, K. S. Graphene Plasmonics. *Nat. Photonics* **2012**, *6*, 749-758.

87. Chen, J.; Badioli, M.; Alonso-González, P.; Thongrattanasiri, S.; Huth, F.; Osmond, J.; Spasenović, M.; Centeno, A.; Pesquera, A.; Godignon, P., et al. Optical Nano-Imaging of Gate-Tunable Graphene Plasmons. *Nature* **2012**, *487*, 77-81.

88. Fan, Y.; Shen, N.-H.; Zhang, F.; Zhao, Q.; Wu, H.; Fu, Q.; Wei, Z.; Li, H.; Soukoulis, C. M. Graphene Plasmonics: A Platform for 2D Optics. *Adv. Opt. Mater.* **2019**, *7*, 1800537.

89. Geim, A. K.; Novoselov, K. S. The Rise of Graphene. *Nat. Mater.* **2007**, *6*, 183-191.

90. Ni, G. X.; McLeod, A. S.; Sun, Z.; Wang, L.; Xiong, L.; Post, K. W.; Sunku, S. S.; Jiang, B. Y.; Hone, J.; Dean, C. R., et al. Fundamental Limits to Graphene Plasmonics. *Nature* **2018**, *557*, 530-533.

91. Ogawa, S.; Fukushima, S.; Shimatani, M. Graphene Plasmonics in Sensor Applications: A Review. *Sensors* **2020**, *20*.

92. Koppens, F. H.; Chang, D. E.; Garcia de Abajo, F. J. Graphene Plasmonics: A Platform for Strong Light-Matter Interactions. *Nano Lett.* **2011**, *11*, 3370-7.

93. Fang, Z.; Thongrattanasiri, S.; Schlather, A.; Liu, Z.; Ma, L.; Wang, Y.; Ajayan, P. M.; Nordlander, P.; Halas, N. J.; García de Abajo, F. J. Gated Tunability and Hybridization of Localized Plasmons in Nanostructured Graphene. *ACS Nano* **2013**, *7*, 2388-2395.

94. Cox, J. D.; Silveiro, I.; Garcia de Abajo, F. J. Quantum Effects in the Nonlinear Response of Graphene Plasmons. *ACS Nano* **2016**, *10*, 1995-2003.

95. Giovannini, T.; Bonatti, L.; Polini, M.; Cappelli, C. Graphene Plasmonics: Fully Atomistic Approach for Realistic Structures. *J. Phys. Chem. Lett.* **2020**, *11*, 7595-7602.

96. Birks, J. B.; Christophorou, L. G.; Huebner, R. H. Excited Electronic States of Benzene and Naphthalene. *Nature* **1968**, *217*, 809-812.

97. Compton, R. N.; Huebner, R. H.; Reinhardt, P. W.; Christophorou, L. G. Threshold Electron Impact Excitation of Atoms and Molecules: Detection of Triplet and Temporary Negative Ion States. *J. Chem. Phys.* **1968**, *48*, 901-909.

98. Ligthart, J. A. M.; Karcher, W.; Fordham, R. J.; Dubois, J. J.; Glaude, P. G. J. M. *Spectral Atlas of Polycyclic Aromatic Compounds*; United States: Kluwer Academic Publishers, Norwell, MA, 1985.

99. Coulson, C. A. Excited Electronic Levels in Conjugated Molecules: I. Long Wavelength Ultra-Violet Absorption of Naphthalene, Anthracene and Homologs. *Proc. Phys. Soc.* **1948**, *60*, 257-269.

100. Hashimoto, T.; Nakano, H.; Hirao, K. Theoretical Study of the Valence $\pi \rightarrow \pi^*$ Excited States of Polyacenes: Benzene and Naphthalene. *J. Chem. Phys.* **1996**, *104*, 6244-6258.

101. Smith, S. M.; Li, X.; Markevitch, A.; Romanov, D.; Levis, R. J.; Schlegel, H. B. Numerical Simulation of Nonadiabatic Electron Excitation in the Strong-Field Regime. 3. Polyacene Neutrals and Cations. *J. Phys. Chem. A* **2007**, *111*, 6920-6932.

102. Sony, P.; Shukla, A. Large-Scale Correlated Calculations of Linear Optical Absorption and Low-Lying Excited States of Polyacenes: Pariser-Parr-Pople Hamiltonian. *Phys. Rev. B* **2007**, *75*.

103. Krykunov, M.; Grimme, S.; Ziegler, T. Accurate Theoretical Description of the ^1L_a and ^1L_b Excited States in Acenes Using the All Order Constricted Variational Density Functional Theory Method and the Local Density Approximation. *J. Chem. Theory Comput.* **2012**, *8*, 4434-4440.

104. Guidez, E. B.; Aikens, C. M. Origin and TDDFT Benchmarking of the Plasmon Resonance in Acenes. *J. Phys. Chem. C* **2013**, *117*, 21466-21475.

105. Hartland, G. V. Optical Studies of Dynamics in Noble Metal Nanostructures. *Chem. Rev.* **2011**, *111*, 3858-3887.

106. Sönnichsen, C.; Franzl, T.; Wilk, T.; von Plessen, G.; Feldmann, J.; Wilson, O.; Mulvaney, P. Drastic Reduction of Plasmon Damping in Gold Nanorods. *Phys. Rev. Lett.* **2002**, *88*, 077402/1-4.

107. Lehmann, J.; Merschdorf, M.; Pfeiffer, W.; Thon, A.; Voll, S.; Gerber, G. Surface Plasmon Dynamics in Silver Nanoparticles Studied by Femtosecond Time-Resolved Photoemission. *Phys. Rev. Lett.* **2000**, *85*, 2921-2924.

108. van Exter, M.; Lagendijk, A. Ultrashort Surface-Plasmon and Phonon Dynamics. *Phys. Rev. Lett.* **1988**, *60*, 49-52.

109. Donati, G.; Lingerfelt, D. B.; Aikens, C. M.; Li, X. Molecular Vibration Induced Plasmon Decay. *J. Phys. Chem. C* **2017**, *121*, 15368-15374.

110. Yan, L.; Ding, Z.; Song, P.; Wang, F.; Meng, S. Plasmon-Induced Dynamics of H_2 Splitting on a Silver Atomic Chain. *Appl. Phys. Lett.* **2015**, *107*, 083102.

111. Atkins, P.; de Paula, J. *Physical Chemistry*, 08 ed.; Oxford University Press, 2006.

112. Boyd, R. W. *Nonlinear Optics*; Boston : Academic Press: Boston, 1992.

113. Grand, J.; Auguié, B.; Le Ru, E. C. Combined Extinction and Absorption UV–Visible Spectroscopy as a Method for Revealing Shape Imperfections of Metallic Nanoparticles. *Analytical Chemistry* **2019**, *91*, 14639-14648.

114. Nayyar, I. H.; Masunov, A. E.; Tretiak, S. Comparison of TD-DFT Methods for the Calculation of Two-Photon Absorption Spectra of Oligophenylvinylenes. *J. Phys. Chem. C* **2013**, *117*, 18170-18189.

115. Majles Ara, M. H.; Dehghani, Z.; Sahraei, R.; Daneshfar, A.; Javadi, Z.; Divsar, F. Diffraction Patterns and Nonlinear Optical Properties of Gold Nanoparticles. *J. Quant. Spectrosc. Radiat. Transf.* **2012**, *113*, 366-372.

116. Schuller, J. A.; Barnard, E. S.; Cai, W.; Jun, Y. C.; White, J. S.; Brongersma, M. L. Plasmonics for Extreme Light Concentration and Manipulation. *Nat. Mater.* **2010**, *9*, 193-204.

117. Gieseking, R. L. M. Third-Order Nonlinear Optical Properties of Ag Nanoclusters: Connecting Molecule-like and Nanoparticle-like Behavior. *Chem. Mater.* **2019**, *31*, 6850-6859.

118. Wu, K.; Li, J.; Lin, C. Remarkable Second-Order Optical Nonlinearity of Nano-Sized Au_{20} Cluster: A TDDFT Study. *Chem. Phys. Lett.* **2004**, *388*, 353-357.

119. Yan, L.; Guan, M.; Meng, S. Plasmon-Induced Nonlinear Response of Silver Atomic Chains. *Nanoscale* **2018**, *10*, 8600-8605.

120. Christopher, P.; Linic, S. Shape- and Size-Specific Chemistry of Ag Nanostructures in Catalytic Ethylene Epoxidation. *ChemCatChem* **2010**, *2*, 78-83.

121. Szabo, A. S.; Ostlund, N. S. *Modern Quantum Chemistry : Introduction to Advanced Electronic Structure Theory*; Dover Publications: Mineola, N.Y., 1996.

122. Born, M.; Oppenheimer, R. Zur Quantentheorie der Molekeln. *Ann. Phys. (Berl.)* **1927**, *389*, 457-484.

123. Sutcliffe, B. T., The Born-Oppenheimer Approximation. In *Methods in Computational Molecular Physics*, Wilson, S.; Diercksen, G. H. F., Eds. Springer US: Boston, MA, 1992; pp 19-46.

124. Levine, I. N. *Quantum Chemistry*, 5th ed.; Prentice Hall: Upper Saddle River, N.J., 2000.

125. Friesner, R. A. Ab Initio Quantum Chemistry: Methodology and Applications. *Proc. Natl. Acad. Sci. U.S.A.* **2005**, *102*, 6648.

126. Atkins, P. W. *Molecular Quantum Mechanics*, 4th ed.; New York : Oxford University Press: New York, 2005.

127. Kahn, L. R.; Hay, P. J.; Cowan, R. D. Relativistic Effects in Ab Initio Effective Core Potentials for Molecular Calculations. Applications to the Uranium Atom. *J. Chem. Phys.* **1978**, *68*, 2386-2397.

128. Autschbach, J. Perspective: Relativistic Effects. *J. Chem. Phys.* **2012**, *136*, 150902.

129. Dolg, M.; Cao, X. Relativistic Pseudopotentials: Their Development and Scope of Applications. *Chem. Rev.* **2012**, *112*, 403-480.

130. Xu, X.; Truhlar, D. G. Accuracy of Effective Core Potentials and Basis Sets for Density Functional Calculations, Including Relativistic Effects, As Illustrated by Calculations on Arsenic Compounds. *J. Chem. Theory Comput.* **2011**, *7*, 2766-2779.

131. Hay, P. J.; Wadt, W. R. Ab Initio Effective Core Potentials for Molecular Calculations. Potentials for the Transition Metal Atoms Sc to Hg. *J. Chem. Phys.* **1985**, *82*, 270-283.

132. Hay, P. J. Gaussian Basis Sets for Molecular Calculations. The Representation of 3d Orbitals in Transition-Metal Atoms. *J. Chem. Phys.* **1977**, *66*, 4377-4384.

133. Hohenberg, P.; Kohn, W. Inhomogeneous Electron Gas. *Phys. Rev.* **1964**, *136*, B864-B871.

134. Dreizler, R. M. *Density functional theory : an approach to the quantum many-body problem*; Berlin, New York : Springer-Verlag: Berlin, New York, 1990.

135. Becke, A. D., Density Functional Theories in Quantum Chemistry. In *The Challenge of d and f Electrons*, American Chemical Society: 1989; Vol. 394, pp 165-179.

136. Kohn, W.; Sham, L. J. Self-Consistent Equations Including Exchange and Correlation Effects. *Phys. Rev.* **1965**, *140*, A1133-A1138.

137. Geerlings, P.; De Proft, F.; Langenaeker, W. Conceptual Density Functional Theory. *Chem. Rev.* **2003**, *103*, 1793-1874.

138. Kurth, S.; Marques, M. A. L.; Gross, E. K. U., Density-Functional Theory. In *Encyclopedia of Condensed Matter Physics*, Bassani, F.; Liedl, G. L.; Wyder, P., Eds. Elsevier: Oxford, 2005; pp 395-402.

139. Wang, Y.; Xu, Z.; Moe, Y. N. On the Performance of Local Density Approximation in Describing the Adsorption of Electron Donating/Accepting Molecules on Graphene. *Chem. Phys.* **2012**, *406*, 78-85.

140. Pines, D. *Elementary Excitations in Solids*; CRC Press, 2018.

141. Sousa, S. F.; Fernandes, P. A.; Ramos, M. J. General Performance of Density Functionals. *J. Phys. Chem. A* **2007**, *111*, 10439-10452.

142. Perdew, J. P. Density-Functional Approximation for the Correlation Energy of the Inhomogeneous Electron Gas. *Phys. Rev. B* **1986**, *33*, 8822-8824.

143. Becke, A. D. Density-Functional Exchange-Energy Approximation with Correct Asymptotic Behavior. *Phys. Rev. A.* **1988**, *38*, 3098-3100.

144. Becke, A. D. A New Mixing of Hartree–Fock and Local Density-Functional Theories. *J. Chem. Phys.* **1993**, *98*, 1372-1377.

145. Stephens, P. J.; Devlin, F. J.; Chabalowski, C. F.; Frisch, M. J. Ab Initio Calculation of Vibrational Absorption and Circular Dichroism Spectra Using Density Functional Force Fields. *J. Phys. Chem.* **1994**, *98*, 11623-11627.

146. Tirado-Rives, J.; Jorgensen, W. L. Performance of B3LYP Density Functional Methods for a Large Set of Organic Molecules. *J. Chem. Theory Comput.* **2008**, *4*, 297-306.

147. Leininger, T.; Stoll, H.; Werner, H.-J.; Savin, A. Combining Long-Range Configuration Interaction with Short-Range Density Functionals. *Chem. Phys. Lett.* **1997**, *275*, 151-160.

148. Iikura, H.; Tsuneda, T.; Yanai, T.; Hirao, K. A Long-Range Correction Scheme for Generalized-Gradient-Approximation Exchange Functionals. *J. Chem. Phys.* **2001**, *115*, 3540-3544.

149. Tawada, Y.; Tsuneda, T.; Yanagisawa, S.; Yanai, T.; Hirao, K. A Long-Range-Corrected Time-Dependent Density Functional Theory. *J. Chem. Phys.* **2004**, *120*, 8425-8433.

150. Gerber, I. C.; Ángyán, J. G. Hybrid Functional with Separated Range. *Chem. Phys. Lett.* **2005**, *415*, 100-105.

151. Sekino, H.; Maeda, Y.; Kamiya, M. Influence of the Long-Range Exchange Effect on Dynamic Polarizability. *Mol. Phys.* **2005**, *103*, 2183-2189.

152. Vydrov, O. A.; Scuseria, G. E. Assessment of a Long-Range Corrected Hybrid Functional. *J. Chem. Phys.* **2006**, *125*, 234109.

153. Karton, A. Can Density Functional Theory 'Cope' with Highly Fluxional Shapeshifting Molecules? *Chem. Phys.* **2021**, *540*, 111013.

154. Marques, M. A. L.; Oliveira, M. J. T.; Burnus, T. Libxc: A Library of Exchange and Correlation Functionals for Density Functional Theory. *Comput. Phys. Commun.* **2012**, *183*, 2272-2281.

155. Lehtola, S.; Steigemann, C.; Oliveira, M. J. T.; Marques, M. A. L. Recent Developments in libxc — A Comprehensive Library of Functionals for Density Functional Theory. *SoftwareX* **2018**, *7*, 1-5.

156. Runge, E.; Gross, E. K. U. Density-Functional Theory for Time-Dependent Systems. *Phys. Rev. Lett.* **1984**, *52*, 997-1000.

157. Casida, M. E., Time-Dependent Density Functional Response Theory for Molecules. In *Recent Advances in Density Functional Methods*, Chong, D. P., Ed. World Scientific: 1995; Vol. 1, pp 155-192.

158. Petersilka, M.; Gossmann, U. J.; Gross, E. K. U. Excitation Energies from Time-Dependent Density-Functional Theory. *Phys. Rev. Lett.* **1996**, *76*, 1212-1215.

159. Yabana, K.; Nakatsukasa, T.; Iwata, J. I.; Bertsch, G. F. Real-Time, Real-Space Implementation of the Linear Response Time-Dependent Density-Functional Theory. *Phys. Status Solidi B* **2006**, *243*, 1121-1138.

160. Goings, J. J.; Lestrange, P. J.; Li, X. Real-Time Time-Dependent Electronic Structure Theory. *Wiley Interdiscip. Rev. Comput. Mol. Sci.* **2018**, *8*, e1341/1-19.

161. Elliott, P.; Furche, F.; Burke, K., Excited States from Time-Dependent Density Functional Theory. In *Rev. Comput. Chem.*, 2009; Vol. 26, p 91.

162. Dreuw, A.; Head-Gordon, M. Single-Reference ab Initio Methods for the Calculation of Excited States of Large Molecules. *Chem. Rev.* **2005**, *105*, 4009-4037.

163. Marques, M. A.; Maitra, N. T.; Nogueira, F. M.; Gross, E. K.; Rubio, A. *Fundamentals of Time-Dependent Density Functional Theory*; Springer Science & Business Media, 2012; Vol. 837.

164. Rüger, R. Approximations in Density Functional Based Excited State Calculations. Vrije Universiteit, 2018.

165. Casida, M. E. Time-Dependent Density-Functional Theory for Molecules and Molecular Solids. *Comput. Theor. Chem.* **2009**, *914*, 3-18.

166. Yabana, K.; Bertsch, G. F. Time-Dependent Local-Density Approximation in Real Time. *Phys. Rev. B* **1996**, *54*, 4484-4487.

167. Provorse, M. R.; Isborn, C. M. Electron Dynamics with Real-Time Time-Dependent Density Functional Theory. *Int. J. Quantum Chem.* **2016**, *116*, 739-749.

168. Li, X.; Govind, N.; Isborn, C.; DePrince, A. E.; Lopata, K. Real-Time Time-Dependent Electronic Structure Theory. *Chem. Rev.* **2020**, *120*, 9951-9993.

169. Li, X.; Smith, S. M.; Markevitch, A. N.; Romanov, D. A.; Levis, R. J.; Schlegel, H. B. A Time-Dependent Hartree–Fock Approach for Studying the Electronic Optical Response of Molecules in Intense Fields. *Phys. Chem. Chem. Phys.* **2005**, *7*, 233-239.

170. Ding, F.; Van Kuiken, B. E.; Eichinger, B. E.; Li, X. An Efficient Method for Calculating Dynamical Hyperpolarizabilities Using Real-Time Time-Dependent Density Functional Theory. *J. Chem. Phys.* **2013**, *138*, 064104.

171. Ding, F.; Guidez, E. B.; Aikens, C. M.; Li, X. Quantum Coherent Plasmon in Silver Nanowires: A Real-Time TDDFT Study. *J. Chem. Phys.* **2014**, *140*, 244705/1-7.

172. Senanayake, R. D.; Lingerfelt, D. B.; Kuda-Singappulige, G. U.; Li, X.; Aikens, C. M. Real-Time TDDFT Investigation of Optical Absorption in Gold Nanowires. *J. Phys. Chem. C* **2019**, *123*, 14734-14745.

173. Kuda-Singappulige, G. U.; Lingerfelt, D. B.; Li, X.; Aikens, C. M. Ultrafast Nonlinear Plasmon Decay Processes in Silver Nanoclusters. *J. Phys. Chem. C* **2020**, *124*, 20477-20487.

174. de Carvalho, F. F.; Bouduban, E. M.; Curchod, F. B.; Tavernelli, I. Nonadiabatic Molecular Dynamics Based on Trajectories. *Entropy* **2014**, *16*.

175. Kühne, T. D. Second Generation Car–Parrinello Molecular Dynamics. *Wiley Interdiscip. Rev. Comput. Mol. Sci.* **2014**, *4*, 391-406.

176. Curchod, B. F. E.; Martínez, T. J. Ab Initio Nonadiabatic Quantum Molecular Dynamics. *Chem. Rev.* **2018**, *118*, 3305-3336.

177. Iftimie, R.; Minary, P.; Tuckerman, M. E. Ab Initio Molecular Dynamics: Concepts, Recent Developments, and Future Trends. *Proc. Natl. Acad. Sci. U.S.A.* **2005**, *102*, 6654.

178. Mazur, A. K. Common Molecular Dynamics Algorithms Revisited: Accuracy and Optimal Time Steps of Störmer–Leapfrog Integrators. *J. Comput. Phys.* **1997**, *136*, 354-365.

179. Hockney, R. W. The Potential Calculation and Some Applications. *Methods Comput. Phys.* **1970**, *9*, 136.

180. Verlet, L. Computer "Experiments" on Classical Fluids. I. Thermodynamical Properties of Lennard-Jones Molecules. *Phys. Rev.* **1967**, *159*, 98-103.

181. Levesque, D.; Verlet, L. Molecular Dynamics and Time Reversibility. *J. Stat. Phys.* **1993**, *72*, 519-537.

182. Li, X.; Tully, J. C.; Schlegel, H. B.; Frisch, M. J. Ab Initio Ehrenfest Dynamics. *J. Chem. Phys.* **2005**, *123*, 084106.

183. Nakamura, H. *Nonadiabatic Transition*; WORLD SCIENTIFIC, 2002.

184. Yonehara, T.; Hanasaki, K.; Takatsuka, K. Fundamental Approaches to Nonadiabaticity: Toward a Chemical Theory beyond the Born–Oppenheimer Paradigm. *Chem. Rev.* **2012**, *112*, 499-542.

185. Nanbu, S.; Ishida, T.; Nakamura, H. Future Perspectives of Nonadiabatic Chemical Dynamics. *Chem. Sci.* **2010**, *1*, 663-674.

186. Crespo-Otero, R.; Barbatti, M. Recent Advances and Perspectives on Nonadiabatic Mixed Quantum-Classical Dynamics. *Chem. Rev.* **2018**, *118*, 7026-7068.

187. Ding, F.; Goings, J. J.; Liu, H.; Lingerfelt, D. B.; Li, X. Ab Initio Two-Component Ehrenfest Dynamics. *J. Chem. Phys.* **2015**, *143*, 114105.

188. Micha, D. A. Time-Dependent Many-Electron Treatment of Electronic Energy and Charge Transfer in Atomic Collisions. *J. Phys. Chem. A* **1999**, *103*, 7562-7574.

189. Micha, D. A.; Runge, K. Time-dependent many-electron approach to slow ion-atom collisions: The coupling of electronic and nuclear motions. *Phys. Rev. A.* **1994**, *50*, 322-336.

190. Isborn, C. M.; Li, X.; Tully, J. C. Time-dependent density functional theory Ehrenfest dynamics: Collisions between atomic oxygen and graphite clusters. *J. Chem. Phys.* **2007**, *126*, 134307.

191. Stucky, G. D.; Marder, S. R.; Sohn, J. E., Linear and Nonlinear Polarizability. In *Materials for Nonlinear Optics*, American Chemical Society: 1991; Vol. 455, pp 2-30.

192. Brabec, T.; Krausz, F. Intense Few-Cycle Laser Fields: Frontiers of Nonlinear Optics. *Rev. Mod. Phys.* **2000**, *72*, 545-591.

193. Cotton, F. A. *Chemical Applications of Group Theory*, 3rd ed.; Wiley: New York, 1990.

194. McClain, W. M. Two-Photon Molecular Spectroscopy. *Acc. Chem. Res.* **1974**, *7*, 129-135.

195. Wirth, M. J.; Koskelo, A.; Sanders, M. J. Molecular Symmetry and Two-Photon Spectroscopy. *Appl. Spectrosc.* **1981**, *35*, 14-21.

196. Wang, W.; Yu, P.; Zhong, Z.; Tong, X.; Liu, T.; Li, Y.; Ashalley, E.; Chen, H.; Wu, J.; Wang, Z. Size-Dependent Longitudinal Plasmon Resonance Wavelength and Extraordinary Scattering Properties of Au Nanobipyramids. *Nanotechnology* **2018**, *29*, 355402/1-8.

197. Zhang, Q.; Ge, J.; Goebl, J.; Hu, Y.; Sun, Y.; Yin, Y. Tailored Synthesis of Superparamagnetic Gold Nanoshells with Tunable Optical Properties. *Adv. Mater.* **2010**, *22*, 1905-1909.

198. Giannini, V.; Fernández-Domínguez, A. I.; Heck, S. C.; Maier, S. A. Plasmonic Nanoantennas: Fundamentals and Their Use in Controlling the Radiative Properties of Nanoemitters. *Chem. Rev.* **2011**, *111*, 3888-3912.

199. Xiao, M.; Jiang, R.; Wang, F.; Fang, C.; Wang, J.; Yu, J. C. Plasmon-Enhanced Chemical Reactions. *J. Mater. Chem. A* **2013**, *1*, 5790-5805.

200. Ueno, K.; Oshikiri, T.; Sun, Q.; Shi, X.; Misawa, H. Solid-State Plasmonic Solar Cells. *Chem. Rev.* **2018**, *118*, 2955-2993.

201. Barizuddin, S.; Bok, S.; Gangopadhyay, S. Plasmonic Sensors for Disease Detection - A Review. *J. Nanomed. Nanotechnol.* **2016**, *7*, 373-373.

202. Elahi, N.; Kamali, M.; Baghersad, M. H. Recent Biomedical Applications of Gold Nanoparticles: A Review. *Talanta* **2018**, *184*, 537-556.

203. Kailasa, S. K.; Koduru, J. R.; Desai, M. L.; Park, T. J.; Singhal, R. K.; Basu, H. Recent Progress on Surface Chemistry of Plasmonic Metal Nanoparticles for Colorimetric Assay of Drugs in Pharmaceutical and Biological Samples. *Trends Anal. Chem.* **2018**, *105*, 106-120.

204. Zhang, Z.; Wang, H.; Chen, Z.; Wang, X.; Choo, J.; Chen, L. Plasmonic Colorimetric Sensors Based on Etching and Growth of Noble Metal Nanoparticles: Strategies and Applications. *Biosens. Bioelectron.* **2018**, *114*, 52-65.

205. Genevet, P.; Tetienne, J.-P.; Gatzogiannis, E.; Blanchard, R.; Kats, M. A.; Scully, M. O.; Capasso, F. Large Enhancement of Nonlinear Optical Phenomena by Plasmonic Nanocavity Gratings. *Nano Lett.* **2010**, *10*, 4880-4883.

206. Grubisic, A.; Ringe, E.; Cobley, C. M.; Xia, Y.; Marks, L. D.; Van Duyne, R. P.; Nesbitt, D. J. Plasmonic Near-Electric Field Enhancement Effects in Ultrafast Photoelectron Emission: Correlated Spatial and Laser Polarization Microscopy Studies of Individual Ag Nanocubes. *Nano Lett.* **2012**, *12*, 4823-4829.

207. Kauranen, M.; Zayats, A. V. Nonlinear Plasmonics. *Nat. Photonics* **2012**, *6*, 737-748.

208. Panoiu, N. C.; Sha, W. E. I.; Lei, D. Y.; Li, G. C. Nonlinear Optics in Plasmonic Nanostructures. *J. Opt.* **2018**, *20*, 083001.

209. Sivis, M.; Pazos-Perez, N.; Yu, R.; Alvarez-Puebla, R.; García de Abajo, F. J.; Ropers, C. Continuous-Wave Multiphoton Photoemission from Plasmonic Nanostars. *Commun. Phys.* **2018**, *1*, 13.

210. Maier, S. A. *Plasmonics: Fundamentals and Applications*; Springer, New York, NY, 2007.

211. Kretschmann, E.; Raether, H. Radiative Decay of Non Radiative Surface Plasmons Excited by Light. *Z. Naturforsch. A* **1968**, *23*, 2135-2136.

212. Liau, Y.-H.; Unterreiner, A. N.; Chang, Q.; Scherer, N. F. Ultrafast Dephasing of Single Nanoparticles Studied by Two-Pulse Second-Order Interferometry. *J. Phys. Chem. B* **2001**, *105*, 2135-2142.

213. Lazzarini, C. M.; Tadzio, L.; Fitzgerald, J. M.; Sánchez-Gil, J. A.; Giannini, V. Linear Ultrafast Dynamics of Plasmon and Magnetic Resonances in Nanoparticles. *Phys. Rev. B* **2017**, *96*, 235407/1-11.

214. Mie, G. Beiträge zur Optik trüber Medien, speziell kolloidaler Metallösungen. *Ann. Phys. (Berl.)* **1908**, *330*, 377-445.

215. Draine, B. T.; Flatau, P. J. Discrete-Dipole Approximation For Scattering Calculations. *J. Opt. Soc. Am. A* **1994**, *11*, 1491-1499.

216. Zhao, J.; Pinchuk, A. O.; McMahon, J. M.; Li, S.; Ausman, L. K.; Atkinson, A. L.; Schatz, G. C. Methods for Describing the Electromagnetic Properties of Silver and Gold Nanoparticles. *Acc. Chem. Res.* **2008**, *41*, 1710-1720.

217. Törmä, P.; Barnes, W. L. Strong Coupling Between Surface Plasmon Polaritons and Emitters: A Review. *Rep. Prog. Phys.* **2014**, *78*, 013901/1-34.

218. Baseggio, O.; Fronzoni, G.; Stener, M. A New Time Dependent Density Functional Algorithm for Large Systems and Plasmons in Metal Clusters. *J. Chem. Phys.* **2015**, *143*, 024106/1-12.

219. Castro, A.; Appel, H.; Oliveira, M.; Rozzi, C. A.; Andrade, X.; Lorenzen, F.; Marques, M. A. L.; Gross, E. K. U.; Rubio, A. Octopus: A Tool for the Application of Time-Dependent Density Functional Theory. *Phys. Status Solidi B* **2006**, *243*, 2465-2488.

220. Castro, A.; Marques, M. A. L.; Rubio, A. Propagators for the Time-Dependent Kohn–Sham Equations. *J. Chem. Phys.* **2004**, *121*, 3425-3433.

221. Kuisma, M.; Sakko, A.; Rossi, T. P.; Larsen, A. H.; Enkovaara, J.; Lehtovaara, L.; Rantala, T. T. Localized Surface Plasmon Resonance in Silver Nanoparticles: Atomistic First-Principles Time-Dependent Density-Functional Theory Calculations. *Phys. Rev. B* **2015**, *91*, 115431/1-8.

222. Tussupbayev, S.; Govind, N.; Lopata, K.; Cramer, C. J. Comparison of Real-Time and Linear-Response Time-Dependent Density Functional Theories for Molecular Chromophores Ranging from Sparse to High Densities of States. *J. Chem. Theory Comput.* **2015**, *11*, 1102-1109.

223. Baseggio, O.; De Vetta, M.; Fronzoni, G.; Stener, M.; Sementa, L.; Fortunelli, A.; Calzolari, A. Photoabsorption of Icosahedral Noble Metal Clusters: An Efficient TDDFT Approach to Large-Scale Systems. *J. Phys. Chem. C* **2016**, *120*, 12773-12782.

224. Townsend, E.; Bryant, G. W. Plasmonic Properties of Metallic Nanoparticles: The Effects of Size Quantization. *Nano Lett.* **2012**, *12*, 429-434.

225. Kadek, M.; Konecny, L.; Gao, B.; Repisky, M.; Ruud, K. X-ray Absorption Resonances Near L2,3-edges from Real-Time Propagation of the Dirac–Kohn–Sham Density Matrix. *Phys. Chem. Chem. Phys.* **2015**, *17*, 22566-22570.

226. Repisky, M.; Konecny, L.; Kadek, M.; Komorovsky, S.; Malkin, O. L.; Malkin, V. G.; Ruud, K. Excitation Energies from Real-Time Propagation of the Four-Component Dirac–Kohn–Sham Equation. *J. Chem. Theory Comput.* **2015**, *11*, 980-991.

227. Bruner, A.; LaMaster, D.; Lopata, K. Accelerated Broadband Spectra Using Transition Dipole Decomposition and Padé Approximants. *J. Chem. Theory Comput.* **2016**, *12*, 3741-3750.

228. Rossi, T. P.; Kuisma, M.; Puska, M. J.; Nieminen, R. M.; Erhart, P. Kohn–Sham Decomposition in Real-Time Time-Dependent Density-Functional Theory: An Efficient Tool for Analyzing Plasmonic Excitations. *J. Chem. Theory Comput.* **2017**, *13*, 4779-4790.

229. Sinha-Roy, R.; García-González, P.; López Lozano, X.; Whetten, R. L.; Weissker, H.-C. Identifying Electronic Modes by Fourier Transform from δ-Kick Time-Evolution TDDFT Calculations. *J. Chem. Theory Comput.* **2018**, *14*, 6417-6426.

230. Rossi, T. P.; Erhart, P.; Kuisma, M. Hot-Carrier Generation in Plasmonic Nanoparticles: Atomic-Scale Structure Matters. *arXiv e-prints* **2020**, arXiv:2002.12087.

231. Hasan, S. B.; Lederer, F.; Rockstuhl, C. Nonlinear Plasmonic Antennas. *Mater. Today* **2014**, *17*, 478-485.

232. Butet, J.; Brevet, P.-F.; Martin, O. J. F. Optical Second Harmonic Generation in Plasmonic Nanostructures: From Fundamental Principles to Advanced Applications. *ACS Nano* **2015**, *9*, 10545-10562.

233. Krasavin, A. V.; Ginzburg, P.; Zayats, A. V. Free-Electron Optical Nonlinearities in Plasmonic Nanostructures: A Review of the Hydrodynamic Description. *Laser Photonics Rev.* **2018**, *12*, 1700082.

234. Babaze, A.; Esteban, R.; Aizpurua, J.; Borisov, A. G. Second-Harmonic Generation from a Quantum Emitter Coupled to a Metallic Nanoantenna. *ACS Photonics* **2020**, *7*, 701-713.

235. Chauvet, N.; Ethis de Corny, M.; Jeannin, M.; Laurent, G.; Huant, S.; Gacoin, T.; Dantelle, G.; Nogues, G.; Bachelier, G. Hybrid KTP–Plasmonic Nanostructures for Enhanced Nonlinear Optics at the Nanoscale. *ACS Photonics* **2020**, *7*, 665-672.

236. Gürdal, E.; Horneber, A.; Shaqqura, N.; Meixner, A. J.; Kern, D. P.; Zhang, D.; Fleischer, M. Enhancement of the Second Harmonic Signal of Nonlinear Crystals by Self-Assembled Gold Nanoparticles. *J. Chem. Phys.* **2020**, *152*, 104711.

237. Shen, Q.; Jin, W.; Yang, G.; Rodriguez, A. W.; Mikkelsen, M. H. Active Control of Multiple, Simultaneous Nonlinear Optical Processes in Plasmonic Nanogap Cavities. *ACS Photonics* **2020**, *7*, 901-907.

238. Frisch, M. J.; Trucks, G. W.; Schlegel, H. B.; Scuseria, G. E.; Robb, M. A.; Cheeseman, J. R.; Scalmani, G.; Barone, V.; Petersson, G. A.; Nakatsuji, H., et al. *Gaussian Development Version*, Revision J.01+; Gaussian, Inc.: Wallingford CT, 2018.

239. Hay, P. J.; Wadt, W. R. Ab Initio Effective Core Potentials for Molecular Calculations. Potentials for K to Au Including the Outermost Core Orbitals. *J. Chem. Phys.* **1985**, *82*, 299-310.

240. Wadt, W. R.; Hay, P. J. Ab Initio Effective Core Potentials for Molecular Calculations. Potentials for Main Group Elements Na to Bi. *J. Chem. Phys.* **1985**, *82*, 284-298.

241. Harb, M.; Rabilloud, F.; Simon, D.; Rydlo, A.; Lecoultre, S.; Conus, F.; Rodrigues, V.; Félix, C. Optical Absorption of Small Silver Clusters: Ag_n, (n=4–22). *J. Chem. Phys.* **2008**, *129*, 194108.

242. Lopata, K.; Govind, N. Modeling Fast Electron Dynamics with Real-Time Time-Dependent Density Functional Theory: Application to Small Molecules and Chromophores. *J. Chem. Theory Comput.* **2011**, *7*, 1344-1355.

243. Walter, M.; Akola, J.; Lopez-Acevedo, O.; Jadzinsky, P. D.; Calero, G.; Ackerson, C. J.; Whetten, R. L.; Grönbeck, H.; Häkkinen, H. A Unified View of Ligand-Protected Gold Clusters as Superatom Complexes. *Proc. Natl. Acad. Sci. U.S.A.* **2008**, *105*, 9157-9162.

244. Raghunathan, S.; Nest, M. The Lack of Resonance Problem in Coherent Control with Real-Time Time-Dependent Density Functional Theory. *J. Chem. Theory Comput.* **2012**, *8*, 806-809.

245. Provorse, M. R.; Habenicht, B. F.; Isborn, C. M. Peak-Shifting in Real-Time Time-Dependent Density Functional Theory. *J. Chem. Theory Comput.* **2015**, *11*, 4791-4802.

246. Luo, K.; Fuks, J. I.; Maitra, N. T. Studies of Spuriously Shifting Resonances in Time-Dependent Density Functional Theory. *J. Chem. Phys.* **2016**, *145*, 044101.

247. Göppert-Mayer, M. Über Elementarakte mit zwei Quantensprüngen. *Ann. Phys. (Berl.)* **1931**, *401*, 273-294.

248. McClain, W. M. Excited State Symmetry Assignment Through Polarized Two-Photon Absorption Studies of Fluids. *J. Chem. Phys.* **1971**, *55*, 2789-2796.

249. Ye, W.; Long, R.; Huang, H.; Xiong, Y. Plasmonic Nanostructures in Solar Energy Conversion. *J. Mater. Chem. C* **2017**, *5*, 1008-1021.

250. Chen, M.; He, Y. Plasmonic Nanostructures for Broadband Solar Absorption Based on the Intrinsic Absorption of Metals. *Sol. Energy Mater. Sol. Cells* **2018**, *188*, 156-163.

251. Kamat, P. V.; Hartland, G. V. Plasmons for Energy Conversion. *ACS Energy Lett.* **2018**, *3*, 1467-1469.

252. Morawiec, S.; Mendes, M. J.; Priolo, F.; Crupi, I. Plasmonic Nanostructures for Light Trapping in Thin-Film Solar Cells. *Materl. Sci. Semicond. Process.* **2019**, *92*, 10-18.

253. Siavash Moakhar, R.; Gholipour, S.; Masudy-Panah, S.; Seza, A.; Mehdikhani, A.; Riahi-Noori, N.; Tafazoli, S.; Timasi, N.; Lim, Y.-F.; Saliba, M. Recent Advances in Plasmonic Perovskite Solar Cells. *Adv. Sci.* **2020**, *7*, 1902448.

254. Linic, S.; Chavez, S.; Elias, R. Flow and Extraction of Energy and Charge Carriers in Hybrid Plasmonic Nanostructures. *Nat. Mater.* **2021**.

255. Li, S.; Miao, P.; Zhang, Y.; Wu, J.; Zhang, B.; Du, Y.; Han, X.; Sun, J.; Xu, P. Recent Advances in Plasmonic Nanostructures for Enhanced Photocatalysis and Electrocatalysis. *Adv. Mater.* **2021**, *33*, 2000086.

256. Camden, J. P.; Dieringer, J. A.; Zhao, J.; Van Duyne, R. P. Controlled Plasmonic Nanostructures for Surface-Enhanced Spectroscopy and Sensing. *Acc. Chem. Res.* **2008**, *41*, 1653-1661.

257. Luk'yanchuk, B.; Zheludev, N. I.; Maier, S. A.; Halas, N. J.; Nordlander, P.; Giessen, H.; Chong, C. T. The Fano Resonance in Plasmonic Nanostructures and Metamaterials. *Nat. Mater.* **2010**, *9*, 707-715.

258. Boriskina, S. V.; Cooper, T. A.; Zeng, L.; Ni, G.; Tong, J. K.; Tsurimaki, Y.; Huang, Y.; Meroueh, L.; Mahan, G.; Chen, G. Losses in Plasmonics: From Mitigating Energy dissipation to Embracing Loss-Enabled Functionalities. *Adv. Opt. Photonics* **2017**, *9*, 775-827.

259. Hartland, G. V.; Besteiro, L. V.; Johns, P.; Govorov, A. O. What's so Hot about Electrons in Metal Nanoparticles? *ACS Energy Lett.* **2017**, *2*, 1641-1653.

260. Hegde, R. S.; Khatua, S., Hot Carrier Generation in Plasmonic Nanostructures: Physics and Device Applications. In *Nanoelectronics*, Kaushik, B. K., Ed. Elsevier: 2019; pp 289-315.

261. Foerster, B.; Hartelt, M.; Collins, S. S. E.; Aeschlimann, M.; Link, S.; Sönnichsen, C. Interfacial States Cause Equal Decay of Plasmons and Hot Electrons at Gold–Metal Oxide Interfaces. *Nano Lett.* **2020**, *20*, 3338-3343.

262. El-Sayed, M. A. Small Is Different: Shape-, Size-, and Composition-Dependent Properties of Some Colloidal Semiconductor Nanocrystals. *Acc. Chem. Res.* **2004**, *37*, 326-333.

263. Wang, H.; Brandl, D. W.; Nordlander, P.; Halas, N. J. Plasmonic Nanostructures: Artificial Molecules. *Acc. Chem. Res.* **2007**, *40*, 53-62.

264. Aikens, C. M.; Li, S.; Schatz, G. C. From Discrete Electronic States to Plasmons: TDDFT Optical Absorption Properties of Ag_n (n = 10, 20, 35, 56, 84, 120) Tetrahedral Clusters. *J. Phys. Chem. C* **2008**, *112*, 11272-11279.

265. Hou, W.; Cronin, S. B. A Review of Surface Plasmon Resonance-Enhanced Photocatalysis. *Adv. Funct. Mater.* **2012**, *23*, 1612-1619.

266. Ogarev, V. A.; Rudoi, V. M.; Dement'eva, O. V. Gold Nanoparticles: Synthesis, Optical Properties, and Application. *Inorg. Mater. Appl. Res.* **2018**, *9*, 134-140.

267. Sardar, R.; Funston, A. M.; Mulvaney, P.; Murray, R. W. Gold Nanoparticles: Past, Present, and Future. *Langmuir* **2009**, *25*, 13840-13851.

268. Fratoddi, I. Hydrophobic and Hydrophilic Au and Ag Nanoparticles. Breakthroughs and Perspectives. *Nanomaterials* **2018**, *8*, 11.

269. Krutyakov, Y. A.; Kudrinskiy, A. A.; Olenin, A. Y.; Lisichkin, G. V. Synthesis and Properties of Silver Nanoparticles: Advances and Prospects. *Russ. Chem. Rev.* **2008**, *77*, 233-257.

270. Naik, G. V.; Shalaev, V. M.; Boltasseva, A. Alternative Plasmonic Materials: Beyond Gold and Silver. *Adv. Mater.* **2013**, *25*, 3264-3294.

271. West, P. R.; Ishii, S.; Naik, G. V.; Emani, N. K.; Shalaev, V. M.; Boltasseva, A. Searching for Better Plasmonic Materials. *Laser Photonics Rev.* **2010**, *4*, 795-808.

272. Li, Y.; Li, Z.; Chi, C.; Shan, H.; Zheng, L.; Fang, Z. Plasmonics of 2D Nanomaterials: Properties and Applications. *Adv. Sci.* **2017**, *4*, 1600430.

273. Fei, Z.; Rodin, A. S.; Andreev, G. O.; Bao, W.; McLeod, A. S.; Wagner, M.; Zhang, L. M.; Zhao, Z.; Thiemens, M.; Dominguez, G., et al. Gate-Tuning of Graphene Plasmons Revealed by Infrared Nano-Imaging. *Nature* **2012**, *487*, 82-85.

274. Yan, H.; Li, X.; Chandra, B.; Tulevski, G.; Wu, Y.; Freitag, M.; Zhu, W.; Avouris, P.; Xia, F. Tunable Infrared Plasmonic Devices using Graphene/Insulator Stacks. *Nat. Nanotechnol.* **2012**, *7*, 330-334.

275. Ren, Q.; You, J. W.; Panoiu, N. C. Large Enhancement of the Effective Second-Order Nonlinearity in Graphene Metasurfaces. *Phys. Rev. B* **2019**, *99*, 205404.

276. Cox, J. D.; García de Abajo, F. J. Nonlinear Graphene Nanoplasmonics. *Acc. Chem. Res.* **2019**, *52*, 2536-2547.

277. You, J. W.; Panoiu, N. C. Plasmon-Induced Nonlinearity Enhancement and Homogenization of Graphene Metasurfaces. *Opt. Lett.* **2019**, *44*, 3030-3033.

278. Jablan, M. Quasiclassical Nonlinear Plasmon Resonance in Graphene. *Phys. Rev. B* **2020**, *101*, 085424.

279. Soavi, G.; Wang, G.; Rostami, H.; Tomadin, A.; Balci, O.; Paradisanos, I.; Pogna, E. A. A.; Cerullo, G.; Lidorikis, E.; Polini, M., et al. Hot Electrons Modulation of Third-Harmonic Generation in Graphene. *ACS Photonics* **2019**, *6*, 2841-2849.

280. Shen, N.-H.; Tassin, P.; Koschny, T.; Soukoulis, C. M. Comparison of Gold- and Graphene-Based Resonant Nanostructures for Terahertz Metamaterials and an Ultrathin Graphene-Based Modulator. *Phys. Rev. B* **2014**, *90*, 115437.

281. Fan, Y.; Shen, N.-H.; Zhang, F.; Zhao, Q.; Wei, Z.; Zhang, P.; Dong, J.; Fu, Q.; Li, H.; Soukoulis, C. M. Photoexcited Graphene Metasurfaces: Significantly Enhanced and Tunable Magnetic Resonances. *ACS Photonics* **2018**, *5*, 1612-1618.

282. Busby, E.; Berkelbach, T. C.; Kumar, B.; Chernikov, A.; Zhong, Y.; Hlaing, H.; Zhu, X. Y.; Heinz, T. F.; Hybertsen, M. S.; Sfeir, M. Y., et al. Multiphonon Relaxation Slows Singlet Fission in Crystalline Hexacene. *J. Am. Chem. Soc.* **2014**, *136*, 10654-10660.

283. Fuemmeler, E. G.; Sanders, S. N.; Pun, A. B.; Kumarasamy, E.; Zeng, T.; Miyata, K.; Steigerwald, M. L.; Zhu, X. Y.; Sfeir, M. Y.; Campos, L. M., et al. A Direct Mechanism of Ultrafast Intramolecular Singlet Fission in Pentacene Dimers. *ACS Cent. Sci.* **2016**, *2*, 316-324.

284. Morrison, A. F.; Herbert, J. M. Evidence for Singlet Fission Driven by Vibronic Coherence in Crystalline Tetracene. *J. Phys. Chem. Lett.* **2017**, *8*, 1442-1448.

285. Deng, G.-H.; Wei, Q.; Han, J.; Qian, Y.; Luo, J.; Harutyunyan, A. R.; Chen, G.; Bian, H.; Chen, H.; Rao, Y. Vibronic Fingerprint of Singlet Fission in Hexacene. *J. Chem. Phys.* **2019**, *151*, 054703.

286. Sanders, S. N.; Kumarasamy, E.; Fallon, K. J.; Sfeir, M. Y.; Campos, L. M. Singlet Fission in a Hexacene Dimer: Energetics Dictate Dynamics. *Chem. Sci.* **2020**, *11*, 1079-1084.

287. Anak, B.; Bencharif, M.; Rabilloud, F. Time-Dependent density functional study of UV-Visible absorption spectra of small noble metal clusters (Cu_n, Ag_n, Au_n, n = 2–9, 20). *RSC Adv.* **2014**, *4*, 13001-13011.

288. Bae, G.-T.; Aikens, C. M. Time-Dependent Density Functional Theory Studies of Optical Properties of Au Nanoparticles: Octahedra, Truncated Octahedra, and Icosahedra. *J. Phys. Chem. C* **2015**, *119*, 23127-23137.

289. Johnson, H. E.; Aikens, C. M. Electronic Structure and TDDFT Optical Absorption Spectra of Silver Nanorods. *J. Phys. Chem. A* **2009**, *113*, 4445-4450.

290. Liao, M.-S.; Bonifassi, P.; Leszczynski, J.; Ray, P. C.; Huang, M.-J.; Watts, J. D. Structure, Bonding, and Linear Optical Properties of a Series of Silver and Gold Nanorod Clusters: DFT/TDDFT Studies. *J. Phys. Chem. A* **2010**, *114*, 12701-12708.

291. Rabilloud, F. Assessment of the Performance of Long-Range-Corrected Density Functionals for Calculating the Absorption Spectra of Silver Clusters. *J. Phys. Chem. A* **2013**, *117*, 4267-4278.

292. Rohringer, N.; Gordon, A.; Santra, R. Configuration-Interaction-Based Time Dependent Orbital Approach for Ab Initio Treatment of Electronic Dynamics in a Strong Optical Laser Field. *Phys. Rev. A.* **2006**, *74*, 043420.

293. Greenman, L.; Ho, P. J.; Pabst, S.; Kamarchik, E.; Mazziotti, D. A.; Santra, R. Implementation of the Time-Dependent Configuration-Interaction Singles Method for Atomic Strong-Field Processes. *Phys. Rev. A.* **2010**, *82*, 023406.

294. Peng, W.-T.; Fales, B. S.; Levine, B. G. Simulating Electron Dynamics of Complex Molecules with Time-Dependent Complete Active Space Configuration Interaction. *J. Chem. Theory Comput.* **2018**, *14*, 4129-4138.

295. Krause, P.; Klamroth, T.; Saalfrank, P. Time-Dependent Configuration-Interaction Calculations of Laser-Pulse-Driven Many-Electron Dynamics: Controlled Dipole Switching in Lithium Cyanide. *J. Chem. Phys.* **2005**, *123*, 074105.

296. Isborn, C. M.; Li, X. Modeling the Doubly Excited State with Time-Dependent Hartree–Fock and Density Functional Theories. *J. Chem. Phys.* **2008**, *129*, 204107.

297. Walker, B. G.; Molteni, C.; Marzari, N. Ab Initio Molecular Dynamics of Metal Surfaces. *J. Phys. Condens. Matter* **2004**, *16*, S2575-S2596.

298. Mark, E. T. Ab Initio Molecular Dynamics: Basic Concepts, Current Trends and Novel Applications. *J. Phys. Condens. Matter* **2002**, *14*, R1297-R1355.

299. Hassanali, A. A.; Cuny, J.; Verdolino, V.; Parrinello, M. Aqueous Solutions: State of the Art in Ab Initio Molecular Dynamics. *Philos. Trans. R. Soc. A* **2014**, *372*, 20120482.

300. Marx, D.; Hutter, J. *Ab Initio Molecular Dynamics: Basic Theory And Advanced Methods*; Cambridge University Press: Cambridge, 2009.

301. Curchod, B. F. E.; Rothlisberger, U.; Tavernelli, I. Trajectory-Based Nonadiabatic Dynamics with Time-Dependent Density Functional Theory. *ChemPhysChem* **2013**, *14*, 1314-1340.

302. Wang, F.; Yam, C. Y.; Hu, L.; Chen, G. Time-Dependent Density Functional Theory Based Ehrenfest Dynamics. *J. Chem. Phys.* **2011**, *135*, 044126.

303. Donati, G.; Lingerfelt, D. B.; Petrone, A.; Rega, N.; Li, X. "Watching" Polaron Pair Formation from First-Principles Electron–Nuclear Dynamics. *J. Phys. Chem. A* **2016**, *120*, 7255-7261.

304. Lee, C.; Yang, W.; Parr, R. G. Development of the Colle-Salvetti Correlation-Energy Formula into a Functional of the Electron Density. *Phys. Rev. B* **1988**, *37*, 785-789.

305. Petersson, G. A.; Bennett, A.; Tensfeldt, T. G.; Al-Laham, M. A.; Shirley, W. A.; Mantzaris, J. A Complete Basis Set Model Chemistry. I. The Total Energies of Closed-Shell Atoms and Hydrides of the First-Row Elements. *J. Chem. Phys.* **1988**, *89*, 2193-2218.

306. Francl, M. M.; Pietro, W. J.; Hehre, W. J.; Binkley, J. S.; Gordon, M. S.; DeFrees, D. J.; Pople, J. A. Self-Consistent Molecular Orbital Methods. XXIII. A Polarization-Type Basis Set for Second-Row Elements. *J. Chem. Phys.* **1982**, *77*, 3654-3665.

307. Hariharan, P. C.; Pople, J. A. The Influence of Polarization Functions on Molecular Orbital Hydrogenation Energies. *Theor. Chim. Acta* **1973**, *28*, 213-222.

308. Hehre, W. J.; Ditchfield, R.; Pople, J. A. Self-Consistent Molecular Orbital Methods. XII. Further Extensions of Gaussian-Type Basis Sets for Use in Molecular Orbital Studies of Organic Molecules. *J. Chem. Phys.* **1972**, *56*, 2257-2261.

309. Ditchfield, R.; Hehre, W. J.; Pople, J. A. Self-Consistent Molecular-Orbital Methods. IX. An Extended Gaussian-Type Basis for Molecular-Orbital Studies of Organic Molecules. *J. Chem. Phys.* **1971**, *54*, 724-728.

310. Momma, K.; Izumi, F. *VESTA 3* for Three-Dimensional Visualization of Crystal, Volumetric and Morphology Data. *J. Appl. Crystallogr.* **2011**, *44*, 1272-1276.

311. Bergman, A.; Jortner, J. Two-Photon Absorption Spectra of Crystalline Naphthalene and of the Naphthalene Molecule in Solution. *Chem. Phys. Lett.* **1974**, *26*, 323-326.

312. Campbell, C. T. The Selective Epoxidation of Ethylene Catalyzed by Ag(111): A Comparison with Ag(110). *J. Catal.* **1985**, *94*, 436-444.

313. Van Santen, R. A.; Kuipers, H. P. C. E., The Mechanism of Ethylene Epoxidation. In *Advances in Catalysis*, Eley, D. D.; Pines, H.; Weisz, P. B., Eds. Academic Press: 1987; Vol. 35, pp 265-321.

314. Gravil, P. A.; Bird, D. M.; White, J. A. Adsorption and Dissociation of O_2 on Ag(110). *Phys. Rev. Lett.* **1996**, *77*, 3933-3936.

315. Khasin, A. V. Kinetic Evidence for the Identical Nature of Active Centers for Partial and Deep Oxidation of Ethylene on Silver. *React. Kinet. Catal. Lett.* **2002**, *76*, 327-334.

316. Linic, S.; Barteau, M. A. Formation of a Stable Surface Oxametallacycle that Produces Ethylene Oxide. *J. Am. Chem. Soc.* **2002**, *124*, 310-317.

317. Bocquet, M.-L.; Michaelides, A.; Loffreda, D.; Sautet, P.; Alavi, A.; King, D. A. New Insights into Ethene Epoxidation on Two Oxidized Ag{111} Surfaces. *J. Am. Chem. Soc.* **2003**, *125*, 5620-5621.

318. Hagen, J.; Socaciu, L. D.; Le Roux, J.; Popolan, D.; Bernhardt, T. M.; Wöste, L.; Mitrić, R.; Noack, H.; Bonačić-Koutecký, V. Cooperative Effects in the Activation of Molecular Oxygen by Anionic Silver Clusters. *J. Am. Chem. Soc.* **2004**, *126*, 3442-3443.

319. Linic, S.; Piao, H.; Adib, K.; Barteau, M. A. Ethylene Epoxidation on Ag: Identification of the Crucial Surface Intermediate by Experimental and Theoretical Investigation of its Electronic Structure. *Angew. Chem., Int. Ed.* **2004**, *43*, 2918-2921.

320. Hahn, J. R.; Ho, W. Chemisorption and Dissociation of Single Oxygen Molecules on Ag(110). *J. Chem. Phys.* **2005**, *123*, 214702.

321. Bukhtiyarov, V. I.; Knop-Gericke, A., Ethylene Epoxidation over Silver Catalysts. In *Nanostructured Catalysts: Selective Oxidations*, Hess, C.; Schlögl, R., Eds. The Royal Society of Chemistry: 2011; pp 214-247.

322. Rawal, T. B.; Hong, S.; Pulkkinen, A.; Alatalo, M.; Rahman, T. S. Adsorption, Diffusion, and Vibration of Oxygen on Ag(110). *Phys. Rev. B* **2015**, *92*, 035444.

323. Qaseem, A.; Chen, F.; Wu, X.; Johnston, R. L. Pt-Free Silver Nanoalloy Electrocatalysts for Oxygen Reduction Reaction in Alkaline Media. *Catal. Sci. Technol.* **2016**, *6*, 3317-3340.

324. Jones, T. E.; Wyrwich, R.; Böcklein, S.; Carbonio, E. A.; Greiner, M. T.; Klyushin, A. Y.; Moritz, W.; Locatelli, A.; Menteş, T. O.; Niño, M. A., et al. The Selective Species in Ethylene Epoxidation on Silver. *ACS Catal.* **2018**, *8*, 3844-3852.

325. Erikson, H.; Sarapuu, A.; Tammeveski, K. Oxygen Reduction Reaction on Silver Catalysts in Alkaline Media: a Minireview. *ChemElectroChem* **2019**, *6*, 73-86.

326. Christopher, P.; Linic, S. Engineering Selectivity in Heterogeneous Catalysis: Ag Nanowires as Selective Ethylene Epoxidation Catalysts. *J. Am. Chem. Soc.* **2008**, *130*, 11264-11265.

327. Özbek, M. O.; van Santen, R. A. The Mechanism of Ethylene Epoxidation Catalysis. *Catal. Lett.* **2013**, *143*, 131-141.

328. Yan, L.; Xu, J.; Wang, F.; Meng, S. Plasmon-Induced Ultrafast Hydrogen Production in Liquid Water. *J. Phys. Chem. Lett.* **2018**, *9*, 63-69.

329. Zhang, Y.; Nelson, T.; Tretiak, S.; Guo, H.; Schatz, G. C. Plasmonic Hot-Carrier-Mediated Tunable Photochemical Reactions. *ACS Nano* **2018**, *12*, 8415-8422.

330. Yan, L.; Wang, F.; Meng, S. Quantum Mode Selectivity of Plasmon-Induced Water Splitting on Gold Nanoparticles. *ACS Nano* **2016**, *10*, 5452-5458.

331. Udaya Bhaskara Rao, T.; Pradeep, T. Luminescent Ag_7 and Ag_8 Clusters by Interfacial Synthesis. *Angew. Chem., Int. Ed.* **2010**, *49*, 3925-3929.

332. Xie, Y.-P.; Shen, Y.-L.; Duan, G.-X.; Han, J.; Zhang, L.-P.; Lu, X. Silver Nanoclusters: Synthesis, Structures and Photoluminescence. *Mater. Chem. Front.* **2020**, *4*, 2205-2222.

333. Rohrdanz, M. A.; Martins, K. M.; Herbert, J. M. A Long-Range-Corrected Density Functional That Performs Well for Both Ground-State Properties and Time-Dependent Density Functional Theory Excitation Energies, Including Charge-Transfer Excited States. *J. Chem. Phys.* **2009**, *130*, 054112/1-8.

334. Bode, B. M.; Gordon, M. S. Macmolplt: A Graphical User Interface for GAMESS. *J. Mol. Graph. Model* **1998**, *16*, 133-138.

335. Yabana, K.; Bertsch, G. F. Optical Response of Small Silver Clusters. *Phys. Rev. A.* **1999**, *60*, 3809-3814.

336. Huda, M. N.; Ray, A. K. Electronic Structures and Magic Numbers of Small Silver Clusters: A Many-Body Perturbation-Theoretic Study. *Phys. Rev. A.* **2003**, *67*, 013201.

337. Radcliffe, P.; Przystawik, A.; Diederich, T.; Döppner, T.; Tiggesbäumker, J.; Meiwes-Broer, K.-H. Excited-State Relaxation of Ag_8 Clusters Embedded in Helium Droplets. *Phys. Rev. Lett.* **2004**, *92*, 173403.

338. Tian, D.; Zhang, H.; Zhao, J. Structure and Structural Evolution of Ag_n (n=3–22) Clusters using a Genetic Algorithm and Density Functional Theory Method. *Solid State Commun.* **2007**, *144*, 174-179.

339. Tully, J. C. Molecular Dynamics with Electronic Transitions. *J. Chem. Phys.* **1990**, *93*, 1061-1071.

340. Smith, B.; Shakiba, M.; Akimov, A. V. Nonadiabatic Dynamics in Si and CdSe Nanoclusters: Many-Body vs Single-Particle Treatment of Excited States. *J. Chem. Theory Comput.* **2021**, *17*, 678-693.

Appendix A - Character table for C2v point group symmetry

	E	C_2 (z)	σ_v(xz)	σ_v(yz)	linear, rotations	quadratic
A_1	1	1	1	1	z	x^2, y^2, z^2
A_2	1	1	-1	-1	R_z	xy
B_1	1	-1	1	-1	x, R_y	xz
B_2	1	-1	-1	1	y, R_x	yz

Adapted from https://www.webqc.org/printable-symmetrypointgroup-ct-c2v.html

Appendix B - Supporting Information for "Ultrafast Nonlinear Plasmon Decay Processes in Silver Nanoclusters"

Coordinates of tetrahedral Ag_8 cluster

Ag	-1.640891	-1.640891	-1.640891
Ag	1.640891	1.640891	-1.640891
Ag	1.640891	-1.640891	1.640891
Ag	-1.640891	1.640891	1.640891
Ag	-1.021397	1.021397	-1.021397
Ag	1.021397	-1.021397	-1.021397
Ag	1.021397	1.021397	1.021397
Ag	-1.021397	-1.021397	1.021397

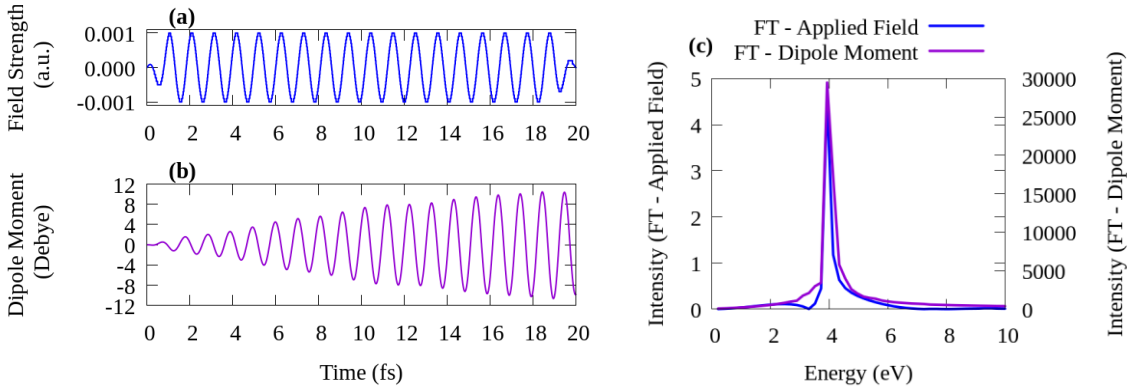

Figure B-1. Time variation of (a) a continuous wave electric field applied with a frequency of 3.96 eV and (b) the resulting dipole moment of Ag_8 from 0 fs to 20 fs. (c) Fourier transforms of (a) and (b).

Table B-1. Transitions responsible for the peak at 3.05 eV in Ag_8 (T_d) from LR-TDDFT. (color code: 1P, 1D, 2S, d band)

Energy (eV)	Wavelength (nm)	Oscillator strength	Transitions	Weight
3.05	407	0.269	74 → 79	-0.331

			75 → 78	-0.331
			76 → 80	0.387
			76 → 81	-0.228
			76 → 82	-0.270
3.05	407	0.269	74 → 77	0.331
			75 → 80	0.387
			75 → 81	-0.120
			75 → 82	0.332
			76 → 78	-0.331
3.05	407	0.269	74 → 80	0.387
			74 → 81	0.348
			75 → 77	0.331
			76 → 79	-0.331

Table B-2. Transitions responsible for the peak at 3.96 eV in Ag_8 (T_d) from LR-TDDFT. (color code: 1P, 1D, 2S, d band)

Energy (eV)	Wavelength (nm)	Oscillator strength	Transitions	Weight
3.96	313	0.750	67 → 77	-0.110
			74 → 79	-0.186
			75 → 78	-0.186
			76 → 80	0.159
			76 → 81	0.367
			76 → 82	0.435
3.96	313	0.750	74 → 77	-0.186
			75 → 80	-0.159
			75 → 81	-0.194
			75 → 82	0.535
			76 → 78	0.186
3.96	313	0.750	66 → 78	0.111
			74 → 80	-0.159

			74 → 81	0.560
			75 → 77	-0.186
			76 → 79	0.186

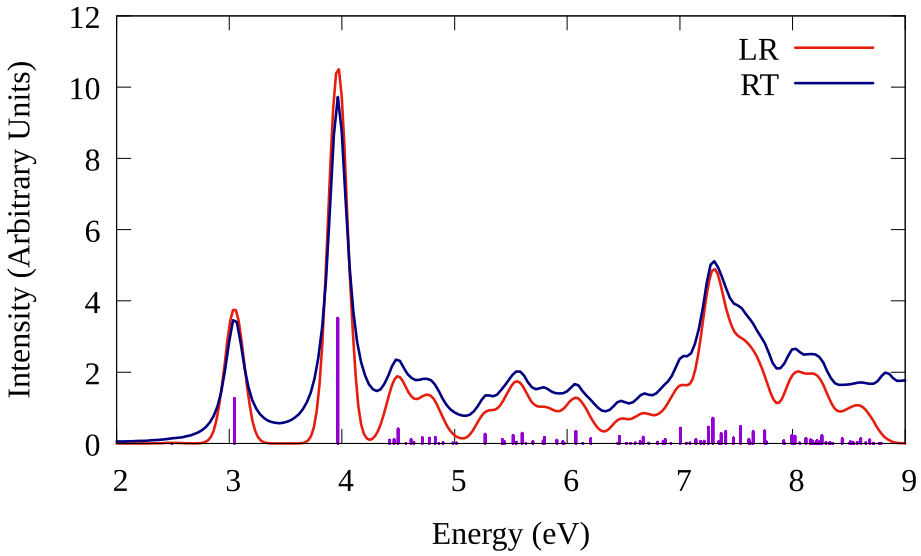

Figure B-2. Absorption spectrum of Ag_8 calculated from linear response theory (LR) and real-time propagation (RT). (Purple: LR stick spectrum; red: Convoluted LR spectrum with gaussian curves of FWHM = 0.2 eV; blue: RT spectrum)

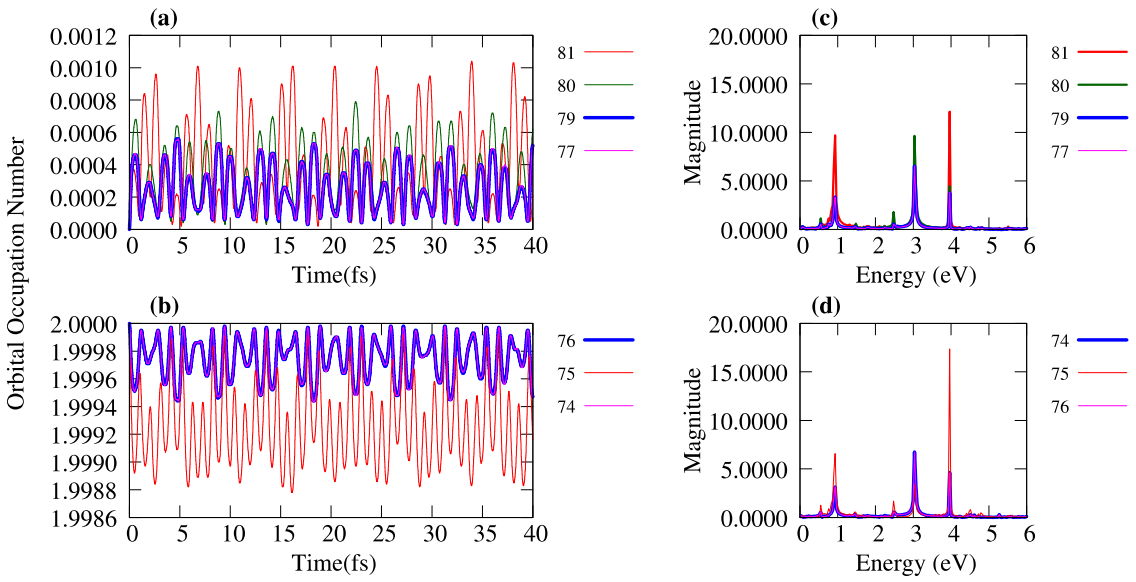

Figure B-3. Variation of (a) virtual and (b) occupied orbital occupation numbers of Ag_8; (c) and (d) corresponding Fourier transforms.

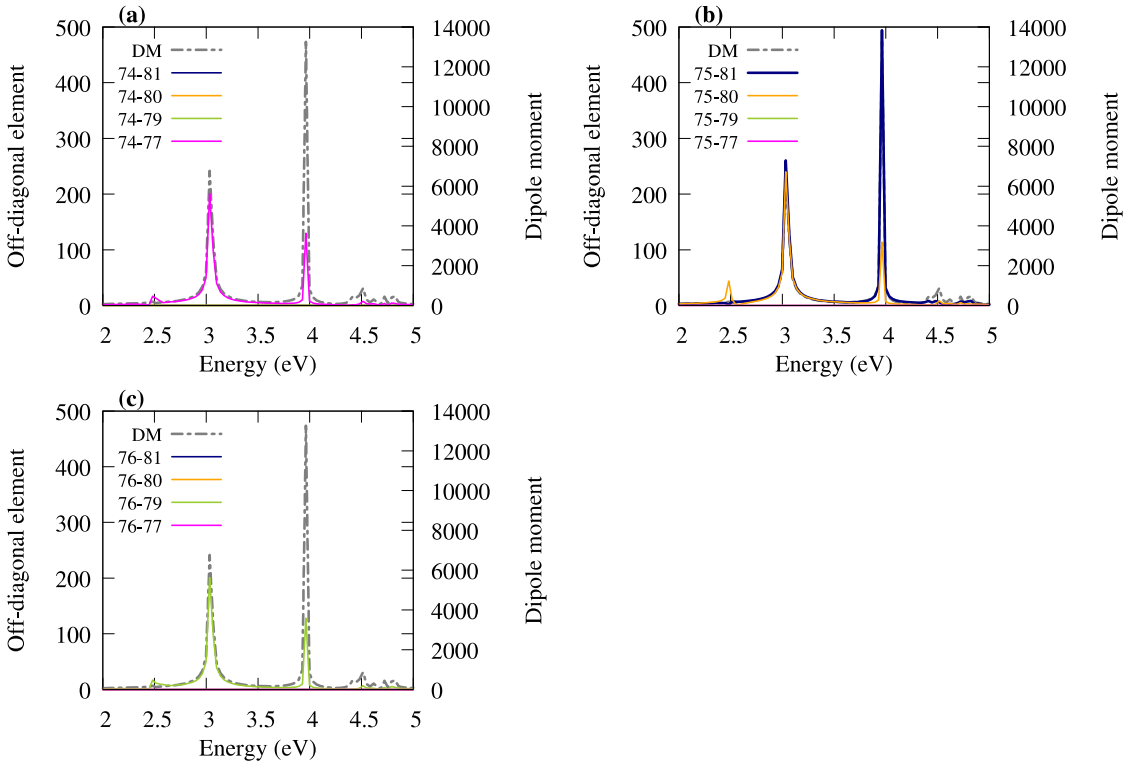

Figure B-4. Fourier transforms of time-dependent off-diagonal density matrix elements from Ag_8 real-time propagation. Density matrix elements corresponding to transitions from occupied levels (a) 74, (b) 75, and (c) 76 to selected unoccupied levels are shown. Peak positions are compared with the Fourier transform of the dipole moment (DM) variation during RT-TDDFT (grey dashed line).

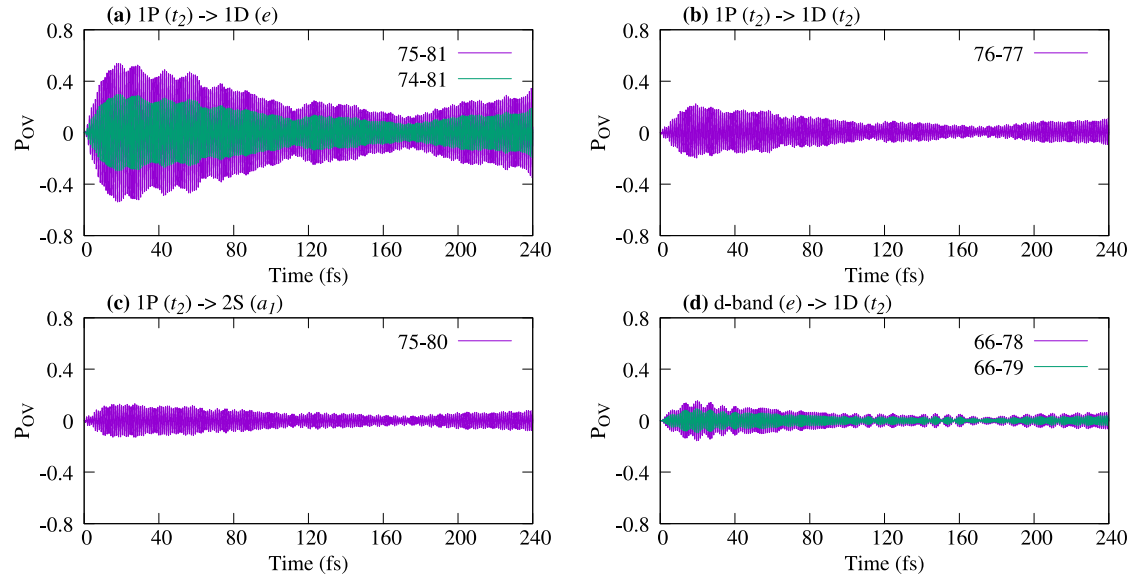

Figure B-5. Variation of density matrix elements oscillating with a frequency corresponding to 4.03 eV. P_{OV} corresponding to transitions between (a) 1P (t_2) and 1D (e); (b) 1P (t_2) and 1D (t_2); (c) 1P (t_2) and 2S (a_1); (d) d-band (e) and 1D (t_2) orbitals. The continuous wave electric field is applied with a frequency of 3.96 eV.

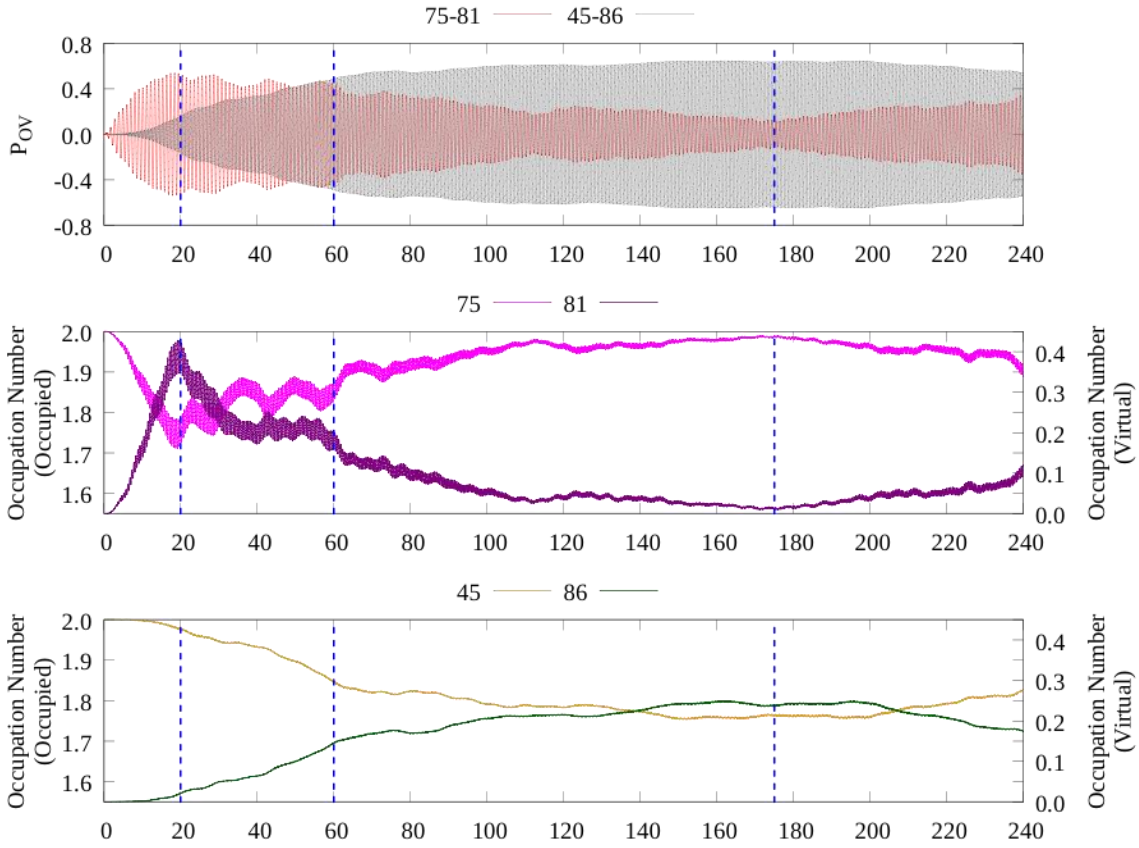

Figure B-6. Variation of $P_{75\text{-}81}$ and $P_{54\text{-}86}$ (top); occupation numbers in orbitals 75 and 81 (middle) and in orbitals 45 and 86 (bottom). The continuous wave electric field is applied with a frequency of 3.96 eV.

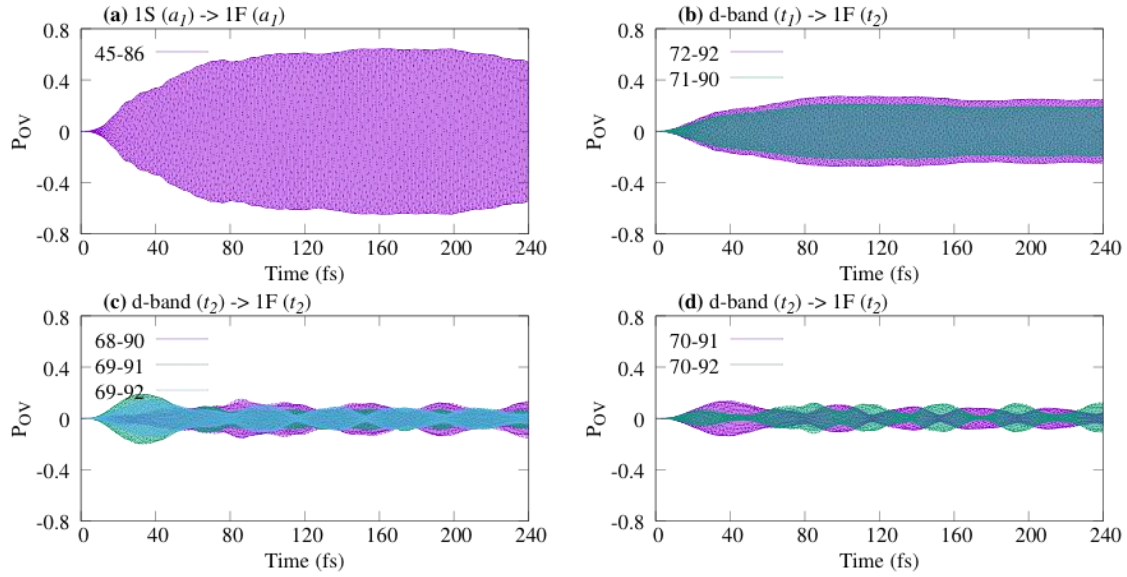

Figure B-7. Variation of density matrix elements oscillating with a frequency corresponding to 8.07 eV. P_{OV} corresponding to transitions between (a) 1S (a_1) and 1F (a_1); (b) d-band (t_1) and 1F (t_2); (c), (d) d-band (t_2) and 1F (t_2) orbitals. The continuous wave electric field is applied with a frequency of 3.96 eV. Various (t_2) → (t_2) transitions are shown separately in (c) and (d) for clarity.

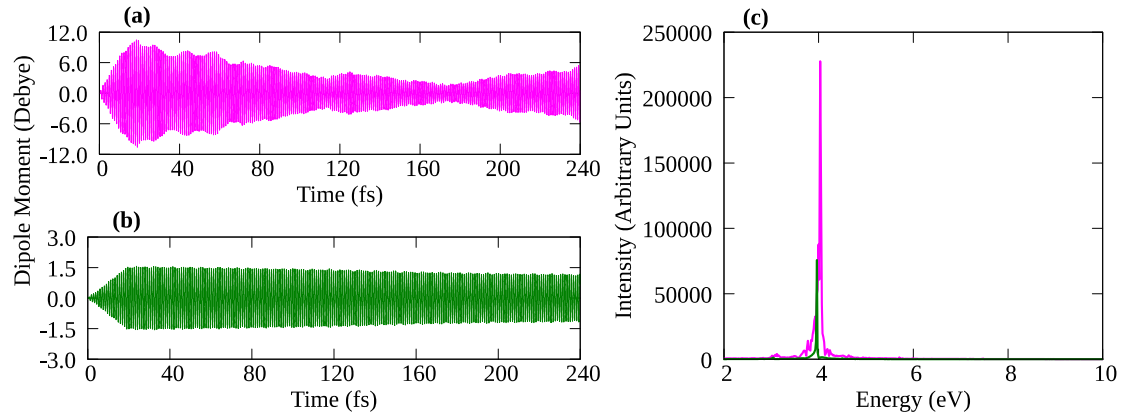

Figure B-8. Variation of dipole moment for the applied field strength (a) 0.001 a.u.; (b) 0.0001 a.u.; (c) corresponding Fourier transforms (pink: 0.001 a.u.; green: 0.0001 a.u.). The continuous wave electric field is applied with a frequency of 3.96 eV. Note that the y-axis in (b) is scaled down by a factor of 4 compared to that of (a).

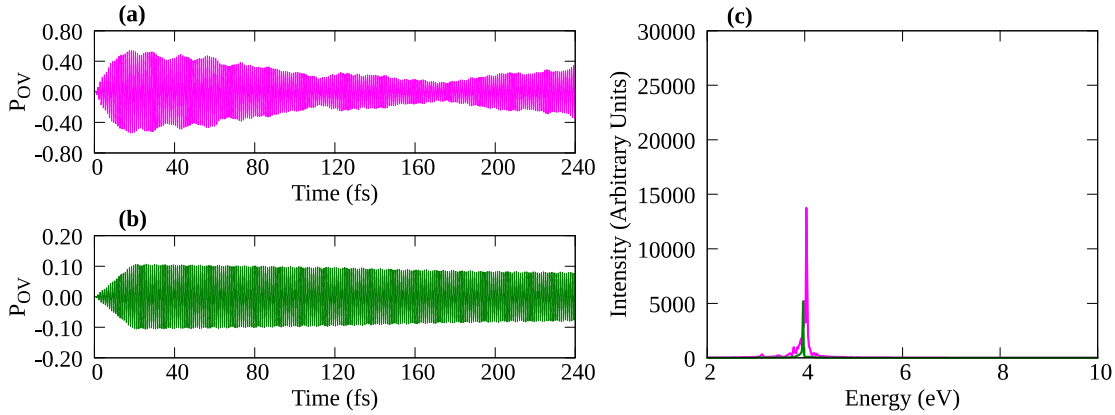

Figure B-9. Variation of density matrix elements corresponding to a one-photon allowed transition between occupied and virtual pairs 75-81 (1P – 1D) for the applied field strength (a) 0.001 a.u.; (b) 0.0001 a.u.; (c) corresponding Fourier transforms (pink: 0.001 a.u.; green: 0.0001 a.u.). The continuous wave electric field is applied with a frequency of 3.96 eV. Note that the y-axis in (b) is scaled down by a factor of 4 compared to that of (a).

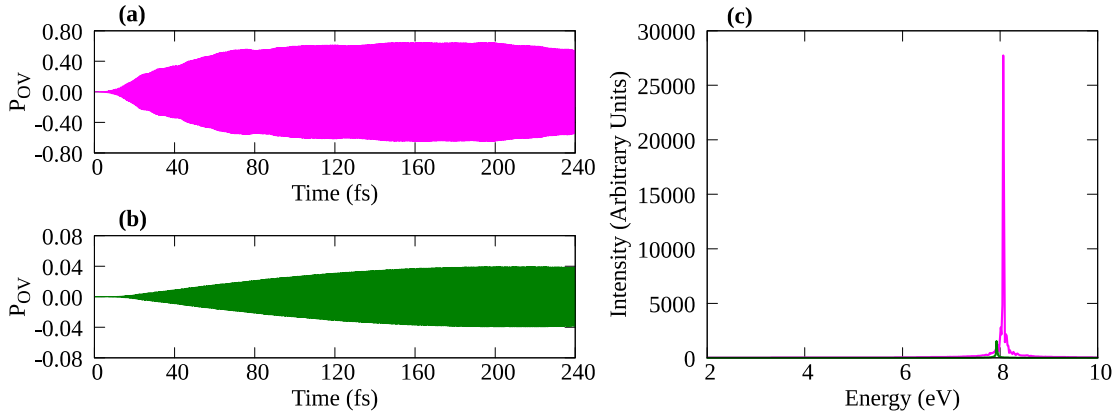

Figure B-10. Variation of density matrix elements corresponding to a two-photon allowed transition between occupied and virtual pairs 45-86 (1S – 1F) for the applied field strength (a) 0.001 a.u.; (b) 0.0001 a.u.; (c) corresponding Fourier transforms (pink: 0.001 a.u.; green: 0.0001 a.u.). The continuous wave electric field is applied with a frequency of 3.96 eV. Note that the y-axis in (b) is scaled down by a factor of 10 compared to that of (a).

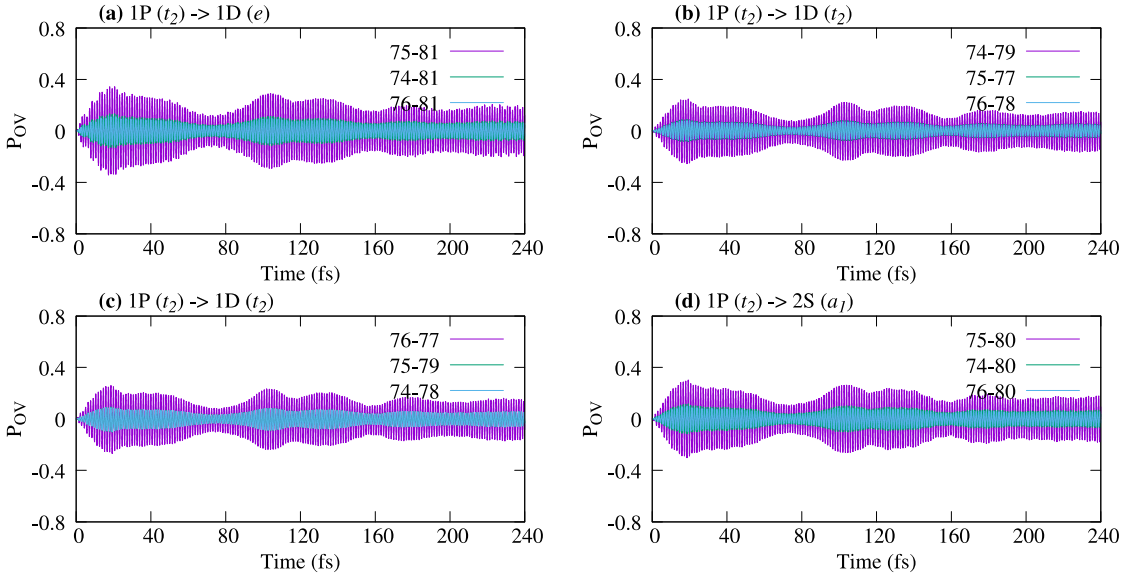

Figure B-11. Variation of density matrix elements oscillating with a frequency corresponding to 3.07 eV. P_{OV} corresponding to transitions between (a) 1P (t_2) and 1D (e); (b), (c) 1P (t_2) and 1D (t_2); (d) 1P (t_2) and 2S (a_1) orbitals. The continuous wave electric field is applied with a frequency of 3.05 eV. Various (t_2) → (t_2) transitions are shown separately in (b) and (c) for clarity.

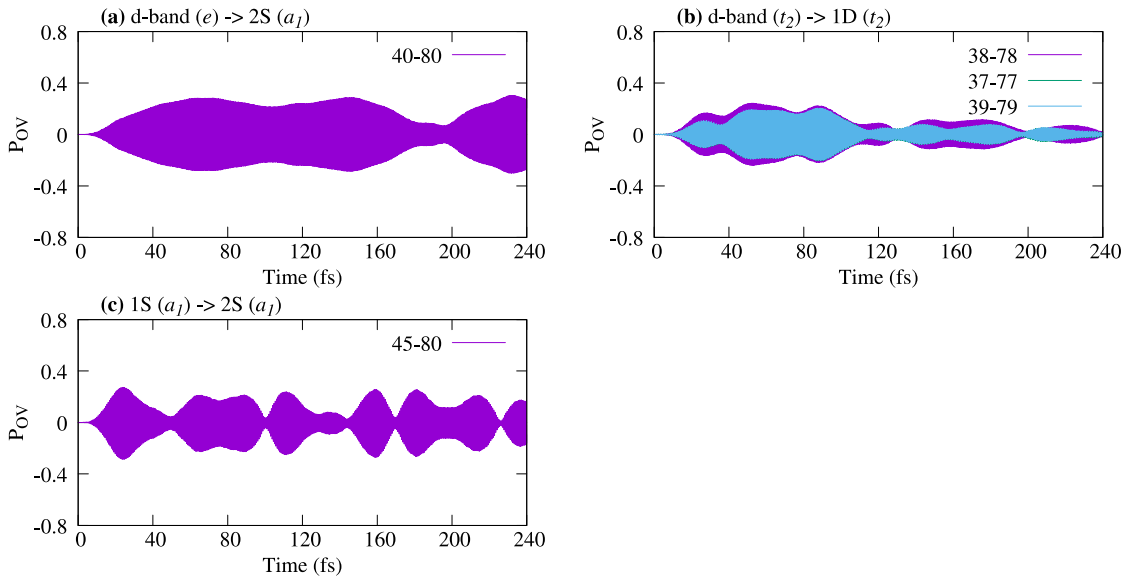

Figure B-12. Variation of density matrix elements oscillating with a frequency corresponding to 6.19 eV. P_{OV} corresponding to transitions between (a) d-band (*e*) and 2S (a_1); (b) d-band (t_1) and 1D (t_2); (c) 1S (a_1) and 2S (a_1) orbitals. The continuous wave electric field is applied with a frequency of 3.05 eV.

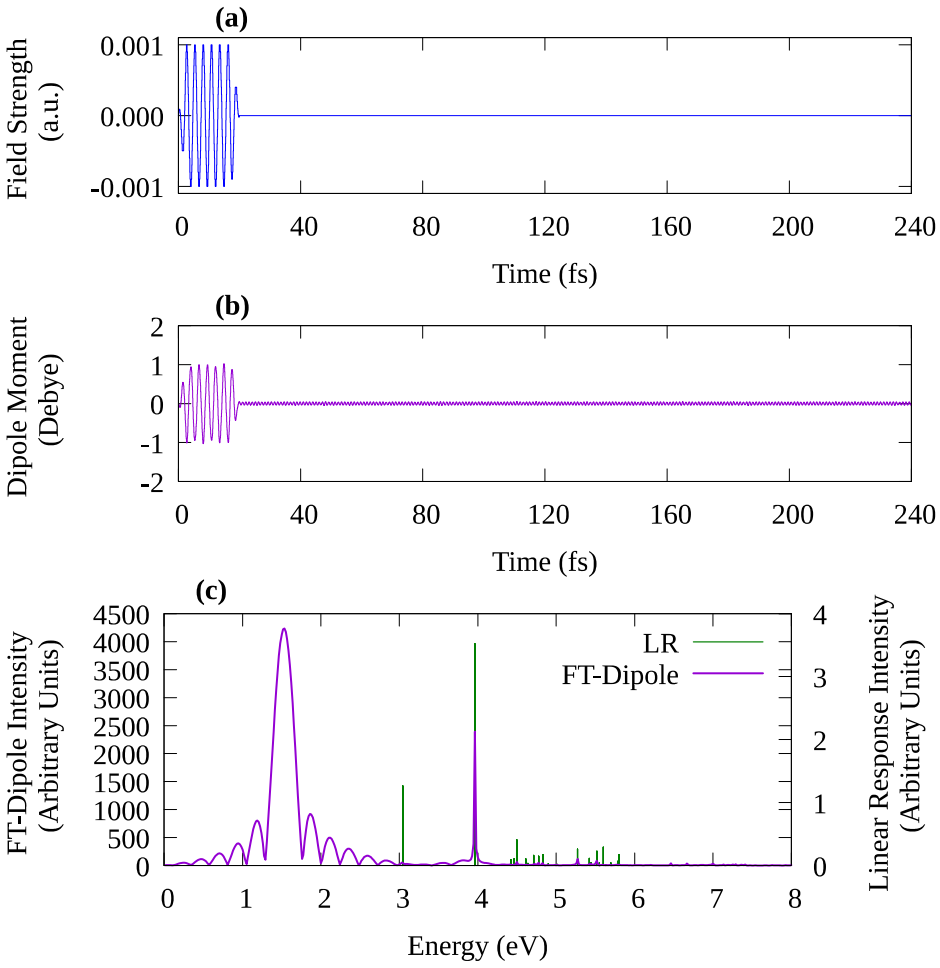

Figure B-13. Variation of (a) applied field, (b) dipole moment along z axis, and (c) Fourier transformed dipole moment (peak positions compared with the LR results in green sticks) for the continuous wave electric field oscillating with an energy of 1.525 eV.

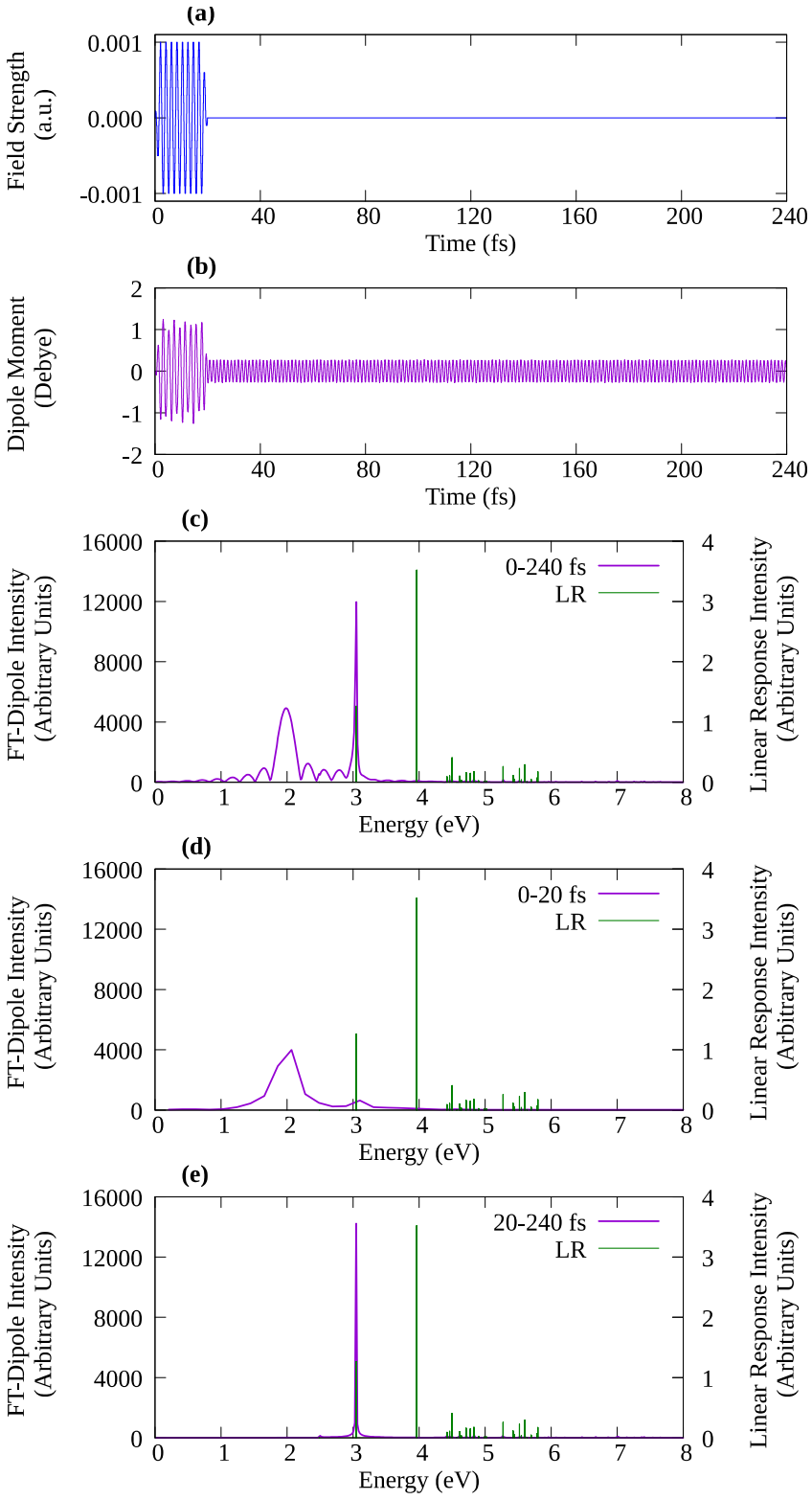

Figure B-14. Variation of (a) applied field, (b) dipole moment along z axis and (c, d, e) Fourier transformed dipole moment (peak positions compared with the LR results in green sticks) for the continuous wave electric field oscillating with an energy of 1.98 eV. Part (c)

shows the Fourier transform over the full 240 fs. Fourier transforms of the dipole moment are also shown for (d) the first 0-20 fs and (e) 20-240 fs.

Appendix C - Supporting Information for "Non-Linear Optical Properties in Silver Nanoclusters"

Table C-1. The molecular orbital transitions responsible for the excited state at 3.91 eV in Ag_{10}^{+2} (T_d) cluster and the weights calculated from LR-TDDFT. Ground-state point group symmetries of molecular orbitals are also listed.

State	Energy (eV)	Oscillator strength	Single-particle transitions	Symmetry	Direct product decomposition into irreducible representation	Weight
16	3.91	0.6295	84 → 95	$t_2 \rightarrow t_2$	$A_1 + E + T_1 + \boldsymbol{T_2}$	-0.10130
			85 → 97	$t_2 \rightarrow t_2$	$A_1 + E + T_1 + \boldsymbol{T_2}$	-0.10130
			91 → 96	$e \rightarrow t_2$	$T_1 + \boldsymbol{T_2}$	-0.13627
			92 → 98	$t_2 \rightarrow a_1$	$\boldsymbol{T_2}$	0.25445
			92 →100	$t_2 \rightarrow e$	$T_1 + \boldsymbol{T_2}$	0.46100
			93 → 95	$t_2 \rightarrow t_2$	$A_1 + E + T_1 + \boldsymbol{T_2}$	-0.25290
			94 → 97	$t_2 \rightarrow t_2$	$A_1 + E + T_1 + \boldsymbol{T_2}$	-0.25289
17	3.91	0.6295	84 → 96	$t_2 \rightarrow t_2$	$A_1 + E + T_1 + \boldsymbol{T_2}$	0.10130
			86 → 97	$t_2 \rightarrow t_2$	$A_1 + E + T_1 + \boldsymbol{T_2}$	0.10130
			91 → 95	$e \rightarrow t_2$	$T_1 + \boldsymbol{T_2}$	-0.11524
			92 → 97	$t_2 \rightarrow t_2$	$A_1 + E + T_1 + \boldsymbol{T_2}$	0.25291
			93 → 96	$t_2 \rightarrow t_2$	$A_1 + E + T_1 + \boldsymbol{T_2}$	0.25292
			94 → 98	$t_2 \rightarrow a_1$	$\boldsymbol{T_2}$	-0.25447
			94 → 99	$t_2 \rightarrow e$	$T_1 + \boldsymbol{T_2}$	0.39762
			94 →100	$t_2 \rightarrow e$	$T_1 + \boldsymbol{T_2}$	0.23339
18	3.91	0.6295	85 → 96	$t_2 \rightarrow t_2$	$A_1 + E + T_1 + \boldsymbol{T_2}$	-0.10130
			86 → 95	$t_2 \rightarrow t_2$	$A_1 + E + T_1 + \boldsymbol{T_2}$	-0.10130
			90 → 97	$e \rightarrow t_2$	$T_1 + \boldsymbol{T_2}$	-0.14520
			92 → 95	$t_2 \rightarrow t_2$	$A_1 + E + T_1 + \boldsymbol{T_2}$	-0.25289
			93 → 98	$t_2 \rightarrow a_1$	$\boldsymbol{T_2}$	0.25446
			93 → 99	$t_2 \rightarrow e$	$T_1 + \boldsymbol{T_2}$	0.40089
			93 →100	$t_2 \rightarrow e$	$T_1 + \boldsymbol{T_2}$	-0.22763
			94 → 96	$t_2 \rightarrow t_2$	$A_1 + E + T_1 + \boldsymbol{T_2}$	-0.25289

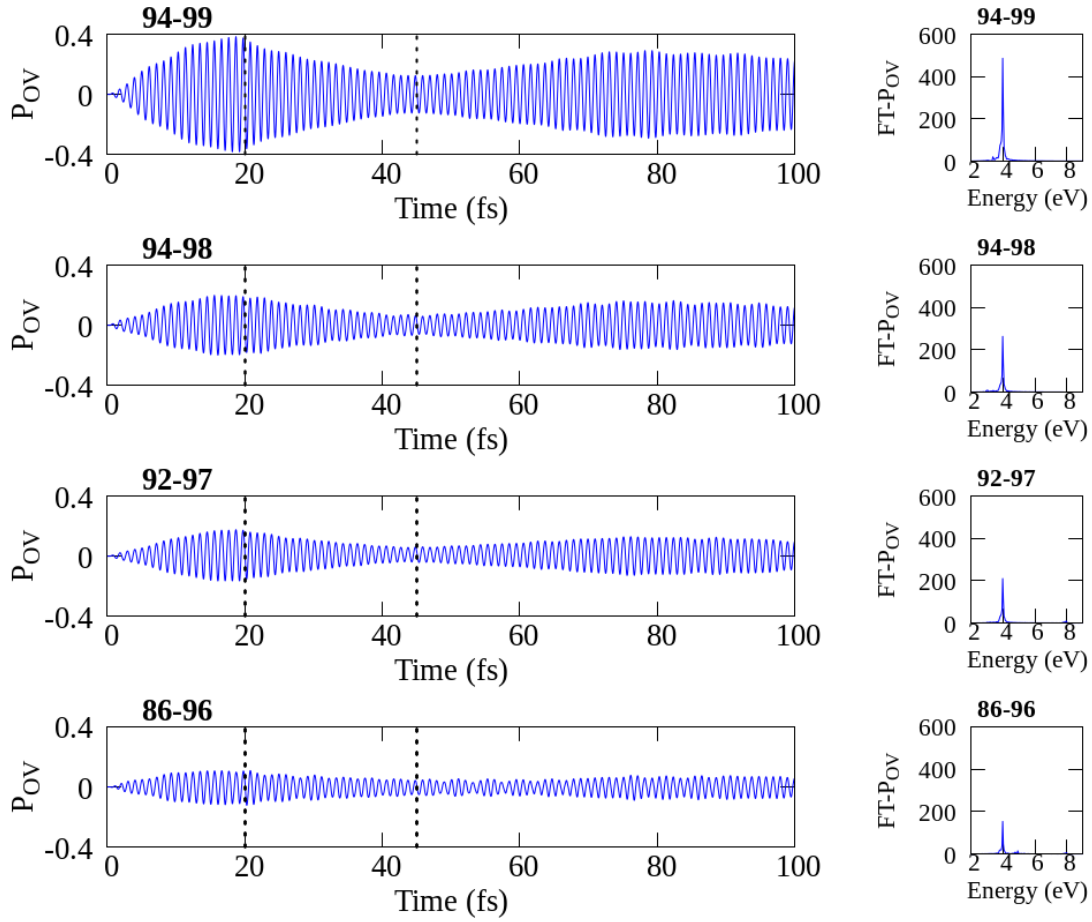

Figure C-1. Left: Variation of P_{OV} elements oscillating with resonant frequency (3.91 eV). Right: The corresponding Fourier transforms. The 3.91 eV state of Ag_{10}^{+2} (T_d) is activated.

Table C-2. Symmetry-adapted selection rules for one- and two-photon allowed transitions of 3.91 eV state in Ag_{10}^{+2} (T_d). The irreducible representations of allowed excitations are shown in bold. Ground-state point group symmetries of molecular orbitals are listed.

	Single-particle transitions	Symmetry	Direct product decomposition into irreducible representation
One-photon allowed	94 → 99	$t_2 \rightarrow e$	$T_1 + \mathbf{T_2}$
	92 → 97 86 → 96	$t_2 \rightarrow t_2$	$A_1 + E + T_1 + \mathbf{T_2}$
	94 → 98	$t_2 \rightarrow a_1$	$\mathbf{T_2}$
Two-photon allowed	78 → 104	$e \rightarrow a_1$	$\mathbf{E}$
	84 → 110 86 → 109	$t_2 \rightarrow t_2$	$\mathbf{A_1} + \mathbf{E} + T_1 + \mathbf{T_2}$
	84 → 108 87 → 109	$t_1 \rightarrow t_2$	$A_2 + \mathbf{E} + T_1 + \mathbf{T_2}$

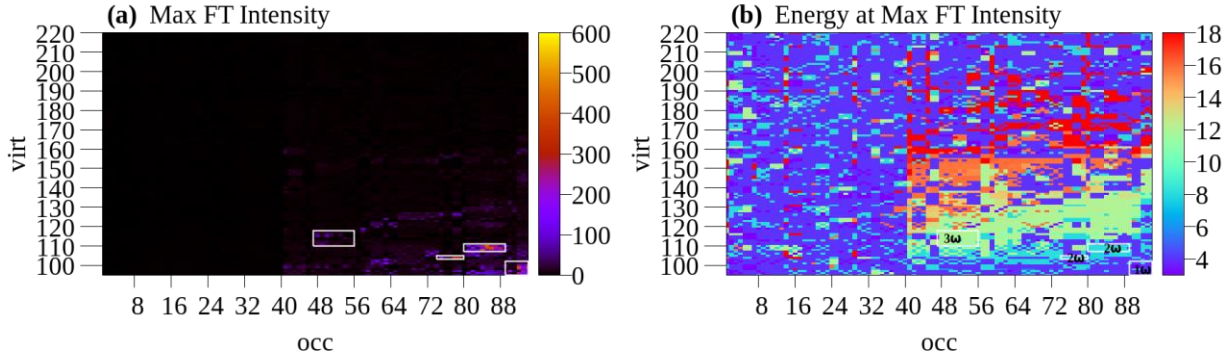

Figure C-2. Off-diagonal elements corresponding to the entire molecular orbital range in Ag_{10}^{+2} (T_d). (a) Maximum intensity of P_{OV} (ω) and (b) corresponding energy at maximum intensity when the 3.91 eV state of Ag_{10}^{+2} (T_d) is activated. Areas with strong intensities are highlighted in white boxes.

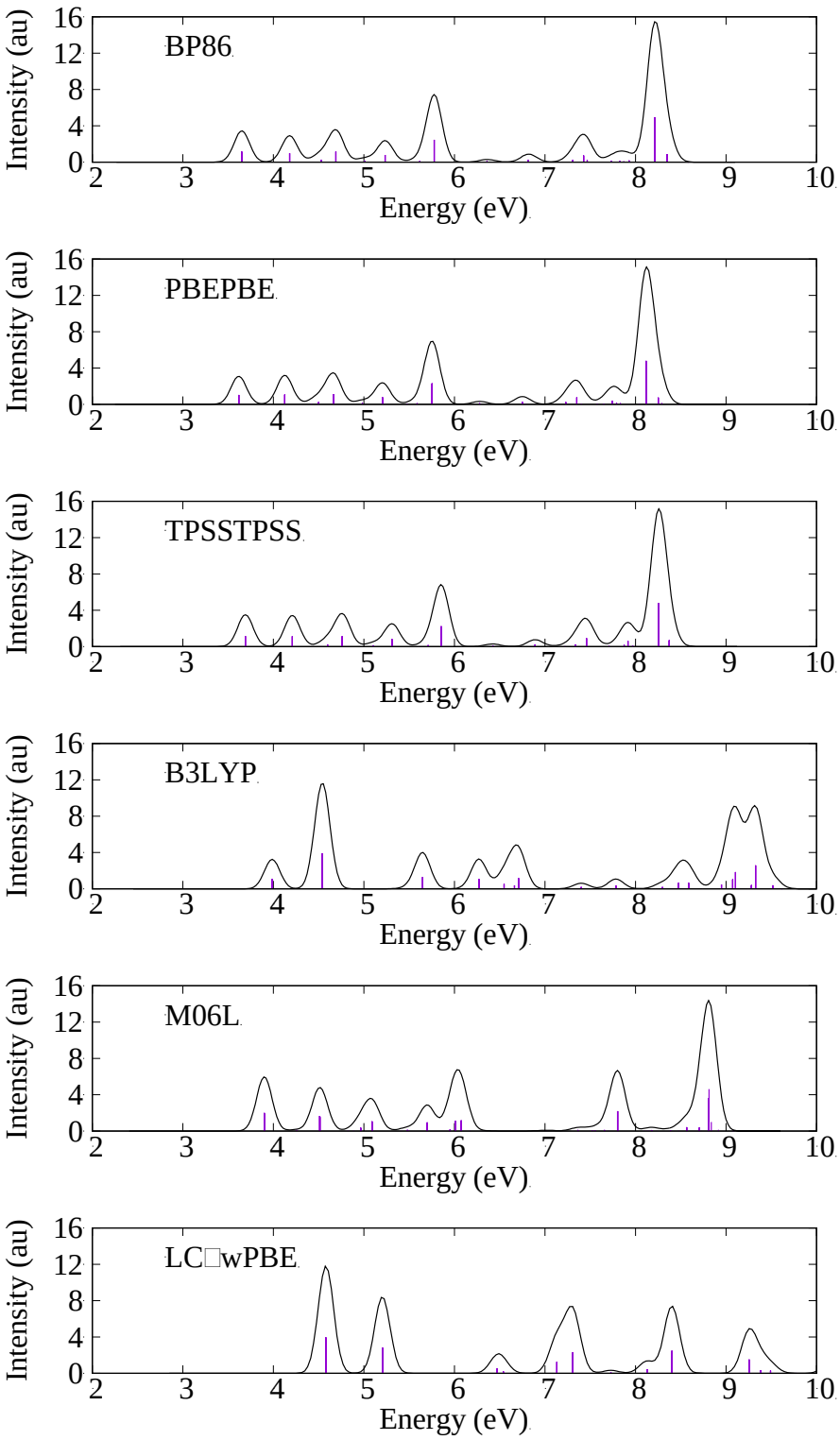

Figure C-3. Absorption spectra for Ag_{13}^{+5} (I_h) calculated with various exchange-correlation functionals.

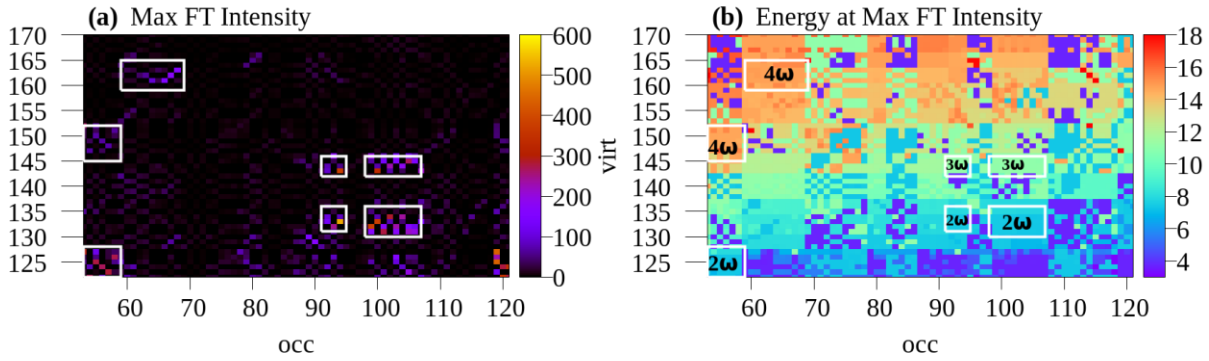

Figure C-4. (a) Maximum intensity of P_{OV} (ω) and (b) corresponding energy at maximum intensity when the 3.65 eV state of Ag_{13}^{+5} (I_h) is activated. Single-particle transitions with strong multiphoton absorption are highlighted in white rectangles.

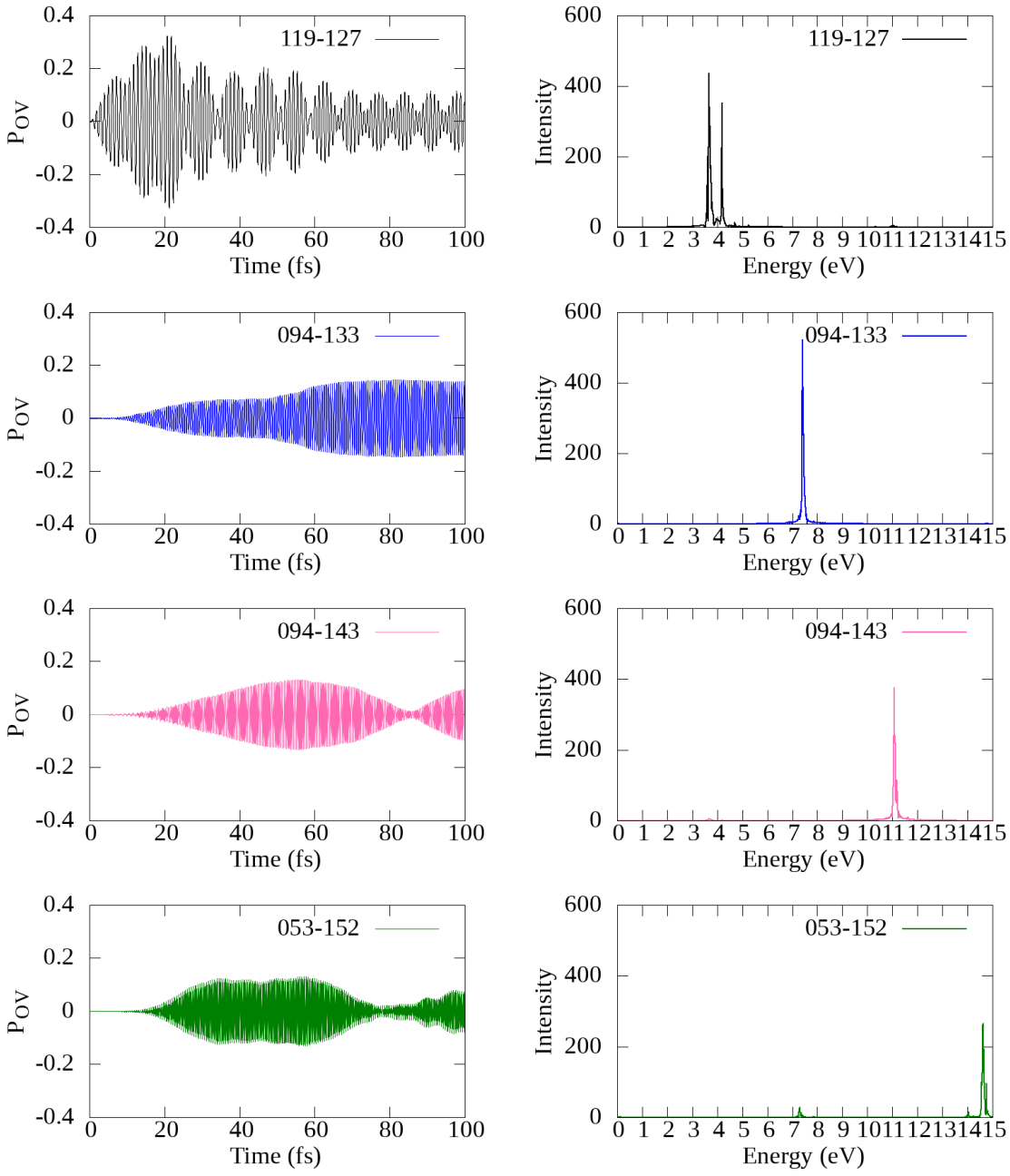

Figure C-5. Left: Variation of P_{OV} (t) elements oscillating with 1, 2, 3, and 4ω energy when the 3.65 eV state of Ag_{13}^{+5} (I_h) is activated. Right: Corresponding Fourier transforms.

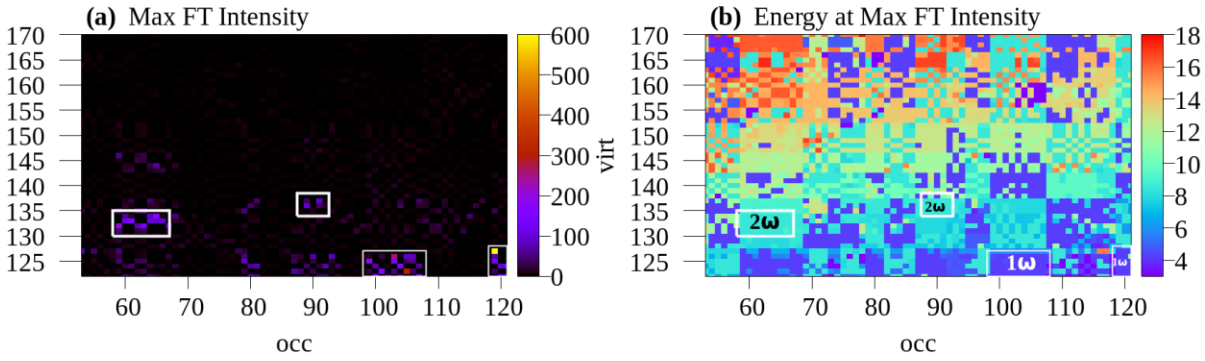

Figure C-6. (a) Maximum intensity of P_{OV} (ω) and (b) corresponding energy at maximum intensity when the 4.18 eV state of Ag_{13}^{+5} (I_h) is activated. Single-particle transitions with strong one-photon absorption and transitions with weaker two-photon absorption are highlighted in white rectangles.

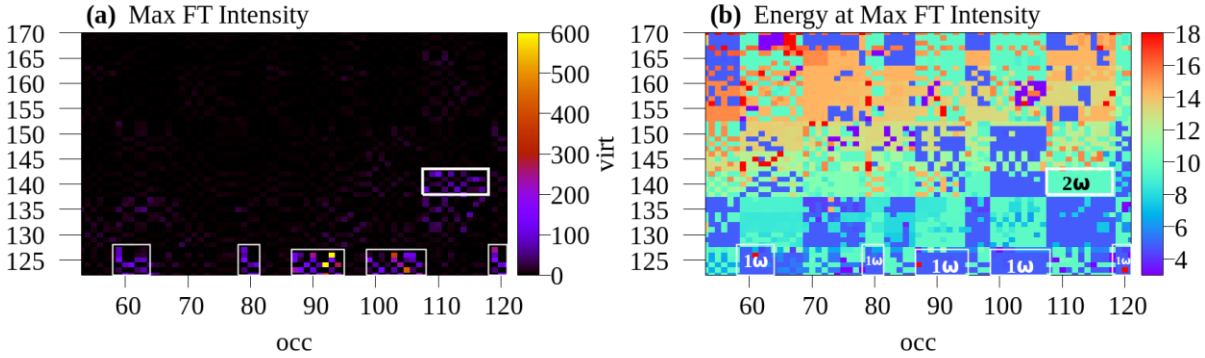

Figure C-7. (a) Maximum intensity of P_{OV} (ω) and (b) corresponding energy at maximum intensity when the 4.69 eV state of Ag_{13}^{+5} (I_h) is activated. Single-particle transitions with strong one-photon absorption and transitions with weaker two-photon absorption are highlighted in white rectangles.

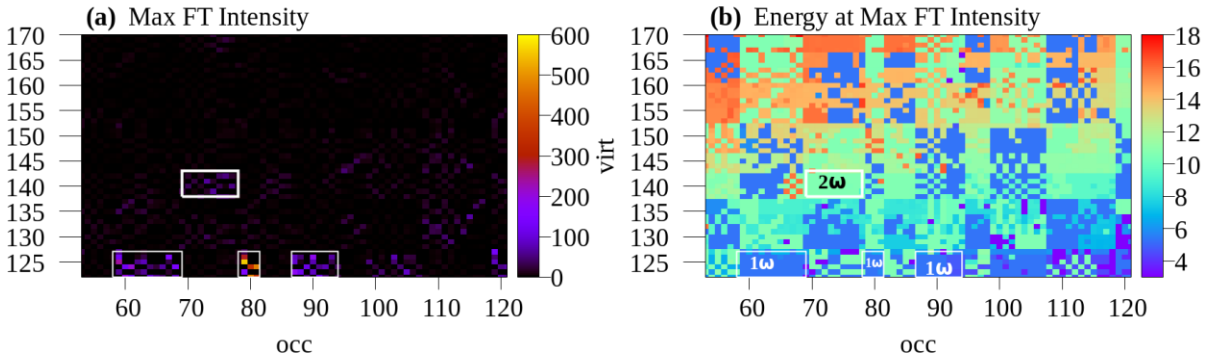

Figure C-8. (a) Maximum intensity of P_{OV} (ω) and (b) corresponding energy at maximum intensity when the 5.24 eV state of Ag_{13}^{+5} (I_h) is activated. Single-particle transitions with

strong one-photon absorption and transitions with weaker two-photon absorption are highlighted in white rectangles.

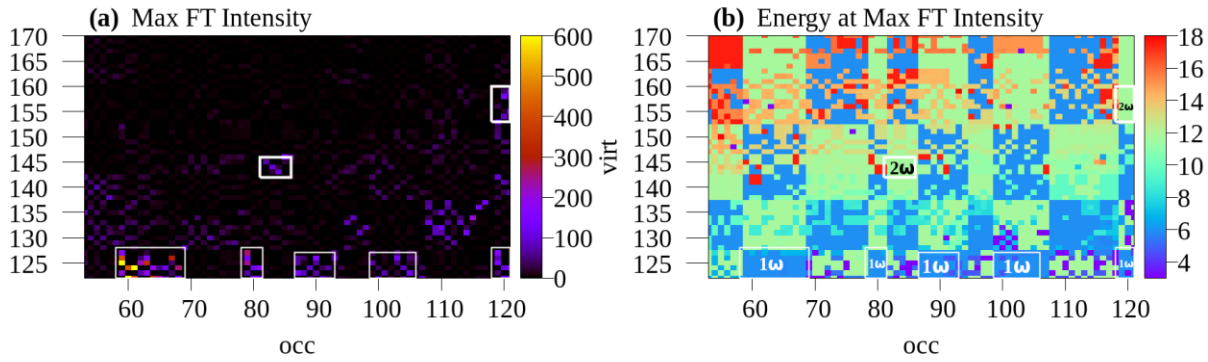

Figure C-9. (a) Maximum intensity of P_{OV} (ω) and (b) corresponding energy at maximum intensity when the 5.78 eV state of Ag_{13}^{+5} (I_h) is activated. Single-particle transitions with strong one-photon absorption and transitions with weaker two-photon absorption are highlighted in white rectangles.

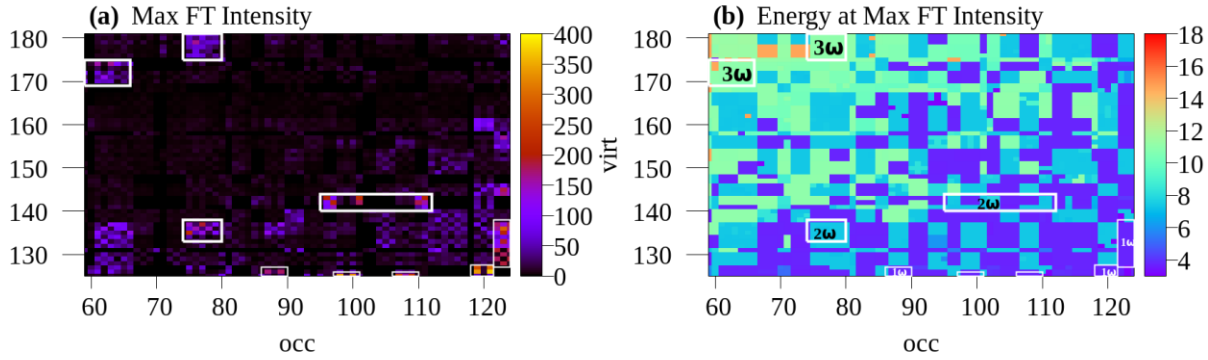

Figure C-10. (a) Maximum intensity of P_{OV} (ω) and (b) corresponding energy at maximum intensity when the 3.58 eV state of Ag_{13}^{-1} (O_h) is activated. Single- particle transitions with strong one-, two-, and three-photon absorption are highlighted in white rectangles.

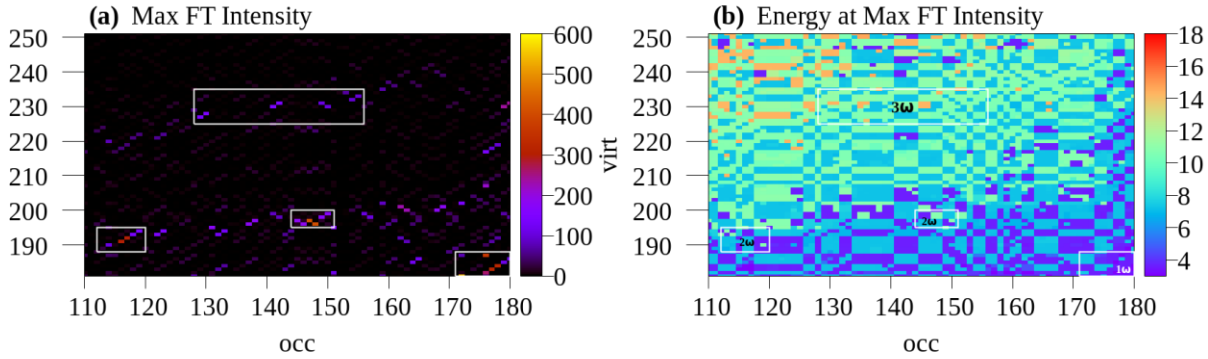

Figure C-11. (a) Maximum intensity of P_{OV} (ω) and (b) corresponding energy at maximum intensity when the 3.51 eV state (longitudinal) of Ag_{19}^{-1} (D_{5h}) is activated. Single-particle transitions with one- and two-photon absorption (strong) and three-photon absorption (weak) are highlighted in white rectangles.

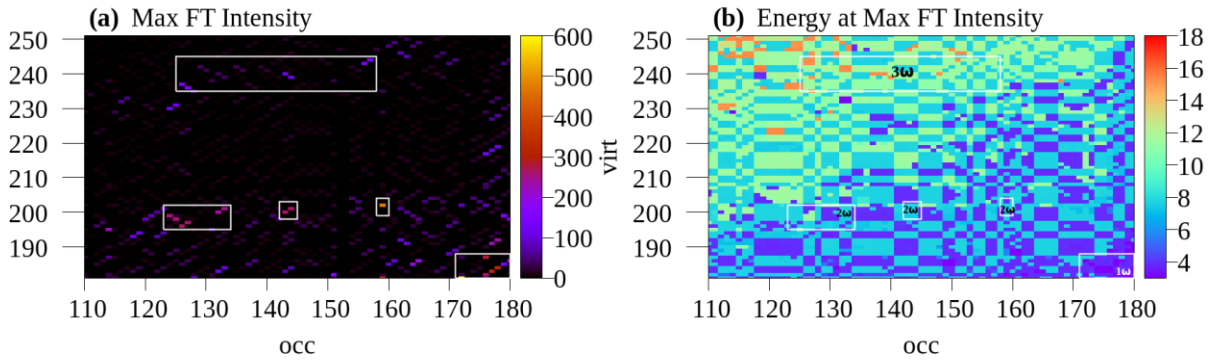

Figure C-12. (a) Maximum intensity of P_{OV} (ω) and (b) corresponding energy at maximum intensity when the 3.76 eV state (longitudinal) of Ag_{19}^{-1} (D_{5h}) is activated. Single-particle transitions with one- and two-photon absorption (strong) and three-photon absorption (weak) are highlighted in white rectangles.

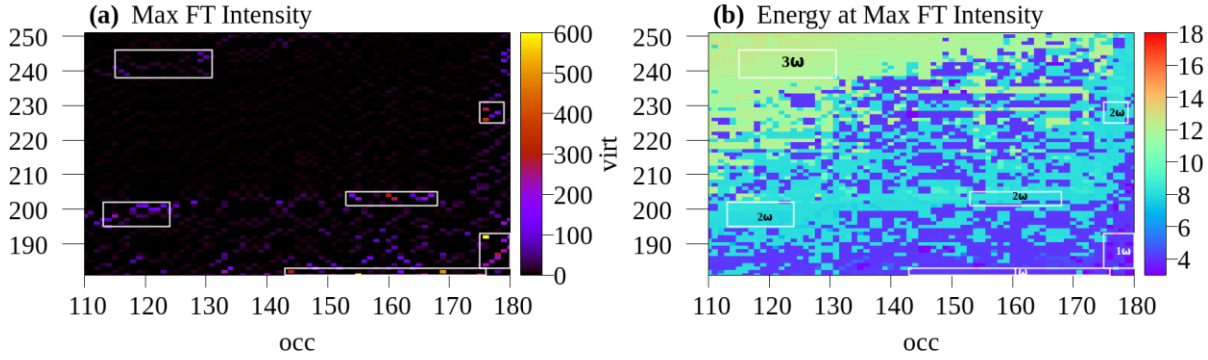

Figure C-13. (a) Maximum intensity of P_{OV} (ω) and (b) corresponding energy at maximum intensity when the 3.99 eV state (transverse) of Ag_{19}^{-1} (D_{5h}) is activated. Single-particle transitions with one- and two-photon absorption (strong) and three-photon absorption (weak) are highlighted in white rectangles.

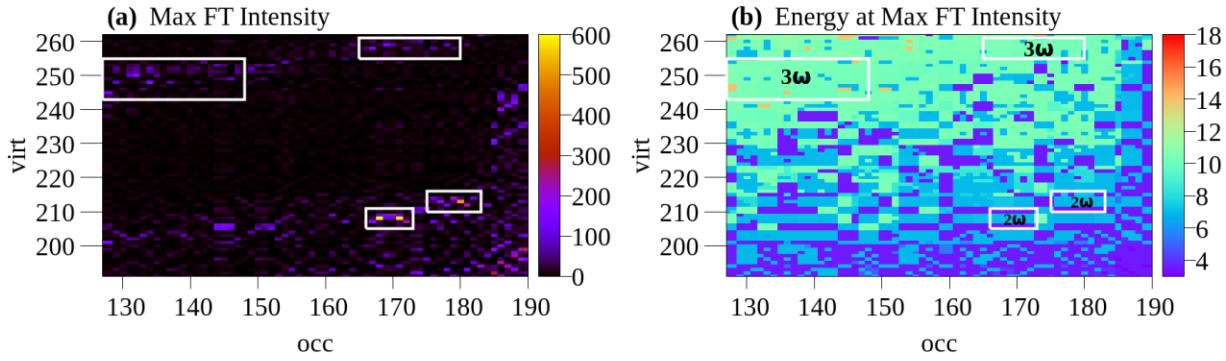

Figure C-14. (a) Maximum intensity of P_{OV} (ω) and (b) corresponding energy at maximum intensity when the 3.41 eV state of Ag_{20} (T_d) is activated. Single-particle transitions with strong two- and weaker three-photon absorption are highlighted in white boxes.

Table C-3. The molecular orbital transitions responsible for the excited states at 3.27, 3.39, and 3.56 eV in Ag_{55}^{-3} (I_h) cluster, with their weights calculated from LR-TDDFT. Three types of transitions that make mutual contributions to the plasmon-like state at 3.27 eV were found and are colored in purple ($a_g \rightarrow t_{1u}$), green ($t_{1u} \rightarrow t_{1g}$), and red ($g_g \rightarrow t_{2u}$). Even though these single-particle transitions do not necessarily follow the spherical symmetry rules due to the symmetry breaking, they do follow the symmetry rules within the icosahedral point group symmetry.

3.27 eV		3.39 eV		3.56 eV	
Single-particle transitions	Weight	Single-particle transitions	Weight	Single-particle transitions	Weight
State 557 f = 2.8596		State 595 f = 0.1212		State 663 f = 0.7961	
505 → 533	-0.12007	513 → 552	-0.1386	505 -> 531	-0.30361
511 → 528	-0.10055	514 → 554	-0.10616	505 -> 533	-0.13381
513 → 552	0.15095	515 → 554	-0.12192	513 -> 552	0.31415
514 → 528	0.10123	521 → 581	-0.16649	513 -> 553	0.1156
514 → 554	0.1089	522 → 581	0.16526	513 -> 556	-0.11043
515 → 554	0.13395	523 → 580	0.28998	514 -> 558	0.10282
521 → 534	-0.10106	524 → 579	0.50878	515 -> 554	0.32922
523 → 580	0.10573	524 → 580	0.11357		
524 → 541	-0.10554				
524 → 579	0.19186				
State 558 f = 2.8587		State 595 f = 0.1207		State 664 f = 0.7962	
505 → 531	0.12012	513 → 553	0.13854	505 -> 531	0.13358
513 → 553	-0.15093	514 → 554	-0.12194	505 -> 533	-0.30365
514 → 554	0.13388	515 → 554	0.1063	513 -> 552	0.11547
515 → 554	-0.10892	521 → 581	0.48759	513 -> 553	-0.31408
516 → 531	-0.11101	522 → 581	0.1645	513 -> 557	0.11029
520 → 538	-0.10142	523 → 579	-0.32231	514 -> 554	0.32947
521 → 581	0.17851	523 → 580	0.15237		
523 → 579	-0.1236	524 → 580	-0.15758		
State 559 f = 2.8574		State 595 f = 0.1215		State 665 f = 0.8003	
505 → 532	0.12566	514 → 552	-0.15934	505 -> 532	0.3314
514 → 552	0.17012	515 → 553	-0.15956	513 -> 555	-0.10273
515 → 553	0.17016	521 → 579	-0.20001	514 -> 552	0.32936
519 → 536	0.11317	521 → 580	-0.11324	514 -> 556	0.11351
522 → 580	0.1911	522 → 580	0.50766	515 -> 553	0.32906
523 → 581	0.11475	523 → 581	0.30905	515 -> 557	0.11351
		524 → 581	0.10052	522 -> 580	0.10207

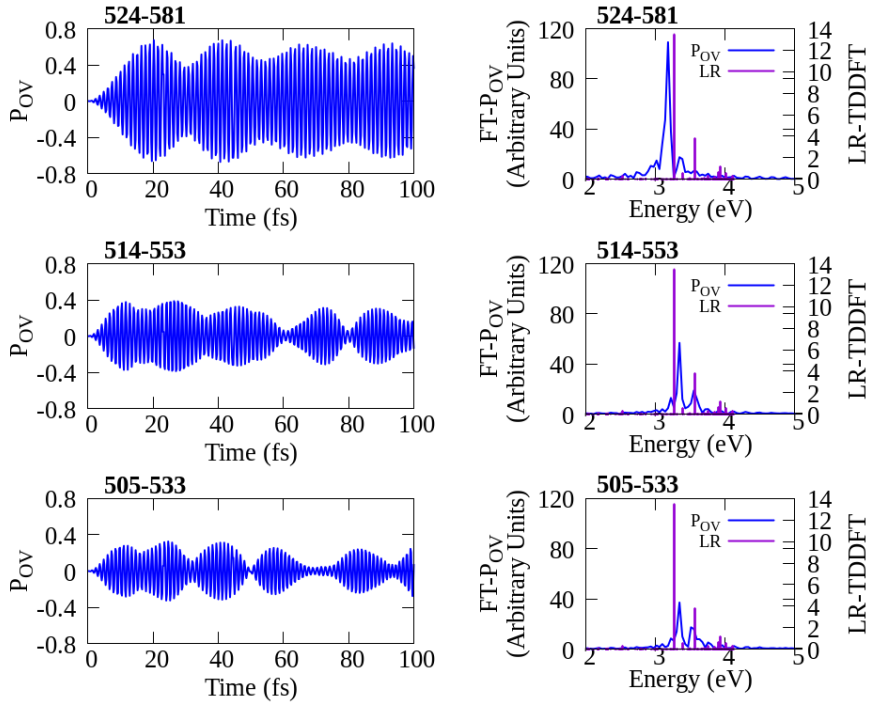

Figure C-15. Left: Variation of P_{OV} (t) elements in Ag_{55}^{-3} (I_h) corresponding to the single-particle transitions that are mutually contributing to the 3.27, 3.39, and 3.56 eV states. Right: The corresponding Fourier transforms. The Ag_{55}^{-3} (I_h) is excited with the 3.27 eV state.

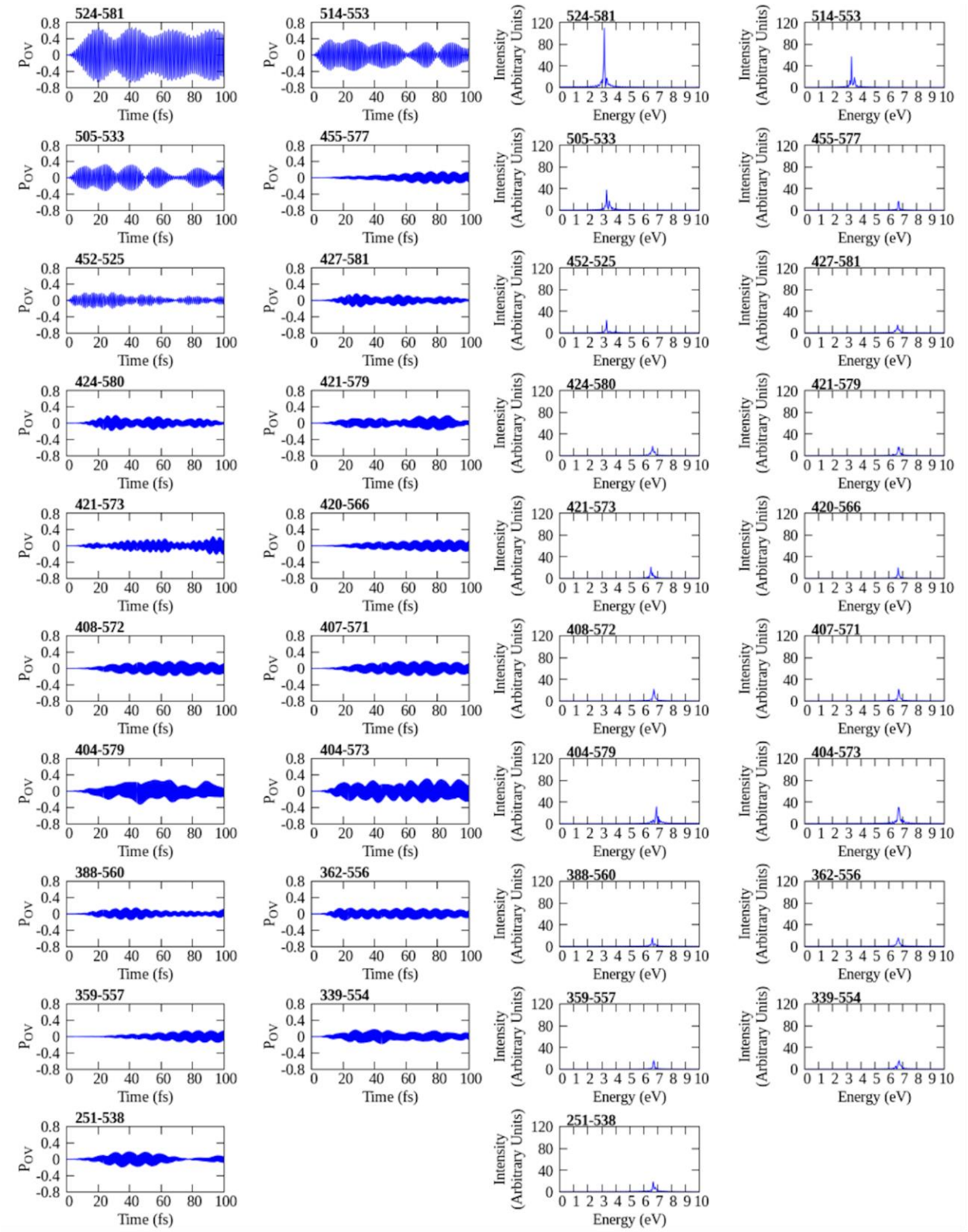

Figure C-16. Variation of selected P_{OV} (t) elements and their Fourier transforms P_{OV} (ω), when Ag_{55}^{-3} (I_h) the 3.27 eV state is excited by a resonant electric field.

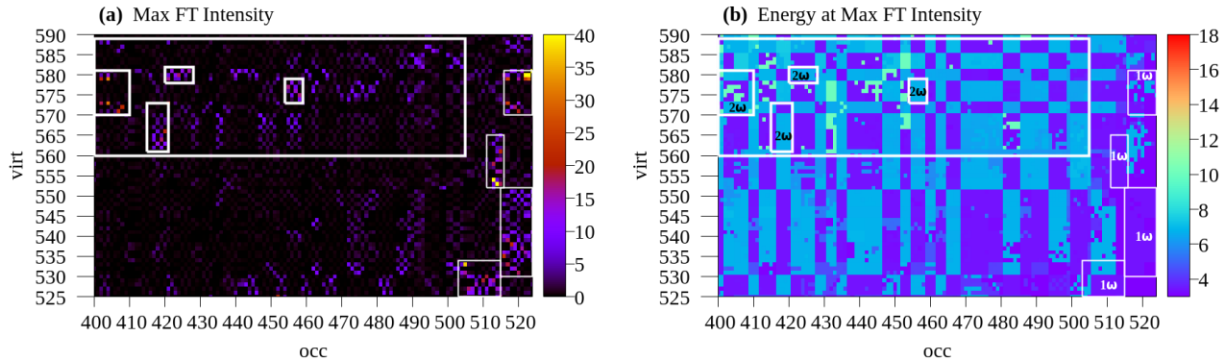

Figure C-17. (a) Maximum intensity of P_{OV} (ω) and (b) corresponding energy at maximum intensity when the 3.27 eV state of Ag_{55}^{-3} (I_h) is activated. Single-particle transitions with one- and two-photon absorption are highlighted in white rectangles.

Appendix D - Supporting Information for "Ultrafast Nonradiative Decay of a Dipolar Plasmon-like State in Naphthalene"

Table D-1. Optimized coordinates of naphthalene at the B3LYP/6-31G(d,p) level of theory

H	-1.245080	0.000000	3.377170
C	-0.708340	0.000000	2.433020
H	-2.489500	0.000000	1.242170
C	-1.402480	0.000000	1.244600
C	1.402480	0.000000	1.244600
C	-0.716870	0.000000	0.000000
C	0.708340	0.000000	2.433020
C	0.716870	0.000000	0.000000
C	-1.402480	0.000000	-1.244600
H	1.245080	0.000000	3.377170
H	2.489500	0.000000	-1.242170
H	2.489500	0.000000	1.242170
C	-0.708340	0.000000	-2.433020
H	-2.489500	0.000000	-1.242170
H	-1.245080	0.000000	-3.377170
C	0.708340	0.000000	-2.433020
H	1.245080	0.000000	-3.377170
C	1.402480	0.000000	-1.244600

Table D-2. MO transitions responsible for the α peak, β peak, three p-band peaks and the 6th excited state for the equilibrium geometry of naphthalene at the B3LYP/6-31G(d,p) level of theory.

Classification	Energy (eV)	Wavelength (nm)	Oscillator strength	Transitions	Weight
p-band 1	4.46	278.18	0.0603	HOMO – 1 → LUMO + 1	0.157
				HOMO → LUMO	0.685
α peak	4.52	274.27	0.0002	HOMO – 1 → LUMO	0.505
				HOMO → LUMO + 1	-0.493
β peak	6.10	203.20	1.2078	HOMO – 1 → LUMO	0.493
				HOMO → LUMO + 1	0.506
p-band 2	6.26	197.94	0.1821	HOMO – 2 → LUMO + 2	0.161
				HOMO – 1 → LUMO + 1	0.673
				HOMO → LUMO	-0.139
6th Excited State	6.37	194.71	0.0000	HOMO – 3 → LUMO	0.125
				HOMO – 2 → LUMO + 1	0.498
				HOMO – 1 → LUMO + 2	-0.480
p-band 3	8.22	150.74	0.4716	HOMO – 2 → LUMO + 2	0.679
				HOMO – 1 → LUMO + 1	-0.138
				HOMO → LUMO	0.113

Table D-3. Normal modes of naphthalene, their symmetry representations, and their energies

Mode	Symmetry	Energy		Mode	Symmetry	Energy	
		(cm^{-1})	(eV)			(cm^{-1})	(eV)
1	B_{2u}	176.57	0.022	25	B_{3u}	1154.58	0.143
2	A_u	189.61	0.024	26	B_{2g}	1177.30	0.146
3	B_{3u}	364.09	0.045	27	B_{1u}	1178.05	0.146
4	B_{3g}	397.05	0.049	28	A_g	1189.20	0.147
5	B_{1g}	481.18	0.060	29	B_{1u}	1240.97	0.154
6	B_{2u}	491.96	0.061	30	B_{2g}	1272.80	0.158
7	B_{2g}	517.83	0.064	31	B_{3u}	1291.69	0.160
8	A_g	520.51	0.065	32	B_{1u}	1407.82	0.175
9	A_u	633.74	0.079	33	A_g	1415.74	0.176
10	B_{1u}	634.99	0.079	34	B_{3u}	1424.94	0.177
11	B_{3g}	734.91	0.091	35	B_{2g}	1501.48	0.186
12	A_g	776.04	0.096	36	A_g	1502.53	0.186
13	B_{1g}	784.42	0.097	37	B_{1u}	1562.44	0.194
14	B_{2u}	803.36	0.100	38	A_g	1628.24	0.202
15	B_{3u}	807.57	0.100	39	B_{3u}	1655.90	0.205
16	A_u	853.64	0.106	40	B_{2g}	1686.24	0.209
17	B_{1g}	899.19	0.111	41	B_{2g}	3173.11	0.393
18	B_{2g}	947.96	0.118	42	B_{3u}	3174.91	0.394
19	B_{3g}	951.78	0.118	43	B_{1u}	3176.77	0.394
20	B_{2u}	968.40	0.120	44	A_g	3180.25	0.394
21	A_u	989.08	0.123	45	B_{2g}	3191.63	0.396
22	B_{1g}	997.04	0.124	46	B_{3u}	3192.82	0.396
23	B_{1u}	1042.85	0.129	47	B_{1u}	3204.69	0.397
24	A_g	1053.49	0.131	48	A_g	3205.87	0.397

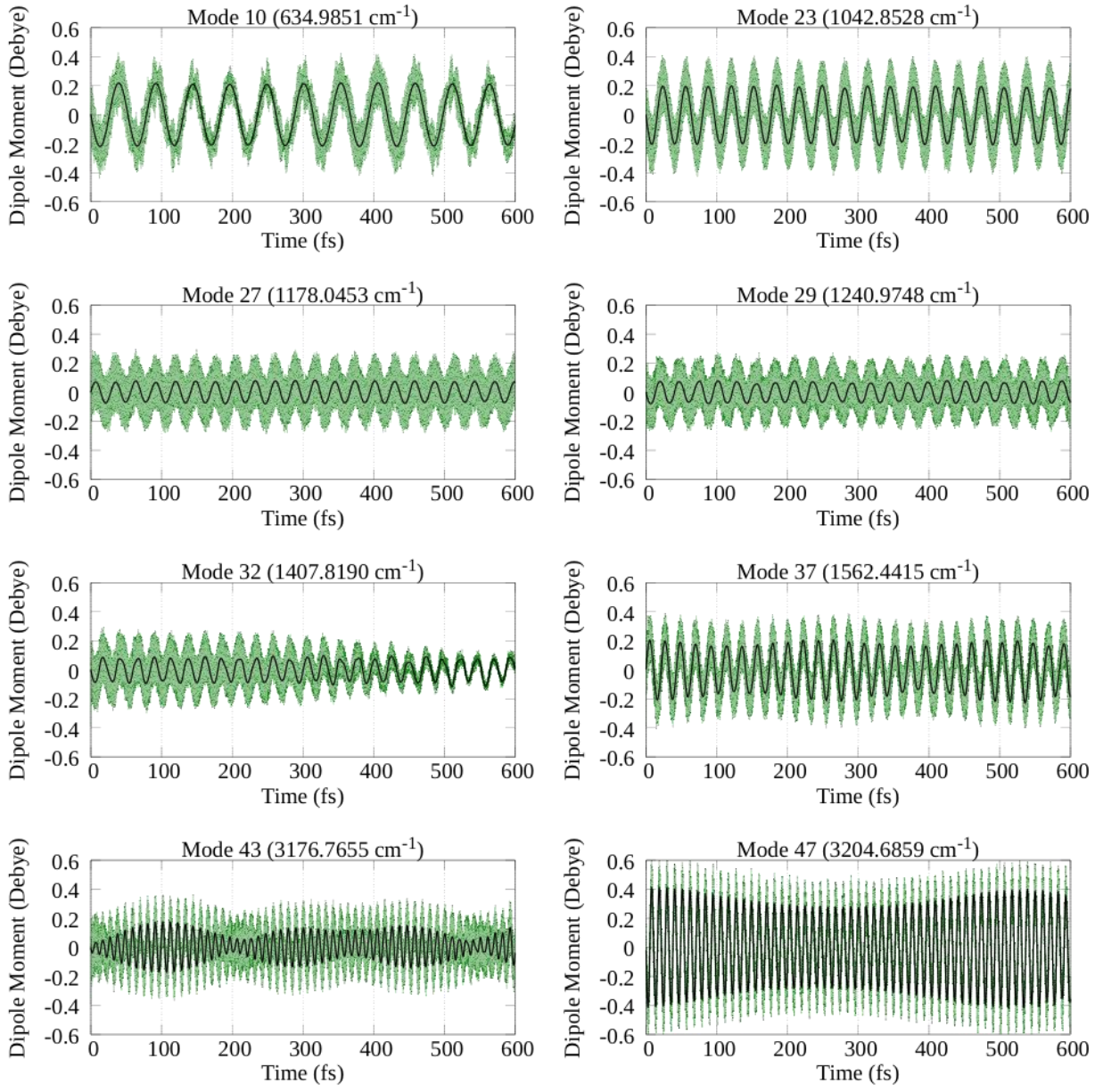

Figure D-1. Variation of the *z*-component of the dipole moment for B_{1u} normal modes of naphthalene. Green: Average dipole moment during an Ehrenfest dynamics with electrons excited along the *z* direction and black: Born-Oppenheimer molecular dynamics (BOMD) in the ground electronic state.

Symmetry-adapted selection rules for pure electronic transitions and vibronic transitions[191]

The intensity of a transition from state *i* to state *j* is given by eq S1 where $\hat{\mu}$ is the transition dipole moment operator and ψ_i and ψ_j are the initial and final electronic wave functions respectively. Note that to a first approximation, the total wavefunction Ψ for a molecule can be written as a product of an electronic wavefunction ψ_e, a vibrational wavefunction ψ_v, and a rotational wave function ψ_r ($\Psi = \psi_e \cdot \psi_v \cdot \psi_r$). Assuming that the three wavefunctions are independent from each other, the wave equation can be simplified into three different equations. Under this assumption, for an electronic transition to be allowed, the integral $\int \psi_i \hat{\mu} \psi_j d\tau$ should be nonzero for the initial and final electronic states and the dipole polarization direction *x*, *y* or *z*. According to the symmetry-adapted selection rules, this integral will be nonzero if the direct product of the point group representations of the initial and final electronic wavefunctions and the transition dipole moment operator contains the totally symmetric representation. Since the initial electronic state is totally symmetric, the electric dipole transition will be allowed with *x*, *y* or *z* polarization if the final state shares the same representation as the *x*, *y* or *z* linear functions, respectively. For instance, in the D_{2h} point group, the totally symmetric initial state belongs to the A_g representation and the *x*, *y* and *z* linear functions independently belong to the B_{3u}, B_{2u} and B_{1u} representations respectively. When the β peak is excited, which belongs to the B_{1u} representation, dipole response only along the *z* axis can be expected from the above selection rules.

$$I \propto \int \psi_i \hat{\mu} \psi_j d\tau \qquad (S1)$$

If the initial and final states account for coupling of the electronic (*e*) and vibrational (*v*) wavefunctions, the integral would now look like eq S2. Since both the ground electronic and vibrational wavefunctions are totally symmetric, the symmetries of both the excited electronic and vibrational states must be considered.

$$\int (\psi_i^e \psi_i^v) \hat{\mu} (\psi_j^e \psi_j^v) d\tau \qquad (S2)$$

In the case where the electrons are excited along the *z* axis with excitation of normal mode 35, the representations of the final electronic and vibrational states can be identified as B_{1u} and B_{2g} respectively. The direct product of these representations ($B_{1u} \otimes B_{2g}$) then gives rise to a B_{3u} representation, meaning that the coupling between these electronic and vibrational states yields a dipole response along the *x* cartesian direction. Therefore, activation of the *x*-component of the dipole moment is allowed via vibronic coupling when the B_{2g} vibrational mode is activated along with excitation of a B_{1u} electronic state. Likewise, B_{3g} vibrational modes coupled with the B_{1u} electronic state can give rise to B_{2u} electronic states that are polarized along the *y* direction.

When the electronic and vibrational excited states belong to B_{1u} (in the case of mode 32), the direct product representation becomes A_g. However, this totally symmetric excitation is dipole-forbidden in a molecule with D_{2h} symmetry like naphthalene.

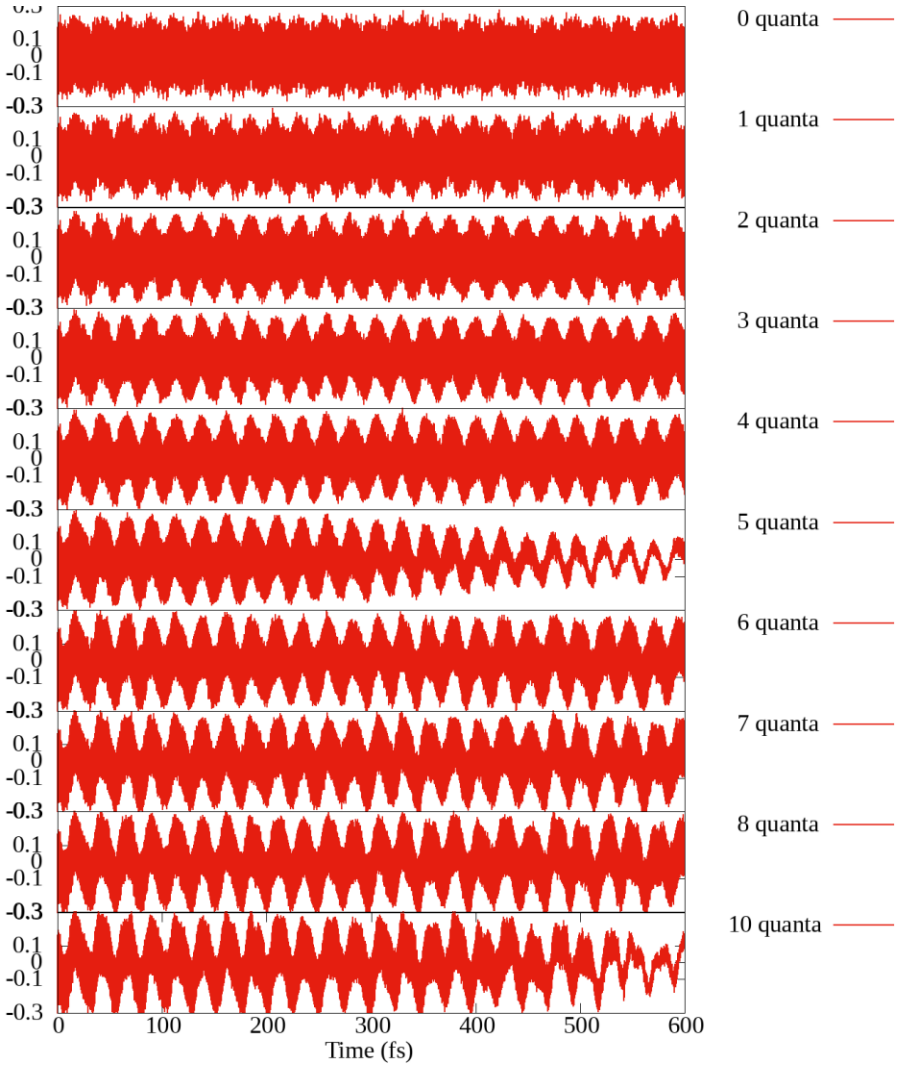

Figure D-2. *z*-component of the dipole moment when mode 32 (B_{1u}) is activated with different number of quanta.

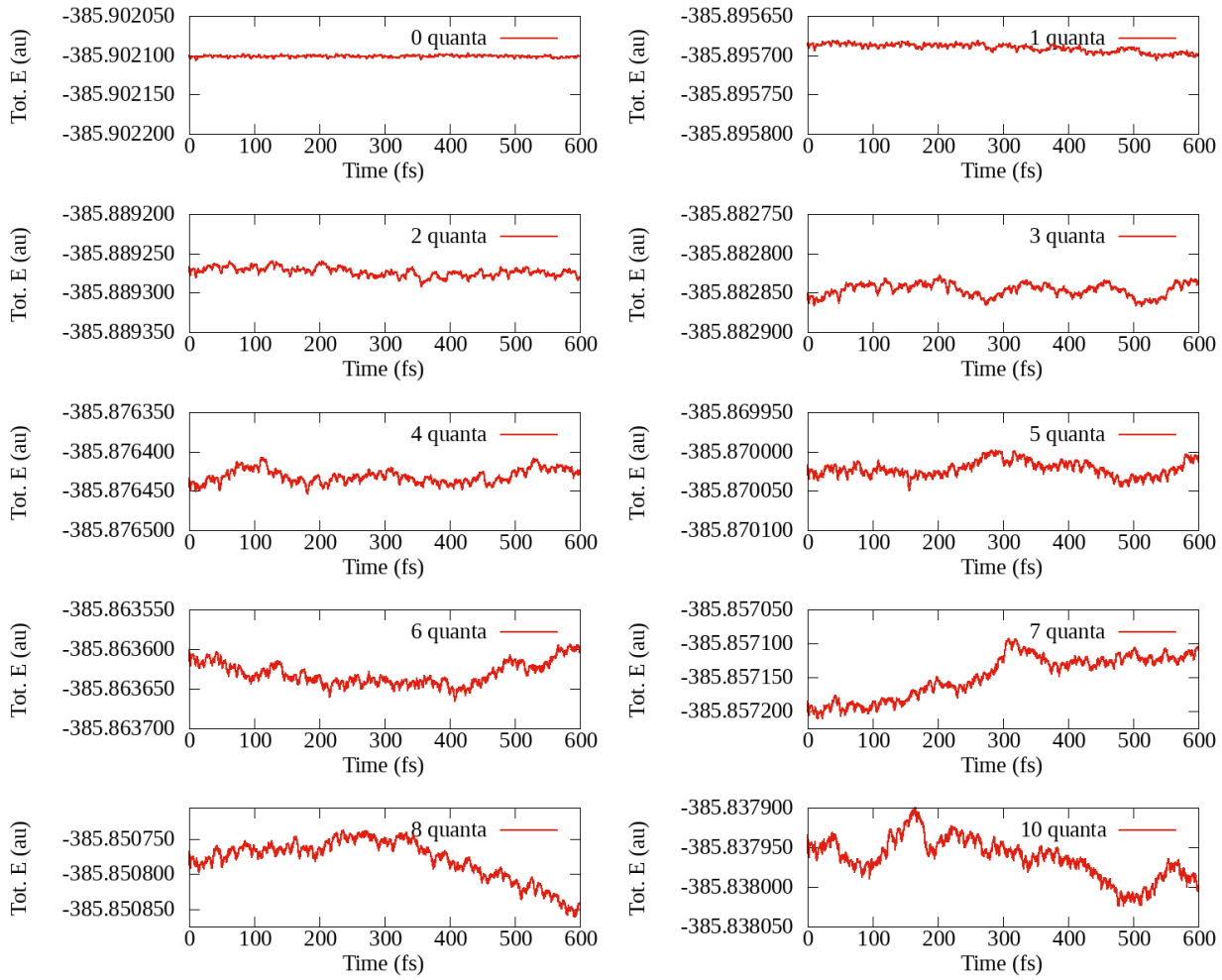

Figure D-3. Total energy conservation during an Ehrenfest molecular dynamics simulation when mode 32 (B_{1u}) is activated with different number of quanta.

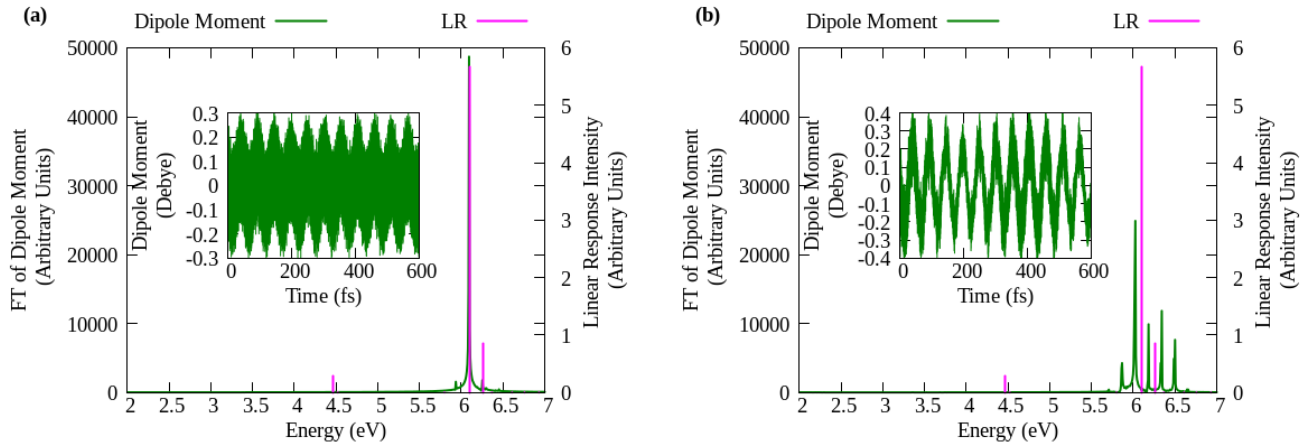

Figure D-4. Fourier transform of z-component of the dipole moment when mode 10 (B_{1u}) is activated with (a) 0 quanta and (b) 5 quanta (green) compared with the LR-TDDFT stick spectrum (pink). The insets show the time variation of the dipole moment.

Table D-4. B3LYP/6-31G(d,p) MO transitions responsible for the peaks at 5.96 eV and 6.46 eV for the most distorted geometry of naphthalene during activation of normal mode 10 (geometry at 40.0 fs). Note that the transitions with A_g irreducible representation in D_{2h} point group symmetry are forbidden, but they become allowed when the structural symmetry is lowered to C_{2v} because the transitions with A_1 representation are allowed in C_{2v} point group symmetry.

Energy (eV)	Wavelength (nm)	Oscillator strength	Transitions	Symmetry of Transitions		Weight
				D_{2h}	C_{2v}	
5.96	207.92	0.8781	HOMO – 2 → LUMO + 1	A_g	A_1	0.174
			HOMO – 1 → LUMO	B_{1u}	A_1	-0.452
			HOMO – 1 → LUMO + 2	A_g	A_1	-0.216
			HOMO → LUMO + 1	B_{1u}	A_1	0.465
6.46	192.05	0.3060	HOMO – 3 → LUMO	A_g	A_1	-0.135
			HOMO – 2 → LUMO + 1	A_g	A_1	0.466
			HOMO – 1 → LUMO	B_{1u}	A_1	0.190
			HOMO – 1 → LUMO + 2	A_g	A_1	-0.428
			HOMO → LUMO + 1	B_{1u}	A_1	-0.199

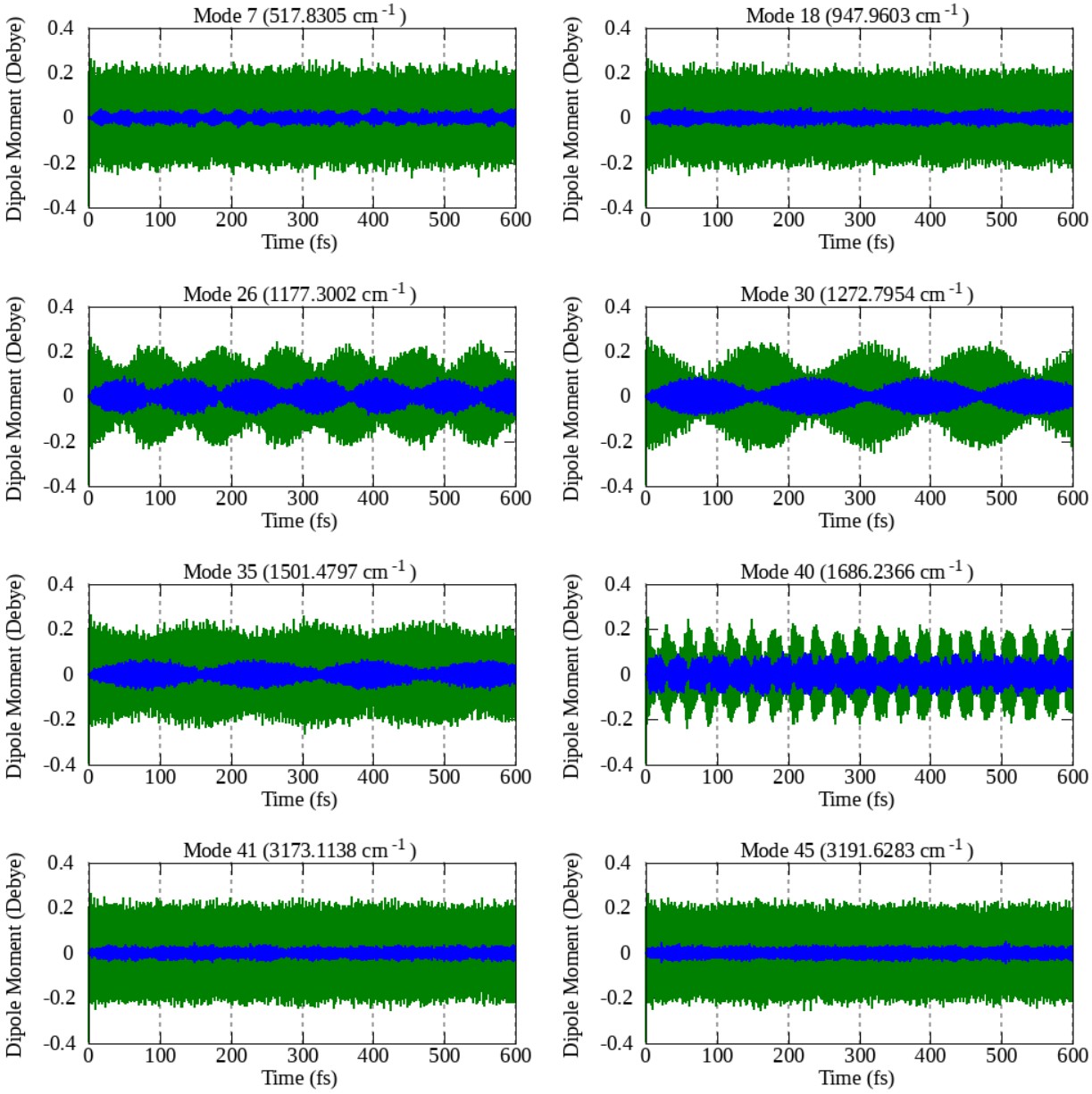

Figure D-5. Variation of dipole moment during an Ehrenfest dynamics with electrons excited along the *z* direction and B_{2g} normal modes of naphthalene are activated with zero quanta. green: *z*-component; blue: *x*-component of the dipole moment.

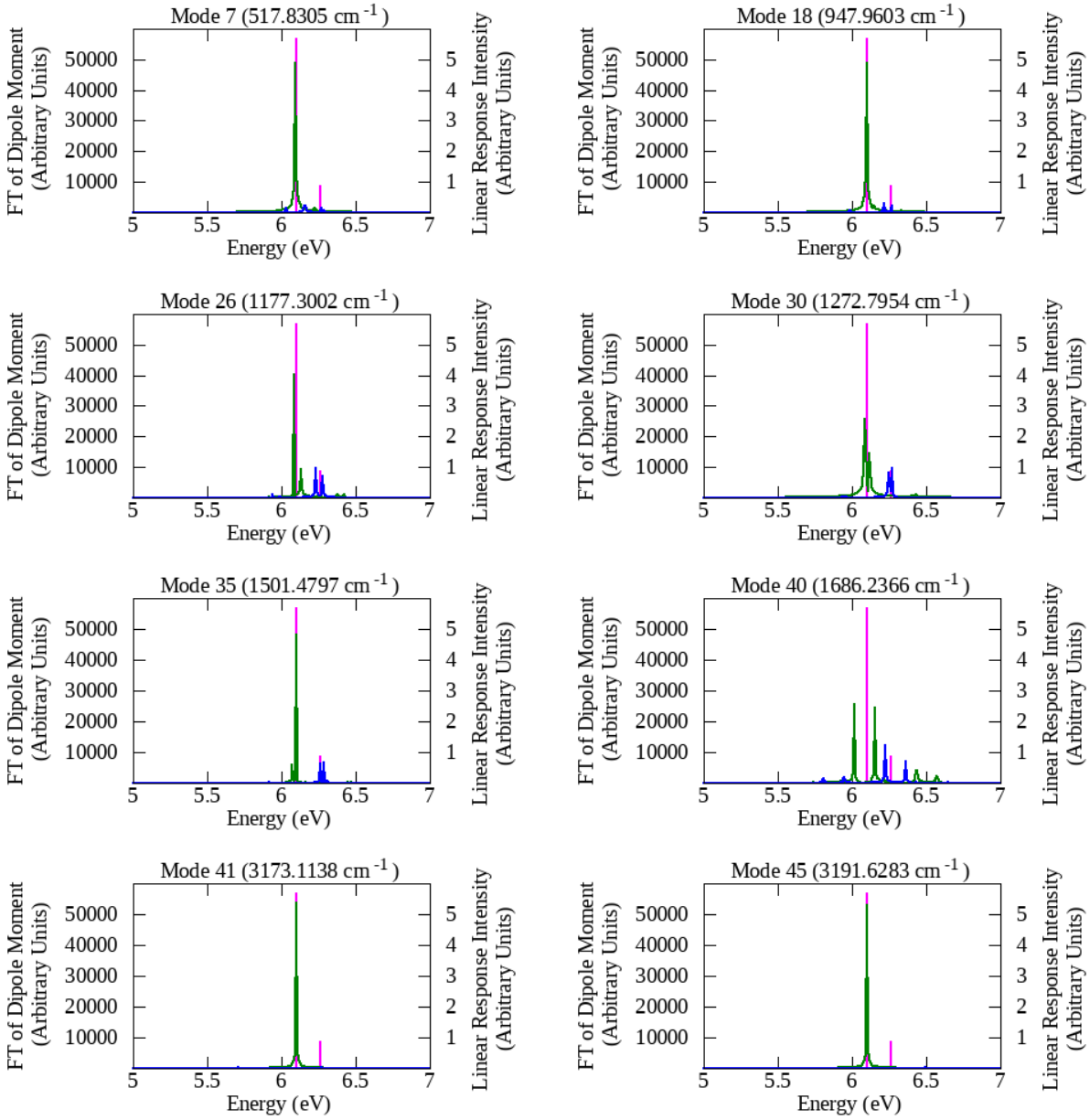

Figure D-6. Fourier transforms of dipole moment components during an Ehrenfest dynamics with electrons excited along the *z* direction and B_{2g} normal modes of naphthalene are activated with zero quanta. Peak positions are compared with the LR-TDDFT excitation energy positions. green: *z*-component; blue: *x*-component of the dipole moment; pink: LR-TDDFT stick spectrum.

Appendix E - Supporting Information for "Theoretical Insights into Plasmon-Driven Oxygen Activation on a Tetrahedral Ag_8 Cluster"

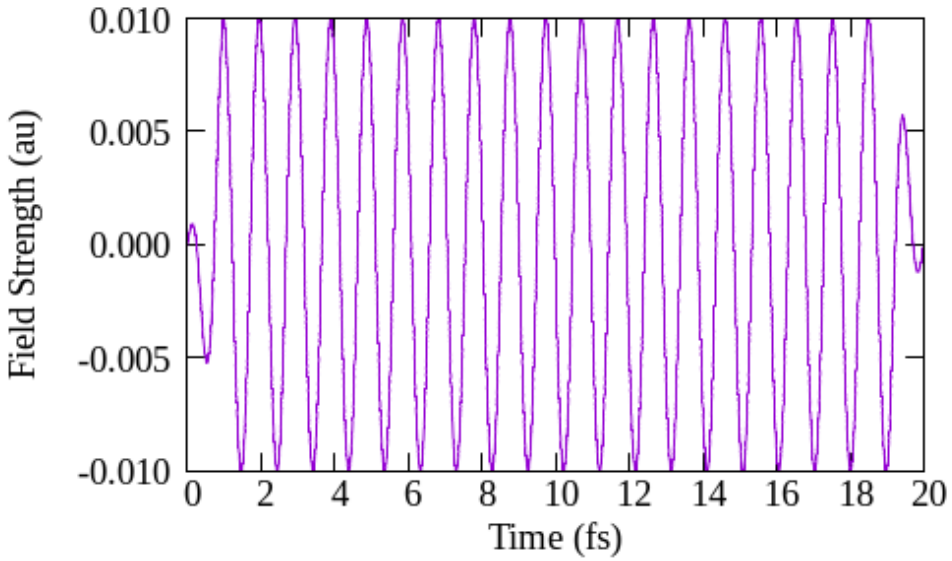

Figure E-1. Variation of the applied electric field with time. Frequency of oscillation = 4.25 eV, maximum field strength = 0.01 au.

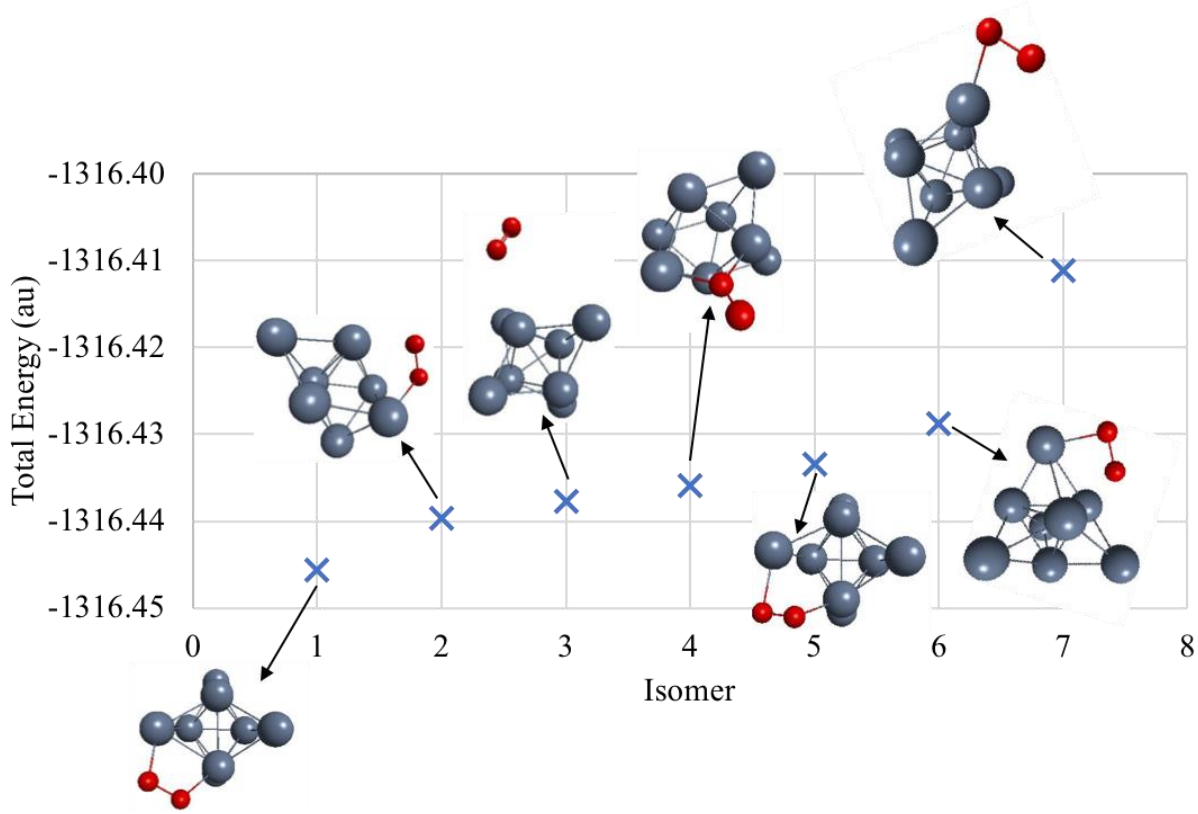

Figure E-2. Total energies of optimized structures of possible configurations of O_2 on Ag_8 cluster.

Coordinates of O_2@Ag_8-01 structure

Ag	-2.05767488	-1.64451301	0.16615035
Ag	0.40618479	0.93537617	-2.94600773
Ag	2.71477842	-1.47671688	0.39808580
Ag	0.13157415	2.28767800	1.47005939
Ag	-1.14633322	0.86721039	-0.64204210
Ag	0.39123443	-1.38710928	-1.17220759
Ag	1.70897174	0.96965933	-0.49207181
Ag	0.24318846	-0.71326888	1.52197468
O	0.00000000	0.22350860	3.59331131
O	-0.05127397	1.58141100	3.59331131

Table E-1. Energy, components of transition electric dipole moment, oscillator strengths, MO transitions and their weights for the O_2@Ag_8 composite. The alpha and beta spin orbitals are indicated as α and β respectively; the beta spin orbital transitions are shown in grey.

No.	Energy (eV)	Wavelength (nm)	Transition Electric Dipole Moments (au)			Oscillator Strength	Transitions	Weight
			X	Y	Z			
1	3.31	374	1.366	0.571	-0.193	0.1808	83α → 89α	0.1939
							83α → 91α	0.1564
							84α → 86α	0.4191
							84α → 87α	-0.2303
							84α → 88α	-0.1690
							84α → 89α	0.3592
							85α → 88α	-0.1068
							85α → 89α	-0.1004
							85α → 90α	-0.1780
							85α → 91α	0.2205
							82β → 85β	-0.3417
							82β → 86β	0.1366
							82β → 87β	-0.4036
							83β → 85β	-0.1135
							83β → 86β	0.1342
2	3.73	332	1.528	-1.303	0.889	0.4406	83α → 86α	0.1582
							83α → 87α	0.1556
							83α → 88α	-0.1684
							83α → 89α	0.3350
							83α → 90α	0.4334
							83α → 91α	-0.1319
							84α → 86α	0.1491
							84α → 87α	0.1205
							84α → 88α	0.1012
							84α → 89α	-0.1736
							85α → 90α	-0.1804
							82β → 85β	-0.1732
							82β → 86β	-0.1615
							82β → 87β	0.1623

							82β → 88β	-0.3451
							83β → 86β	0.1381
							83β → 87β	0.3417
							83β → 89β	0.1382
3	3.81	325	2.335	0.165	0.042	0.5121	83α → 87α	0.2253
							83α → 90α	-0.3015
							84α → 86α	0.2001
							84α → 88α	0.2230
							84α → 89α	-0.2410
							85α → 90α	-0.2184
							69β → 84β	0.1025
							82β → 85β	-0.2069
							82β → 87β	0.3078
							82β → 88β	0.5058
							83β → 86β	0.2953
							83β → 89β	0.1335
4	4.25	292	-0.122	0.550	2.064	0.4765	83α → 89α	0.1630
							83α → 93α	-0.1252
							84α → 90α	-0.3307
							84α → 91α	0.1143
							84α → 92α	0.1687
							85α → 91α	-0.2581
							74β → 84β	-0.1456
							78β → 84β	-0.1434
							80β → 84β	0.2191
							81β → 85β	0.2201
							81β → 87β	0.2277
							82β → 89β	0.4290
							82β → 91β	0.1653
							83β → 88β	-0.1177
							83β → 90β	-0.2026
5	4.58	271	-0.093	0.952	-0.127	0.1044	82α → 91α	0.1186
							83α → 91α	-0.1503
							84α → 92α	-0.1960
							60β → 84β	0.1257

							64β → 84β	0.3142
							64β → 88β	0.1124
							65β → 92β	0.1284
							66β → 84β	-0.1023
							73β → 84β	-0.1301
							74β → 84β	-0.1633
							76β → 84β	0.1997
							79β → 91β	0.1675
							79β → 92β	-0.2360
							81β → 85β	-0.1121
							82β → 91β	0.1390
							82β → 92β	-0.2935
							83β → 90β	-0.2257
							83β → 93β	0.2009

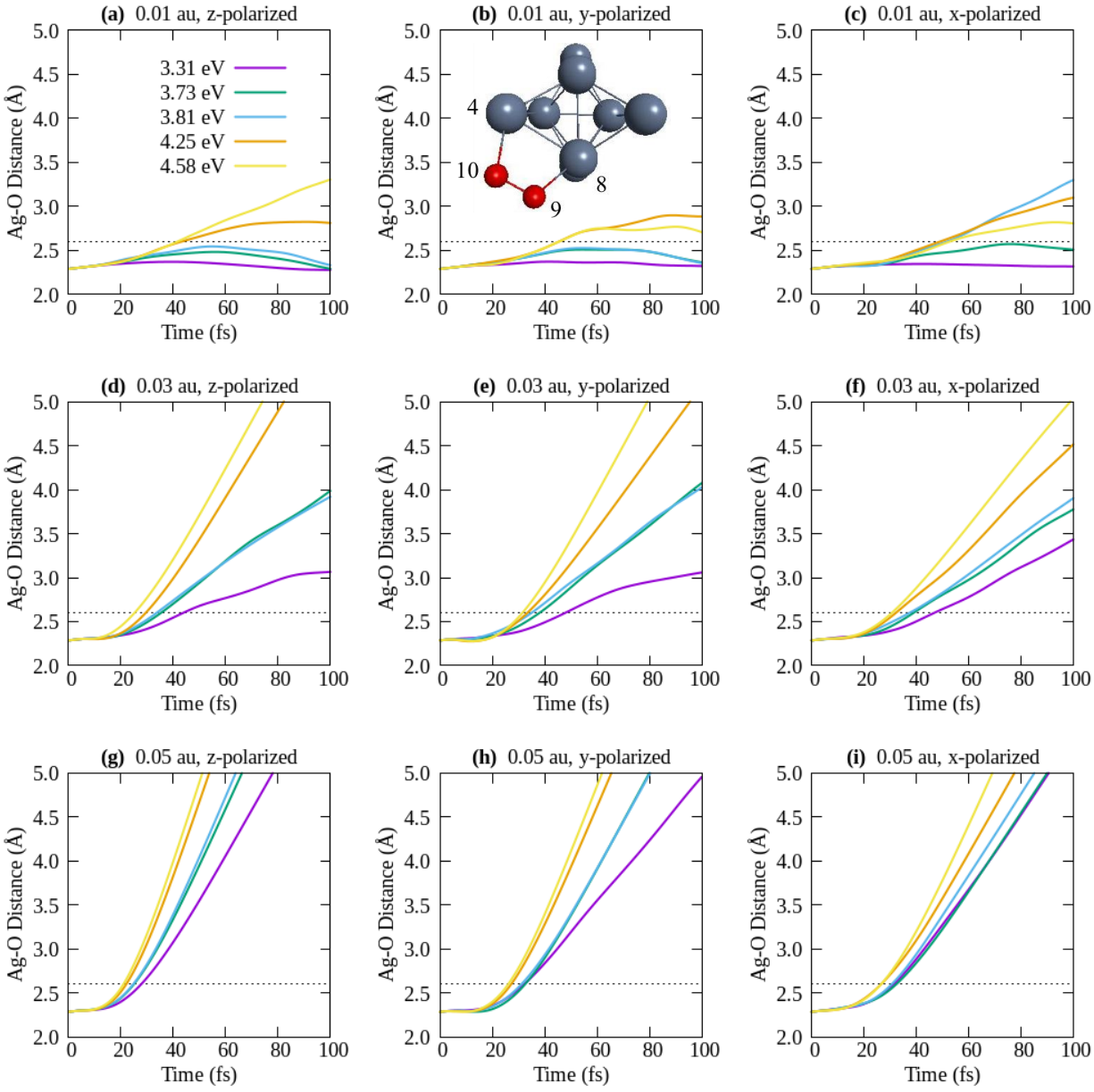

Figure E-3. Variation of Ag(8)-O(9) distance during Ehrenfest dynamics. The three rows represent the maximum field strengths of the applied field (0.01 au, 0.03 au and 0.05 au) and the three columns separate the polarization directions of the field (x, y and z). Excitation energies are shown with different colors. The horizontal dotted line marks the desorption limit of Ag-O distance = 2.6 Å considered in this work.

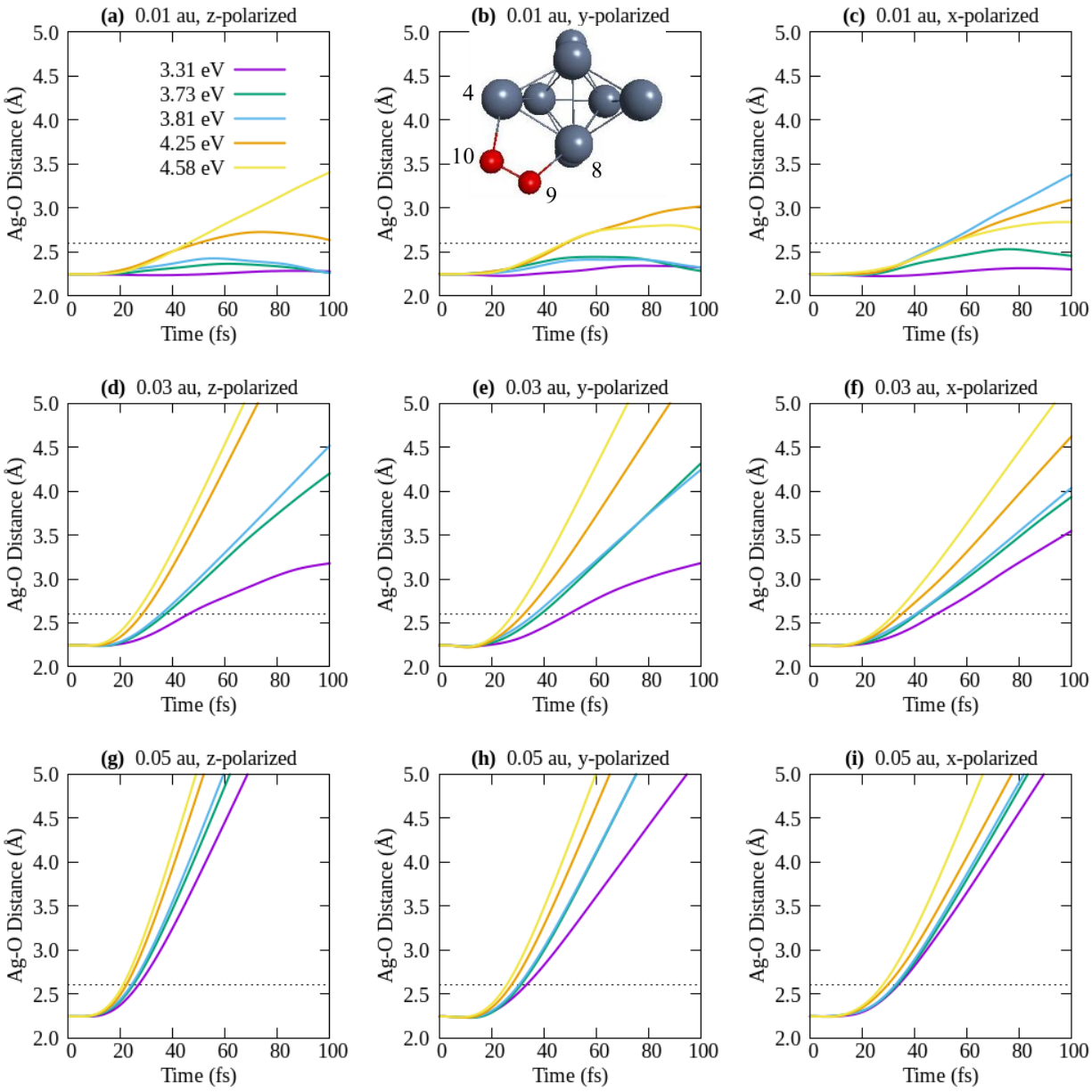

Figure E-4. Variation of Ag(4)-O(10) distance during Ehrenfest dynamics. The three rows represent the maximum field strengths of the applied field (0.01 au, 0.03 au and 0.05 au) and the three columns separate the polarization directions of the field (x, y and z). Excitation energies are shown with different colors. The horizontal dotted line marks the desorption limit of Ag-O distance = 2.6 Å considered in this work.